STUDY OF HYDRODYNAMIC BEHAVIOUR IN A CONICAL FLUIDIZED BED DRYER USING PRESSURE FLUCTUATION ANALYSIS AND X-RAY DENSITOMETRY

A Thesis Submitted to the College of

Graduate Studies and Research

In Partial Fulfillment of the Requirements

For the Degree of Doctor of Philosophy

In the Department of Chemical Engineering

University of Saskatchewan

Saskatoon

By

Michael Wormsbecker

Permission to Use

In presenting this thesis in partial fulfilment of the requirements for a Postgraduate degree from the University of Saskatchewan, I agree that the Libraries of this University may make it freely available for inspection. I further agree that permission for copying of this thesis in any manner, in whole or in part, for scholarly purposes may be granted by the professor who supervised my thesis work or, in his absence, by the Head of the Department or the Dean of the College in which my thesis work was done. It is understood that any copying or publication or use of this thesis or parts thereof for financial gain shall not be allowed without my written permission. It is also understood that due recognition shall be given to me and to the University of Saskatchewan in any scholarly use which may be made of any material in my thesis.

Requests for permission to copy or to make other use of material in this thesis in whole or part should be addressed to:

Head of the Department of Chemical Engineering
University of Saskatchewan
Saskatoon, Saskatchewan S7N 5A9
Canada

Abstract

Fluidized bed dryers (FBDs) are used in the pharmaceutical industry to remove excess moisture from granule prior to tablet formation. Currently, the hydrodynamics associated with FBDs are not fully understood and consequently a number of product quality and control issues still exist. To improve the understanding of FBDs, the hydrodynamics of drying and the influence of important fluidized bed design parameters, such as distributor design and vessel geometry, were studied using pressure fluctuation analysis and x-ray densitometry.

As granule moisture content is reduced from its initial to final state, the velocity required to fully fluidize the granule decreases and the bed voidage increases. The changes in these fluidization properties are attributed to the decrease in the interparticle force load created by a reduction in liquid bridging as moisture is removed. During constant velocity drying in a conical FBD, these fluidization properties result in a bubbling fluidization state, which evolves into a bubble coalescing regime as drying proceeds. This behaviour was identifiable using pressure fluctuation time-series analysis techniques. This demonstrates the viability of using pressure fluctuation analysis as a monitoring tool for fluidized bed drying processes.

Distributor design studies using dry and wet granule in a conical fluidized bed suggest that the punched plate design limits bubble coalescence when compared to the perforated plate and Dutch weave mesh designs. Furthermore, the Dutch weave results in extensive segregation, which is undesirable from a fluidization perspective. Local drying

hydrodynamic measurements using x-ray densitometry found that the punched and perforated plates generate a centralized bubbling core region during drying with a defluidized bed periphery in a cylindrical FBD. This fluidized core region grows as drying proceeds until the defluidized region disappears. Under the same operating conditions, a porous plate distributor creates extensive channelling and defluidization across the entire bed cross-section during the constant rate period of drying. These poor fluidization characteristics result from the porous plate introducing the gas into the bed as a fine dispersion.

Lastly, the hydrodynamics associated with the conical vessel geometry improves the circulation and mixing patterns in FBDs. This is especially the case in the entry region of the conical bed where the high inlet gas velocity prevents defluidization around the periphery of the bed. The straight walled geometry of the cylindrical bed resulted in defluidization in this area. As a result, the hydrodynamics associated with bubbling differ between the geometries over the course of drying.

Acknowledgements

As my Ph.D. comes to an end, I think it is obvious who deserve my thanks. First and foremost, I would like to thank to my supervisor, Todd Pugsley, for the opportunity to work with him, but also for providing me countless research opportunities during my Ph.D. program. These opportunities have provided me with invaluable research, but also life, experiences that I am very grateful for. It has been a pleasure working with him and I hope it continues into my future endeavours.

On that note, I would also like to thank the people, and their associated institutes, that have provided me the opportunity to collaborate with them. First, I would like to say "dank u wel" to both Ruud van Ommen and John Nijenhuis, my co-supervisors from Delft University of Technology. I had a great time working with their research group and experiencing their country during the time I was there. Also, I would like to thank Helen Tanfara of Merck Frosst Canada Ltd. She has provided me with endless support on the work I did during my short time at Merck Frosst.

Finally, I would like to thank two of my closest colleagues during my studies – Gareth Chaplin and Jason Wiens. I would never, ever, have made it through these years without either of them. Not because of their abilities as researchers, but for enabling me in my endless pursuit of coffee, or better yet beer! As we all know, a Ph.D. thesis has its ups, downs, successes and failures and through it all they were there to experience it with me. I hope it was as fun for them as it was for me.

“An expert is a person who has made all the mistakes that can be made in a very narrow field.” Niels Bohr (1885 - 1962)

Table of Contents

List of Tables

List of Figures

CHAPTER 1 - Introduction

Contribution to Overall Study

This chapter provides insight regarding fluidization and the relevant theory related to this thesis. Firstly, the concept of fluidization is explained along with its importance to the chemical process industry. Secondly, the chapter then goes on to present fundamental fluidization theory and its relevance to drying. Thirdly, the motivation of this thesis is presented, along with the underlying objectives.

1.1 Fluidization

In its simplest terms, fluidization is a physical process that transforms solid particles into a fluidized state through suspension in a liquid or gas [1]. Fluidization is most commonly considered with gas-solid systems in mind, but the use of liquid-solid contacting is also a very important research area. However, for the purpose of this thesis, only gas-solid fluidization will be considered as this type of solids contacting is used in fluidized bed drying.

Although it may be difficult to imagine, proper gas-solids contacting will result in the solids taking on similar attributes to that of a fluid. In simple terms, fluidized solids will take the shape of their container, a classical definition of a fluid. More specifically though, less dense material will float, levels between tanks subjected to identical head pressure will equalize and a pressure drop across a bed of fluidized solids will exist, and be appreciable; all similar to that of liquids [1]. These properties allow the chemical process industry to carry out many processes involving fluidization of solids as the increased ability of solids to flow, along with other process specific advantages, can be exploited.

1.1.1 Fluidization and Drying

The application of fluidization is widespread in the chemical process industry. For example, processing units including catalytic reactors, combustors, incinerators and dryers all use fluidized bed technology to optimize the efficiency of their operation. Fluidized bed technology is used for many reasons, but mostly due to its superior heat and mass transfer capabilities obtained from the mixing phenomenon generated by fluidization.

As mentioned above, fluidized beds are used throughout industry as a means of drying material. Crushed minerals, pharmaceuticals, polymers, fertilizers, and agriculture products are all dried via fluidized beds. Fluidized bed drying processes are advantageous because they are compact and have low capital costs as compared to alternative dryer technologies. They are also simple to construct and have few moving parts, creating

reliable operation and low maintenance. Fluidized bed dryers generate highly efficient thermal conditions through rapid mixing established by fluidization. This allows for good temperature control and distribution throughout the bed. Excellent mass transfer capabilities, which are important to the drying process, are produced from the extensive mixing as well. Finally, fluidized beds are useful for handling friable materials as fluidization creates a smooth liquid-like flow of particles. The possibility for particle breakage and attrition is still present but is believed to be reduced in fluidized bed operation as compared to other mechanical-based dryers [1].

The pharmaceutical industry is one such industry that incorporates fluidization into its manufacturing processes. Many solid dosage pharmaceuticals are dried in batch fluidized bed dryers prior to tablet formation. Hot air is passed through a bed of wet particles (a.k.a. granule) as a means to remove the moisture. Fluidized bed drying is chosen for this application because fluidization promotes an environment that results in uniform drying and reduces the residual moisture content in the granule to very low levels. Furthermore, batch fluidized bed dryers provide favourable conditions for drying processes that require strict quality control or contain heat sensitive materials. This is because the mixing properties in batch fluidized bed dryers bring about homogeneity throughout the bed, therefore limiting moisture and temperature gradients.

1.1.2 Fluidization Regimes

The understanding of fluidization regimes is a fundamental aspect of fluidization research. By changing the fluidization gas velocity, distinct fluidization states, referred to

as regimes, that have unique characteristics are encountered. The differences between the classical fluidization regimes as outlined by Kunii and Levenspiel [1] are summarized below and illustrated schematically in Fig. 1.1 [2].

At very low gas velocities, gas simply percolates through the voids between the stationary particles as the momentum carried by the gas is too low to fluidize the particles. Increasing the gas velocity will eventually result in a state in which the drag induced by the upward flowing gas will balance out with the weight of the particles. This fluidization state is commonly referred to as incipient or minimum fluidization; the point at which the particles are just fluidized. The gas velocity associated with minimum fluidization is referred to as the minimum fluidization velocity. Increasing the gas velocity beyond that of minimum fluidization will result in excess gas being introduced into the fluidized bed. The excess gas will coalesce to form bubbles causing greater instability in the bed. This regime, as its name implies, is known as the bubbling regime. The bubbling regime also demonstrates more aggressive particle movement within the bed itself as particles are carried up through the bed in the wake created by the passing bubble. Operating at higher gas velocities within the bubbling fluidization regime will result in the formation of larger bubbles. If a situation occurs where a bed is sufficiently deep as compared to its width, there is a potential for bubbles to become so large that they spread across the entire bed cross-section. This is referred to as a slugging regime. Depending on the characteristics of the fluidized particles, different types of slugging regimes exist.

Eventually, a maximum stable bubble size is reached in the bubbling fluidization regime and bubble splitting will begin to replace bubble coalescence as the primary mechanism of bubble interaction in the bed. The point at which bubble splitting dominates bubble coalescence is marked as the transition to the turbulent fluidization regime. In the turbulent fluidization regime, bubble splitting results in irregular shaped voids which appear as streaks or channels within the fluidized bed. The proposed mechanism describing the bubble splitting phenomenon has been reported by Cai et al. [3].

Further increasing the gas velocity past the turbulent fluidization regime will result in a situation where solids carry-over, known as entrainment, becomes significant. This occurs because the terminal velocity of the fluidized particles is exceeded by the velocity of the fluidization gas, hence entraining the particles in the gas flow stream. There are two important fluidization regimes associated with this type of behaviour: fast fluidization and pneumatic conveying or pneumatic transport. As mentioned, these types of regimes occur at very high fluidization velocities and therefore are employed in operations where solids flow-through is desirable (e.g., circulating fluidized beds).

The ability to differentiate between fluidization regimes and predict their transition points is critical to efficient process operation. For example, work by Grace and Sun [4] demonstrates that improved heat and mass transport properties are encountered when transitioning into the turbulent fluidization regime. Conversely, understanding undesirable states of fluidization, namely defluidization, can be used to avoid such

operation that could be detrimental to the process operation. With all this in mind, it is important to remember that fluidization behaviour varies due to particle and fluidized bed characteristics. Therefore it is imperative to distinguish fluidization regimes with specific particles and bed configurations in mind.

1.2 Geldart Classification

The Geldart particle classification system is the primary means of predicting fluidization behaviour based on the size and density of particles [5]. Geldart determined four distinct fluidization behaviours within a wide range of these two particle characteristics. They are described by Kunii and Levenspiel [1] as follows:

Geldart C (Cohesive): Very fine particles which are difficult to fluidize because of their high interparticle forces. Typically these particles result in plug flow in small-scale fluidized beds and channeling in larger scale fluidized beds.

Geldart A (Aeratable): Relatively small size and/or low density particles that fluidize well. Smooth fluidization at low velocities and controlled bubbling with relatively small bubbles is observed at higher velocities. Visible circulation of particles exists even when in the presence of only a few bubbles.

Geldart B (Sand-like): Larger and denser particles than compared to Geldart A particles which result in vigorous bubbling and distinct coalescence. Gross circulation of particles results from the aggressive bubbling.

Geldart D (Spoutable): Very large and/or dense particles that result in channeling or large exploding bubbles due to rapid coalescence. Slower moving bubbles with a low voidage dense phase exists with these particles as compared to the other fluidization states.

Fig. 1.2 provides a schematic of the particle classification divisions described above under ambient conditions. Obviously, the transitions between particle classifications are not as rigid as shown here. Other factors, including particle size distribution of solids and interparticle forces, will have an influence on the fluidization behaviour and therefore transitions between particle classifications. Thus, when using Geldart's classification to describe particle fluidization behaviour, all factors that contribute to the hydrodynamic behaviour must be considered.

1.3 Interparticle Forces

The role of interparticle forces in fluidization processes is of great importance. Interparticle forces impact the fluidization behaviour which in turn can affect the quality of fluidization in fluidized bed processes. The interparticle forces important to the fluidization conditions encountered in this thesis are briefly outlined in this section along with their importance to the understanding of fluidization behaviour.

1.3.1 van der Waals Forces

The intermolecular force between two or more molecules is known as the van der Waals force. Dipole-dipole, dipole-induced-dipole, and induced–dipole–induced-dipole

interactions are the interactions incorporated into the van der Waals force. The above mentioned interactions between molecules within different particles create the interparticle forces attributed to the van der Waals force. It is important to note that even though van der Waals forces are very small, they can still contribute to the interparticle forces between particles, which influence particle interaction in fluidized beds.

1.3.2 Electrostatic Forces

The interparticle forces created by electrostatic charge are known as electrostatic forces. These types of forces can have adverse effects on fluidization behaviour and in chemical processes. For example, these forces can create dust clouds, which can spark and potentially lead to ignition or explosion within fluidized beds. Electrostatic forces are significant in a dry fluidization media as the electrostatic forces distinctly suppress bubble formation in fluidization containing fine powders [6].

Electrostatic forces exist due to the presence of an electric charge between particles. These charges are generated through the separation of opposite charge when two surfaces are in contact with each other. Upon separation, equal and opposite charges are carried by each surface. There are three important electrostatic forces, as presented by Seville et al. [7]:

Coulombic: Force between two charged particles.

Space-charge: Interaction forces of charged particles in close proximity to one another.

Image-charge: Induced when a charged particle approaches a surface. The charged particle is attracted to the surface as if there was an oppositely charged particle on the other side of that surface at a symmetrically equal separation distance.

1.3.3 Electrostatics and Humidity

In the presence of water, electrostatic charge is dissipated. This means that electrostatic forces present in dry bed fluidization experiments will vary to some degree based on the humidity of the air used to fluidize the particles. Low humidity will result in charge build up and the particles may take on cohesive fluidization behaviour if particles are fine enough. As humidity increases, charge dissipation occurs and a decrease in the overall interparticle forces takes place, resulting in smoother fluidization. However, at very high relative humidity, small amounts of liquid can condense from the fluidization air onto the particle surface. This condensation smoothes the asperities on the surface of particles effectively bringing them closer together. The presence of this adsorbed liquid layer results in an increase in interparticle forces as compared to van der Waals forces. The effect of humidity on interparticle forces described above is reported by Coelho and Harnby [8] and Karra and Fuerstenau [9].

1.3.4 Liquid Bridging Forces

If a significant film of mobile liquid is present on the surface of the particles, points of contact between particles will result in liquid bridges. The strong boundary forces associated with the liquid surface tension and the capillary forces generated by the curvature of the liquid form a bridge that draws the particles together [7]. Liquid bridging

forces greatly increase interparticle forces when considered with respect to van der Waals forces and have a significant impact on fluidization behaviour. A schematic of a liquid bridge is shown in Fig. 1.3.

1.3.5 Comparison of Interparticle Forces

Fig. 1.4 illustrates the theoretical tensile strengths of agglomerates formed with some of the different interparticle forces discussed above. As can be seen in this figure, van der Waals, adsorbed liquid layer and liquid bridging forces become significant below particle sizes of 1, 80 and 500 μm, respectively. This indicates that although the van der Waals and adsorbed liquid forces exist, they only have relevance to Geldart C and some A particles whereas liquid bridging forces are significant to all of the Geldart particle classifications.

1.3.6 Interparticle Forces and Fluidization

Molerus [11] was the first to relate the effect of interparticle forces to the classical particle classification of Geldart. Molerus determined that the difference between Geldart A and C powders was related to the strong cohesive forces attributed to Geldart C particles as compared to A. The difference between Geldart A and B powders was simply the unimportance of cohesive forces in Geldart B particles. Geldart A powders have significant interparticle forces compared to the drag force exerted on the particle. In Geldart B powders, the interparticle forces are considerably smaller. As for the physical transition between Geldart B and D particles, the dominance of the weight force of the larger D powders causes variations in the fluidization properties of B and D powders.

It is apparent from this that altering the magnitude of interparticle forces through the addition of liquid will result in different fluidized bed behaviour in particles as well. Seville and Clift [12], and later McLaughlin and Rhodes [13], took the work of Molerus a step further and included the influence of non-volatile liquid on fluidization behaviour of Geldart B particles. Both groups found that indeed a transition from Geldart B to A and even to C can occur in the presence of liquid. The notion of liquid addition is analogous to liquid removal processes such as drying.

1.4 Drying Fundamentals

Fluidized bed drying is not as simple a process as one may assume it to be. There are different mechanisms and therefore different drying characteristics that exist over the course of drying a batch of solids. The drying kinetics of the bulk solids phase and of the individual particles are of equal importance as proper drying of solids material depends on both. The material discussed in the following sections related to drying is taken from McCabe et al. [14] and Rhodes [15].

1.4.1 Constant Rate Drying Regime

The constant rate drying regime occurs when solids contain excess amounts of free moisture as compared to the humidity of the fluidization gas. In this drying regime, the particles are so wet it is as if the particles are completely covered with a continuous thin film of water. If the particles are non-porous, then the water removed is essentially surface moisture. However, if the particle has significant porosity, then water from within the pores will migrate to the surface and also be removed.

This abundance of moisture on the surface of the particles results in heat transfer limitations being reached very rapidly within the dense bed. The fluidization air reaches the saturation temperature of the entering gas and therefore cannot dry the particles further. Therefore the constant rate regime is limited by heat transfer capabilities of the process conditions. As a result, it is also referred to as heat transfer limited drying. Solids dry at their maximum rate in the constant rate drying regime.

1.4.2 Falling Rate Drying Regime

As moisture content of the solids decreases past a certain point, the rate of drying starts to decrease as well. This critical point, denoted as the critical moisture content, occurs when a continuous film of water cannot be maintained on the surface of the particles. For non-porous solids, this takes place when the surface moisture is completely evaporated. In porous media, the critical point is when the rate of moisture removal from the particle does not equal the rate of evaporation under saturation conditions.

Once the critical free moisture content is surpassed, the amount of water held by the solids does not allow heat transfer conditions to reach equilibrium. This results in the increase of the exiting fluidization gas temperature past the saturation temperature of the entering gas. This occurs because the mass transfer of moisture from within the granule to the surface of the particle cannot occur fast enough. The mechanism controlling this regime is therefore the diffusion rate of bound moisture from within the solids. The falling rate regime is also known as diffusion limited drying.

Fig. 1.5 illustrates a batch drying operation representative of the drying of pharmaceutical granule. The drying curve exhibits both constant and falling rate drying regimes. Fig. 1.5 also demonstrates the exiting gas temperature profile. Before the critical point, the temperature is constant at the saturation temperature, but as the rate of drying decreases the temperature increases towards the inlet temperature.

1.4.3 Single Particle Drying Kinetics

As the particle is dried, the radial distribution of the moisture content within the particle will change, with the centre of the particle being the wettest. The particle will dry from the outside towards the middle until the equilibrium moisture content is reached throughout the particle.

Unfortunately, particle drying characteristics can change as a particle dries. Solids can experience shrinkage as the moisture bound within a relatively non-porous solid is evaporated. Also, the outer surface of the particle can lose a considerably greater amount of moisture than compared to the interior of the particle. This results in the outer surface contracting against the inner volume that is not changing in size. Ultimately, the dry outside layer can check, crack or warp depending on the severity of the differential moisture content within the particle. Diffusivity also will change as the outer surface dries. This can further limit the movement of moisture from the inner portions of the particle and contribute to the distorting effects. The combination of shrinkage and decrease in diffusivity can lead to the formation of a skin-like layer on the surface of the

particle. This is known as casehardening. Casehardening traps the bound moisture in the particle producing a situation that makes drying the particle virtually impossible.

Single particle kinetics can be controlled by the rate of drying. By increasing the inlet gas humidity, the rate of drying decreases as the driving force, which is the moisture content between the drying air and particles, is limited. Decreasing the rate of drying will also create a more uniform moisture distribution through the particle. Furthermore, the potential for shrinkage and casehardening will be reduced drastically.

1.5 Pressure Fluctuations

The use of pressure fluctuations to distinguish details of fluidized bed hydrodynamic states has been widely accepted [16]. Current research tools such as electrical capacitance tomography (ECT) and x-ray densitometry imaging are feasible to determine fluidized bed hydrodynamics through local voidage profiles in small scale fluidized bed units, as in research, but have not be proven sufficient for monitoring larger scale units. Pressure fluctuation measurements have great potential to be used as a means of monitoring fluidized bed processes due to its simplicity and ease of application. Pressure fluctuations can be employed as a measure of fluidization regimes or merely as an early warning system for the onset of poor operating conditions in fluidized beds.

Pressure fluctuations in fluidized beds are generated by temporary changes in local bed voidage and gas velocity. These changes come about from a multitude of phenomena that occur during the fluidization process (bubble generation, passage,

coalescence, bubble eruption, etc.). These phenomena create compression waves of various magnitudes that propagate and attenuate through fluidized beds depending on the source. As described by van der Schaaf [17], the passage of a single bubble through a bed of particles generates a pressure fluctuation that can be broken down into three phases (see Fig. 1.6).

First phase: Corresponds to bubble formation at the distributor. The homogenous oscillation illustrates the pressure variation experienced through changes in local voidage in the bed due to particle acceleration and deceleration caused by bubble formation.

Second phase: An excited state caused by the uplifted particulate mass by the gas bubble. The sudden pressure decrease below the pre-pulse state in the second phase is a result of the void space left by the passing bubble.

Third phase: Represents bubble eruption at the bed surface. After this stage the bed pressure returns to its pre-pulsed state.

Inherently, this type of monitoring tool seems limited due to its dependence on local measurements. However, extensive research by van Ommen [18] has proven that one pressure probe is sufficient for monitoring lab scale fluidized beds. Van Ommen has developed a statistical technique, referred to as the S-statistic, to evaluate the hydrodynamic state of fluidized bed systems. The S-statistic utilizes pressure fluctuations measurements in its evaluation since they are known to indicate variations in

hydrodynamics. The S-statistic compares the difference between two hydrodynamic states using attractor reconstruction of the pressure time-series. An attractor is analogous to a "fingerprint" characterizing the hydrodynamic state of a fluidized bed.

The benefit of the S-statistic is that it is capable of identifying subtle changes in hydrodynamic states that are otherwise indistinguishable from other monitoring techniques such as bed pressure drop. Furthermore, differences noted by the S-statistic allow for a true mathematical comparison between hydrodynamic states which can be used as a means to gauge the degree of change in hydrodynamics from a reference state. The problem with this method, however, is that the S-statistic does not provide specific information about the hydrodynamics of the system, only that they have changed. From a monitoring perspective, this limits its overall effectiveness as other techniques would have to be used if distinguishing the phenomena is important.

The S-statistic has recently been extended to fluidized bed dryers at the University of Saskatchewan by Chaplin [19]. This work has successfully identified the S-statistic as a capable analysis tool for monitoring fluidized bed dryers. With respect to the hydrodynamics, the S-statistic identified two stable hydrodynamic states during drying; one at the beginning and the other at the end of the drying process. They have linked the change in hydrodynamics to the influence of moisture as the granule dries. However, because the S-statistic does not provide quantitative information about the hydrodynamics, the hydrodynamic changes that result during the drying process are not understood.

In this thesis, the hydrodynamic analysis is limited to the discussion of the hydrodynamics with respect to its global phenomena. Global phenomena refer to the various events associated with bubbling in a fluidized bed (i.e. bubble formation, passing, coalescence and eruption at the bed surface). This is because only one pressure fluctuation measurement, which was located in the dense bed, was taken during all experiments. In order to separate the pressure signal caused by the phenomena of passing bubbles at a specific location in the fluidized bed from that of the other pressure waves generating phenomena described above, cross-spectral analysis of two simultaneously measured signals is required. Typically, the second measurement required is positioned in either the windbox or just above the distributor plate where bubble passage does not occur.

Fortunately, the global hydrodynamics are still indicative of the bubble behaviour in fluidized beds so the analysis in this study is valuable. However, the hydrodynamic data resulting from the analysis techniques at the given measurement location will not be directly related to the passing of bubbles at the measurement point. Rather the analysis will provide a general state of the hydrodynamics.

1.6 Project Motivation

Research on fluidized bed dryers has focused primarily on the use of pressure fluctuation analysis, namely the S-statistic, as a tool for monitoring the drying process. However, limited attention has been given to understanding the hydrodynamics

associated with fluidized bed dryers, namely the influence of moisture on the fluidization behaviour. To complement basic understanding, as well as to get a better overall understanding of fluidized bed drying hydrodynamics, design features of fluidized beds are also important to consider. Other than operating parameters such as bed loading and superficial gas velocity, distributor design as well as vessel geometry have an impact on the hydrodynamics of drying. With this wide variety of hydrodynamic studies regarding fluidized bed drying, monitoring of drying processes using the S-statistic, or any other techniques, will become more meaningful.

1.7 Objectives

This thesis will investigate fluidized bed drying hydrodynamics as it relates to the pharmaceutical industry. The influence of moisture on hydrodynamic behaviour, along with distributor design and vessel geometry effects, will be examined. Pressure fluctuation analysis will be used as the primary measure of hydrodynamics in this thesis. However, x-ray densitometer will also be used to measure localized hydrodynamic behaviour. These objectives will be met by conducting the following studies.

1. The influence of moisture on the fluidization behaviour of porous pharmaceutical granule
2. Interpretation of the hydrodynamic behaviour in a conical fluidized bed dryer
3. Distributor induced hydrodynamics in a conical fluidized bed dryer containing dry pharmaceutical granule
4. The influence of distributor design on fluidized bed dryer hydrodynamics

5. Evaluation of distributor level hydrodynamics using one-dimensional x-ray densitometry imaging in a fluidized bed dryer
6. The influence of vessel geometry on fluidized bed dryer hydrodynamics

This thesis is formatted as a manuscript-based thesis. Therefore, each of the above studies is presented as a chapter, with a relevant literature review and reference list presented in each chapter.

1.8 References

[1] D. Kunii, O. Levenspiel (1991). Fluidization Engineering 2nd Ed., Butterworth-Heinemann, London, p. 1-92.

[2] K.S. Lim, J.X. Zhu, J.R. Grace, Hydrodynamics of gas-solids fluidization, Int. J. Multiphase Flow 21 (1995) 141-193.

[3] P. Cai, Y. Jin, Z.-W. Wang. Mechanism of flow regime transitions from bubbling to turbulent fluidization. AIChE J. 36(6) (1990) 955-956.

[4] J.R. Grace, G. Sun, Influence of particle size distribution on the performance of fluidized bed reactors, Can. J. Chem. Eng. 69 (1991) 1126-1134.

[5] D. Geldart, Types of gas fluidization, Powder Technol. 7 (1973) 285-292.

[6] J.A. Agbim, A.W. Nienow, P.N. Rowe. Inter-particle forces that suppress bubbling in gas fluidized beds, Chem. Eng. Sci. 26 (1971) 1293-1294.

[7] J.P.K Seville, U. Tüzün, R. Clift (1997). Particle mechanics, in: B. Scarlett, & G. Jimbo (Eds.), Processing of particulate solids, Blackie Academic & Professional, London, p. 99.

[8] M.C. Coelho, N. Harnby, Moisture bonding in powders, Powder Technol. 20 (1978) 201-205.

[9] V.K. Karra and D.W. Fuerstenau, The effect of humidity on the trace mixing kinetics in fine powders, Powder Technol. 16 (1977) 97-105.

[10] H. Rumpf (1962). Strength of granules and agglomerates, in: Knepper, W.A. (Ed.), Agglomeration, Wiley, New York, p. 379.

[11] O. Molerus, Interpretation of Geldart's type A,B,C and D powders by taking into account interparticle cohesion forces, Powder Technol. 33 (1982) 81-87.

[12] J.P.K. Seville, R. Clift, The effect of thin liquid layers on fluidisation characteristics, Powder Technol. 37 (1984) 117-129.

[13] L. McLaughlin, M. Rhodes, Prediction of fluidized bed behaviour in the presence of liquid bridges. Powder Technol. 114 (2001) 213-223.

[14] W.L. McCabe, J.C. Smith, P. Harriot (2001). Drying of Solids, in: E.D. Glandt, M.T. Klein, T.F. Edgar (Eds.), Unit Operations of Chemical Engineering, McGraw-Hill, New York, p.773.

[15] M. Rhodes (1998). Size Enlargement, Introduction to Particle Technology, John Wiley & Sons, New York, p. 267.

[16] H.T. Bi, N. Ellis, I.A. Abba, J.R. Grace, State-of-the-art review of gas-solid turbulent fluidization. Chem. Eng. Sci. 55 (2000) 4789-4825.

[17] J. van der Schaaf, Dynamics of Gas-Solids Fluidized Beds, Ph.D. Thesis, Delft University of Technology, 2002.

[18] J.R. van Ommen, Monitoring Fluidized Bed Hydrodynamics, Ph.D. Thesis, Delft University of Technology, 2001.

[19] G. Chaplin, Monitoring Fluidized Bed Dryer Hydrodynamics Using Pressure Fluctuations and Electrical Capacitance Tomography, Ph.D. Thesis, University of Saskatchewan, 2005.

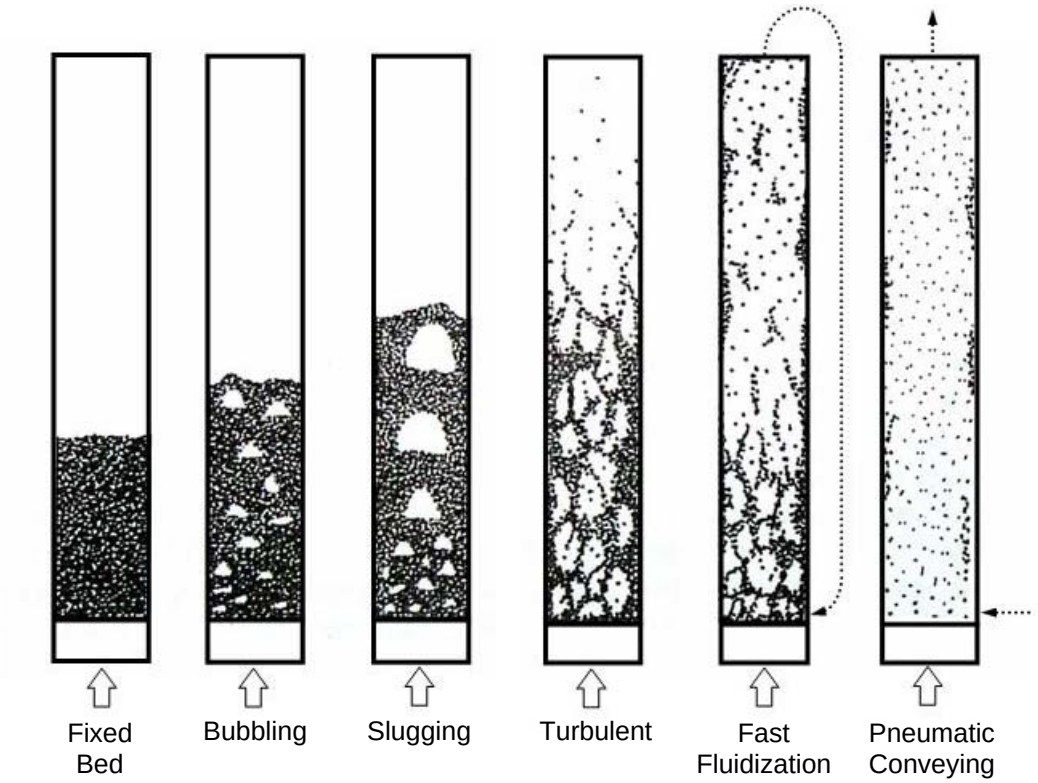

Figure 1.1: Gas-solid fluidization regimes (modified after Lim et al. [3]).

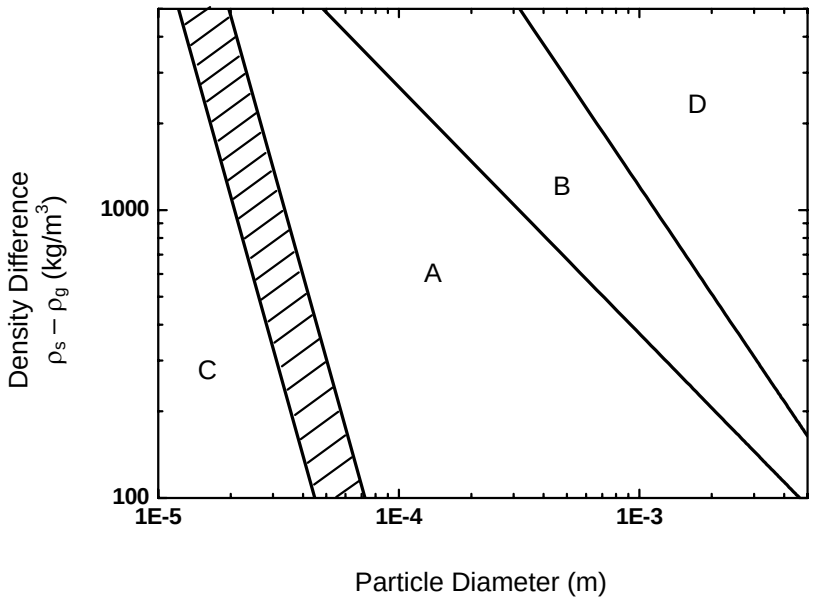

Figure 1.2: Geldart classification of particles (modified after Kunii and Levenspiel [1]).

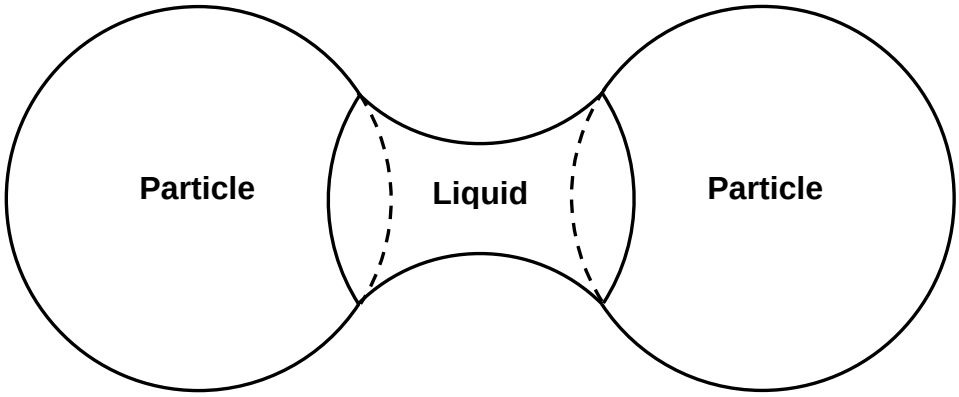

Figure 1.3: Schematic of a liquid bridge.

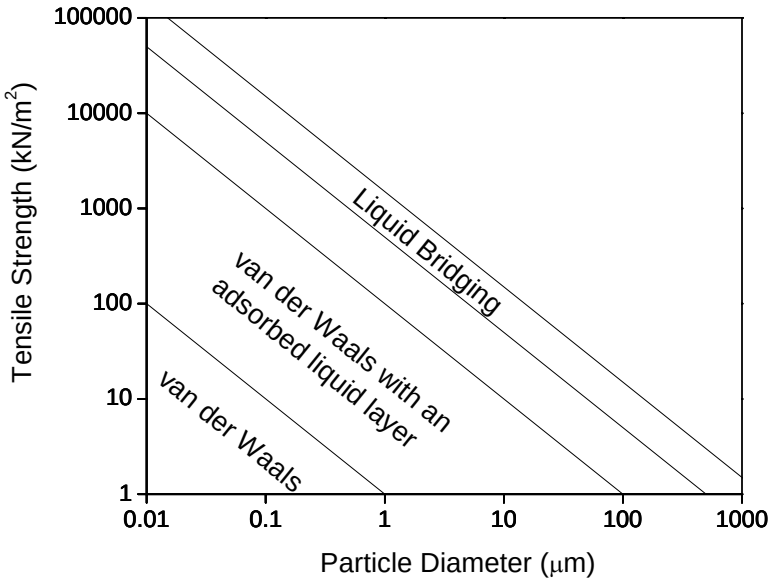

Figure 1.4: Bonding strengths of various interparticle forces (modified after Rumpf [10]).

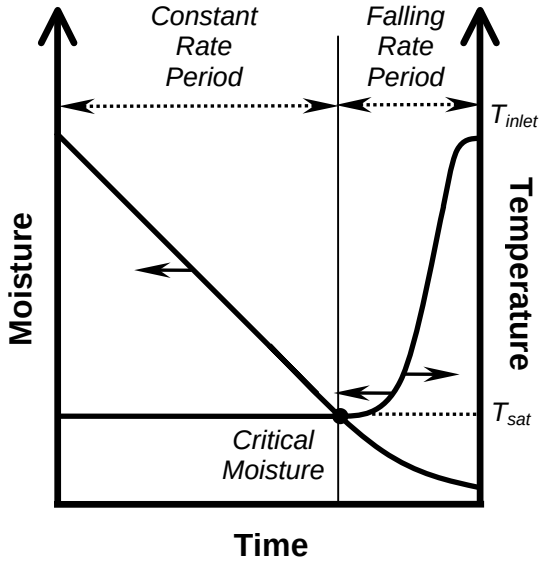

Figure 1.5: Moisture and temperature characteristics of drying (modified after Kunii and Levenspiel [1]).

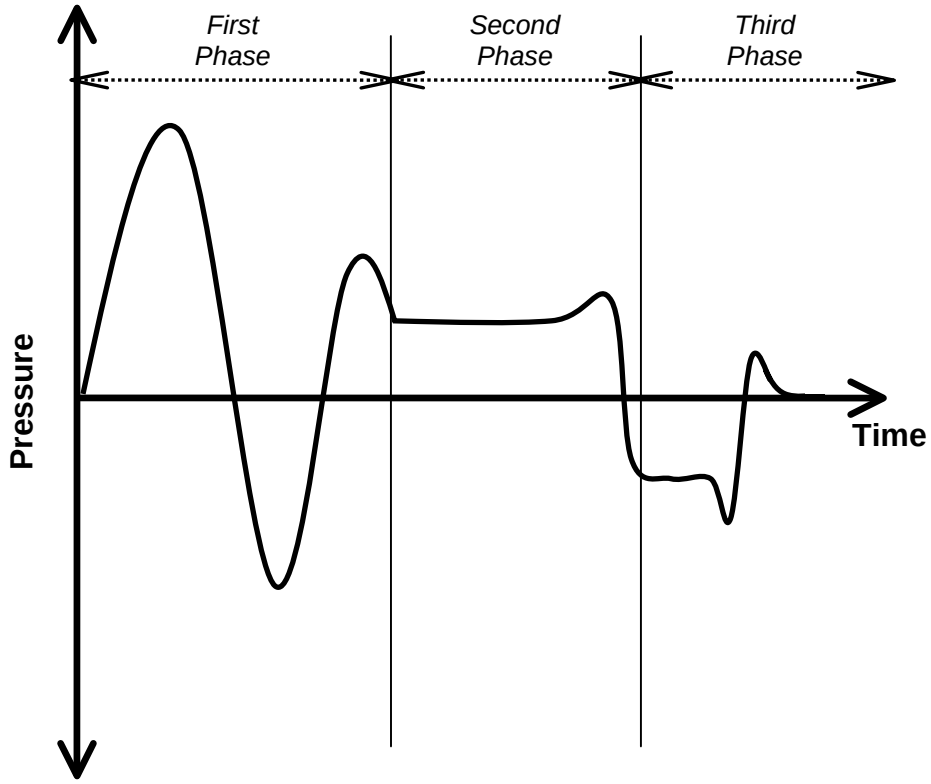

Figure 1.6: Phase breakdown of a single pressure fluctuation (from van der Schaaf [17]).

CHAPTER 2 - The Influence of Moisture on the Fluidization Behaviour of Porous Pharmaceutical Granule

The contents of this chapter have been published in the journal ***Chemical Engineering Science***. It has been published in a version similar to what appears in this chapter.

Citation

Wormsbecker, M., Pugsley, T. (2008). The influence of moisture on the fluidization behaviour of porous pharmaceutical granule. Chem Eng Sci 63, 4063 – 4069.

Contribution of Ph.D. Candidate

Experiments were planned and performed by Michael Wormsbecker. Todd Pugsley provided consultation regarding the experimental program. The software for all data collection and analysis was developed by Michael Wormsbecker. All of the writing of the submitted manuscript was done by Michael Wormsbecker with Todd Pugsley providing editorial guidance regarding the style and content of the paper.

Contribution of this Paper to the Overall Study

This paper quantifies the fluidization characteristics of pharmaceutical granule as its moisture content is varied. More specifically, its behaviour is characterized with respect to moisture removal in order to compare it to the hydrodynamics of drying. Understanding the granule's fluidization properties will allow the transient hydrodynamics, which will be discussed later in this thesis, to be addressed quantitatively.

2.1 Abstract

The influence of moisture content on the fluidization behaviour of placebo pharmaceutical granule has been studied in a 14 cm diameter cylindrical fluidized bed column. The dry granule has a mean diameter of 207 +/- 9μm and exhibits a bimodal size distribution with modes of 169 and 1600 μm. Bed pressure drop profiles and tap density measurements were generated for granule moisture contents between 5 to 30 wt.%, which corresponds to typical final and initial moisture contents experienced during drying. At high moisture contents, the wet granule exhibits Geldart C type powder behaviour as channelling and defluidization exist. As the moisture content is reduced, the granule fluidity improves and demonstrates behaviour characteristic of Geldart B powders. The changing fluidization behaviour was quantified using parameters such as the full support velocity, full support bed voidage and Hausner ratio. These parameters were found to increase significantly above granule moisture contents of 10 wt.%. The increase in the Hausner ratio suggests that the interparticle force load in the bed

increases. This change in interparticle force load is responsible for the increase in the full support velocity and bed voidage.

2.2 Introduction

The presence of moisture can have a significant effect on the hydrodynamic behaviour in fluidized beds. This behaviour is particularly evident in pharmaceutical fluidized bed dryers where the granule is initially 35 to 50 wt.% liquid. When the granule is wet, a sufficiently high fluidization velocity is required to avoid segregation, defluidization and channelling. However, if the velocity is too high, undesirable phenomena such as particle entrainment and pulverization can occur towards the end of drying. This poor fluidization behaviour can have an adverse effect on the product quality and ultimately lead to the rejection of batches of high-value material.

The impact of moisture on fluidized bed drying hydrodynamics is not clearly understood. As a result, many fluidized bed dryers used in the pharmaceutical industry are controlled manually using visual observations collected through a sight-glass in the product bowl. Obviously, this technique is prone to error as it relies on human discretion to make changes in the process operating conditions. Therefore, understanding the role of moisture on fluidization behaviour will provide further insight towards the hydrodynamic behaviour in fluidized bed dryers and ultimately improve their control.

Fluidization behaviour has been extensively covered in the published and patent literature. The most common classification of this behaviour was introduced by Geldart

[1]. Geldart classified the fluidization behaviour of various powders based on their mean diameter and particle density using both visual observations and numerical criteria. Later, Molerus [2] developed a semi-empirical approach to relate the differences in these fluidization behaviours to the adhesion forces that exist between particles (see Table 2.1). With his approach, Molerus was able to confirm the results of Geldart [1] while including transitional regions between particle classifications. These transitional regions were based on the differences in the magnitudes of adhesion forces that can exist between particles of different hardness. Seville [3] agreed with the physical interpretation of Molerus, but proposed that the transition from Geldart B to Geldart A behaviour is related to the van der Waals and capillary forces, which are functions of the surface properties of the powder. The capillary forces referred to by Seville [3] were taken from Donsí et al. [4] where fluidization air of 48 – 65% RH was used. The upper end of this humidity range has been shown by many authors [5-7] to have a potentially significant influence on hydrodynamic behaviour compared to relatively dry air conditions.

The study of Geldart [1], which is widely accepted for characterizing fluidization behaviour of powders, was derived for classifying the fluidization behaviour of dry particle systems. The presence of external forces that can alter the force balance between particles, and ultimately affect the hydrodynamic behaviour [8-12], were not incorporated into this work. Seville and Clift [12] applied the interpretation of Molerus [2] and induced changes in the interparticle forces through the addition of non-volatile liquids to a bed of non-porous glass ballotini. Using various sizes of Geldart B ballotini, they found that a transition from Geldart B behaviour to Geldart A, and even to C, could

occur in the presence of liquid loadings of less than 0.2 wt.%. In a subsequent study, McLaughlin and Rhodes [10] used a similar approach which supported the notion that the transition between Geldart B, A, and C behaviour occurs at specific interparticle to fluidized drag force ratios. In this study, non-porous Geldart B particles of 1.09 mm transitioned to Geldart A behaviour at liquid loadings of 0.08 – 0.09 vol.%, depending on the liquid viscosity.

Whereas the previously mentioned studies used non-porous ballotini, d'Amore et al. [13] examined the influence of moisture on porous catalytic powders. They found that an existing pore network allows considerable amounts of moisture to accumulate in the particulate system without affecting the particle surface properties as compared to non-porous powders.

The transition in fluidization behaviour due to liquid addition has also been quantified in the literature in terms of particle characteristics such as minimum fluidization velocity (U_{mf}) and minimum fluidization voidage (ε_{mf}). With Geldart B and D powders, U_{mf} and ε_{mf} were found to increase with liquid addition [12, 14, 15]. Seville [3] suggests that liquid added to these types of powders increases the interparticle forces thus creating a more stable bed structure. This structure of higher voidage (due to the interparticle force strength of liquid bridging) has a lower pressure drop per unit length and therefore requires a higher velocity in order to fluidize the bed as compared to the same bed of dry particles. Similar studies have also been conducted with Geldart A powders. d'Amore et al. [13] determined that U_{mf} and ε_{mf} increase with moisture addition

as well. This is supported in part by Geldart et al. [16]. They found that liquid addition results in increased bed expansion at high velocities. However, Geldart et al. [16] also observed a slight degree of bed contraction at low velocities with Geldart A powders in the presence of liquid.

In the literature cited, liquid has been shown to have a significant impact on the fluidization behaviour of fluidized beds. However, the majority of these studies were done by adding liquid to non-porous materials which resulted in only a small liquid weight percent required to induce changes in hydrodynamic behaviour. Pharmaceutical granule is highly porous and as a result can have as much as 50 wt.% water in the initial bed mass and a moisture content below 5 wt.% by the end of drying. In the current study, the effect of moisture on the fluidization behaviour of placebo pharmaceutical granule will be examined using bed pressure drop versus velocity profiles. Tapped density measurements will also be performed to quantify the interparticle force strength of the granule.

2.3 Materials and Methods

2.3.1 Granulation Preparation and Characterization

The ingredients used in the preparation of the placebo granule, including their mass fractions (W) and initial moisture contents (Q_c), are listed in Table 2.2. The placebo granule is comprised of two fillers (lactose monohydrate and microcrystalline cellulose), a binder (hydroxypropyl methylcellulose) and a disintegrant (croscarmellose sodium). These substances are added in proportions typical of solid dosage formulations used in

the pharmaceutical industry. These materials were stored in air-tight containers to limit the effect of laboratory conditions on their initial moisture contents. To prepare the granule, a low shear mixer was used. A H1/8VV-650017 VeeJet standard flat spray nozzle (Spraying Systems Co., Wheaton, USA) attached to a pressure pot operating at 2.5 barg generated a constant flow rate of 63 mL/min of water to the granulator. The dry ingredients were loaded into the mixing bowl starting with microcrystalline cellulose, followed by HPMC, croscarmellose sodium and finally lactose. These excipients were mixed for two minutes at the lowest setting to limit entrainment of materials from the bowl yet still fully mix the excipients prior to the water addition phase. Next, the water was introduced through the nozzle over a five-minute period. This was followed by an additional two minutes of post mixing. Once finished, the material was discharged from the bowl and manually sieved through a 3.36-mm sieve tray. This was done to break up any loosely formed agglomerates, but also remove the largest granules that formed due to poor granulation. This was required because differences in granulation techniques (high vs. low shear) lead to increased formation of large granules in this work. By removing the excess amount of large granules, a distribution that better reflects an industrially relevant granular material was achieved.

The particle size distribution of the dry granule was measured using sieve analysis. Fig. 2.1 illustrates three separate particle size frequency distribution conducted on the granule where X is the mass fraction of the granule that corresponds to the average particle size (d_p) based on the sieve sizes used in the particle size analysis. The size distribution is bimodal with modes of 169 and 1600 μm and a mean particle diameter of

207 +/- 9 μm (see Fig. 2.1). An earlier study by our group [17] found the particle density of dry pharmaceutical granule to be 830 kg/m^3.

2.3.2 Fluidized Bed Apparatus

The fluidized bed used in this study was a 14.0-cm diameter acrylic cylindrical fluidized bed (see Fig. 2.2). The column was 1.5 m tall with a cloth filter used to capture any entrained particles from the exhaust air. A 7.0% open area perforated plate with 2.0-mm diameter orifices drilled on a 6.0-mm square pitch was used to distribute the gas across the bed inlet. Along with the distributor plate, 2.0-cm PVC Raschig rings were placed in the windbox to aid gas distribution. The fluidization air was supplied by a 2-hp SCL K05-MS regenerative blower (F.P.Z. Effepizeta srl., Milan, Italy) with the flow rate measured using an orifice plate and water manometer setup. The orifice plate was designed according to ASME standards for fluid flow in closed conduits. The temperature of the fluidization air was measured to be approximately 40˚C. This value was the steady-state discharge temperature of the blower.

Bed pressure drop was measured with a DP15 differential pressure transducer (Validyne Engineering Corp., Northridge, USA). A 6.0-mm diameter stainless steel tube covered by a 45 μm mesh at the tip was attached to the pressure transducer and flush-mounted to the inner wall of the fluidized bed. The bed pressure drop was measured across the freeboard and 3 cm above the distributor plate. The pressure drop measurements were collected at 400 Hz. This is to ensure that all frequencies relevant to the analysis of the hydrodynamics are captured. The data was collected using a STA-300

terminal board with a KPCI-3101 PCI card (Keithley Instruments Inc., Cleveland, USA). The data acquisition equipment was interfaced with a continuous data logging program built with LabVIEW® (National Instruments®, Austin, USA).

The moisture content of the granule was determined by taking samples from the bed. These samples were taken from the middle region of a well-mixed bed therefore assuming spatial homogeneity of moisture in the bed. The granule samples were analyzed for moisture content with a HB43 moisture analyzer (Mettler Toledo CmbH, Greifensee, Switzerland).

2.3.3 Experimental Conditions

Experiments were carried out at granule moisture contents of 30 to 5 +/- 1 wt.% (decreasing in 5 wt.% increments). This represents the typical range of moisture experienced during drying of pharmaceutical granule. Starting with 2.0 kg of granule at 30 wt.% moisture, static pressure drop measurements were collected over the velocity range of 0.04 to 0.8 m/s. The data collected at each velocity were recorded for two minutes. After each pressure drop *versus* velocity experiment, a granule sample was taken from the bed and the moisture content was measured to ascertain the change in moisture content that had occurred. After concluding an experiment, the granule was then dried to reduce the moisture content to the next desired value. Once this moisture content was achieved, another pressure drop *versus* velocity experiment was run. This procedure was repeated until a granule moisture content of 5 wt.% was reached. Three

batches of granule were dried in this manner to check for reproducibility in the pressure drop *versus* gas velocity experiment conducted.

It should be noted that the lost bed mass due to drying was not made up between moisture content experiments. Although these changes are significant, minimum fluidization velocity and bed voidage are particle properties and therefore not influenced by bed mass.

2.4 Results and Discussion

2.4.1 Pressure Drop Profiles

Table 2.3 provides the initial and final moisture contents of the granule (Q_g) corresponding to the nominal moisture conditions for each of the three trials run. As shown in Table 2.3, the differences between the initial and final moisture contents for a given experiment are significantly greater for the experiments conducted at 20 wt.% moisture and above as compared to the experiments at moisture contents below 20 wt.%. The differences are due to the higher fluidization velocities coupled with the presence of excess surface moisture with granule of 20 wt% moisture and above. Although these changes in moisture content during given fluidization experiments introduce variability into the study, the 5 wt.% intervals in moisture content are sufficiently large to allow for discrete differences in the data to be observed.

Fig. 2.3 illustrates the pressure drop (ΔP) *versus* velocity (U_o) profiles for granule moisture contents of 30, 20, 15 and 5 wt.%. These moisture contents were chosen

because they represent the changes in the fluidization behaviour as moisture was removed. It is important to note that the velocity range studied narrows for the pressure drop profiles with decreasing moisture content. This was done to limit the elutriation of fines from the bed since fluidization conditions were experienced at lower velocities as the moisture content decreased. The discussion of the results will start with the highest moisture content and proceed to the lowest. The full pressure drop data sets are presented in Tables A.1 – 6 in Appendix A.

At 30 wt.% moisture, the granule was very cohesive in nature; demonstrating many Geldart C powder characteristics. For example, the entire bed mass rose as a plug once the blower was turned on. To circumvent this problem, the plug was manually broken by piercing it with a rod through a vacant port in the bed. Once broken, a fluidization state with limited segregation and defluidization around the bed periphery was established at a superficial gas velocity of 0.76 m/s. Fig. 2.3(a) is the pressure drop *versus* fluidization gas velocity for granule of 30 wt.% moisture for the three trials. Most noticeable in this figure is the variability in the results. This variability can be attributed to channelling in the bed and its associated instabilities. However, when operated above 0.60 m/s, the data are reproducible between the trials. This occurs because the bed was fully fluidized as described above. Below 0.60 m/s, varying degrees of channelling occurred. For instance, the pressure drop associated with trial #1 starts decreasing gradually from 0.60 to 0.40 m/s, then drops off sharply and stays constant at 5.0 mbar from 0.30 to 0.10 m/s. The former behaviour is a result of a partially defluidized state observed, whereas the latter behaviour is a result of fully established channelling. The

other trials also have varying degrees of channelling. In trial #2, channelling sets in immediately below 0.60 m/s, whereas the partially defluidized state was more prevalent during trial #3. In all cases, a permanent channel developed and eventually broke, giving rise to pressure drop characteristics expected of a packed bed. The variability in the slope of the packed bed pressure drop is a result of varying degrees of permanent voids which exist in the packed bed and that were observed through the vessel walls.

As moisture was removed, the fluidity of the granule improved greatly. By the time the granule reached 20 wt.% moisture (see Fig. 2.3(b)), the bed mass could be fully fluidized at 0.36 m/s without defluidization at the base. However, a greater degree of particle segregation was observed through the acrylic walls. This segregation occurred at velocities of 0.60 m/s and typically established itself on one side of the bed. Below 0.36 m/s, the pressure drop decreases gradually with velocity. This decrease in pressure drop is again associated with the partial defluidization of the bed mass. However, unlike the higher moisture content experiments, no channelling developed. Instead, the bed was defluidized from the base of the bed to the surface on one side and bubbling on the other. It is interesting to note that the bubbling side of the bed was situated on the side where the majority of segregated granule tended to accumulate. This is logical given that the large granules possess little resistance to the gas flow as compared to the defluidized side. Again, the bed eventually became totally defluidized with the presence of permanent voids at the walls.

There was a marked change in the fluidization behaviour between 20 and 15 wt.% moisture. At 15 wt.% moisture, the pressure drop versus velocity curve is more typical of a theoretical profile (see Fig. 2.3(c)). As was seen with the previous moisture contents, the velocity required to fully fluidize the bed has dropped again to 0.25 m/s. At this moisture content, partial defluidization never developed; rather the base of the bed experienced an increasing degree of segregation as the gas velocity decreased to 0.080 m/s. A gradual decrease in pressure drop accompanies the changes observed between the fully fluidized and packed bed states. This pressure drop behaviour is similar to that first described by Saxena and Vogel [18] for systems containing wide particle size distributions. They also observed partial segregation of particles, which at a sufficiently high velocity become completely fluidized. Using the slope of the packed and fluidized regions, the minimum fluidization velocity was found to be 0.093 m/s.

Once the material has been dried to 10 wt.% moisture and below, a very reproducible pressure drop profile exists. This is exemplified by the pressure drop profile for granule of 5 wt.% moisture shown in Fig. 2.3(d). The fluidization behaviour is similar to that of the 15 wt.% granule: good fluidity with varying degrees of segregation depending on the gas velocity. There is also limited bed expansion and bubbles being formed just beyond minimum fluidization. This suggests the granule behaves more like Geldart B powders at these moisture contents. With granule of 10 and 5 wt.% moisture, the pressure drop profiles render experimental minimum fluidization velocities of 0.072 and 0.070 m/s, respectively.

2.4.2 Full Support Velocity, U_{fs}

The pressure drop profiles of Fig. 2.3 illustrate that the velocity required to fully fluidize the bed is a function of granule moisture content. Unfortunately, there is no way to quantify the differences in fluidization behaviour in terms of the minimum fluidization velocity due to the unstable operating conditions exhibited at higher moisture contents. Instead, the velocity required to fully fluidize the bed, which has been termed the full support velocity (U_{fs}) by Dry et al. [19], is presented as a characteristic velocity. Dry et al. [19] defined this velocity in reference to cohesive powders that did not follow typical pressure drop profiles expected of Geldart A powders. Their criterion to demarcate the full support velocity was the velocity "at which the bed pressure differential first begins to fall". A similar, but more quantitative, criterion was used to determine U_{fs} in this study. It was chosen as the lowest velocity where the mean pressure drop value is still within two standard deviations of the fluidized bed pressure drop.

The premise of the full support velocity is that it is physically linked to the particulate system through the total bed pressure drop. In particularly, that the theoretical bed pressure drop at a specific moisture content ($\Delta P_{theor,i}$) is related to the bed mass ($m_{bed,i}$) through

$$\Delta P_{theor,i} = \left(\frac{m_{bed,i} \cdot g}{A_{bed}} \right), \qquad \text{(Eq. 2.1)}$$

where g represents the gravitational acceleration constant and A_{bed} is the cross-sectional area of the fluidized bed. To verify this physical interpretation, a comparison between the experimental and theoretical pressure drop was performed. The theoretical bed pressure drop was calculated based on the initial bed mass ($m_{bed,0}$) and moisture content ($Q_{g,0}$) as

$$\Delta P_{theor,\,i} = \left(\frac{\left(m_{bed,0} \left(1 - Q_{g,0} + Q_{g,i} \right) - i \cdot 0.015 \right) \cdot g}{A_{bed}} \right) \qquad \text{(Eq. 2.2)}$$

$$\text{where, } \left\{ Q_{g,i} = \frac{(30 - 5i)}{100} : i \in 0,1,2,...5 \right\}.$$

The additional term, $i \cdot 0.015$, accounts for the cumulative mass of moisture samples removed from the bed after each experiment. Based on the sample sizes used, approximately 15 g of sample was removed per experiment to determine the initial and final moisture contents of the granule.

Comparison of the theoretical to experimental bed pressure drop *versus* granule moisture content demonstrates that the full support velocity pressure drop is related to the bed mass (see Fig. 2.4). The percent differences between the calculated and measured values are 2 - 6% over the entire moisture range. The error bars associated with the experimental data points represent two standard deviations in the experimental data. The differential pressure measured across the bed deviates from the theoretical value at higher moisture contents. This is likely a result of varying degrees of segregation and/or defluidization that occur at the base of the bed. Regardless, the similarity between the experimental and theoretically predicted bed pressure drops means that the full support velocity, like the minimum fluidization velocity, represents the point at which the drag induced by the gas velocity is sufficient to support the weight of the bed.

Plotting the full support velocity *versus* granule moisture content demonstrates the influence moisture has on the fluidization behaviour of the granule. As shown in Fig.

2.5, the velocity required to establish a fully fluidized state increases significantly with moisture content. At 30 wt.% moisture, U_{fs} is 0.60 m/s whereas the 5 wt.% granule has a value of 0.11 m/s. The trend in U_{fs} is similar to that of the effect of liquid feed rate on fluidized bed granulator operation whereby increasing liquid feed rates increased the required operation velocity [20].

2.4.3 Tapped Density

The Hausner ratio (*HR*), which is the ratio between the bulk tapped density (ρ_t) and poured (ρ_p) density of a powder, is a simple measure typically used to characterize the flowability of solids in hopper flow [21]. The poured density demonstrates the strength of the interparticle forces whereas the tapped density minimizes them through compaction of the material. This ratio is therefore an indirect measure of the interparticle forces that exist between particles in a static environment. Particles with a high Hausner ratio (significantly greater than 1) exhibit looser packing and are therefore stabilized due to higher interparticle forces, whereas particles with relatively weak interparticle forces have a ratio closer to unity. Geldart et al. [16] have taken this ratio and applied it to the Geldart classification of powders. They found that the transition from Group A to Group C behaviour occurs at a Hausner ratio of 1.25 - 1.4.

Using a Varian tap density meter (Varian Inc, Palo Alto, USA), 100 mL of granule was loaded into the graduated cylinder and subsequently weighed. The granule was then tapped 1500 times through a stroking distance of 14 mm with cylinder rotation to ensure optimal compaction. Using the poured and tapped volumes with the granule

mass, the poured and tapped densities were calculated. With these densities, the Hausner ratio was calculated using

$$HR_i = \frac{\rho_{t,i}}{\rho_{p,i}}. \qquad \text{(Eq. 2.3)}$$

Fig. 2.6 illustrates the influence of moisture on the relative strength of the interparticle forces between granules. At low moisture contents (7 wt.% and below), the Hausner ratio of the granule is 1.18 - 1.22. However, with increased levels of moisture in the bed, the Hausner ratio increases linearly. This indicates that as moisture levels increase, the interparticle forces of the granule in a static environment also increase. Above 20 wt.%, the Hausner ratio is greater than 1.4, which based on the work of Geldart et al. [16] suggests that the granule should exhibit Geldart C powder behaviour. As described previously, Geldart C characteristics such as channelling and defluidization do exist in this range of moisture contents. Refer to Table A.7 for the data required to calculate the Hausner ratio.

2.4.4 Voidage

Tap density measurements indicate that the packing density of the granule under static conditions decreases with increasing moisture content. If considered in terms of packed bed voidage of a fluidized bed, this suggests an increase in voidage will occur. Although the Hausner ratio is a static measurement, it is logical that the bed voidage in a dynamic environment (i.e. during fluidization) will also be impacted by moisture content through increasing interparticle forces. Typically, researchers use packed bed pressure

drop data with the Ergun equation to calculate the minimum fluidization voidage. In the current study, the instability in the fluidization behaviour at high moisture contents renders this technique ineffective. However, using the fact that the bed pressure drop measured at the full support velocity is representative of the actual bed mass, its pressure drop per unit length $\left(\Delta P/L\right)_{fs}$ can be related to the bed voidage (ε_{fs}) through

$$\left(\Delta P/L\right)_{fs,i} = \left(1-\varepsilon_{fs,i}\right)\left(\rho_{s,i}-\rho_g\right)g\,, \qquad \text{(Eq. 2.4)}$$

where ρ_s and ρ_g represent the particle and gas density, respectively. The pressure drop per unit length was obtained using the measured bed pressure drop in conjunction with the fluidized bed height at the full support velocity (bed height data provided in Tables A.1 – A.6). The bed height was measured visually using a graduated scale on the outside wall of the fluidized bed. The bed depth used to calculate $\left(\Delta P/L\right)_{fs,i}$ accounted for the fact that the pressure tap was positioned 3 cm above the distributor plate.

The difficulty with Eq. 2.4 is that the particle density ($\rho_{s,i}$) is a function of the granule moisture content. To incorporate the density dependence on moisture, the particle density was assumed to be related to the tapped density of the granule through its packing density (ε_t) by

$$\rho_{s,i} = \rho_{t,i} / \varepsilon_t \quad , \qquad \text{(Eq. 2.5)}$$

where ε_t is assumed to be equal to the random close packing density (the packing state for granular material that has been shaken or tapped until the material does not compact any further). For mono-dispersed spherical particles, the random close packing solids fraction is 0.64 while non-spherical particles can have packing densities that are greater than this; but still less than the theoretical packing solids fraction of 0.74. Considering that the granule exhibits a bi-modal distribution, a packing arrangement denser than random close packing should result as the smaller granule will fill the voids created by contact points between larger ones.

Fig. 2.7 illustrates the estimated bed voidage at the full support velocity for the granule moisture contents studied. As shown in this figure, an increase in moisture content results in an increase in bed voidage. Below 10 wt.% moisture, the estimated voidage is relatively constant at approximately 0.52. This value is similar to that reported by Tanfara et al. [22] of 0.48 for the packed bed voidage of dry pharmaceutical granule with a bimodal distribution. Above 10 wt.% moisture, the voidage increases sharply to approximately 0.70 where the voidage remains relatively constant for granule moisture contents of 20 wt.% and above. The increase in voidage demonstrated by the data supports the statement of Seville [3] that the liquid bridging creates a stabilized bed structure resulting in greater voidage.

It is worthwhile to note that unlike previous studies [12, 13], the increase in voidage experienced through the presence of moisture in this study is much more predominant. This is most likely due to the fact that the classical definition of the minimum fluidization is not used as a comparison point, and as a result, allows for higher granule moisture contents to be studied. Furthermore, with the use of the full support velocity, some bubbling was present in the fluidized state. This will result in the representation of an overall bed voidage rather than a dense phase voidage such as that calculated by the Ergun equation.

2.5 Conclusions

This study has used the full support velocity, full support bed voidage and the Hausner ratio to demonstrate the impact of liquid bridging on the fluidization behaviour associated with porous pharmaceutical granule. At high granule moisture contents (20 wt.% and above), the granule exhibits Geldart C type fluidization behaviour, whereas granule fluidity characteristic of Geldart B powders is observed at moisture contents of 10 wt.% and below. The full support velocity has been used as a primary indicator of the global effect of moisture on fluidization behaviour. The data presented have shown that a significant increase in the fluidization velocity is required to fully support the granule mass as moisture content increases. Quantifying this in terms of actual granule moisture content is vital as it provides a basis of interpretation for describing the transient hydrodynamic behaviour associated with the batch-wise drying of pharmaceutical granule; a field of research that is relevant to many industrial practices, including pharmaceutics.

In addition to an increase in the full support velocity, an increase in bed voidage and Hausner ratio supports the conclusion that the presence of moisture increases the magnitude of interparticle forces in the system. The full support bed voidage suggests that there is a transition in bed material stability between 10 and 20 wt.% as it changes significantly over this range of moisture contents. Similarly, the Hausner ratio indicates that granule below 7 wt.% is not affected by liquid induced interparticle forces. However, above this moisture content the Hausner ratio increases linearly, signifying that the interparticle forces strengthen with increasing moisture contents.

2.6 Nomenclature

A_{bed}	cross-sectional area of the fluidized bed, m^2
d_p	particle diameter, μm
g	gravitational acceleration, 9.81m/s^2
HR	Hausner ratio, -
m_{bed}	bed mass, kg
ΔP	experimental pressure drop, mbar
ΔP_{theor}	theoretical pressure drop, mbar
$(\Delta P/L)_{fs}$	pressure drop per unit length at the full support velocity, Pa/m
Q_c	moisture content of raw material, wt.%
Q_g	moisture content of granule, wt.%
U_{fs}	full support velocity, m/s
U_{mf}	minimum fluidization velocity, m/s
U_o	superficial gas velocity, m/s
W	mass fraction of excipients used in the formulation, wt.%
X	size distribution fraction, wt.%
ε_{fs}	full support voidage, -
ε_{mf}	minimum fluidization voidage, -
ε_t	volume fraction of solids after tapping, -
ρ_g	density of fluidization gas, kg/m^3
ρ_p	bulk poured density, kg/m^3
ρ_s	solids density, kg/m^3
ρ_t	bulk tapped density, kg/m^3

Subscripts

i	value at a specific moisture content

2.7 References

[1] Geldart, D. (1973). Types of gas fluidization. Powder Technology 7, 285 - 292.

[2] Molerus, O. (1982). Interpretation of Geldart's type A, B, C and D powders by taking into account interparticle cohesion forces. Powder Technology 33, 81 - 87.

[3] Seville, J.P.K. (1987). Particle cohesion in gas/solid fluidisation, in: Briscoe, B.J., Adams, M.J. (Eds.), Tribology in Particulate Technology, Adam Holger, Bristol, p. 173.

[4] Donsí, G., Moser S., Massimilla, L., (1975). Solid-solid interactions between particles of a fluid bed catalyst. Chemical Engineering Science 30, 1533 - 1535.

[5] Coelho, M.C., Harnby, N., (1987). The effect of humidity on the form of water retention in a powder. Powder Technology 20, 197 - 200.

[6] Turner, G.A., Balasubramanian, M., (1974). Investigation of the contributions to the tensile strengths of weak particulate masses, Powder Technology 10, 121 - 127.

[7] Yao, L., Bi, H.T., Park, A.-H., (2002). Characterization of electrostatic charges in freely bubbling beds with dielectric particles. Journal of Electrostatics 56, 183 - 197.

[8] Agbim, J.A., Nienow, A.W., Rowe, P.N., (1971). Inter-particle forces that suppress bubbling in gas fluidised beds. Chemical Engineering Science 26, 1293 - 1294.

[9] Kleijn van Willigen, F., van Ommen, J.R., van Turnhout, J., van den Bleek, C.M., (2005). Bubble size reduction in electric-field-enhanced fluidized beds. Journal of Electrostatics 63, 943 - 948.

[10] McLaughlin, L., Rhodes M., (2001). Prediction of fluidized bed behaviour in the presence of liquid bridges. Powder Technology 114, 213 - 223.

[11] Rhodes, M.J., Wang, X.S., Forsyth, A.J., Gan, K.S., Phadtajaphan, S., (2001). Use of a magnetic fluidized bed in studying Geldart Group B to A transition. Chemical Engineering Science 56, 5429 - 5436.

[12] Seville, J.P.K., Clift, R., (1984). The effect of thin liquid layers on fluidisation characteristics. Powder Technology 37, 117 - 129.

[13] d'Amore, M., Donsí, G., Massimilla, L. (1979). The influence of bed moisture on fluidization characteristics of fine powders. Powder Technology 23, 253 - 259.

[14] Baerns, M., (1966). Effect of interparticle adhesive forces on fluidization of fine particles. Industrial and Engineering Chemistry 5(4), 508 - 517.

[15] Egerer, B., Zimmermann, K., Bauer, W., (1985). Flow and fluidization behaviour of yeasts in gas/solid fermentation and drying. Institution of Chemical Engineers Symposium Series vol 91, 257 - 269.

[16] Geldart, D., Harnby, N., Wong, A.C.Y., (1984). Fluidization of cohesive powders. Powder Technology 37, 25 - 37.

[17] Wormsbecker, M., Adams, A., Pugsley, T., Winters, C., (2005). Segregation by size difference in a conical fluidized bed of pharmaceutical granule. Powder Technology 153, 72 - 80.

[18] Saxena, S.C. and Vogel, G.J. (1977). The measurement of incipient fluidization velocities in a bed of coarse dolomite at temperature and pressure. Transactions of the Institution of Chemical Engineers 55(3), 184 - 189.

[19] Dry, R.J., Judd, M.R., Shingles, T., (1983). Two-phase theory and fine powders. Powder Technology 34, 213 - 223.

[20] Maroglou, A. and Nienow, A.W. (1985). Fluidised bed granulation: a procedure for determining its feasibility and suitable operating parameters. Institution of Chemical Engineers Symposium Series vol 91, 15 - 25.

[21] Hausner, H.H., (1967). Friction conditions in a mass of metal powder. International Journal of Powder Metallurgy 3(4), 7 - 13.

[22] Tanfara, H., Pugsley, T., Winters, C., (2002). Effect of particle size distribution on the local voidage in a bench-scale conical fluidized bed dryer. Drying Technology 20(6), 1273 - 1289.

Table 2.1: Molerus' interpretation of the Geldart classification [2]

Transition	Explanation
C → A	Free particle motion is suppressed by the dominance of cohesive forces with Geldart C powders as compared to A.
A → B	Geldart A powders have significant adhesive forces compared to the fluid drag force exerted on the particle. Geldart B powders are negligibly influenced by adhesive forces as compared the drag force.
B → D	Geldart D behaviour exists when the dynamic pressure of the fluidization gas exceeds a distinct value based on the size and density of the powder at minimum fluidization.

Table 2.2: Placebo granule formulation

Component	W, wt.% (wet basis)	Q_c, wt.%
Lactose Monohydrate (filler)	35	0.1
Microcrystalline Cellulose (filler)	31	3.6
Hydroxypropyl Methylcellulose (binder)	3	1.4
Croscarmellose Sodium (disintegrant)	1	4.8
USP Distilled Water	30	-

Table 2.3: Initial and final granule moisture contents for the fluidization experiments of each trial

Trial No.	Q_g, wt.% (initial/final)					
	30	25	20	15	10	5
1	30.3 / 25.8	24.8 / 20.4	20.4 / 17.4	15.3 / 13.8	10.6 / 9.0	5.3 / 4.0
2	30.6 / 26.5	25.7 / 22.1	18.6 / 16.2	14.5 / 12.5	10.0 / 8.6	5.2 / 3.5
3	30.1 / 28.4	25.5 / 21.5	20.3 / 17.3	15.6 / 12.9	10.1 / 8.8	5.4 / 3.7

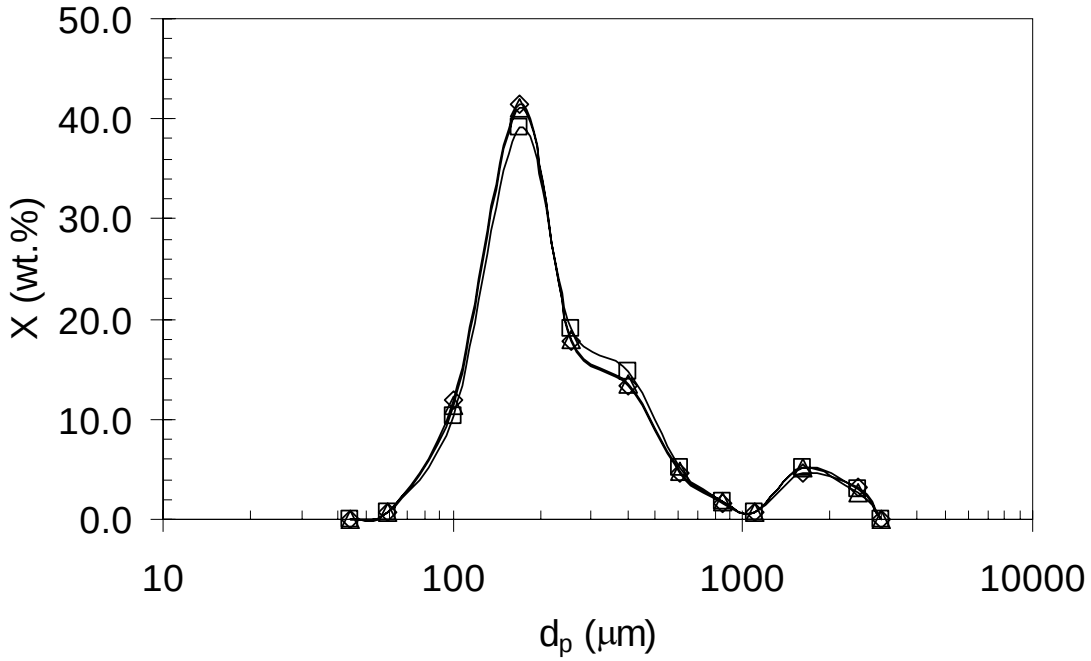

Figure 2.1: Particle size distribution of dry placebo pharmaceutical granule.

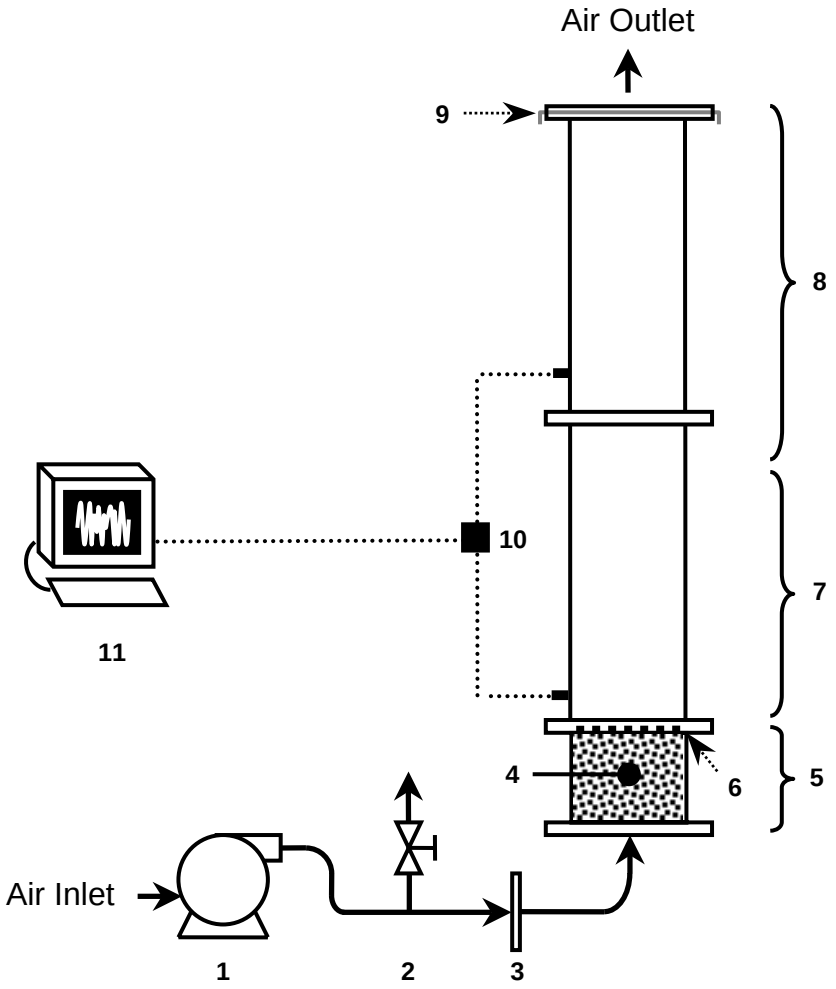

Figure 2.2: Experimental apparatus: (1) blower, (2) bypass valve, (3) orifice plate, (4) Raschig rings, (5) windbox, (6) distributor, (7) cylindrical fluidized bed, (8) freeboard section, (9) cloth filter, (10) differential pressure transducer, (11) data acquisition system.

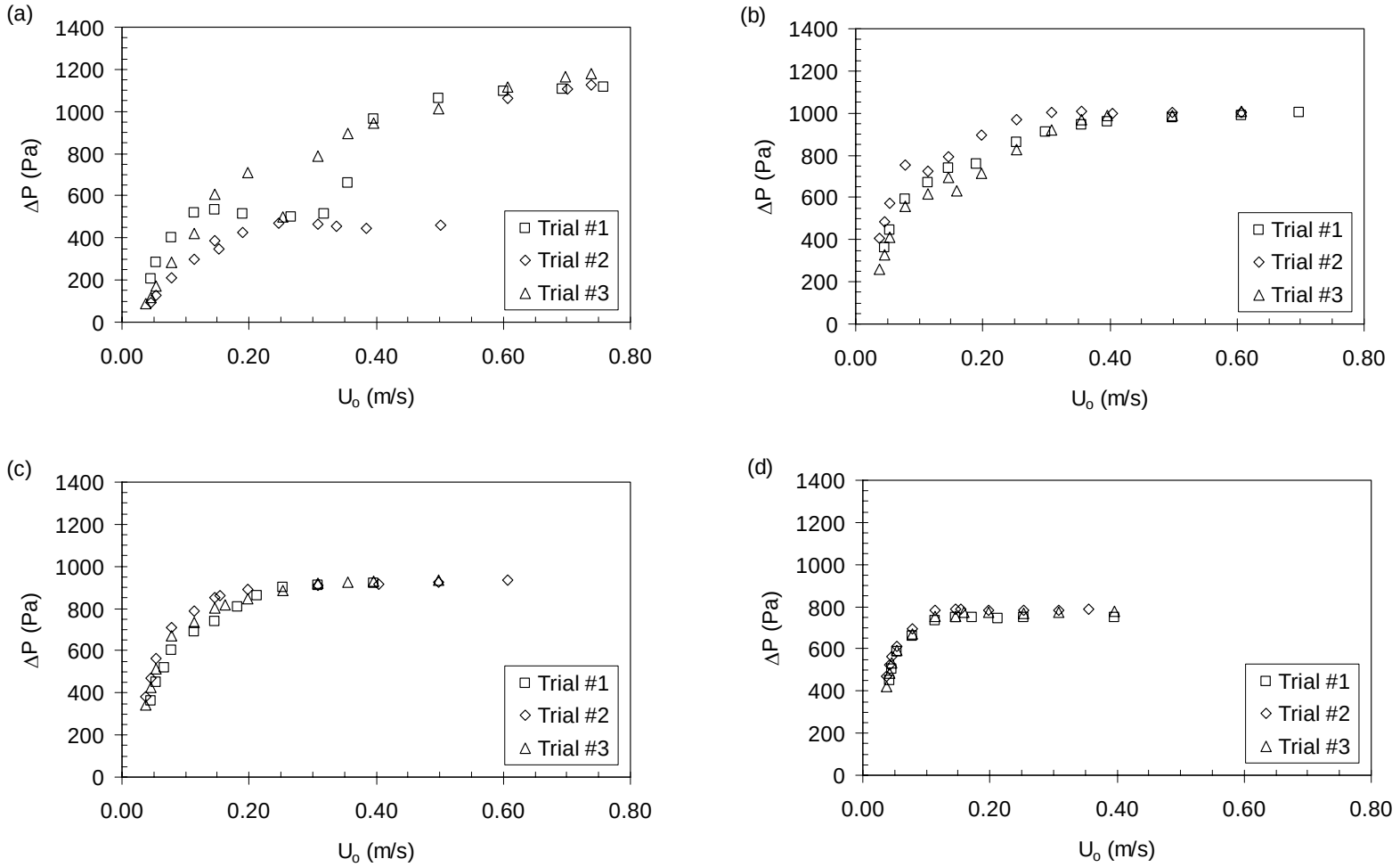

Figure 2.3: Pressure drop profiles at (a) 30 wt.%, (b) 20 wt.%, (c) 15 wt.%, (d) 5 wt.% moisture.

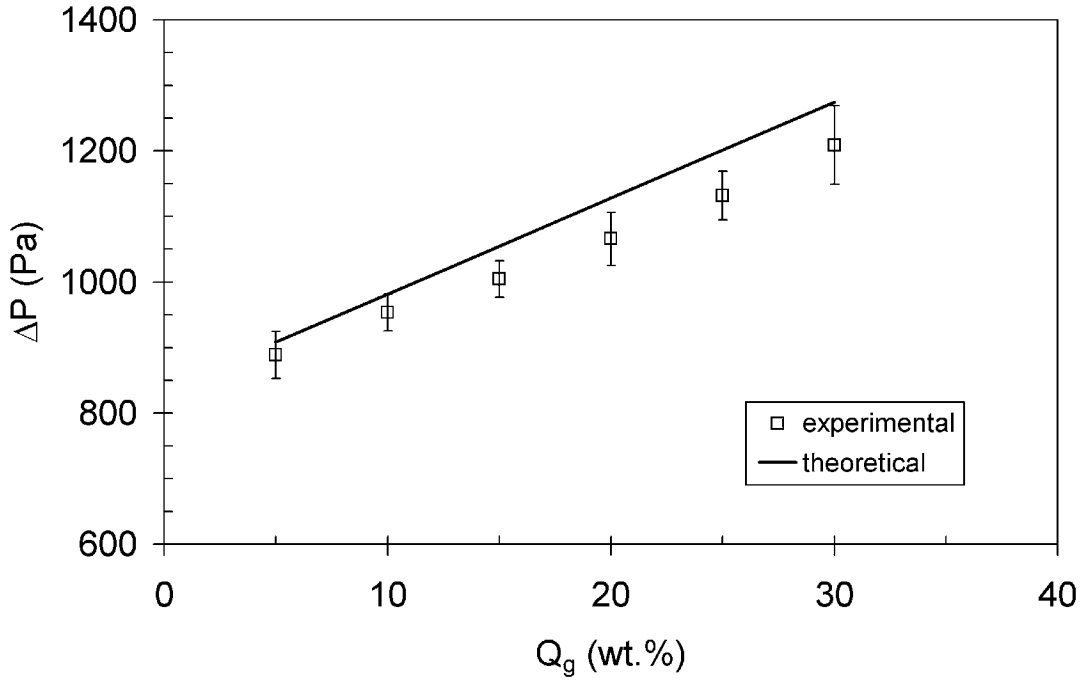

Figure 2.4: Comparison of theoretical and experimental bed pressure drops. The theoretical bed pressure drop was calculated using Eq. 2.2. The error bars associated with the experimental data represent ± 2σ of ΔP_{bed}.

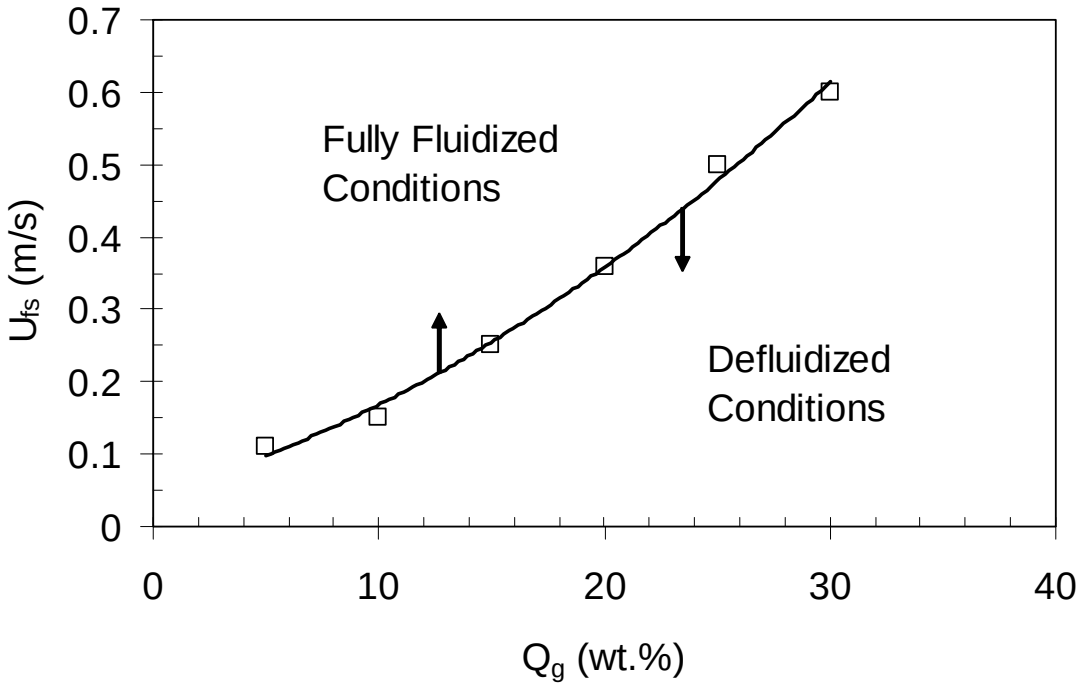

Figure 2.5: Influence of moisture on the fluidization velocity required to reach a fully fluidized state. Defluidized conditions include channelling, partial defluidization and packed bed states.

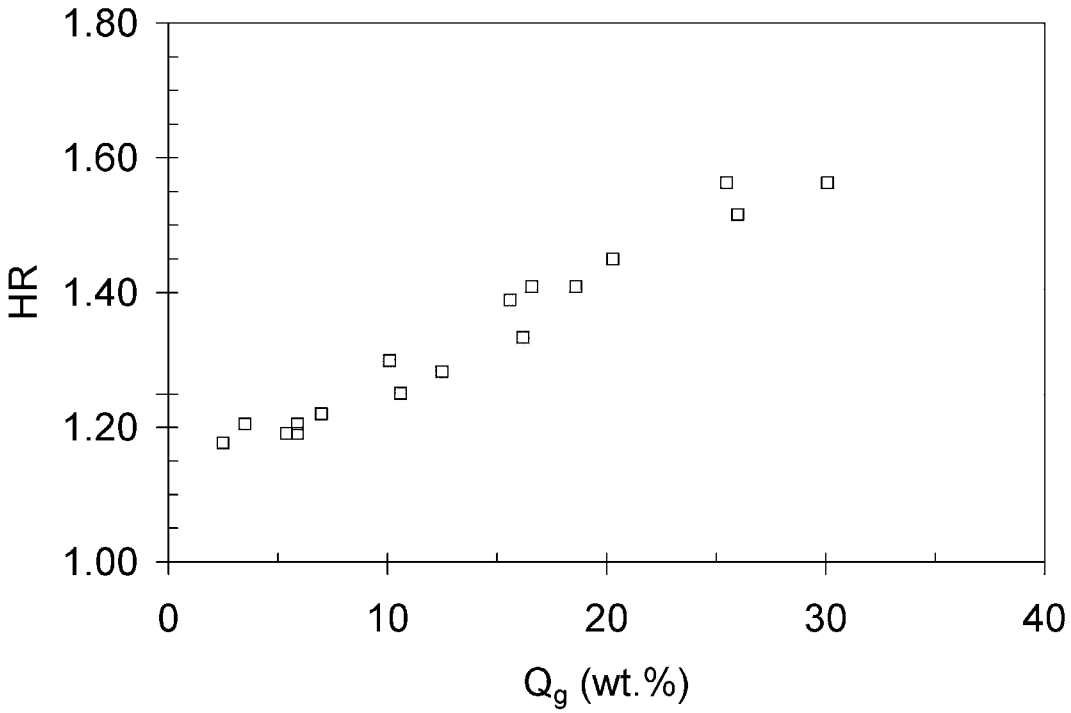

Figure 2.6: Hausner ratio for granule at various moisture contents. Shaded region represents the Geldart A/C transition region presented by Geldart et al. [16].

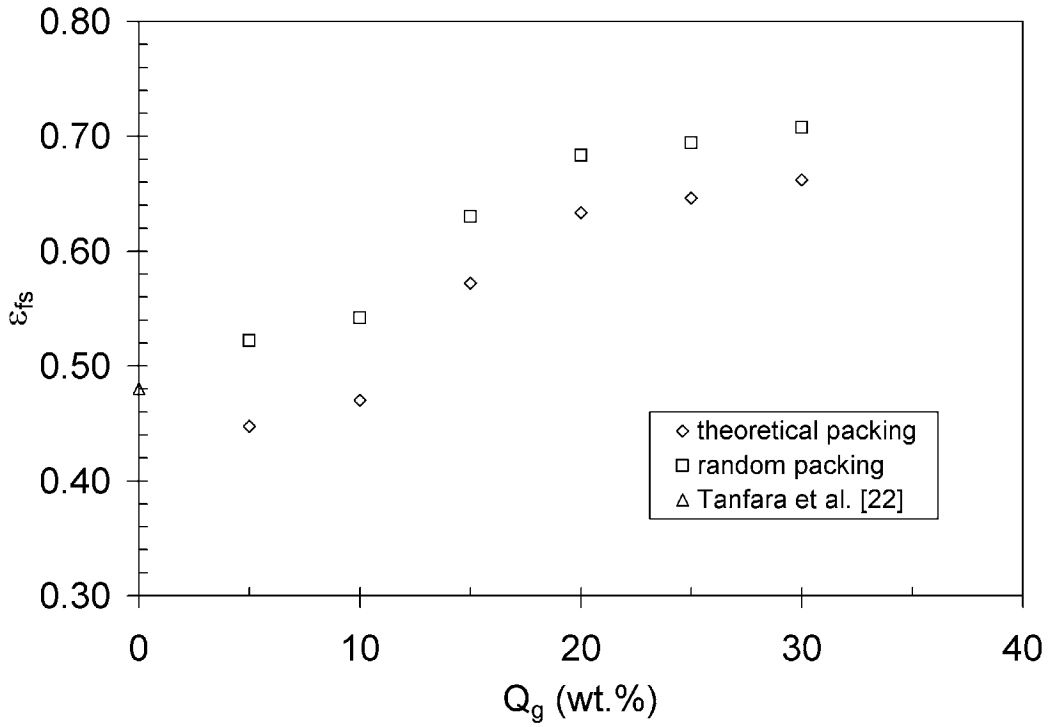

Figure 2.7: Calculated bed voidage at the full support velocity at various moisture contents. Voidages were calculated using Eq. 2-4.

CHAPTER 3 - Interpretation of the Hydrodynamic Behaviour in a Conical Fluidized Bed Dryer

The contents of this chapter have been submitted for publication to the journal ***Chemical Engineering Science*** in a similar version to what appears in this chapter.

Citation

Wormsbecker, M., Pugsley, T. Interpretation of the hydrodynamic behaviour in a conical fluidized bed dryer. Submitted to Chemical Engineering Science in February 2008 (Ref No. CES-D-08-00186).

Contribution of Ph.D. Candidate

Experiments were planned and performed by Michael Wormsbecker. Todd Pugsley and Helen Tanfara (Merck Frosst Canada Ltd.) provided consultation regarding the experimental program. The software for all data collection and analysis was developed by Michael Wormsbecker. All of the writing of the submitted manuscript was done by Michael Wormsbecker with Todd Pugsley and Helen Tanfara providing editorial guidance regarding the style and content of the paper.

Contribution of this Paper to the Overall Study

The focus of this paper is to address the transient hydrodynamic behaviour that occurs when pharmaceutical granule is dried in a conical fluidized bed. The hydrodynamics are described using the findings presented in Chapter 2. This paper will be used hereafter as a basis for understanding the effect of design features, such as distributor design and reactor geometry, discussed in the following chapters.

3.1 Abstract

Wet batches of placebo pharmaceutical granule were dried at inlet superficial gas velocities of 0.64 and 1.3 m/s in a Glatt GPCG-1 conical fluidized bed. Using pressure fluctuation analysis, the hydrodynamic behaviour indicates a transition from a multiple bubbling regime to a coalescence dominated regime as drying proceeds. The transitional fluidization behaviour is linked to the physical mechanisms associated with the constant and falling rate periods of drying porous materials. Excess surface moisture present during the constant rate period increases interparticle forces through liquid bridging. These liquid bridges stabilize the bed structure which limits bubble formation in the bed. Once the falling rate period is reached, the liquid bridges cannot be maintained and bubble coalescence increases. The resulting bubbling bed hydrodynamics can be explained using the simple two-phase model proposed by Toomey and Johnstone [Chem. Eng. Prog. 48 (1952), 220 - 226] using the full support velocity and bed voidage characteristics of the granule at varying moisture contents.

3.2 Introduction

Many solid dosage form pharmaceuticals are created via wet granulation and then dried in batch fluidized bed dryers prior to tablet formation. Warm air is passed through a bed of wet particles, referred to as granule, in order to remove the moisture. The product and exhaust air temperatures are carefully monitored while the inlet temperature is controlled. However, the control of the fluidization state during the process is far less advanced. Here, the operator manipulates the fluidizing air velocity based on visual observations through a sight-glass. The problem with this approach is that the optimum superficial gas velocity for operation of the fluidized bed may not be clear to an operator based on observations alone. In order to improve the monitoring techniques associated with fluidized bed drying, a better understanding of the hydrodynamic changes that occur as drying proceeds is necessary.

The influence of moisture on particle behaviour has already been discussed in Section 1.3 of this thesis. Recall, that when material is wet, the moisture present in a bed of solids can create a thin liquid film over the surface of the particles. This film allows for points of contact between particles through the formation of liquid bridges. Liquid bridging forces greatly increase interparticle forces when considered with respect to van der Waals forces [1-2] and therefore have a significant impact on the fluidization behaviour. As moisture is removed, the presence, and therefore strength, of liquid bridges will diminish and dry particle forces, such as electrostatic and van der Waals forces, will become the dominant interparticle forces acting in the bed.

Fluidized bed drying studies typically present the temperature and moisture profiles, such as that illustrated in Fig. 1.5, to describe, and even compare, drying processes [3-6]. Unfortunately, this information provides no information regarding the hydrodynamic behaviour of the material; only the drying rates. Research has shown that the effect of liquid loading has a dramatic effect on the hydrodynamic behaviour of non-porous materials. Liquid loadings less than 0.2 wt% have been shown to initiate Geldart A, and sometimes C, type behaviour in typical Geldart B sized powders [7-8]. In order to address the hydrodynamic behaviour of drying specifically, the fluidization behaviour of commonly dried materials at moisture contents expected during drying has been considered. Typically, this work has characterized the behaviour based on the minimum fluidization velocity and bed voidage [9-10]. Our research group has also done similar experiments with pharmaceutical granule [11], but instead characterized the granule based on 'full support' conditions (minimum velocity where the bed pressure drop equals the bed mass). Like the aforementioned studies, Wormsbecker and Pugsley [11] found that higher moisture contents drastically affect the fluidization behaviour of pharmaceutical granule. In this study, it was shown that an increase in the full support velocity and bed voidage resulted with increased granule moisture content.

While these drying studies demonstrate the influence of moisture on the fluidization behaviour, they do not address the bubbling bed hydrodynamics of drying. Unfortunately, bubbling bed hydrodynamic studies have focused their attention on dry bed studies and the effect of changing operating variables such as gas velocity and particle size distribution [12-14]. Although this work is valuable, it does not apply

directly to processes such as drying, which have the added complexity of moisture in the system. The only work to date related to the hydrodynamics of drying is by Chaplin et al. [15]. They used the S-statistic to demonstrate that two stable hydrodynamic states occur during the drying of placebo pharmaceutical granule. These stable states occurred at the beginning and the end of the drying process and are assumed to be caused by the extent of liquid bridging that exists in the system.

In this current study, the transient hydrodynamic behaviour observed in the work of Chaplin et al. [15] will be further examined using pressure fluctuation analysis. Pressure fluctuation analysis was chosen because of its widespread acceptance as a technique for distinguishing hydrodynamic behaviour in fluidized bed systems [13-20]. The changes in the pressure fluctuation data will be linked to the fluidization properties of the granule presented by Wormsbecker and Pugsley [11] as well as the mechanisms of drying discussed above.

3.3 Materials and Methods

3.3.1 Granulation

The placebo granule was comprised of the same materials outlined in Table 2.2 and described in section 2.3.1 of this thesis. A T.K. Fielder PMA25 high shear granulator was used for preparing the wet granule. The dry ingredients were pre-mixed for five minutes at an impeller rotational speed of 261 RPM and chopper speed of 3600 RPM. After pre-mixing, the chopper speed was reduced to 1800 RPM and the water addition phase commenced. Water was sprayed through a Vee-Jet® H ¼ VV 80015 flat spray

nozzle with a 15˚ fan angle. The nozzle was positioned 7.5 cm from the top of the granulator lid to provide an even spray field in the granulator bowl. The water was sprayed under a constant pressure of 207 kPag over a three-minute period. An additional two minutes of mixing subsequent to the water addition phase was carried out prior to discharging the granule from the bowl. Each granulation was designed to produce 5 kg of wet material.

The dry granule size distribution exhibited bimodal behaviour with modes of 250 and 3500 μm and a mean particle diameter of 254 +/- 16 μm. An earlier study by our group [21] using helium pycnometry found the particle density of the dry granule to be 830 kg/m^3. Using the average mass fractions of the granule with this density, the granule was found to be composed of approximately 10% Geldart A, 34% Geldart A/B, 50% Geldart B and 6% Geldart D material. The A/B transition region was defined by the interpretation of Molerus [22].

3.3.2 Fluidized Bed Apparatus

The fluidized bed used in this study was a Glatt GPCG-1 conical fluidized bed dryer (Glatt Air Techniques Inc., Ramsey, NJ, USA). The Glatt GPCG-1 product bowl has a cone entrance angle of 18° with a 0.145-m inlet diameter and a 0.305-m outlet diameter. The distributor plate used was a perforated plate consisting of 256 holes of 2.7-mm diameter drilled on a 7.5-mm square pitch. This design resulted in an open area of 9.5%. The fluidized bed system allowed for control of both inlet air temperature and superficial gas velocity. The relative humidity of the fluidization air drawn by the

fluidized bed apparatus was 25 ± 2% under ambient conditions. See Fig. 3.1 for a schematic of the apparatus.

Dense bed pressure fluctuations, product temperature and moisture content were measured to monitor the drying process. Pressure fluctuations were collected using a single PCB 106B high-frequency piezoelectric dynamic pressure transducer (Piezotronics, Depew, NY, USA). The pressure transducer was flush-mounted to the inner wall of the conical bed 9 cm above the distributor plate. This sensor position was chosen based on the criterion proposed by van Ommen [19] for measuring pressure fluctuations in a fluidized bed with a single probe. Van Ommen found that the optimum probe location is at a axial location that is 20 – 40% of the total bed height. Pressure fluctuation data were collected at 400 Hz and filtered between 0.5 and 170 Hz. The data were also re-sampled at 20 Hz to remove noise from the average cycle frequency analysis. This re-sample frequency was chosen because typical phenomena related to bubbling occur in the range of 1 - 10 Hz in this study. The pressure fluctuation data were analyzed in two-minute increments for the 1.3-m/s drying velocity condition and four minutes for the 0.64-m/s condition. The product temperature was measured with a thermocouple immersed in the dense region of the fluidized bed and recorded manually.

Finally, the moisture content of the granule was determined by taking samples via a sample thief. Moisture homogeneity was assumed in these samples as they were taken from a well-mixed fluidization state. The granule samples were analyzed for moisture content (loss on drying) using a HB43 moisture analyzer (Mettler Toledo CmbH,

Greifensee, Switzerland). The moisture balance temperature was set at 100°C with the drying interval set to automatic, meaning that the sample would be dried until moisture removal was negligible.

3.3.3 Operating Conditions

Wet bed loadings of 3.0 kg were dried by air at superficial gas velocities of 0.64 and 1.3 m/s. The 0.64-m/s velocity was chosen to achieve a fluidization state just beyond that of the full support fluidization velocity. This was not measured based on pressure drop but visual observation of the fluidization state. The 1.3-m/s drying velocity was chosen to be well in excess of the previously mentioned state so that uniform internal circulation of solid material was achieved. Elevated velocities of 0.85 and 1.5 m/s were required for the first ten minutes of the 0.64 and 1.3-m/s drying experiments, respectively. This was required to achieve the desired fluidization states discussed above throughout this portion of the experiments. The need for these elevated velocities was based on visual observation through a sight-glass in the product bowl and can be related to changing full support velocity with moisture content [11]. The inlet fluidization air was heated from ambient temperatures to 65ºC prior to being introduced to the bed. Each drying experiment was repeated to check the reproducibility of the trends in the results.

3.4 Results

3.4.1 Pressure Fluctuation Analysis

Standard deviation, average cycle frequency and power spectral density analysis methods were used to analyze the pressure fluctuation time series data. The standard

deviation represents the changing amplitude of the pressure fluctuations and therefore corresponds to the relative bubble size in the bed. The average cycle frequency (*ACF*) and the dominant frequency (*DF*), which is obtained through the power spectral density analysis, quantify the frequencies related to the phenomena of bubbling in the system. *ACF* is defined as the number of cycles in the pressure fluctuation data per second, where each cycle is assumed to represent the presence of a bubble. The calculation of *ACF* is based on the number of upward crossings of the mean pressure signal per time increment used in the analysis. The calculation of *DF* is the frequency corresponding to the highest peak in a power spectrum. Based on the definition of a spectral estimate, the dominant frequency is therefore a measure of the dominant sinusoidal waveform in the data. Both frequency identification techniques are presented because time series data do not always resemble sinusoidal waveforms. This can result in the loss of significance in the power spectrum determined by the spectral estimate [23]. Furthermore, *DF* analysis does not represent the entire frequency spectra, so if multiple frequencies are present in a spectrum, *ACF* will better represent the overall bubbling related frequencies in the bed.

Representative transient profiles of these analysis techniques for the 0.64-m/s drying condition are shown in Fig. 3.2. As shown in Fig. 3.2(a), the standard deviation of the pressure fluctuations (σ) is initially low, but as moisture is removed the standard deviation begins to increase. The marked transition in the standard deviation under these drying conditions occurs at the 48 minute mark of drying, with a slight increase in the standard deviation experienced between 12 and 48 minutes. The higher standard deviation values at the beginning of the drying process are a result of the elevated gas

velocity during the first 10 minutes of drying. Beyond 48 minutes, the standard deviation increases significantly until the 68 minute mark of drying. From this point on, the standard deviation increases marginally over the remainder of the drying process.

The bubbling frequency (λ) analyses demonstrate a transition in hydrodynamics during drying as well (see Fig. 3.2(b)). Most noticeable in these data is the difference in the transitions experienced in *DF* and *ACF* due to their calculation methods. The dominant frequency transitions sharply, whereas *ACF* transitions in a more gradual manner similar to the standard deviation. During the first 44 minutes of drying, *DF* averages 4.9 Hz. At the 48 minute mark, *DF* decreases to 2.7 Hz and eventually reduces to 2.3 Hz by 64 minutes. Similar to the dominant frequency, *ACF* is relatively high during the first 44 minutes of drying; its average value is 4.6 Hz. After this, *ACF* begins to steadily decrease until the 68 minute mark is reached. At this point, *ACF* is 2.5 Hz and remains relatively constant until the end of drying.

The standard deviation and frequency profiles for drying at 1.3 m/s follow the same trends. As shown in Fig. 3.3, the standard deviation profile again increases during drying. The difference is that this transition occurs much earlier due to the higher drying rates created by the increase in gas velocity. The transition in standard deviation starts 16 minutes into drying and continues until the 32 minute mark is reached. *DF* and *ACF* have average values of 5.3 and 4.6 Hz for the first 14 minutes of drying, respectively. After this, *DF* immediately decreases to 3.0 Hz whereas the *ACF* decreases to 3.0 Hz after 26 minutes.

The standard deviation and *DF* profiles are similar to those presented by Chaplin et al. [15]. In their study, *DF* transitions from approximately 5 to 3 Hz and the standard deviation increases from approximately 100 to 500 Pa over the course of drying. These ranges of values are comparable to the present work (see Figs. 3.2 and 3.3). Furthermore, Chaplin et al. [15] reported stable hydrodynamic states at the beginning and end of drying through use of the S-statistic. This hydrodynamic behaviour is also observed in this study through the sigmoidal shape of the standard deviation and *ACF* profiles. For the standard deviation and *ACF* analysis of the second drying trial, which is not presented in this chapter, refer to Figs. B.1 and B.2 in Appendix B.

3.4.2 Power Spectra Analysis

More detailed information regarding the drying hydrodynamics can be extracted from the power spectra of the pressure fluctuation data. Figs. 3.4 and 3.5 illustrate a series of power spectra that represent the changes in the hydrodynamic behaviour during drying at 0.64 and 1.3 m/s, respectively. In this chapter, the power of a given frequency (λ) in a spectrum is denoted as Φ. As shown in Fig. 3.4(a), the power spectrum at the start of drying is relatively low power and has two distinct frequencies. The 5-Hz frequency is associated with the bubble related phenomena occurring in the bed, whereas the 1-Hz frequency represents the downward circulation of the material at the wall. This interpretation of the low frequency phenomenon is based on the visual observation of a distinct step-wise, downward movement of material through the sight-glass at approximately this frequency.

The power spectrum illustrated in Fig 3.4(a) is, for the most part, representative of the power spectra prior to the transition point in the frequency data. The only difference is that a mid-range frequency of approximately 3 Hz, which is virtually indistinguishable in Fig. 3.4(a), starts to slowly increase in magnitude. This phenomenon is illustrated in Fig. 3.4(b), which corresponds to the time just prior to the transition in dominant frequency. At this point, there are three distinct frequencies in the bed, with this mid-range frequency of approximately 3 Hz linked to phenomena related to the coalescence of higher frequency bubbles [20].

Fig. 3.4(c) demonstrates the power spectrum at 48 minutes where the dominant frequency and average cycle frequency analyses first show transitional behaviour. Here, bubble coalescence dominates the hydrodynamic behaviour as a significant shift in power occurs. The once dominant 5-Hz frequency has diminished in power and the 3-Hz coalescence frequency becomes the dominant frequency in the spectrum. As drying proceeds, the power associated with the coalescing frequency continues to increase and the higher bubbling frequency that was previously present is no longer a prominent frequency in the bed. The complete disappearance of the 5-Hz frequency occurs at 56 minutes (see Fig. 3.4(d)). Along with this, the low frequency behaviour at 1-Hz is no longer present. This coincided with the visually observed change in downward particle circulation from a step-wise pattern to a more continuous, free flowing one.

As is the case with the early stages of drying, the power spectra beyond 56 minutes do not change considerably. The only difference seen is an increasing power

associated with the coalescing frequency (see Figs. 3.4(d) – (f)). This indicates the increased dominance of the bubbling phenomena related to coalescence in the system and also explains the gradual increase seen in the standard deviation profile (Fig. 3.2(a)) from this point on. Increased coalescence will result in larger voids, which in turn create larger fluctuations in the bed. Finally, Fig. 3.4(f) represents the power spectrum very near the end of the drying process. Here, the low frequency behaviour at 1.2 Hz is assumed to be attributed to the large voids that periodically reach the sensor location.

The 1.3-m/s drying experiments exhibit similar behaviour over the course of drying. As shown in Fig. 3.5, the power spectra again start out with a bubbling frequency of 5 - 6 Hz which transitions to 3 Hz due to bubble coalescence. The only difference is that a 6-Hz frequency phenomenon appears towards the end of drying. This high frequency behaviour can be attributed to bubble splitting that occurs when superficial gas velocities approach those associated with the onset of turbulent fluidization [24]. This frequency behaviour is reported by Wiens and Pugsley [24] in a conical bed operating through the turbulent fluidization regime. This indicates that operation at 1.3 m/s likely results in turbulent fluidization behaviour towards the end of drying. See Figs. B.3 and B.4 for the drying power spectra from the second drying trial conducted for the study.

3.4.3 Drying Curve Analysis

In order to link the hydrodynamic characteristics to the mechanisms of drying, analysis of the product temperature profiles and drying curves is required. Here, the drying curve is the granule moisture content (Q_g) profile during drying. Fig. 3.6 illustrates

representative drying curves and product temperature profiles for drying at superficial gas velocities of 0.64 and 1.3 m/s. Visual inspection of these profiles indicate that the granule exhibits both constant and falling rate periods. To identify the critical moisture, the first significant increase in the product temperature was used. As discussed previously, this represents the transition from the constant rate period to the falling rate period as mass transfer limitations do not allow heat transfer conditions to reach equilibrium. Using this technique, the critical moisture content was reached at 56 minutes for the 0.64-m/s drying condition and 22 minutes for 1.3-m/s drying. Interpolation of the drying curves (see Fig. 3.6) result in critical moisture content values of 13 and 14 wt.% for the 0.64 and 1.3-m/s drying conditions, respectively.

3.5 Discussion

Comparison of the drying curve and pressure fluctuation analyses indicates that the observed changes in hydrodynamic behaviour are linked to the critical moisture content. Under both the 0.64 and 1.3-m/s drying conditions, the time at which the critical moisture content is reached corresponds to the hydrodynamic state where the complete transition to coalescence-dominated bubbling behaviour occurs (see Figs. 3.4(d) and 3.5(d)). This suggests that the high frequency bubbling phenomena in the constant rate period of drying is a result of the excess moisture on the surface of the granule. The excess moisture forms liquid bridges having high interparticle force strength as compared to dry interparticle forces such as van der Waals and electrostatic forces [25]. This in turn stabilizes the granule and limits bubble coalescence. Once this surface moisture cannot

continually be maintained and the transition into the falling rate period occurs, bubble coalescence becomes the dominant hydrodynamic behaviour.

The change in hydrodynamic behaviour can be explained based on the variation of the full support velocity at different granule moisture contents [11] in conjunction with the simple two-phase model proposed by Toomey and Johnstone [26]. In this model, it is assumed that all gas in excess of the minimum fluidization velocity goes into the formation of bubbles. Typically, this model is used with a known, and constant, minimum fluidization velocity. With this, bubble characteristics can be determined for various superficial gas velocities. The two-phase model can be used in a similar fashion since the full support velocity (U_{fs}), defined by Dry et al. [27] as the velocity where the bed is fully fluidized, is analogous to the minimum fluidization velocity [11]. The difference is that for the purpose of this study, the two-phase model must be considered with respect to a constant drying velocity (U_{bed}) and a full support velocity that decreases as moisture is removed from the granule. Taking this into account, the simple two-phase model predicts that the excess gas velocity (U_{ex}) will continually increase as drying proceeds. This suggests that volume of gas in the bubble phase, and therefore bubble size, will increase as drying proceeds. A schematic to help illustrate this is shown in Fig. 3.7.

The qualitative model predictions agree with the changes seen in the standard deviation and frequency data of Figs. 3.2 and 3.3. Immediately following the decrease in gas velocity at 10 minutes, U_{ex} will be minimized. This low excess gas velocity corresponds to smaller bubbles that will less likely coalesce. This creates a bubbling

hydrodynamic state with a relatively high bubbling frequency. Furthermore, small standard deviation in bed pressure fluctuations will occur as the momentum carried by small bubbles cannot displace much bed mass. As the granule dries, U_{ex} increases because U_{fs} decreases. This increase in excess gas results in the formation of larger bubbles at the inlet through coalescence and therefore a lower bubbling frequency. Along with this, the larger bubbles displace greater amounts of bed mass which in turn creates more intense bed fluctuations.

Since U_{fs} decreases monotonically as the granule dries, two-phase theory predicts similar monotonic changes in the standard deviation, *DF* and *ACF* should occur. However, this trend in the data does not emerge. Instead, the standard deviation, *DF* and *ACF* demonstrate distinct transitions in their values prior to reaching the critical moisture content. The marked change seen in these profiles can be clarified when the bed voidage is taken into account; since simple two phase theory assumes that bed voidage is constant. The full support bed voidage reported by Wormsbecker and Pugsley [11] decreased from approximately 0.70 to 0.50 between 20 and 10 wt.%; with the values remaining virtually constant above and below these moisture contents. This change in voidage is explained by a decrease in interparticle force strength due to the reduction of liquid bridging which in turn destabilizes the granule structure. This significant decrease in voidage intensifies the changes seen in the data as a considerable amount of gas is transferred from the emulsion phase to the bubble phase over this portion of the drying process. The period over which the standard deviation and ACF experience the majority of change for both drying velocities occurs over the granule moisture content range of

approximately 17 – 7 wt.%. This range is similar to that of the transition region with respect to the full support bed voidage reported above as well as the transitional region identified by Chaplin et al. [15] using the S-statistic. Furthermore, this change in bed voidage occurs around the critical moisture contents determined for each drying condition. This further supports that the change in hydrodynamics is related to the change in particle surface moisture properties.

Lastly, pressure fluctuations can better predict the critical moisture content. Dominant frequency analysis provides a distinct transition in the hydrodynamics 48 minutes into drying; 8 minutes prior to the product temperature. The power spectra also show a distinct transition from a high frequency bubbling state to a coalescing one around the critical moisture content. This indicates that pressure fluctuation analysis can measure the hydrodynamic transition between drying regimes whereas product temperature can only give an indication of the falling rate period by means of heat transfer properties through the increase in product temperature.

3.6 Conclusions

This study has presented an interpretation of fluidized bed hydrodynamic behaviour during the drying of placebo pharmaceutical granule. During the constant rate period, surface moisture results in extensive liquid bridging that fosters a multiple bubbling type regime. Once the critical moisture content is reached, pressure fluctuation analysis indicates that there is a change in the hydrodynamics as the bubbling phenomena in the bed transitions to a coalescence dominated regime. This is a result of the

disappearance of surface moisture and subsequent increase in excess gas in the system due to the change in bed voidage. Using the simple two-phase bubble theory as a qualitative indicator, the changes in the hydrodynamics measured through analysis of the pressure fluctuations are corroborated.

The implications of this study are far greater than identifying the hydrodynamic tendencies in a fluidized bed dryer. It demonstrates the potential of using pressure fluctuation measurements for the monitoring and control of such systems. By using simple analytic tools such as standard deviation and *ACF* analysis with real-time pressure fluctuation data, the critical moisture content can be better predicted than by conventional methods. An indication of this transition region would provide an operator with an opportunity to mitigate undesired phenomena such as attrition and elutriation [28] by reducing superficial gas velocities. Ultimately, the implementation of advanced control schemes to directly manipulate superficial gas velocities could be made possible through pressure fluctuation measurements. This improved monitoring and control will lead to more efficient operation of batch fluidized bed drying processes, especially where product quality is of great concern.

The results of this study are also applicable to processes other than batch fluidized bed drying. Processes such as particle coating and top spray continuous drying also involve dynamic changes in interparticle forces. Furthermore, processes that suffer from adverse agglomeration effects, most notably fluidized bed combustors and gasifiers, also fall under the scope of this work.

3.7 Nomenclature

ACF	average cycyle frequency, Hz
DF	dominant frequency, Hz
Q_g	granule moisture content, wt.%
t	time, min
T	product temperature, ˚C
U_{bed}	superficial gas velocity at the bed inlet, m/s
U_{ex}	excess gas velocity, m/s
U_{fs}	full support velocity, m/s
Φ	power spectral density, Pa^2/Hz
λ	frequency, Hz
σ	standard deviation, Pa

3.8 References

[1] Seville, J.P.K., Tüzün, U., Clift. R., (1997). Particle mechanics, in: Scarlett, B. & Jimbo, G. (Eds.), Processing of particulate solids, Blackie Academic & Professional, London, p. 99.

[2] Rumpf, H., (1962). Strength of granules and agglomerates, in: Knepper, W.A. (Ed.), Agglomeration, Wiley, New York, p. 379.

[3] Davidson, J.F., Thorpe, R.B., Al-Mansoori, O., Kwong, H., Peck, M., Williamson, R., (2001). Evaporation of water from air-fluidized porous particles. Chemical Engineering Science 56, 6089 - 6097.

[4] Henneberg, M., Heinrich, S., Ihlow, M., Mörl, L., (2003). Fluidized bed air drying: experimental study and model development. The Canadian Journal of Chemical Engineering 81, 176 - 184.

[5] Reyes, A., Eckholt, M., Alvarez, P.I., (2004). Drying and heat transfer characteristics for a novel fluidized bed dryer. Drying Technology 22 (8), 1869 - 1895.

[6] Reyes, A., Campos, C., Vega, R., (2006). Drying of turnip seeds with microwaves in fixed and pulsed fluidized beds. Drying Technology 24, 1469 - 1480.

[7] Seville, J.P.K., Clift, R., (1984). The effect of thin liquid layers on fluidisation characteristics. Powder Technology 37, 117 - 129.

[8] McLaughlin, L., Rhodes M., (2001). Prediction of fluidized bed behaviour in the presence of liquid bridges. Powder Technology 114, 213 - 223.

[9] Egerer, B., Zimmermann, K., Bauer, W., (1985). Flow and fluidization behaviour of yeasts in gas/solid fermentation and drying. Institution of Chemical Engineers Symposium Series vol 91, 257 - 269.

[10] Senadeera, W., Wijesinghe, B., Young, G., Bhandari, B. (2006). Fluidization characteristics of moist food particles. International Journal of Food Engineering 2(1), art. 7.

[11] Wormsbecker M., Pugsley, T., (2008). The influence of moisture on the fluidization behaviour of porous pharmaceutical granule. Chemical Engineering Science 63, 4063 - 4069.

[12] Grace, J.R., Sun, G., (1991) Influence of particle size distribution on the performance of fluidized bed reactors. The Canadian Journal of Chemical Engineering 69 (5), 1126 - 1141.

[13] Johnsson, F., Zijerveld, R.C., Schouten, J.C., van den Bleek, C.M., Leckner, B., (2000). Characterization of fluidization regimes by time-series analysis of pressure fluctuations. International Journal of Multiphase Flow 26, 663 - 715.

[14] Kage, H., Agari, M., Ogura, H., Matsuno, Y., (2000). Frequency analysis of pressure fluctuation and its confidence limit for detection of various modes of fluidization. Advanced Powder Technology 11(4), 459 - 475.

[15] Chaplin, G., Pugsley, T., Winters, C., (2004). Application of chaos analysis to pressure fluctuation data from a fluidized bed dryer containing pharmaceutical granule. Powder Technology 142, 110 - 120.

[16] Bai, D., Issangya, A.S., Grace, J.R., (1999). Characteristics of gas-fluidized beds in different flow regimes. Industrial and Engineering Chemistry Research 38, 803 - 811.

[17] Bi, H.T., Ellis, N., Abba, I.A., Grace, J.R., (2000). State-of-the-art review of gas-solid turbulent fluidization. Chemical Engineering Science 55, 4789 - 4825.

[18] Croxford, A.J., Harrison, A.J.L., Gilbertson, M.A., (2005). The optimization of pressure measurements for the control of bubbling fludised beds. International Journal of Chemical Reactor Engineering 3, A39.

[19] van Ommen, J.R., (2001). Monitoring Fluidized Bed Hydrodynamics, Ph.D. Dissertation, Delft University of Technology.

[20] Zhang, X., (1988). Bubble formation frequency study in a single-jet gas fluidized bed. Journal of Chemical Industry and Engineering 3, 70 - 85.

[21] Wormsbecker, M., Adams, A., Pugsley, T., Winters, C., (2005). Segregation by size difference in a conical fluidized bed of pharmaceutical granule. Powder Technology 153, 72 - 80.

[22] Molerus, O., (1982). Interpretation of Geldart's type A, B, C and D powders by taking into account interparticle cohesion forces. Powder Technology 33, 81 - 87.

[23] van der Schaaf, J., van Ommen, J.R., Takens, F., Schouten, J.C., van den Bleek, C.M., (2004). Similarities between chaos analysis and frequency analysis of pressure fluctuations in fluidized beds. Chemical Engineering Science 59, 1829 - 1840.

[24] Wiens, J., Pugsley, T., (2006). Tomographic imaging of a conical fluidized bed of dry pharmaceutical granule. Powder Technology 169, 49 - 59.

[25] Seville, J.P.K., Willett, C.D., Knight, P.C., (2000). Interparticle forces in fluidisation: a review. Powder Technology 113, 261 - 268.

[26] Toomey, R.D., Johnstone, H.F., (1952) Gas fluidization of solid particles. Chemical Engineering Progress 48, 220 - 226.

[27] Dry, R.J., Judd, M.R., Shingles, T., (1983). Two-phase theory and fine powders. Powder Technology 34, 213 - 223.

[28] Chaplin, G., Pugsley, T., Winters, C., (2005). The S-statistic as an early warning of entrainment in a fluidized bed dryer containing pharmaceutical granule. Powder Technology 149, 148 - 156.

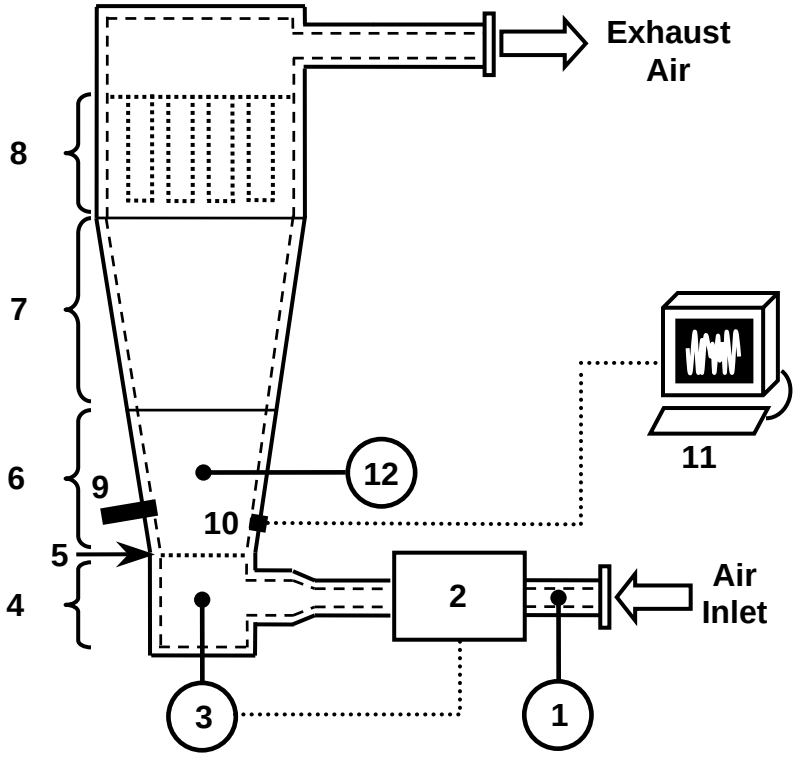

Figure 3.1: Schematic of the Glatt GPCG-1 fluidized bed dryer (not to scale): (1) flow indicator, (2) air heater, (3) inlet temperature thermocouple, (4) windbox, (5) perforated distributor plate, (6) product bowl, (7) expansion chamber, (8) filter bag assembly, (9) sample thief, (10) pressure transducer, (11) data acquisition computer, (12) product temperature thermocouple.

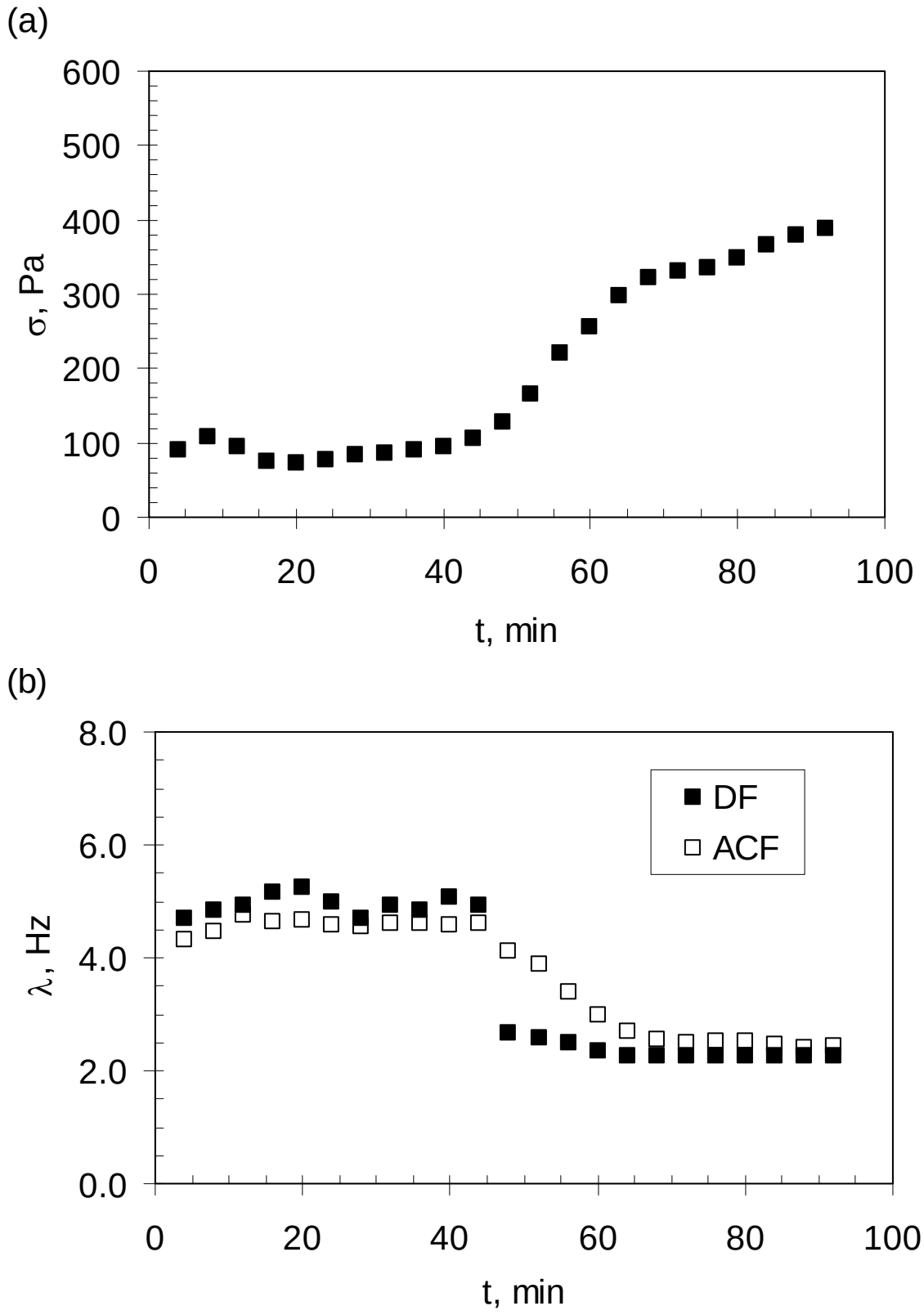

Figure 3.2: Pressure fluctuation analysis for drying at a superficial air velocity of 0.64 m/s: (a) standard deviation, (b) frequency.

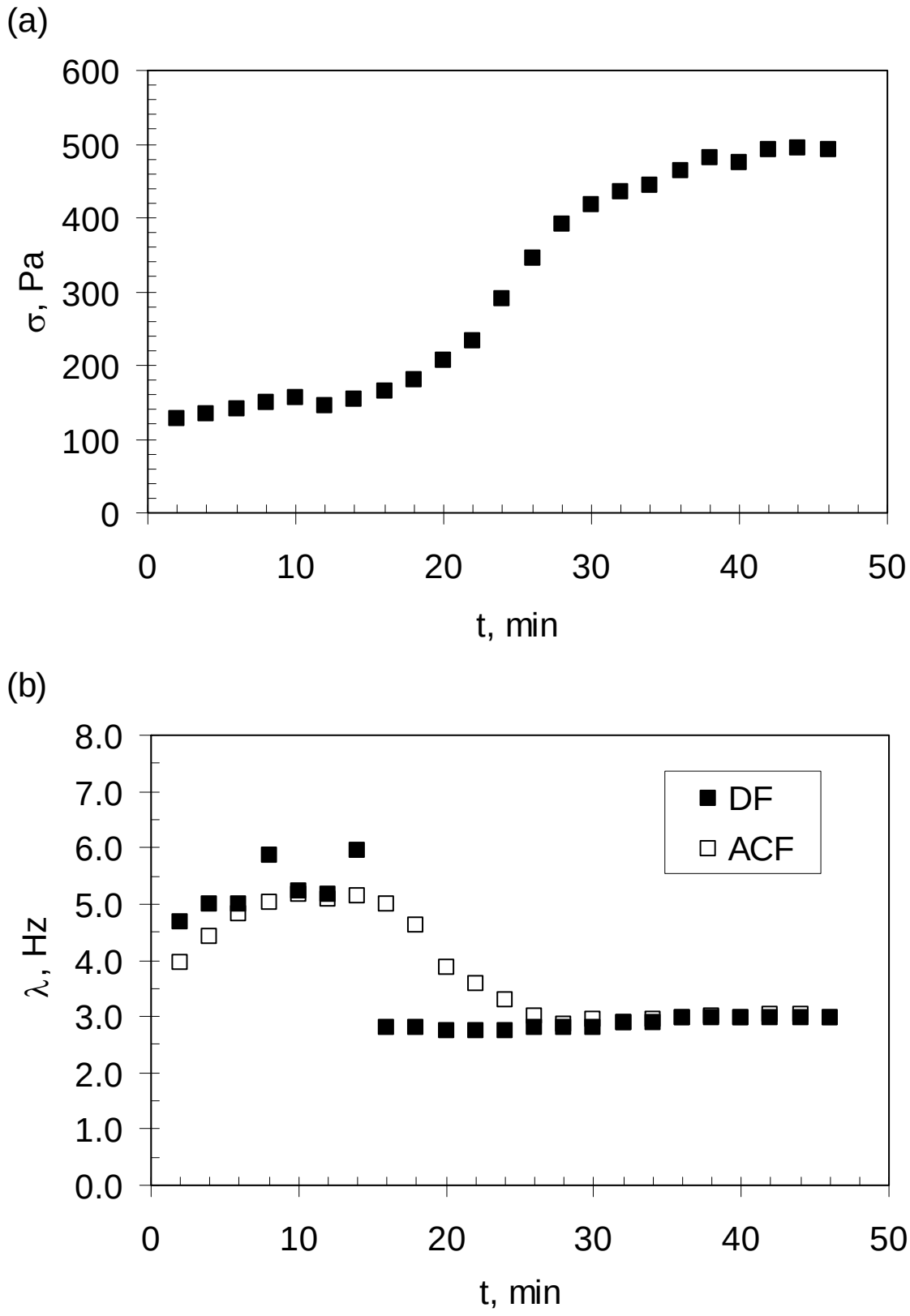

Figure 3.3: Pressure fluctuation analysis for drying at a superficial air velocity of 1.3 m/s: (a) standard deviation, (b) frequency.

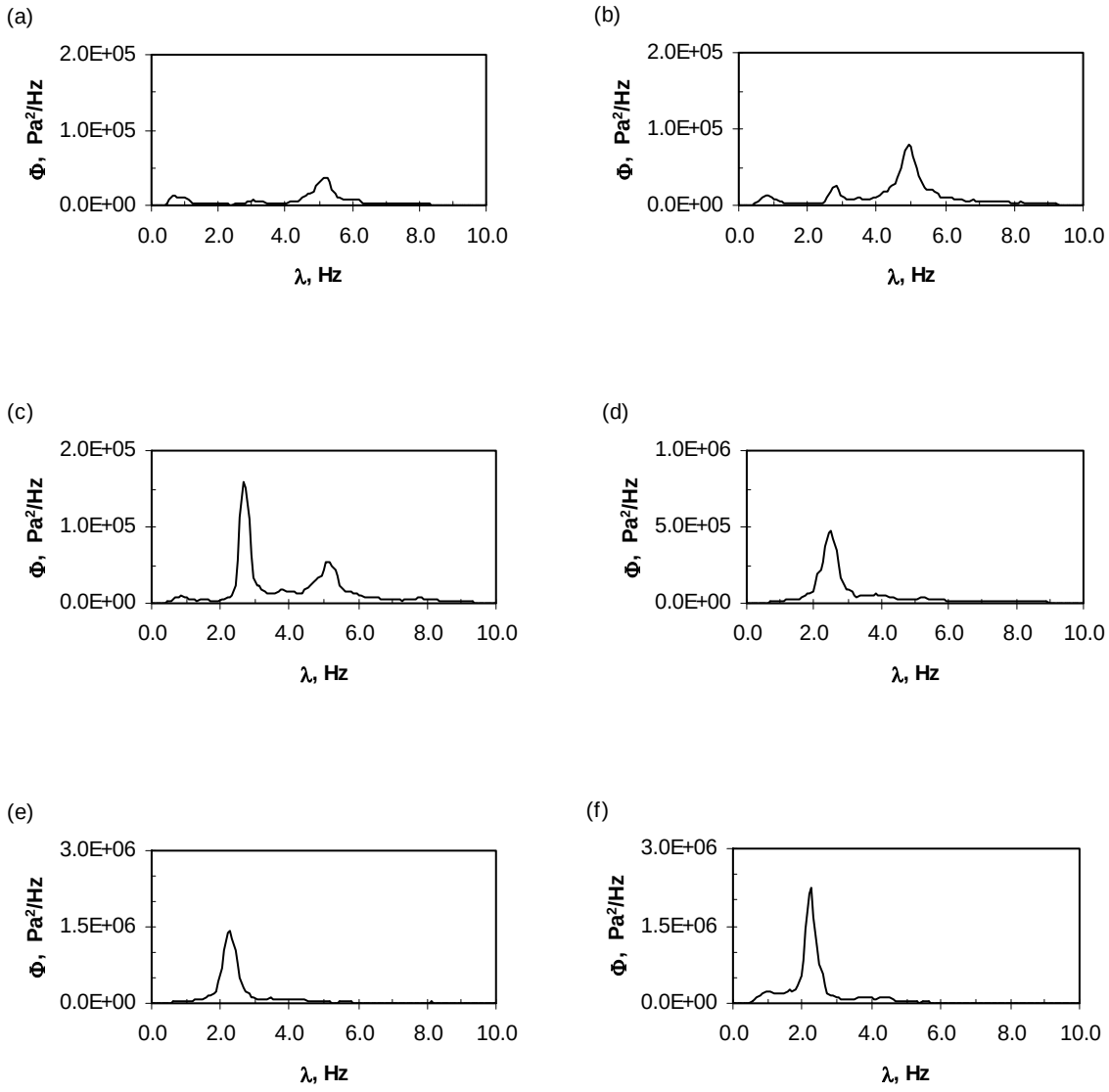

Figure 3.4: Pressure fluctuation power spectra over the course of drying for the 0.64 m/s superficial air velocity condition: (a) 16 minutes, (b) 44 minutes, (c) 48 minutes, (d) 56 minutes, (e) 72 minutes, (f) 88 minutes.

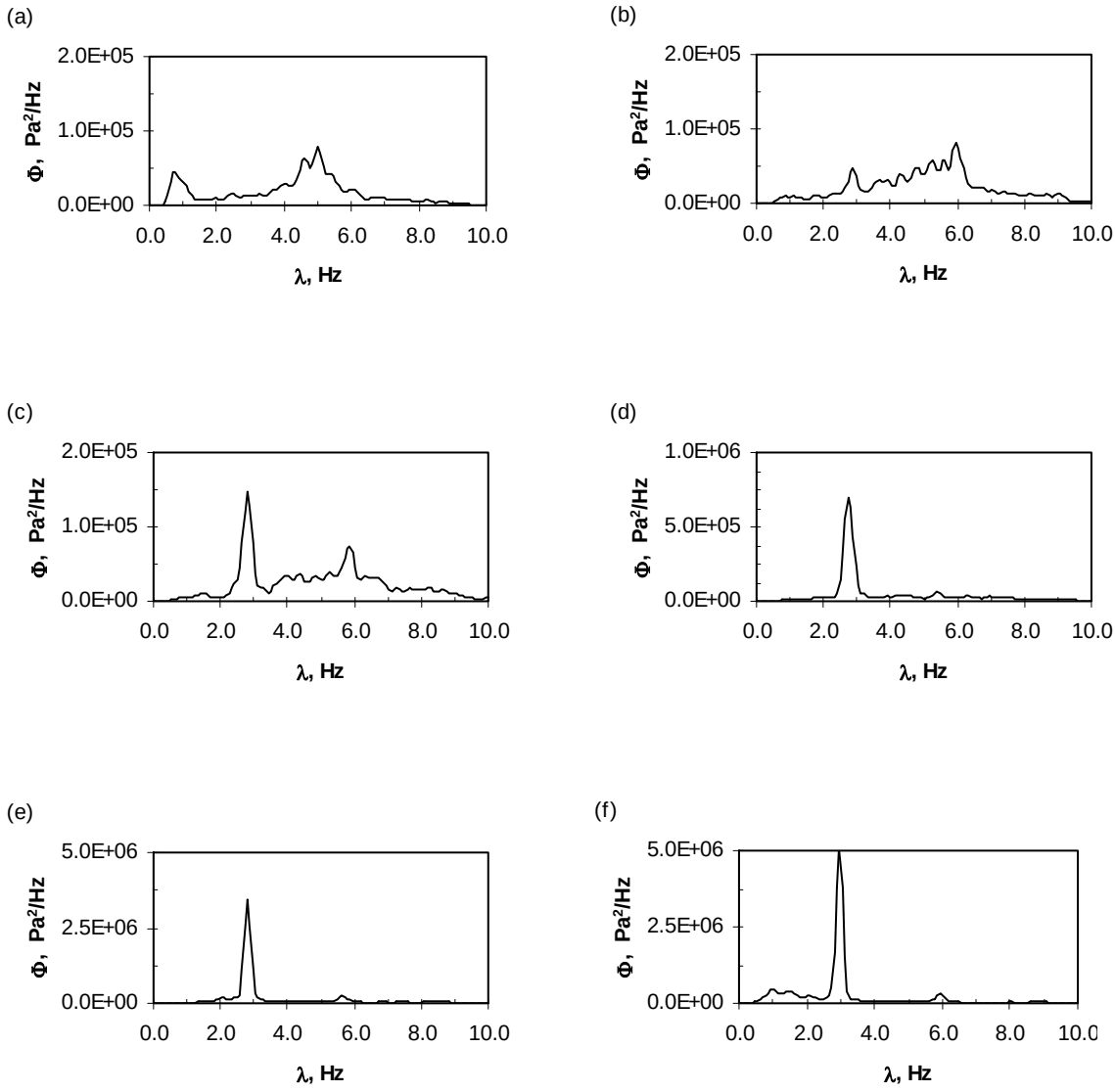

Figure 3.5: Pressure fluctuation power spectra over the course of drying for the 1.3 m/s superficial air velocity condition: (a) 4 minutes, (b) 14 minutes, (c) 16 minutes, (d) 22 minutes, (e) 28 minutes, (f) 42 minutes.

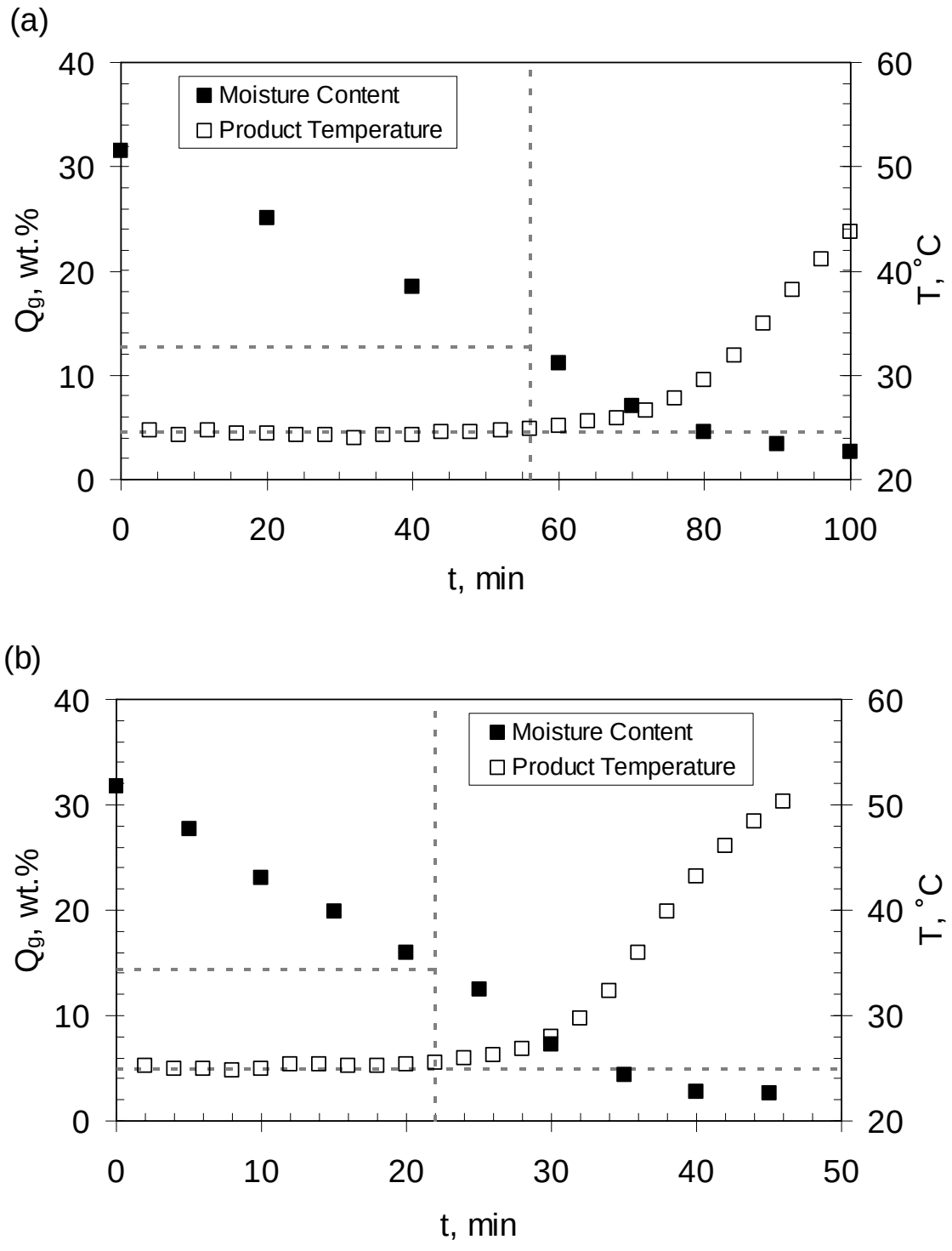

Figure 3.6: Moisture and temperature drying profiles for: (a) 0.64 m/s fluidization condition, (b) 1.3 m/s fluidization condition.

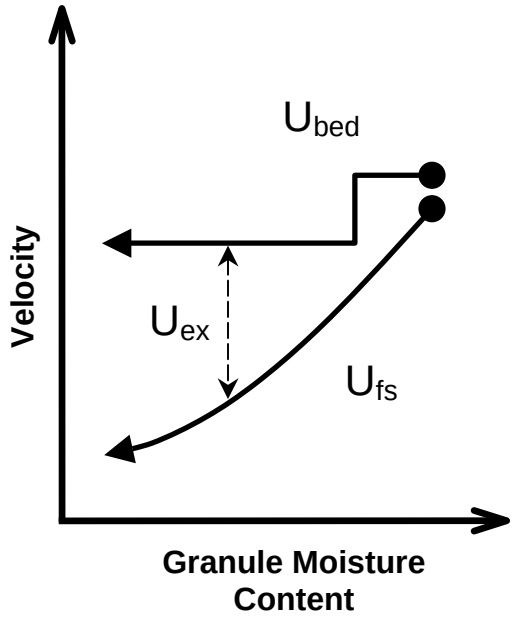

Figure 3.7: Explanation of the simple two phase theory related to drying (modified after [11]). The direction of the arrows for U_{bed} and U_{fs} indicate the change in their values during the drying process. U_{ex} is the difference in gas velocity between U_{bed} and U_{fs}.

CHAPTER 4 - Distributor Induced Hydrodynamics in a Conical Fluidized Bed Dryer containing Dry Pharmaceutical Granule

The contents of this chapter have been submitted for publication in the journal ***Drying Technology – An International Journal*** in a similar version to what appears in this chapter.

Citation

Wormsbecker, M., Pugsley, T. Distributor induced hydrodynamics in a conical fluidized bed dryer. Submitted to Drying Technology in April 2008 (Ref No. not provided).

Contribution of Ph.D. Candidate

Experiments were planned and performed by Michael Wormsbecker. Todd Pugsley provided consultation regarding the experimental program. The software for all data collection and analysis was developed by Michael Wormsbecker. All of the writing of the submitted manuscript was done by Michael Wormsbecker with Todd Pugsley providing editorial guidance regarding the style and content of the paper.

Contribution of this Paper to the Overall Study

This paper provides an initial basis for studying fluidized bed dryer distributor designs used in the pharmaceutical industry. The hydrodynamics resulting from the various distributor designs, as well as the impact of superficial gas velocity, are discussed. By conducting this work with dry pharmaceutical granule, differences in the hydrodynamics can be identified as compared to actual drying experiments because steady-state conditions exist. The differences in hydrodynamics that arise between distributors in this study will be considered when dryer performance based on distributor design is discussed in Chapter 5.

4.1 Abstract

The hydrodynamics induced by perforated, punched and mesh (Dutch weave) distributor plates were studied using dry placebo pharmaceutical granule in a conical fluidized bed dryer at inlet gas velocities of 0.5 to 3.5 m/s. The study found that the punched plate shows improved hydrodynamics up to 2.0 m/s as it demonstrates lower bubbling related frequencies and limited the effect of segregation as compared to the perforated plate and Dutch weave designs. Beyond 2.0 m/s, the influence of gas velocity supersedes that of distributor design as coalescence dominates the hydrodynamic behaviour resulting in low frequency, high intensity spectral density distributions for each distributor design studied.

4.2 Introduction

The design of distributor plates in gas fluidization processes is critical to the overall performance of the process. Uniform distribution of the fluidization gas improves particle fluidization and overall solids transport, while reducing particle deposition tendencies [1]. Many chemical process industries, including pharmaceutics, have used the classical perforated plate as the distributor of choice over the years. However, the pharmaceutical industry has also employed other distributor designs such as the Dutch weave, and more recently punched plates, in attempts to alleviate the fluidization concerns faced by the industry.

The perforated plate distributor with vertical holes continues to be the standard for many industrial processes. Although simple to construct and relatively inexpensive, the perforated plate can develop dead zones between its orifices, give rise to poor bed utilization and result in uneven air distribution across the bed if not designed properly [1]. The Dutch weave is a mesh screen woven to precise tolerances, thus creating openings that are tiny curved, triangular tunnels. These fine apertures created by the weave will eliminate the potential for dead zones between orifices, but the small bubbles generated may not carry sufficient energy to fluidize the larger particles in the bed, resulting in segregation [2]. Furthermore, like the perforated plate, if the pressure drop across the weave is sufficiently low, zones of defluidization can exist due to poor gas distribution [2]. The punched plate design is created by punching out a series of orifices from the bottom of the plate using a die. These orifices are oriented in the same direction on a series of concentric rings on the distributor plate to provide a lateral velocity component

to the gas flow in a circular direction (i.e. swirling flow). The idea behind this plate is that it results in better directional control of gas, and therefore solids, in the bed. Due to the structural design, the punched plate also results in less frequent cleaning and maintenance as compared to a perforated plate, which is beneficial from an operational point of view. Figs. 4.1 and 4.2 are representative schematics of the distributor designs used in the present study.

Few comparative distributor design studies have been put forth in the open literature. Bauer et al. [3] investigated the effect of various distributor designs on fluidized bed reactor performance. Distributor designs including a porous plate, perforated plate and nozzle plate were compared in this work. They concluded that differences in these distributor designs had no impact on the mass transfer coefficients, but did influence bed hydrodynamics. The porous plate provided a much finer dispersion of gas as compared to the perforated plate design, which led to higher reactor conversions. A later study done by Garncarek et al. [4] supported this finding; they reported that the porous plate distributor design provides more even air distribution as compared to the perforated plate.

Ouyang and Levenspiel [5] were the first to design a plate to impart a lateral component to the fluidizing gas; referred to by the authors as a spiral distributor. They found that at gas velocities greater than 10 times minimum fluidization, the spiral design resulted in smaller pressure fluctuations as compared to the porous plate distributor. This suggests that smaller bubbles and less gas bypassing is experienced with the spiral

distributor plate design under these conditions [5]. A more recent study by Chyang and Lin [6] appears to draw parallels to the distributor designs used in the pharmaceutical industry. In this work, the authors compare axial fluidization distributor designs (perforated plate) to lateral fluidization distributor design (right angle nozzle distributor). This work demonstrates that inducing a lateral component to the fluidization gas through unidirectional oriented nozzles results in significant differences in the fluidized bed hydrodynamics as compared to the perforated plate distributor design. These hydrodynamic differences greatly improve fluidization quality as gas-solids contacting is increased and entrainment is limited.

As demonstrated by the literature introduced above, some research has been published on distributor design induced hydrodynamics, including that related to swirling flow distributors. The problem with these studies from a pharmaceutical industry perspective is that the influence of distributor design has been considered with respect to cylindrical fluidized beds and uniform particle size distributions. These two parameters, especially the vessel geometry, have a significant impact on fluidized bed hydrodynamics as compared to their convention. For example, Toyohara and Kawamura [7] have demonstrated the differences in the fluidization regimes associated with a conical fluidized bed geometry. With regards to particle size distribution, Wiens and Pugsley [8] and Grace and Sun [9] have both shown that the hydrodynamics associated with bimodal and wide size distributions differ from that of mono-disperse and narrow size distributions, respectively. Based on these works, it is likely that different distributor designs will induce behaviour that is different from what has been presented in literature

to date when the vessel geometry and particle size distribution are changed. Therefore a study into the impact of distributor design under these conditions, which are tailored towards the pharmaceutical industry, is warranted.

The present study examines the hydrodynamics induced by the various distributor types commonly used in the pharmaceutical industry. A comparative study of the perforated plate, punched plate and Dutch weave distributors is performed in a conical fluidized bed using pressure fluctuation time-series analysis. The objective of the study is to highlight the hydrodynamic differences induced by the different distributors, as well as to demonstrate the ability of pressure fluctuation analysis to describe the hydrodynamics in a conical fluidized bed. This will be done using both time and frequency domain analysis techniques.

4.3 Materials and Methods

The conical fluidized bed illustrated schematically in Fig. 4.3 was used in this study. The vessel has a cone apex angle of 27˚ with a 0.115-m inlet and a 0.25-m cone outlet. The static bed height was maintained at 17 cm, which corresponds to a diameter of 19.7 cm at the upper bed surface. A 1.3-m tall disengagement section is flange-connected to the cone outlet. Any entrained particles leaving the disengagement section are captured in a cyclone and dropped into a fines collection pot. Fluidizing air is supplied by a regenerative blower with the volumetric flow of air to the fluidized bed controlled with two manual bypass valves. The flow of air into the windbox is metered with an orifice plate designed according to ASME standards for fluid flow in closed conduits. The

orifice pressure drop was measured using a water manometer. Finally, the relative humidity was monitored over the duration of the study using an EE Series humidity sensor from EE Electroniks. The relative humidity was measured to be 18 ± 2% over the duration of the study.

Three different distributor designs were investigated. The perforated plate distributor is a 1.5-mm thick aluminum plate with 2.6-mm holes spaced 7.5 mm apart and drilled on a square pitch. This produces a percent open area of 9.5% in the perforated plate. The punched plate was fabricated by Merck Frosst Canada Ltd., Kirkland, Canada. The distributor plate is 1.0 mm thick with each slot being approximately 5.75 mm wide and 1.0 mm in height. There is approximately 16750 slots/m^2 on the punched plate distributor generating a percent open area of 9.6%. Finally, the Dutch weave distributor was a 24 x 110 stainless steel mesh manufactured by NIRO Inc., Columbia, USA. Using microscopy, the nominal size of each opening in the weave was found to be triangular with base and height dimensions of approximately 25 x 90 μm. With this information, the equivalent percent open area was calculated to be 15 ± 1%.

Pre-dried placebo pharmaceutical granule was used as the test material in the present study. Fig. 4.4 illustrates the granule particle size distribution where φ is the mass fraction corresponding to the average particle size (d) for a specific size class. The pharmaceutical granule exhibits a continuous, bi-modal distribution with modes of 168 and 1288 μm. The particle size distribution was measured with the Mastersizer S-Series Long Bench particle size analyzer of Malvern Instruments Inc., Malvern, UK. The

minimum fluidization velocity of this bimodal size distribution was found experimentally to be 0.075 m/s.

Pressure fluctuation analysis was carried out using a single high frequency piezoelectric pressure transducer. The pressure transducer is a Model 106B transducer manufactured by PCB Piezotronics Inc., Depew, USA. A STA-300 screw terminal and a KPCI-3101 PCI card made by Keithley Instruments Inc., Cleveland, USA, were used for data acquisition from the pressure transducer. The interface used for continuous data logging was built using LabVIEW™ software created by National Instruments™, Austin, USA. The pressure transducer was flush-mounted to the inner wall of the conical bed 7 cm above the distributor. This probe position corresponds to 41% of the static bed height of 17 cm, which is in accordance with the recommendation of van Ommen [10] for probe positioning in a bench-scale fluidized bed. Pressure fluctuations in the bed were measured at superficial gas velocities (based on the inlet diameter of the cone) which varied between 0.5 - 3.5 m/s for each distributor. Data were collected for six minutes at 400 Hz for each experiment, resulting in three 2-minute analysis time series. These triplicate experiments were used as a means of demonstrating reproducibility of the fluidization state. The data were filtered with a band pass filter of 0.5 to 170 Hz to remove any low frequency drift in the pressure and meet the Nyquist criteria for signal aliasing.

4.4 Results and Discussion

Figs. 4.5 - 4.7 are samples of pressure time-series data for the perforated plate, punched plate and Dutch weave mesh distributors at superficial gas velocities of 0.5 and 1.5 m/s. As shown by these figures, there is a distinct difference between the pressure fluctuation time series at these velocities. Fluidization at 0.5 m/s generates smaller amplitude, more frequent fluctuations as compared to the 3.0-m/s fluidization state where distinct periodic fluctuations occur with each distributor design. However, identifying differences in distributor design hydrodynamics based on the pressure fluctuation time-series alone is very difficult, if not impossible. Using the proven analysis techniques of standard deviation [9, 11-14], average cycle frequency [15], and frequency analysis using power spectral density [11, 14-17], details regarding the differences between the hydrodynamic states induced using the various distributor designs become more clear. For a more in depth review of time and frequency domain analysis of pressure fluctuations used in this study, refer to Johnsson et al. [11] and van der Schaaf et al. [15].

4.4.1 Time Domain Analysis

Figs. 4.8 and 4.9 compare the average standard deviation (σ) and average cycle frequency (*ACF*) of the pressure fluctuation data for the triplicate experiments as a function of superficial gas velocity (*U*). The standard deviation of the pressure fluctuations was calculated with band-pass filtered data. In contrast, the pressure data were re-sampled at 20 Hz for the calculation of *ACF*. This was done to reduce the influence of noise created by smaller fluctuations in the high frequency components of the data which do not represent bubbling phenomena in the bed. By doing so, *ACF* will

closely correspond to the peak amplitude frequency of a power spectrum assuming a unimodal frequency distribution exists. This peak frequency in the spectrum is commonly referred to as the dominant frequency (*DF*).

With each distributor design, the standard deviation increases with superficial gas velocity until a maximum is reached and the values appear to level off. The maximum in standard deviation, which is generally considered to mark the onset of turbulent fluidization [13], is reached at approximately 3.0 m/s for all of the distributors. The relatively slow transition to turbulence, demonstrated by the leveling off of the standard deviation, can be attributed to the wide size distribution of the granule [9], but also transitions in the axial hydrodynamic behaviour due to the conical geometry of the bed itself [8]. In contrast to the standard deviation profile, *ACF* decreases with gas velocity and reaches a minimum at approximately 2.5 m/s. This type of frequency behaviour was also found in conical beds by Wiens and Pugsley [8]. For the data used in Figs. 4.8 and 4.9, see Table C.1 in Appendix C.

The key difference between the time-series data of the distributors is that the punched plate demonstrates a higher standard deviation in its pressure fluctuations over much of the velocity range studied. Intuitively, an increase in standard deviation would suggest that the bubble size has grown (i.e. through coalescence) creating larger pressure fluctuations in the fluidized bed. However, this cannot be the case as *ACF* associated with the punched plate is higher than the perforated plate over the entire velocity range studied and the Dutch weave over the majority of the range. A higher *ACF* suggests that the

phenomena related to bubbling are occuring at a greater frequency, which is not possible for larger bubbles if the volumetric flow in the system has not changed.

An explanation for this higher standard deviation profile coupled with an increase in bubbling frequency is believed to be attributed to the lateral velocity component imparted on the gas by the punched plate distributor design. By directing the gas in the horizontal direction, the gas will further disperse to the periphery of the bed and form bubbles. These bubbles, which are closer to the pressure sensor, will result in less attenuation of the compression wave generated by the bubbles formed as they have a shorter distance to travel to the sensor face. Less attenuation of the pressure signal will result in a higher intensity fluctuation, which leads to a greater standard deviation.

The idea of radial pressure wave attenuation has been documented and described in the work of van Ommen and co-workers [10]. They have shown that the pressure peak intensity decreases exponentially with radial position of a sensor from a compression wave source. Although this work was considered with a single gas injection and a traversing pressure probe, the phenomenon of pressure wave attenuation can be extrapolated to indicate relative bubble position in a fluidized bed with the use of the standard deviation of the pressure fluctuations. The standard deviation is related to the peak intensity of the pressure as it gives an indication of the deviation of local pressure from the mean pressure, or in other words, the peak intensity confidence limits. Therefore, if the standard deviation has increased, and the bubble size is smaller, or of the same order of magnitude with respect to a given superficial gas velocity, then it suggests

that the bubbles are closer to the bed wall. In addition to these experimental findings, van Ommen [10] also simulated the influence of radial position on standard deviation using the Davidson model [18] and found that the standard deviation does indeed decrease exponentially with radial position.

4.4.2 Frequency Domain Analysis

To further investigate the hydrodynamics induced by the distributor designs, frequency domain analysis was also performed. This is done by first using fast Fourier transforms to convert the pressure fluctuation time series into the frequency domain. The resulting power spectral density (PSD) illustrates the different frequency in the bed (f) and their associated power, or intensity, (ϕ). This power suggests the significance of the frequencies present in the hydrodynamic data. Figs. 4.10 and 4.11 illustrate PSDs for triplicate experiments with the different distributor designs at various velocities. The reproducibility demonstrated through the power spectra illustrates the reproducibility of the hydrodynamics between data sets.

Figs. 4.10(a) through (c) illustrate power spectra for superficial gas velocities of 0.5 - 1.5 m/s for each plate. At 0.5 m/s, the power spectrum for each distributor design exhibits a relatively low power and high frequency PSD as compared to the power spectra at high velocities (see Fig. 4.11). The high frequency and low power associated with each of the power spectra of the distributor designs represent a bubbling fluidization regime of many, but relatively small, bubbles. This hydrodynamic behaviour is reasonable as segregation is expected to occur with the granule used in the present study

at an inlet velocity of 0.5 m/s [19]. It is believed that the segregation will create a partially fluidized bed with a segregated core region made up of the segregated granule [7]. This segregated core will impede gas coalescence, thus limiting bubble growth in the fluidized bed.

At 1.0 m/s, the power spectra shift towards lower frequencies for all the distributor designs. This shift in frequency is consistent with bubble coalescence in the system as the bubbles are passing at a lower rate and therefore must be larger since the volumetric flow rate has also increased. However, the punched plate power spectrum at this velocity is very narrow and significantly more dominant as compared to spectra of the perforated plate and Dutch weave designs. This suggests that the bubbles created by the punched plate do not tend to coalesce randomly with neighbouring bubbles to create a wide range of bubbles of varying sizes and frequencies passing through the bed. Rather, coalescence appears to be minimal, or even non–existent, as the bubbling phenomena frequency has not decreased significantly. Furthermore, the low power, wide frequency distribution of the perforated and Dutch weave designs suggests the presence of a multiple bubbling regime.

Further coalescence related bubbling phenomena is evident as the velocity is increased to 1.5 m/s. This is best illustrated by the perforated plate design and its power spectrum at this velocity (see. Fig. 4.10(a)). The power spectra of the perforated plate show a distinct shift in frequency to 4.3 Hz. This indicates that the system experiences a greater degree of coalescence as the frequency has decreased, but also that this

coalescence has become much more prevalent as it is of much higher intensity. The punched plate shows a similar trend, however, it also exhibits two distinct bubbling phenomena frequencies at 4.3 and 5.5 Hz. This suggests that the coalescence is occurring to some extent, but not fully as is the case with the perforated plate.

It is interesting to note the power spectra of the Dutch weave at 1.5 m/s. The power spectra are still relatively weak in power and broad with respect to its frequency domain. Furthermore, the power spectra have changed little with respect to velocities up to 1.5 m/s. These vastly different power spectra as compared to the perforated and punched plates may be a result of a significantly segregated core region in the bed. Segregation was observed visually through the acrylic walls of the conical bed at 1.5 m/s with the Dutch weave, which was not the case for the other distributor designs. The greater extent of segregation occurs because the small apertures of the Dutch weave do not produce gas jets with adequate momentum to fluidize the larger particles. As a result, the stagnant particles in the bottom of the bed act as a second distributor for the gas to percolate through. This behaviour maintains the multiple bubbling regime identified at this velocity. Segregation was also observed with the perforated plate at 1.0 m/s, which would suggest its spectra at this velocity is also attributable to segregation effects. Again, the segregation study by our group [19] in a conical fluidized bed has shown that particle segregation still exists with the perforated plate at 1.0 m/s, which lends support to the multiple bubbling regime hydrodynamics observed with these two plate designs.

Fig. 4.11 demonstrates that bed hydrodynamics are very similar beyond velocities of 2.0 m/s. As shown in Fig. 4.11, a distinct hydrodynamic frequency is present with each of the distributor designs and these frequency distributions are similar in magnitude and frequency. Visually, it was observed that the fluidized bed was well-fluidized and that the bubbles were erupting violently at the bed surface. These coalescence-dominated bubbling regimes have similar time and frequency domain characteristics as that documented by Johnsson et al. [11] as an exploding bubble regime. In this regime, the bubble size is large with significant through-flow of gas through the bubbles. This results in an eruption at the bed surface that is 'explosive' as compared to a lower velocity, higher frequency bubbling regime. The eruption of the bubble causes a decrease in pressure in the bed which is then followed by an increase in gas velocity for the whole bed; leading to a newly formed large bubble at the distributor level [20]. Due to dependence of the bubble eruption and formation phenomena in the bed, very distinct frequency phenomena in the power spectra are developed. At this point, the hydrodynamics also appear to be influenced more by the fluidization gas than the distributor design. As discussed above, the excess gas coalesces very quickly into large bubbles which in turn create periodic fluctuations in the bed. The power spectra show that this periodicity is present regardless the distributor design suggesting that the coalescence governs the hydrodynamics in the system.

Another characteristic of the power spectra at high velocities is the presence of a higher frequency phenomenon at 3.0 m/s. Referring back to the standard deviation analysis of Fig. 4.8, it was determined that 3.0 m/s corresponds to the transition to

turbulent fluidization for each distributor design. Cai et al. [21] have shown that the transition from bubbling to turbulent fluidization in a cylindrical bed occurs when bubble splitting dominates over bubble coalescence. These smaller bubbles manifest themselves as higher frequencies in the PSD analysis. Work within our group carried out by Wiens and Pugsley [8] using electrical capacitance tomography has shown that this bubble splitting begins to occur at 2.5 m/s. Under these velocity conditions it appears that smaller bubbles are detaching from the parent bubble, which explains the appearance of the higher frequencies in the PSDs of Fig. 4.11.

4.5 Conclusions

Standard deviation, average cycle frequency and spectral analysis were used collectively to illustrate the impact of distributor design on fluidized bed hydrodynamics in a lab-scale conical fluidized bed containing pre-dried pharmaceutical granule. At superficial gas velocities below 2.0 m/s, limited bubble coalescence, with higher bubbling phenomena frequencies were experienced with the punched plate as compared to the perforated plate. This suggests improved hydrodynamics in the bed and better gas-solids contacting. The fluidization characteristics induced by the punched plate below 2.0 m/s are believed to be due to the lateral component of the fluidizing gas velocity created by the design of the punched plate. Above 2.0 m/s, the high gas velocities dictate the hydrodynamics resulting in little difference between the distributor designs. Although differences in standard deviation and average cycle time do exist, the PSD analysis suggests that an exploding bubbling regime exists with all the distributors, which dominates the hydrodynamic tendencies of the system.

A greater extent of core segregation occurs with the Dutch weave and perforated as compared to the punched plate. The resulting power spectra under the segregated conditions suggest an apparently desirable hydrodynamic state based on standard deviation and average cycle frequency analysis. However, this segregation is undesirable from a fluidization point of view, especially with respect to drying. Segregation is believed to be one of the contributors to the axial variation of granule moisture content in fluidized beds. This results in inaccurate monitoring of moisture content during drying which can adversely affect the end of drying product quality. The poor circulation qualities of the Dutch weave renders the distributor plate design ineffective for fluidized bed drying of pharmaceutical granule under the conditions studied.

4.6 Nomenclature

ACF	average cycle frequency, Hz
d	particle size, μm
f	frequency, Hz
P	dynamic pressure, Pa
t	time, s
U	superficial gas velocity at bed inlet, m/s
ϕ	power spectral density, Pa^2/Hz
φ	mass fraction, %
σ	standard deviation of pressure fluctuations, Pa

4.7 References

[1] Masters, K. Industrial fluidized bed drying: trends and developments. In *Fluidization VII*, Brisbane, Australia, May 3-8, 1992; 59-72.

[2] Geldart, D.; Baeyens, J. The design of distributors for gas-fluidized beds. Powder Technology 1985, 42, 67-78.

[3] Bauer, W.; Werther, J.; Emig, G. Influence of gas distributor design on the performance of fluidized bed reactor. German Chemical Engineering 1981, 4, 291-298.

[4] Garncarek, Z.; Przybylski, L.; Botterill, J.S.M.; Broadbent, C.J. A quantitative assessment of the effect of distributor type on particle circulation. Powder Technology 1997, 91, 209-216.

[5] Ouyang, F.; Levenspiel, O. Spiral distributor for fluidized beds. Industrial and Engineering Chemistry Process Design and Development 1985, 25, 504-507.

[6] Chyang, C.-S.; Lin, Y.-C. A study in the swirling fluidization pattern. Journal of Chemical Engineering of Japan 2002, 35(6), 503-512.

[7] Toyohara, H.; Kawamura, Y. Fluidization of a tapered fluidized-bed of a binary particle mixture. International Chemical Engineering 1992, 32(1), 164-171.

[8] Wiens, J.; Pugsley, T. Tomographic imaging of a conical fluidized bed of dry pharmaceutical granule. Powder Technology 2006, 169, 49-59.

[9] Grace, J.R.; Sun, G. Influence of particle size distribution on the performance of fluidized bed reactors. Canadian Journal of Chemical Engineering 1991, 69, 1126-1134.

[10] van Ommen, J.R.; van der Schaaf, J.; Schouten, J.C.; van Wachen, B.G.M.; Coppens, M.-O.; van den Bleek, C.M. Optimal placement of probes for dynamic pressure measurements in large-scale fluidized beds. Powder Technology 2004, 139, 264-276.

[11] Johnsson, F.; Zijerveld, R.C.; Schouten, J.C.; van den Bleek, C.M.; Leckner, B. Characterization of fluidization regimes by time-series analysis of pressure fluctuations. International Journal of Multiphase Flow 2000, 26, 663-715.

[12] Satija, S.; Fan, L.-S. Characteristics of slugging regime and transition to turbulent regime for fluidized beds of large coarse particles. AIChE Journal 1985, 31(9), 1554-1562.

[13] Bi, H.-T.; Ellis, N.; Abba, A.; Grace, J.R. A state-of-the-art review of gas-solid turbulent fluidization. Chemical Engineering Science 2000, 55, 4789-4825.

[14] Cho, H.; Han, G.; Ahn, G. Characteristics of slug flow in a fluidized bed of polyethylene particles, Korean Journal of Chemical Engineering 2002, 19(1), 183-189.

[15] van der Schaaf, J.; van Ommen, J.R.; Takens, F.; Schouten, J.C.; van den Bleek, C.M. Similarity between chaos analysis and frequency analysis of pressure fluctuations in fluidized beds. Chemical Engineering Science 2004, 59, 1829-1840.

[16] Svensson, A.; Johnsson, F.; Leckner, B. Bottom bed regimes in a circulating fluidized bed boiler. International Journal of Multiphase Flow 1996, 22(6), 1187-1204.

[17] Noordergraaf, I.W.; van Dijk, A.; van den Bleek, C.M. Fluidization and slugging in large-particle systems. Powder Technology 1987, 52, 59-68.

[18] Davidson, J.F.; Harrison, D. *Fluidized bed particles*; Cambridge University Press; New York, 1963.

[19] Wormsbecker, M.; Adams, A.; Pugsley, T.; Winters, C. Segregation by size difference in a conical fluidized bed of pharmaceutical granulate. Powder Technology 2005, 153, 72-80.

[20] van der Schaaf, J. Dynamics of gas-solids fluidized beds. Ph.D. Thesis, Delft University of Technology, 2001.

[21] Cai, P.; Jin, Y.; Yu, Z.-Q.; Wang, Z.-W. Mechanism of flow regime transition from bubbling to turbulent fluidization. AIChE Journal 1990, 36(6), 955-956.

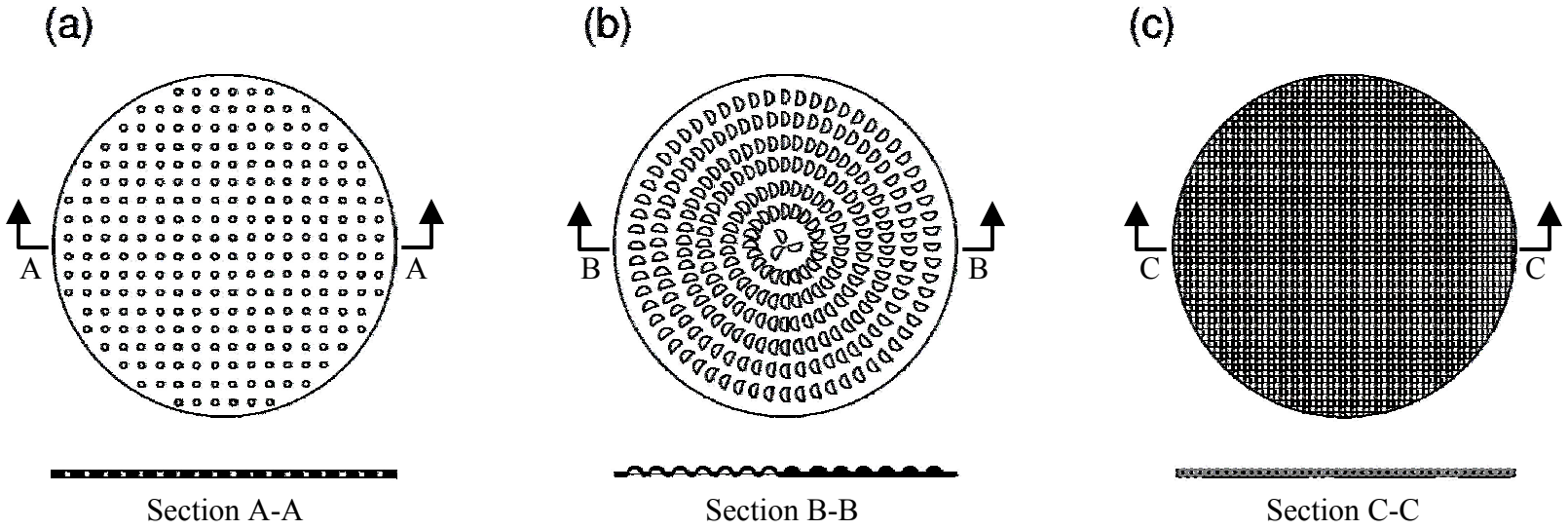

Figure 4.1: Distributor designs: (a) perforated plate, (b) punched plate, (c) Dutch weave mesh.

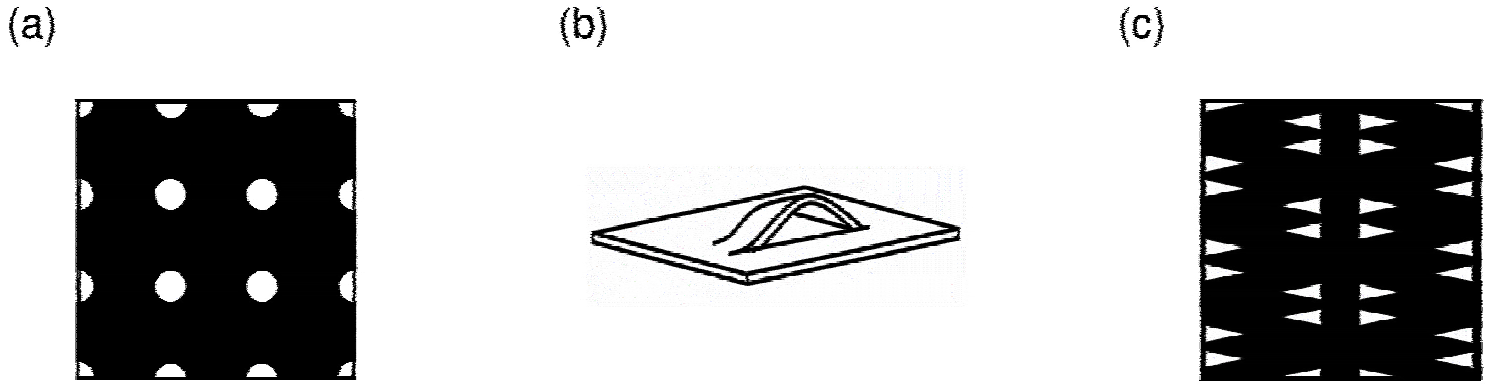

Figure 4.2: Details of distributor designs: (a) perforated plate, (b) punched plate, (c) Dutch weave mesh.

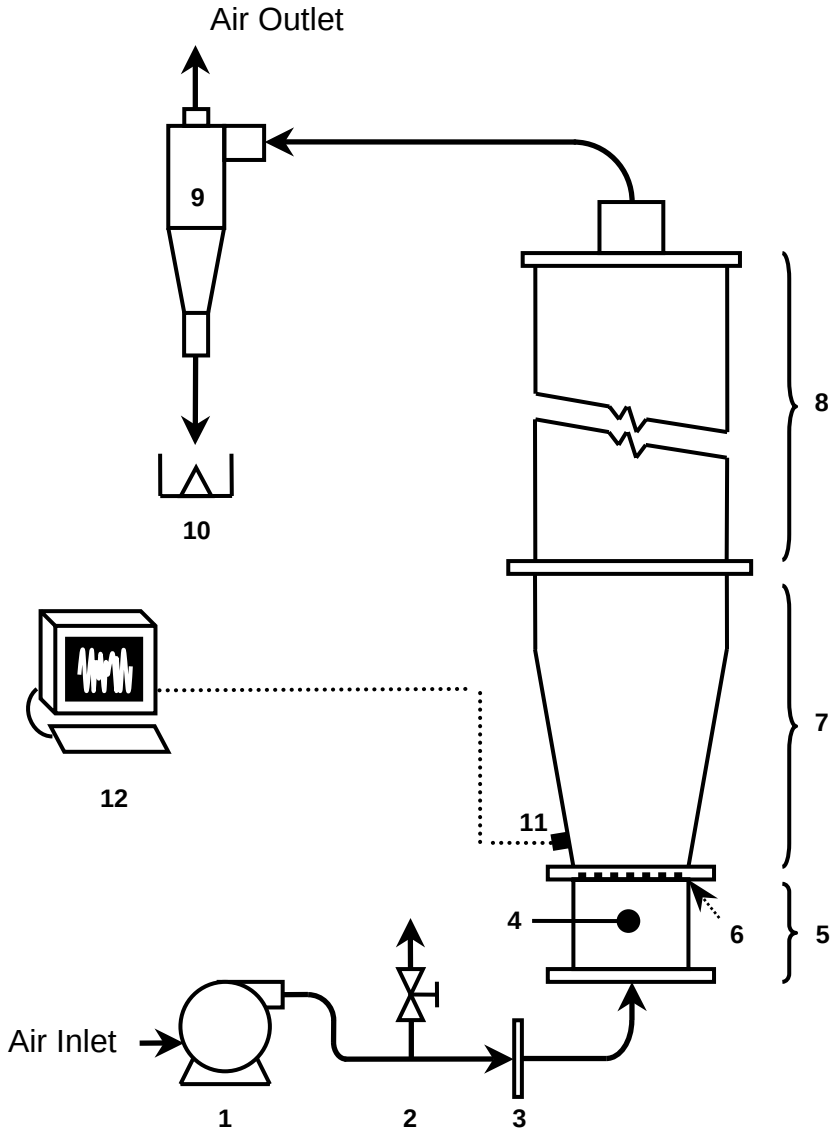

Figure 4.3: Experimental apparatus: (1) blower, (2) bypass valve, (3) orifice plate, (4) humidity sensor, (5) windbox, (6) distributor, (7) conical fluidized bed, (8) freeboard/disengagement section, (9) cyclone, (10) fines collection pot, (11) pressure transducer, (12) data acquisition computer for pressure fluctuations.

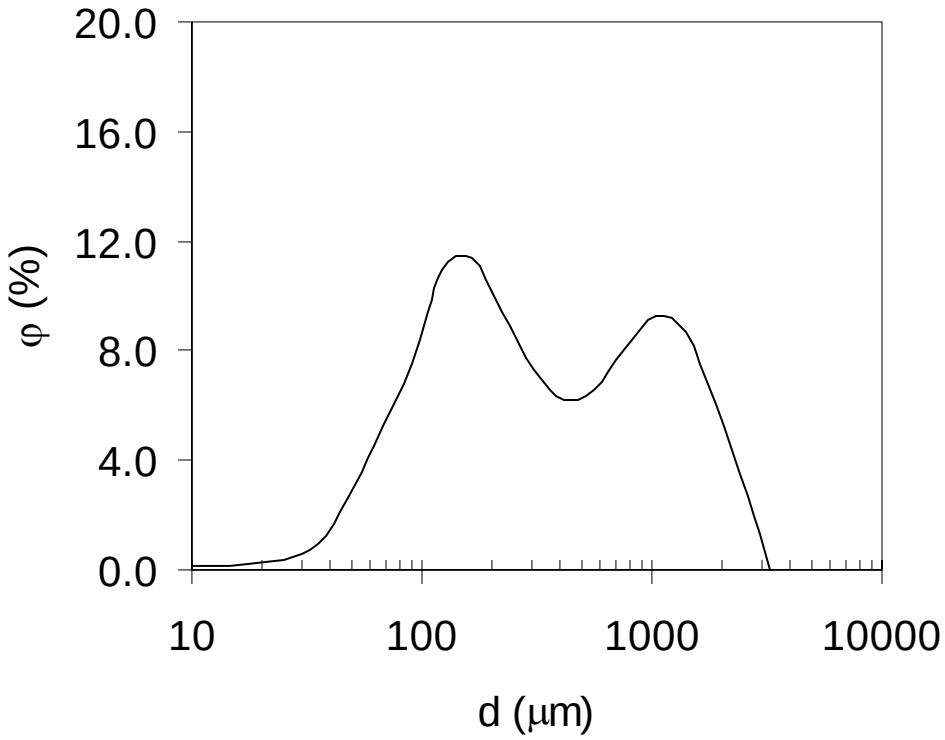

Figure 4.4: Particle size distribution of pharmaceutical granule.

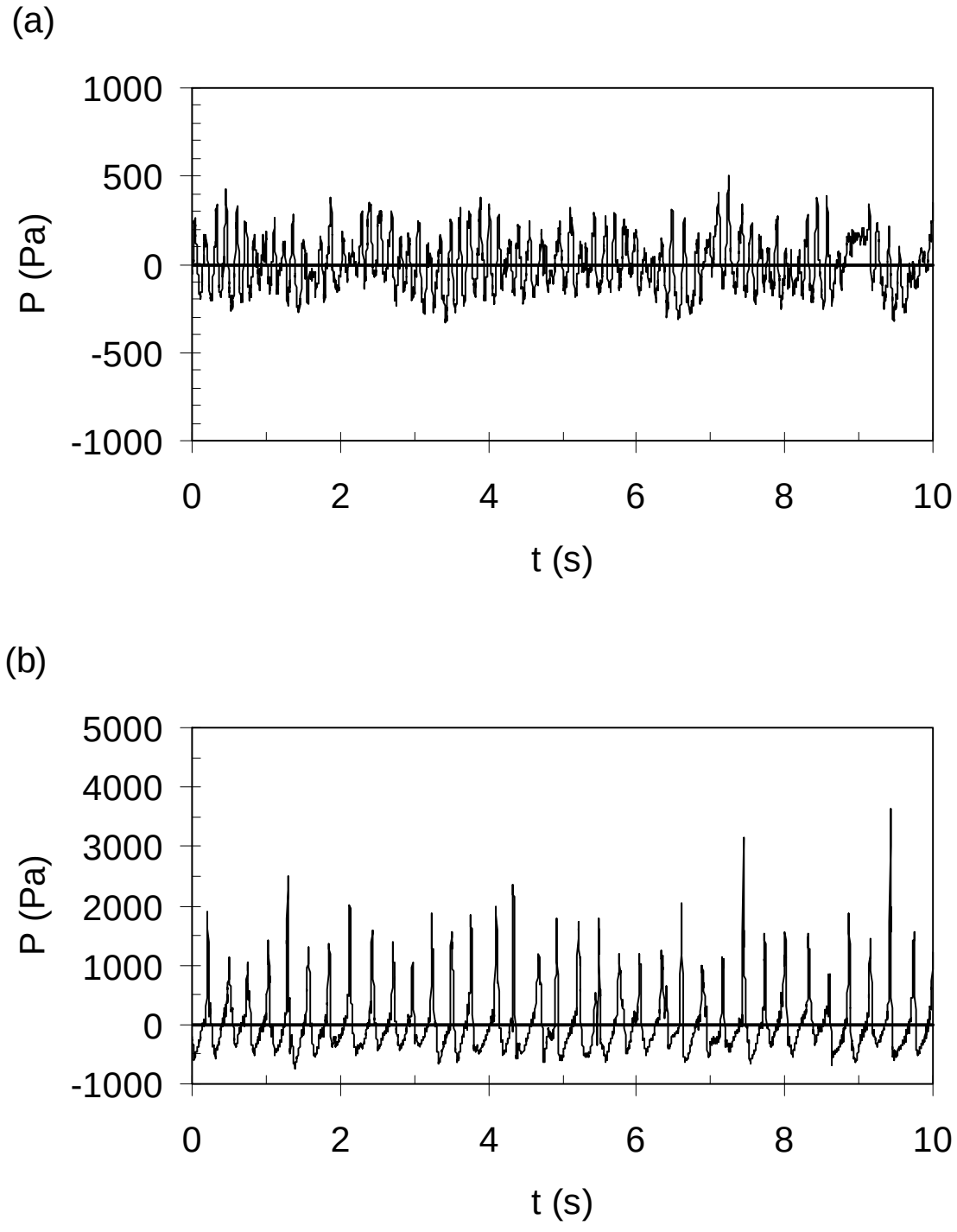

Figure 4.5: Sample pressure time-series for the perforated plate: (a) 0.5 m/s, (b) 3.0 m/s. The dynamic pressure, P, is a measure of the deviation of pressure from the static pressure. Therefore, the static pressure in terms of the dynamic measurement is 0.

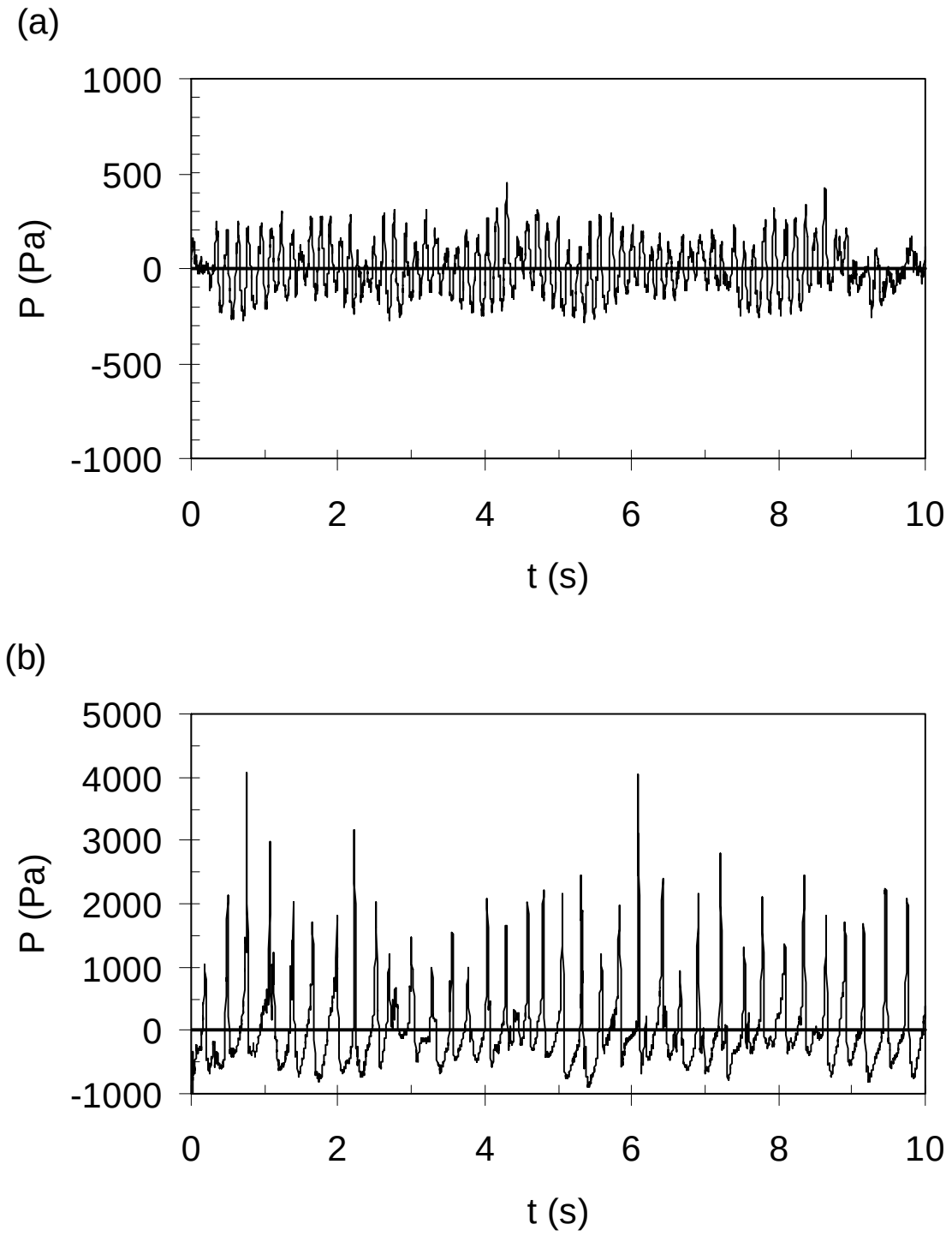

Figure 4.6: Sample pressure time-series for the punched plate: (a) 0.5 m/s, (b) 3.0 m/s. The dynamic pressure, P, is a measure of the deviation of pressure from the static pressure. Therefore, the static pressure in terms of the dynamic measurement is 0.

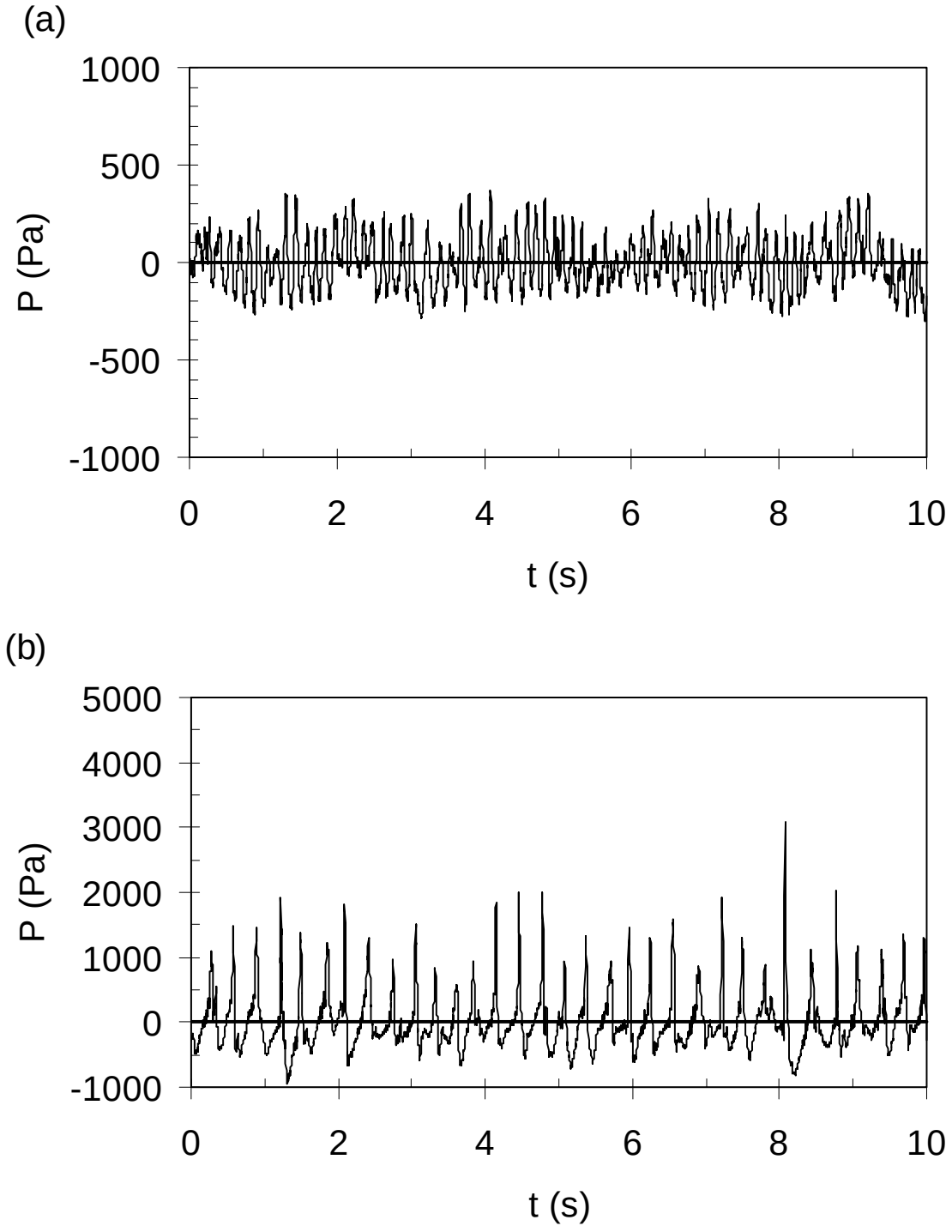

Figure 4.7: Sample pressure time-series for the Dutch weave: (a) 0.5 m/s, (b) 3.0 m/s. The dynamic pressure, P, is a measure of the deviation of pressure from the static pressure. Therefore, the static pressure in terms of the dynamic measurement is 0.

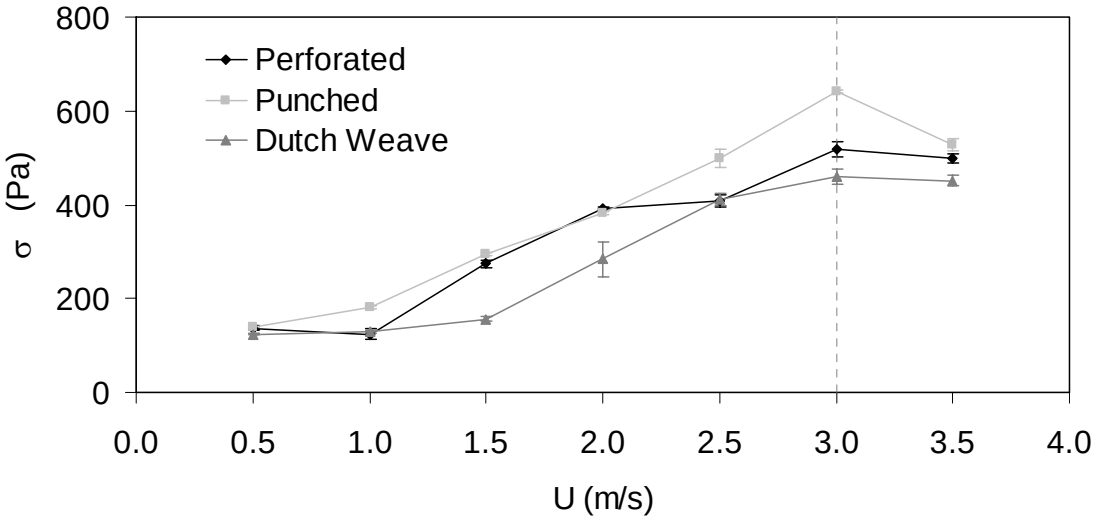

Figure 4.8: Standard deviation of pressure fluctuations. Error bars represent ± 1σ of the triplicate experiments.

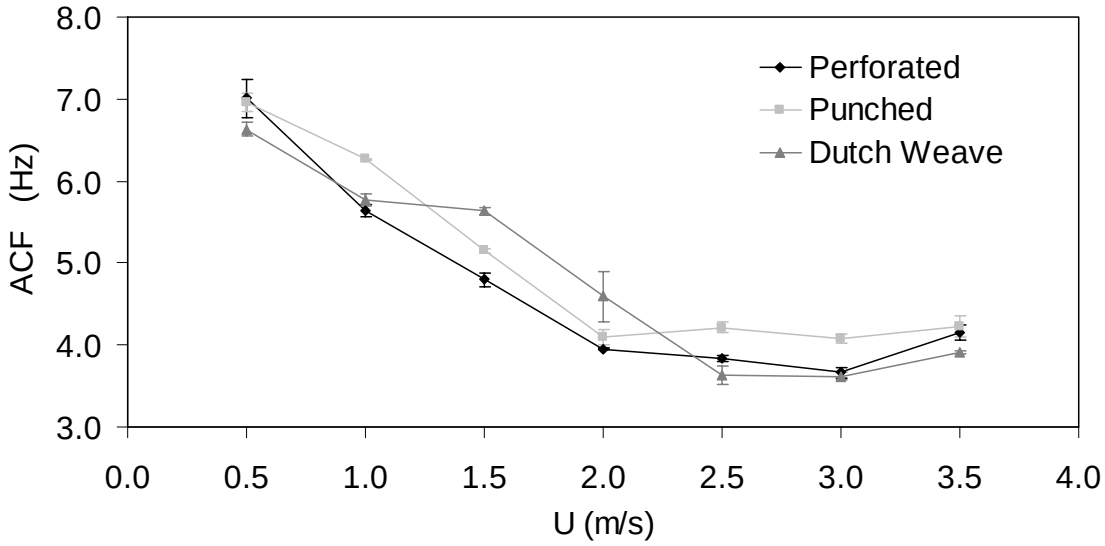

Figure 4.9: Average cycle frequency (ACF) of the pressure fluctuations. Error bars represent ± 1σ of the triplicate experiments.

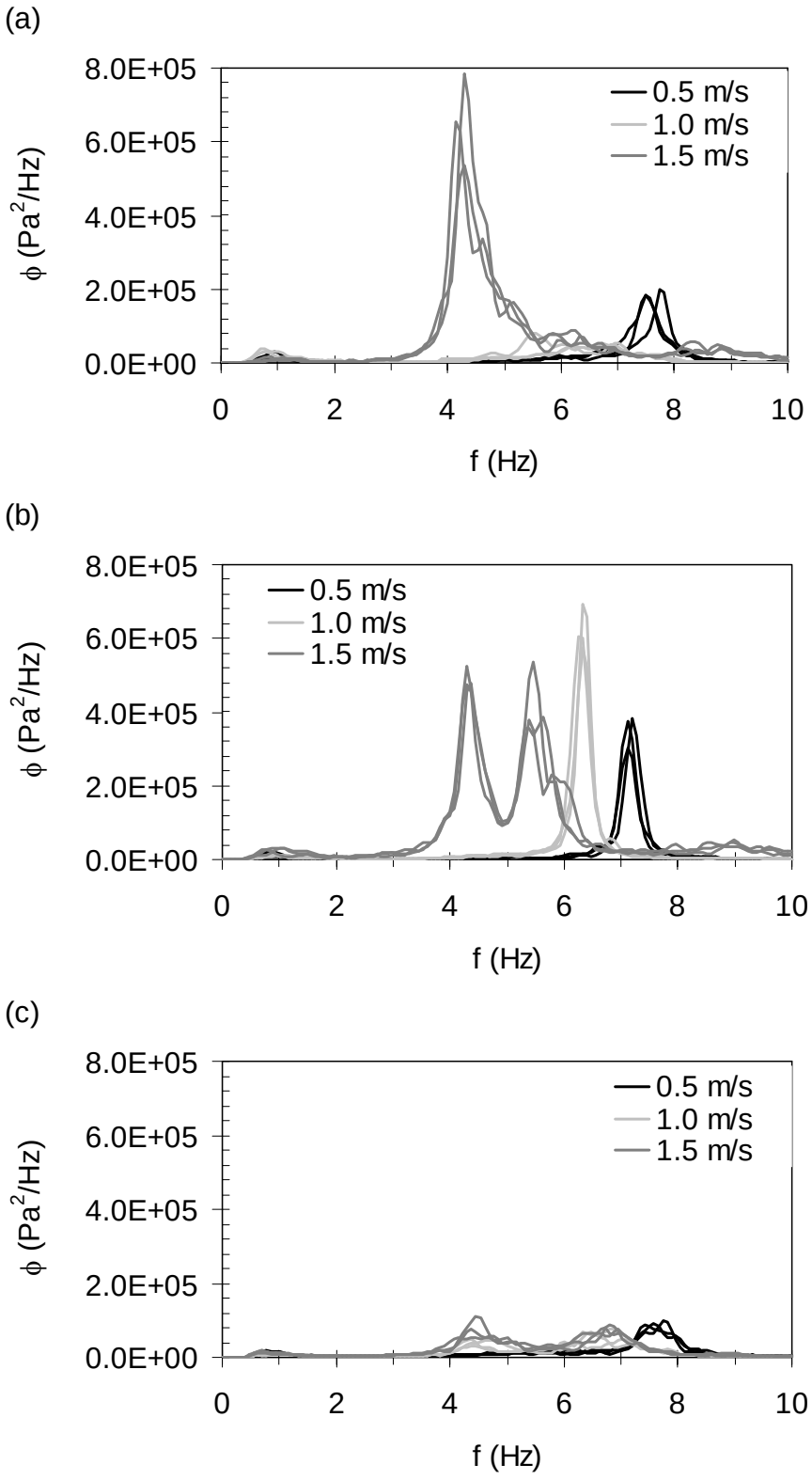

Figure 4.10: PSD analysis for low velocities: (a) perforated plate, (b) punched plate, (c) Dutch weave.

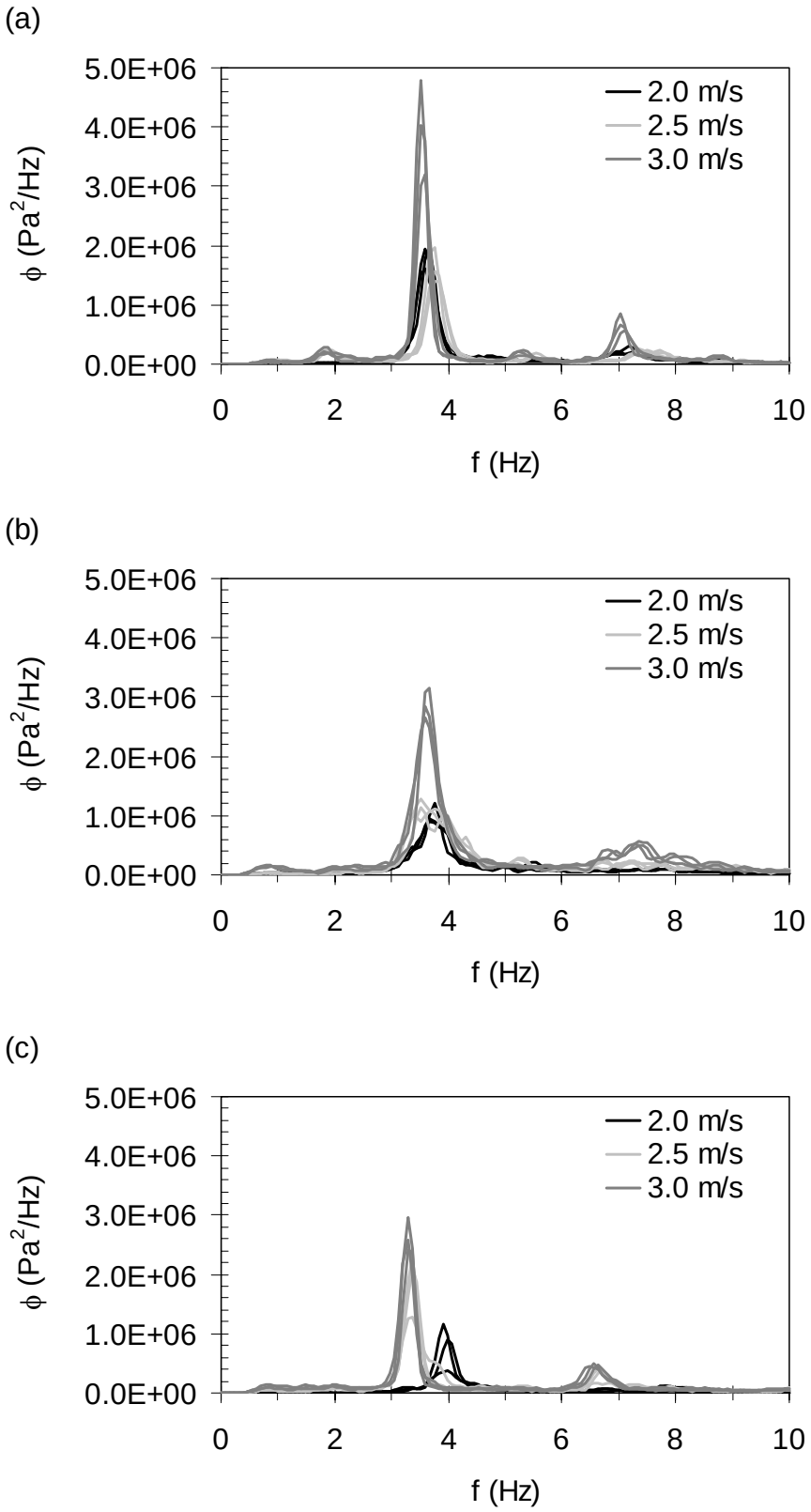

Figure 4.11: PSD analysis for high velocities: (a) perforated plate, (b) punched plate, (c) Dutch weave.

CHAPTER 5 - The Influence of Distributor Design on Fluidized Bed Dryer Hydrodynamics

The contents of this chapter were presented at the Fluidization XII conference at Harrison Hot Springs, British Columbia, Canada, May, 2007. A similar version to what appears in this chapter has been published as part of the peer-reviewed proceedings.

Citation

Wormsbecker, M., Pugsley, T., Tanfara, H., The influence of distributor design on fluidized bed dryer hydrodynamics, in: X. Bi, F. Berruti, T. Pugsley (Eds.), Fluidization XII, New Horizons in Fluidization Engineering, Engineering Conferences International, Brooklyn, 815-822, (2007).

Contribution of Ph.D. Candidate

Experiments were planned and performed by Michael Wormsbecker. Todd Pugsley and Helen Tanfara (Merck Frosst Canada Ltd.) provided consultation regarding the experimental program. The software for all data collection and analysis was developed by Michael Wormsbecker. All of the writing of the submitted manuscript was done by Michael Wormsbecker with Todd Pugsley and Helen Tanfara providing editorial guidance regarding the style and content of the paper.

Contribution of this Paper to the Overall Study

This paper is a 'proof of principle' study to determine the impact of distributor design on dryer performance in a laboratory fluidized bed dryer. The impact is based on the ability of the distributor to invoke changes in the gas-solids contacting in the dryer resulting in changes in the granule drying times. Therefore, hydrodynamic measurements will be considered as means to identify changes in gas-solids contacting. This paper is a follow up study to that discussed in Chapter 4.

5.1 Abstract

The pharmaceutical industry commonly employs three distinct distributor designs in fluidized bed drying of pharmaceutical granule: the Dutch weave mesh, the perforated plate, and the punched plate. In the present study, product temperature, moisture content and pressure fluctuation data were monitored throughout the drying of placebo pharmaceutical granule to compare fluidized bed dryer performance with the different distributor designs. A Glatt GPCG-1 fluidized bed dryer was used to study the drying of 1.0, 2.5 and 3.0-kg wet bed loadings dried at velocities of 0.64 and 1.3 m/s. Differences in drying hydrodynamics were observed between the distributors with both the 2.5 and 3.0-kg bed loadings dried at 0.64 m/s. Standard deviation and frequency analysis of the pressure fluctuation data reveals that the punched plate design results in improved hydrodynamic behaviour under these conditions. At 1.3 m/s, bed loading had no influence on drying hydrodynamics, regardless of distributor plate design. The results from this study suggest that the improved drying hydrodynamics exhibited by the

punched plate distributor under these operating conditions results from the increased radial dispersion developed by the lateral directional component imparted on the fluidization air by its design.

5.2 Introduction

An important component of any fluidized bed is the gas distributor. The role of the distributor is to evenly distribute the fluidization gas across the bed inlet and hence to initiate effective gas-solids contacting. As discussed in Section 4.1 of this thesis, the pharmaceutical industry has traditionally used the perforated plate distributor for fluidized bed drying. However, the shortcomings associated with the perforated plate have lead to the implementation of alternative designs like the woven mesh distributor and more recently the punched plate to improve on the operational concerns that can be encountered in fluidized bed processes. These designs can influence the bed hydrodynamics and therefore potentially alter the rate of heat and mass transfer in fluidized bed processes, including dryers.

Literature related to distributor design performance [1-7] is similar to that already presented in Section 4.1 of this thesis, so it will not be provided again. It is important however to reiterate that the work by Chyang and Lin [7], which studied distributor designs that best parallel those used in the pharmaceutical industry, has illustrated the relative influence of distributor designs on dry bed hydrodynamics. While these results may be used to infer the potential influence of the distributor design on fluidized bed dryer performance, there have been no such studies that have examined this directly.

Therefore, the current study focuses on the influence of the Dutch weave mesh, perforated plate and punched plate distributor designs on the hydrodynamics resulting from the fluidized bed drying of pharmaceutical granule.

5.3 Materials and Methods

5.3.1 Granulation

The placebo granule was comprised of the ingredients listed in Table 2.2. The granulation apparatus and procedures are the same as those presented in Section 3.3.1 of this thesis.

5.3.2 Fluidized Bed Apparatus

The fluidized bed used in this study is the same Glatt GPCG-1 fluidized bed dryer presented in Section 3.3.2 of this thesis.

5.3.3 Distributor Designs

The three distributor designs that were investigated were designed to have similar orifice sizes and percent open areas to those used in Chapter 4 of this thesis. The Dutch Weave mesh distributor used in this study was the same sized mesh (24 x 110 mesh) supplied by NIRO Inc. The weave creates openings that are triangular shaped with base and height dimensions of approximately 25 and 90 μm, respectively. Using microscopy, the percent open area was estimated to be 15 ± 1%. The perforated plate distributor design consisted of 256 holes of 2.7-mm diameter drilled on a 7.5-mm square pitch. This design resulted in an open area of 9.5%. Finally, the punched plate was designed with

hooded openings which are 5.75 mm by 1.0 mm in dimension (refer to Figs. 4.1 and 4.2 for a schematic). The openings were orientated in a circular pattern with 3 mm between adjacent rings. This orientation is designed to produce a swirling effect in the bed. The open area calculated based on these openings was 9.6%. It is important to note that these high percent open areas are typical of pharmaceutical fluidized bed dryers.

5.3.4 Operating Conditions

Wet bed loadings of 1.0, 2.5, and 3.0 kg were used which resulted in initial static bed heights of 12, 22, and 24 cm, respectively. The two higher bed loadings were fluidized by air at superficial gas velocities of 0.64 and 1.3 m/s. The 1.0-kg bed loading was fluidized at 0.64 m/s only because operation at 1.3 m/s resulted in a high rate of particle entrainment. This led to the depletion of a distinct dense bed phase rendering a fluidization state inappropriate for this study. Elevated velocities of 0.85 and 1.5 m/s were required for the first ten minutes of the 0.64 and 1.3-m/s drying experiments, respectively, in order to properly fluidize the wet granule. The need for these elevated velocities was based on visual observation through a sight-glass in the product bowl. It should also be noted that pressure fluctuations could not be obtained for the 1.0-kg bed loading experiments. This bed loading resulted in a shallow bed where the pressure sensor was inadequately covered by material in the dense region of the fluidized bed. The results obtained from the 2.5 and 3.0-kg bed loading experiments will therefore be used to infer upon the influence of distributor design on the dryer performance in the 1.0-kg bed loading experiments.

The inlet fluidization air was heated to 65˚C for drying. The end of drying was marked by the product temperature reaching 40˚C. When dried, the static beds heights of the bed loadings noted above are approximately 8, 15, and 17 cm, respectively. The particle size distributions of the granule from each of the distributor design experiments are very similar with modes of 250 and 3500 μm and an average mean mass diameter of 258 ± 8 μm. The particle density of the dry granule is 830 kg/m^3. Each experimental run was repeated twice to check the reproducibility of the data.

5.4 Results

Conventional dryer monitoring techniques, including product temperature and moisture content profiles, were used along with pressure fluctuations to analyze dryer performance. As illustrated by representative product temperature (T_{bed}) profiles from 0.64-m/s drying (see Fig. 5.1), differences between distributors begin to emerge as bed loading (m) is increased from 1.0 to 3.0 kg. The punched plate distributor dries the 3.0-kg load the fastest, followed by the Dutch weave then the perforated plate. The respective drying times based on product temperature endpoint determination are 81, 85 and 88 minutes, respectively. Moisture content (Q_g) profiles also support this trend. Fig. 5.2 illustrates the average moisture content for both the 1.0 and 3.0-kg bed loadings dried at 0.64 m/s. For the 1.0-kg bed loading, the drying curves are virtually identical for the different distributor designs. As bed loading is increased, a separation in the drying profiles between the punched plate and the other designs appear between the 20 and 40 minute mark. This difference in moisture content profiles is carried throughout the drying process. The 2.5-kg bed loading dried at 0.64 m/s behaves similarly to that of the 3.0-kg

bed loadings. Under 1.3-m/s drying conditions, product temperature and moisture profile are similar between distributor designs for both the 2.5 and 3.0-kg bed loadings. The product temperature and moisture profiles for the 3.0-kg bed loading dried at 1.3 m/s are shown in Fig. 5.3 and 5.4.

In order to better quantify dryer performance for all the conditions studied, the arithmetic average of the drying times of duplicate experiments for a given bed loading (m) and drying velocity (U) was determined. The average drying times were then normalized based on the lowest average drying time amongst the distributor designs at specific bed mass and velocity. The normalized drying times are summarized in Table 5.1. These times imply that for a 1.0-kg bed loading dried at 0.64 m/s there is negligible difference in performance between the distributor designs as the average normalized times are within 3% of one another. However, as the bed loading increases to 3.0 kg, favourable bed hydrodynamics induced by the punched plate distributor design are more evident. The Dutch weave and the perforated plate distributors lead to drying times that are 7 and 10% longer, respectively, than the punched plate. Under 1.3-m/s drying conditions, the average normalized drying times between distributor designs for both the 2.5 and 3.0-kg wet bed loadings are within 3%. This suggests that increasing the fluidization velocity results in similar fluidized bed hydrodynamics between distributor designs at high bed loadings.

Standard deviation and power spectrum analysis of the pressure fluctuations were also used to analyze the hydrodynamic behaviour of the bed during the drying process.

Fig. 5.5 is a representative profile of the standard deviation (σ) of the dense bed pressure fluctuations for 3.0-kg bed loadings dried with each distributor design. The standard deviation of the pressure fluctuations demonstrates a sigmoid-like profile over the drying process for all distributor types. In the early stages of drying, the standard deviations are relatively low and constant. Eventually, the pressure fluctuations begin to increase steadily until another constant state is reached. This signifies that moisture removal is slowing and that the endpoint of drying is near.

The profiles of the standard deviation of the pressure fluctuations are different between distributors for the 0.64-m/s drying velocity. Initially, the standard deviation profiles are all relatively constant, but after the 36 minute mark of the drying process the standard deviation begins to increase for the punched plate. Increases in the standard deviation profiles of the perforated plate and Dutch weave mesh do not occur until after 44 and 48 minutes into drying, respectively. In addition, the standard deviation profile for the punched plate is larger in magnitude throughout the drying process as compared to the other designs. Similar to the 3.0-kg bed loading data, the standard deviation profile for the 2.5-kg bed loading dried at 0.64 m/s takes on a sigmoid-like curvature. Under the higher drying velocity conditions of 1.3 m/s, little to no difference in the standard deviation of the pressure fluctuations occurs (see Fig. 5.5). For the standard deviation profiles of the 2.5-kg bed loadings dried at 0.64 and 1.3 m/s, see Fig. D.1 of Appendix D.

Using power spectral density analysis, details regarding the hydrodynamic behaviour throughout the drying process were also examined. In the early stages of the

drying process (Fig. 5.6(a)), the punched and perforated plates exhibit similar hydrodynamic behaviour with a dominant frequency of 5.2 Hz and a secondary frequency of 0.7 Hz. The dominant frequency represents the phenomena related to bubbling in the fluidized bed, whereas the secondary frequency is associated with the step-wise movement of particles down the wall of the bed that was observed visually at approximately this frequency. The Dutch weave does not display a distinct bubble related frequency; however, it does exhibit the same low frequency movement of material at the bed wall. At the 32 minute mark, differences in the hydrodynamic behaviour are evident. The punched plate exhibits a power spectrum that is stronger in power (ϕ) and contains a dominant frequency that is slightly higher than the dominant frequencies of the perforated plate and Dutch weave designs. The dominant frequency of the punched plate is 5.2 Hz whereas the frequencies are 4.9 and 4.7 Hz for the perforated plate and Dutch weave designs, respectively. Fig. 5.6(c) represents the middle to latter portion of the drying period. The power associated with the power spectra is a scale of magnitude larger than seen in the earlier stages of the drying process. This increase in power is attributed to larger fluctuations in the bed as moisture is removed (see Fig. 5.5). The dominant frequencies have also shifted from a higher to lower frequency indicating that bubble coalescence has increased. Differences in the power spectra between distributor designs still exist, with the punched plate illustrating a higher power dominant frequency as compared to the other designs. Finally, Fig. 5.6(d) compares the hydrodynamic behaviour between distributor designs during dry bed operation. The power spectra of the different distributors are very similar indicating that distributor design has no influence on hydrodynamics under these conditions. The most likely reason for this is that the

significant amount of excess gas in the system results in a high degree of bubble coalescence and therefore negating the impact of the distributor on the system. Similar to the standard deviation analysis for the 1.3 m/s drying experiments, no significant differences in drying hydrodynamics exist between distributor designs when the fluidization velocity is elevated to 1.3 m/s (see Fig. 5.7). The power spectra for the 2.5-kg bed loadings dried at 0.64 and 1.3 m/s are presented in Figs. D.2 and D.3, respectively.

5.5 Discussion

It is believed that similar to the horizontal nozzle distributor used by Chyang and Lin [7], the punched plate promotes the formation of a swirling flow pattern via horizontal gas jets which in turn promotes lateral gas mixing. Horizontal gas jets produce bubbles from their tips as they penetrate the bed [8]. Due to the presumably random nature of the jet formation and subsequent bubble detachment, bubble coalescence is reduced resulting in a higher bubbling frequency. The punched plate illustrates this higher bubble related frequency phenomenon (see Fig. 5.6(b)) and also demonstrates improved lateral gas mixing through the larger magnitude of its standard deviation profile (as discussed in section 4.4.1 of tihs thesis). The smaller, more frequent bubbles along with the improved lateral gas mixing generated in this portion of the drying period explains the improved dryer performance for 2.5 and 3.0-kg bed loadings dried at 0.64 m/s with the punched plate.

The similarities in drying hydrodynamics between distributor designs at 1.3 m/s are thought to be related to improved radial gas dispersion with the perforated plate and

Dutch weave distributors under such conditions. With these types of distributor designs, gas dispersion is more centralized at low gas velocities. This results in limited potential for lateral gas mixing in the fluidized bed [9]. However, as gas velocity increases, gas permeates to the periphery of the bed resulting in improved gas-solids contacting [10].

5.6 Conclusions

The present study has found that the punched plate distributor design provides shorter drying times than the Dutch weave and perforated plate designs when wet bed loadings of 2.5 kg and above are dried at superficial gas velocities typical of the pharmaceutical industry. This study was carried out on a laboratory-scale fluidized bed dryer. It is possible that in larger diameter fluidized beds, such as clinical and production scale dryers, the positive influence of the punched plate may be more pronounced as bed loadings become greater.

5.7 Nomenclature

m	bed mass, kg
Q_g	granule moisture content (mass basis), %
t	time, min
T_{bed}	product temperature, °C
U	superficial gas velocity at bed inlet, m/s
ϕ	power spectral density, Pa^2/Hz
λ	frequency, Hz
σ	standard deviation of pressure fluctuations, Pa

5.8 References

[1] Masters, K. (1992). Industrial fluidized bed dryers: trends and developments. in: Potter, O.E., Nicklin, D.J. (Eds.), *Fluidization VII*, Engineering Foundation, New York, USA, 59-72.

[2] Geldart, D., and Baeyens, J. (1985). "The design of distributors for gas-fluidized beds." *Powder Technol.*, 42, 67-78.

[3] Sreenivasan, B., and Raghavan, V.R. (2002). "Hydrodynamics of a swirling fluidised bed." *Chem. Eng. Process*, 41, 99-106.

[4] Bauer, W., Werther, J., and Emig, G. (1981). "Influence of gas distributor design on the performance of fluidized bed reactor." *Ger. Chem. Eng.*, 4, 291-298.

[5] Ouyang, F., and Levenspiel, O. (1986). "Spiral distributor for fluidized beds." Ind. Chem. Process Des. Dev., 25, 504-507.

[6] Garncarek, Z., Przybylski, L., Botterill, J.S.M., and Broadbent, C.J. (1997). "A quantitative assessment of the effect of distributor type on particle circulation." *Powder Technol.*, 91, 209-216.

[7] Chyang, C.-S., and Lin, Y.-C. (2002). "A study in the swirling fluidization pattern." *J. Chem. Eng. Jpn.*, 35, 503-512.

[8] Merry, J.M.D. (1971). "Penetration of a horizontal gas jet into a fluidised bed." *Trans. Instn. Chem. Engrs.*, 49, 189-195.

[9] Rowe, P.N., and Evans, T.J. (1974). "Dispersion of tracer gas supplied at the distributor of freely bubbling fluidized beds." *Chem. Eng. Sci.*, 29, 2235-2246.

[10] Carmello, D., Garrod, D.B., Pardocchi, M., Ioppi, M., and Foscolo, V. (2000). "Horizontal gas mixing in the distributor region of a fluidised bed reactor." *Chem. Eng. J.*, 76, 153-158.

Table 5.1: Normalized drying times

			m **(kg)**		
Distributor	***U*** **= 0.64 m/s**			***U*** **= 1.3 m/s**	
Design	**1.0**	**2.5**	**3.0**	**2.5**	**3.0**
Dutch Weave	1.00	1.03	1.07	1.01	1.03
Perforated	1.03	1.06	1.10	1.00	1.00
Punched	1.00	1.00	1.00	1.03	1.02

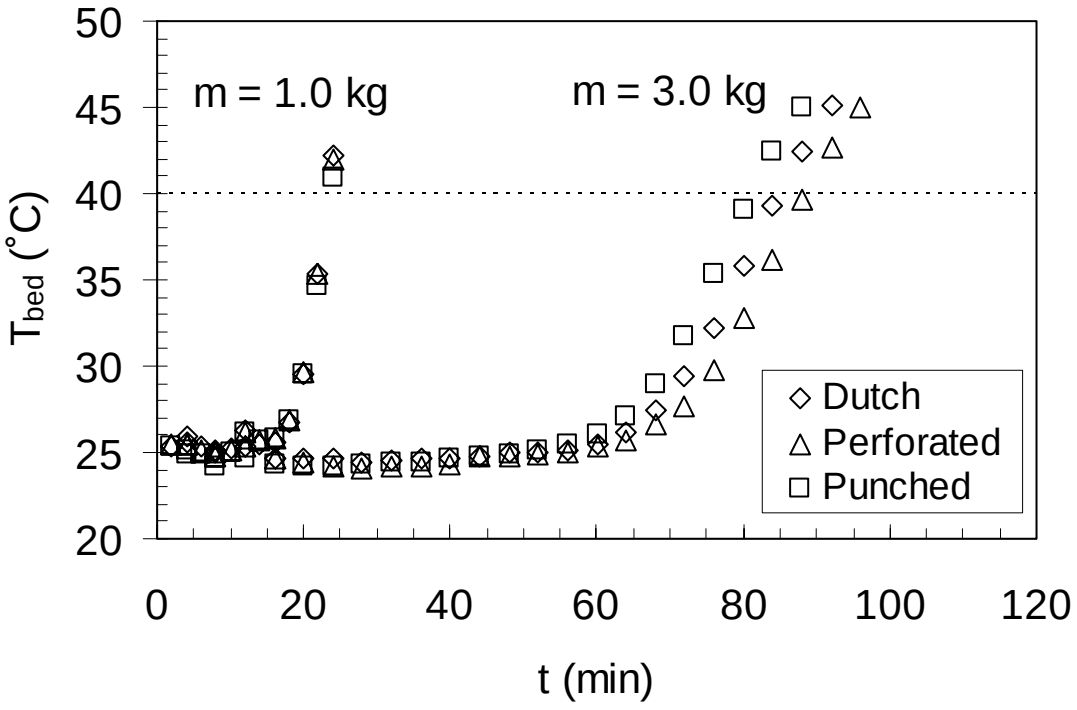

Figure 5.1: Product temperature profile for drying at 0.64 m/s.

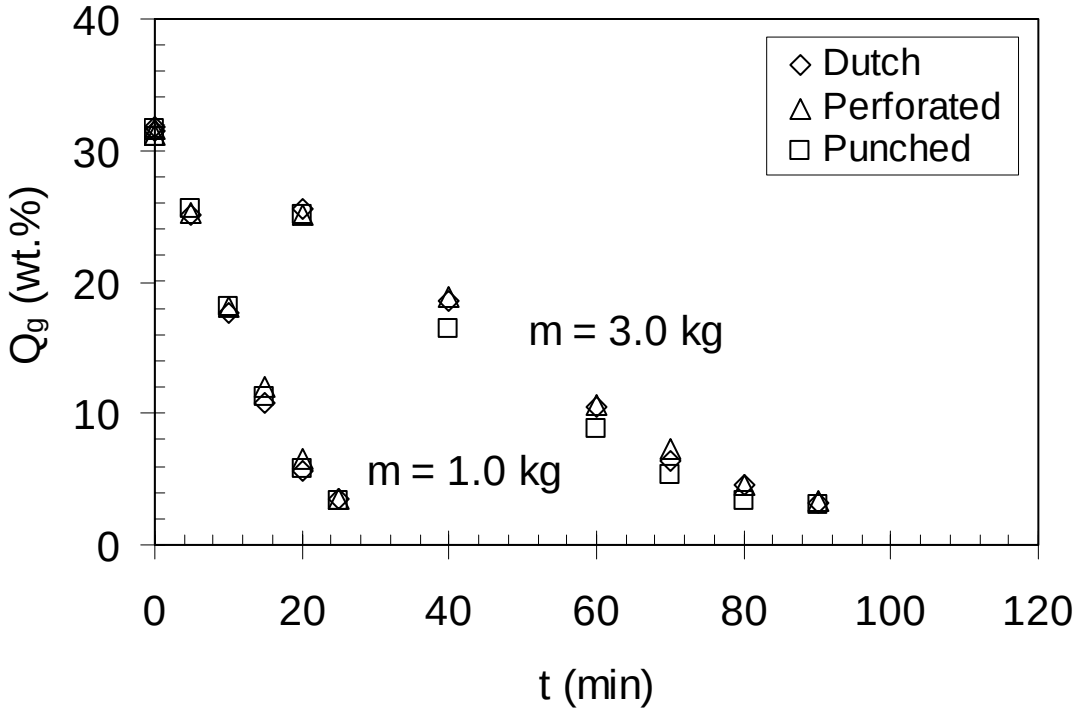

Figure 5.2: Moisture content profile for drying at 0.64 m/s.

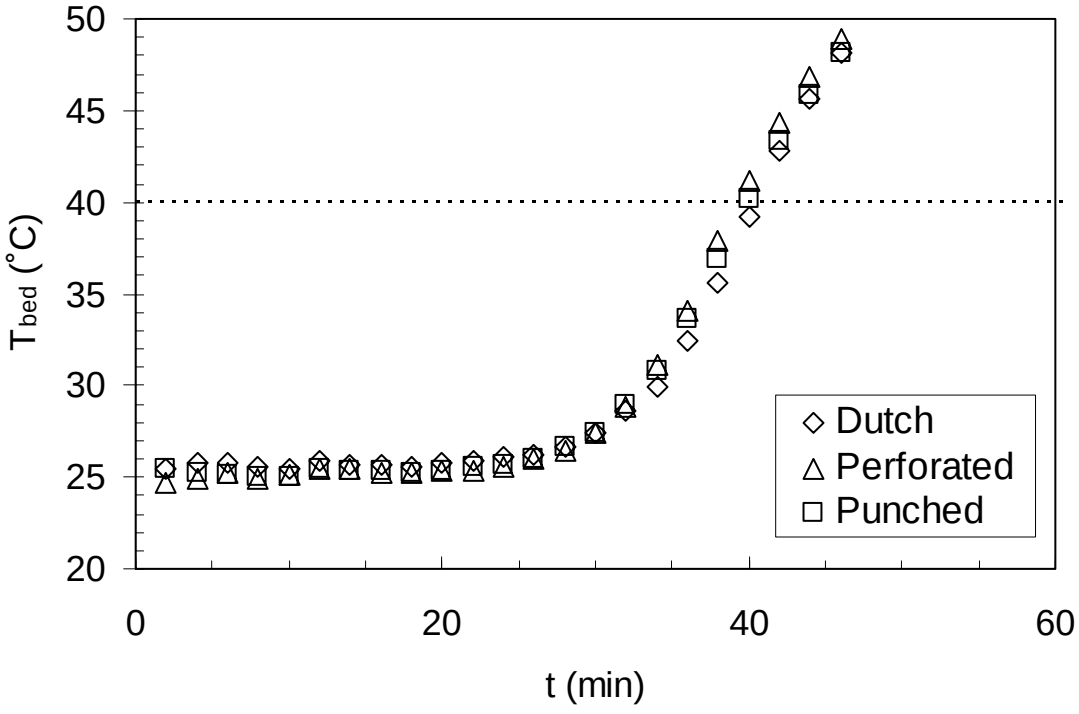

Figure 5.3: Product temperature profile for drying 3.0-kg bed loading at 1.3 m/s.

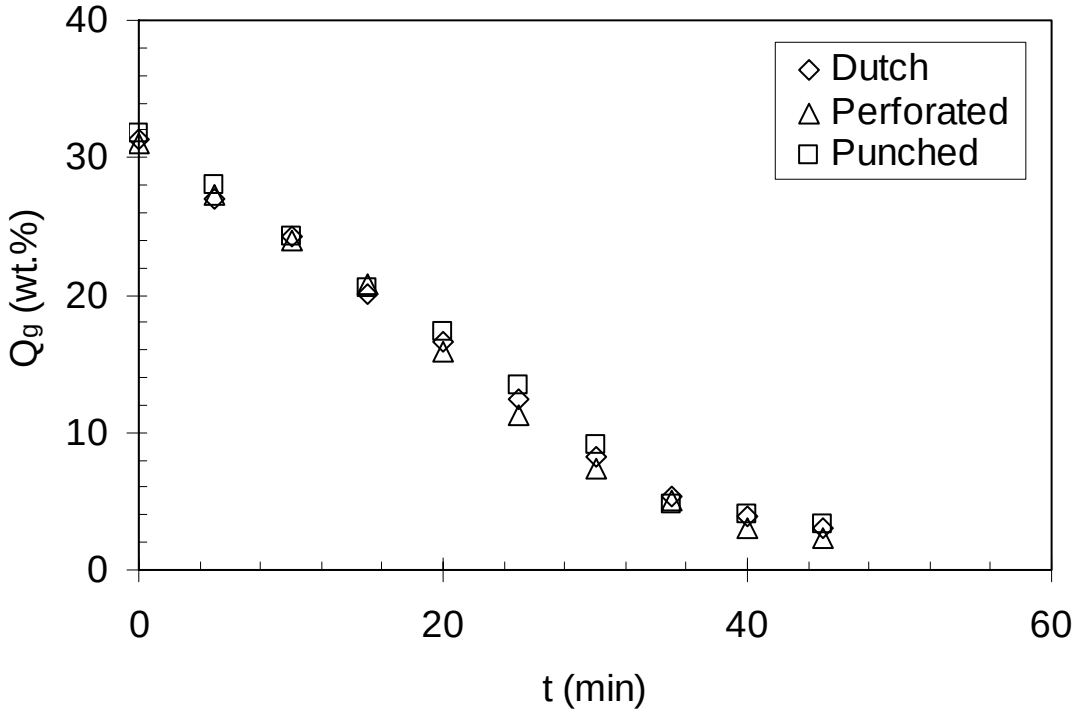

Figure 5.4: Moisture content profile for drying 3.0-kg bed loading at 1.3 m/s.

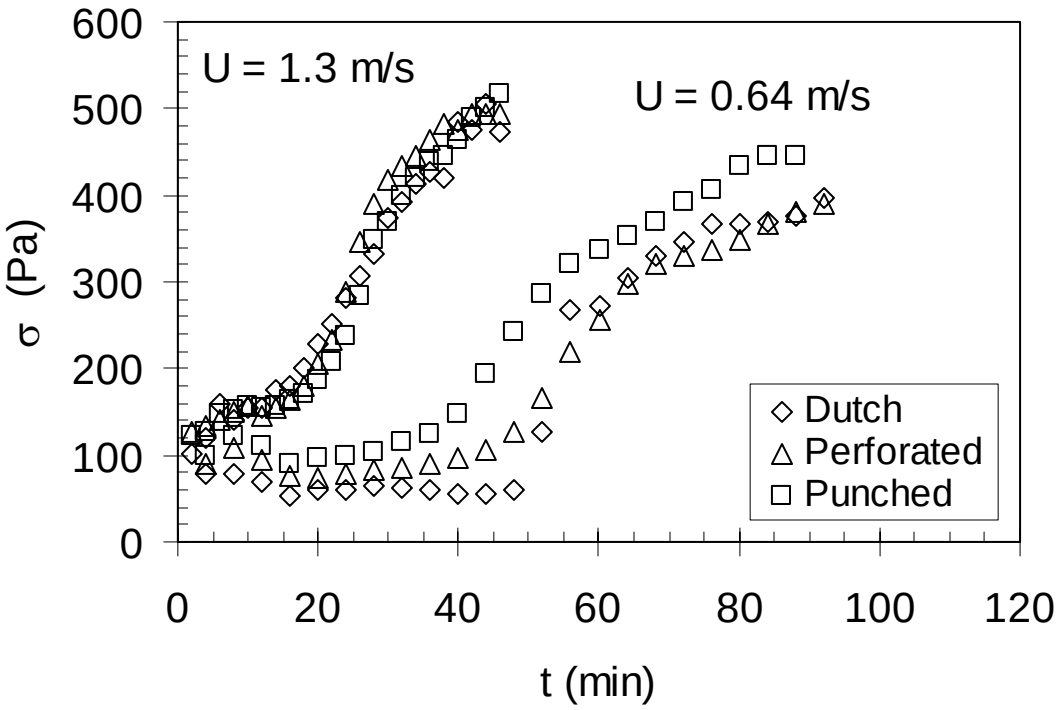

Figure 5.5: Standard deviation of pressure fluctuations for 3.0-kg bed loading.

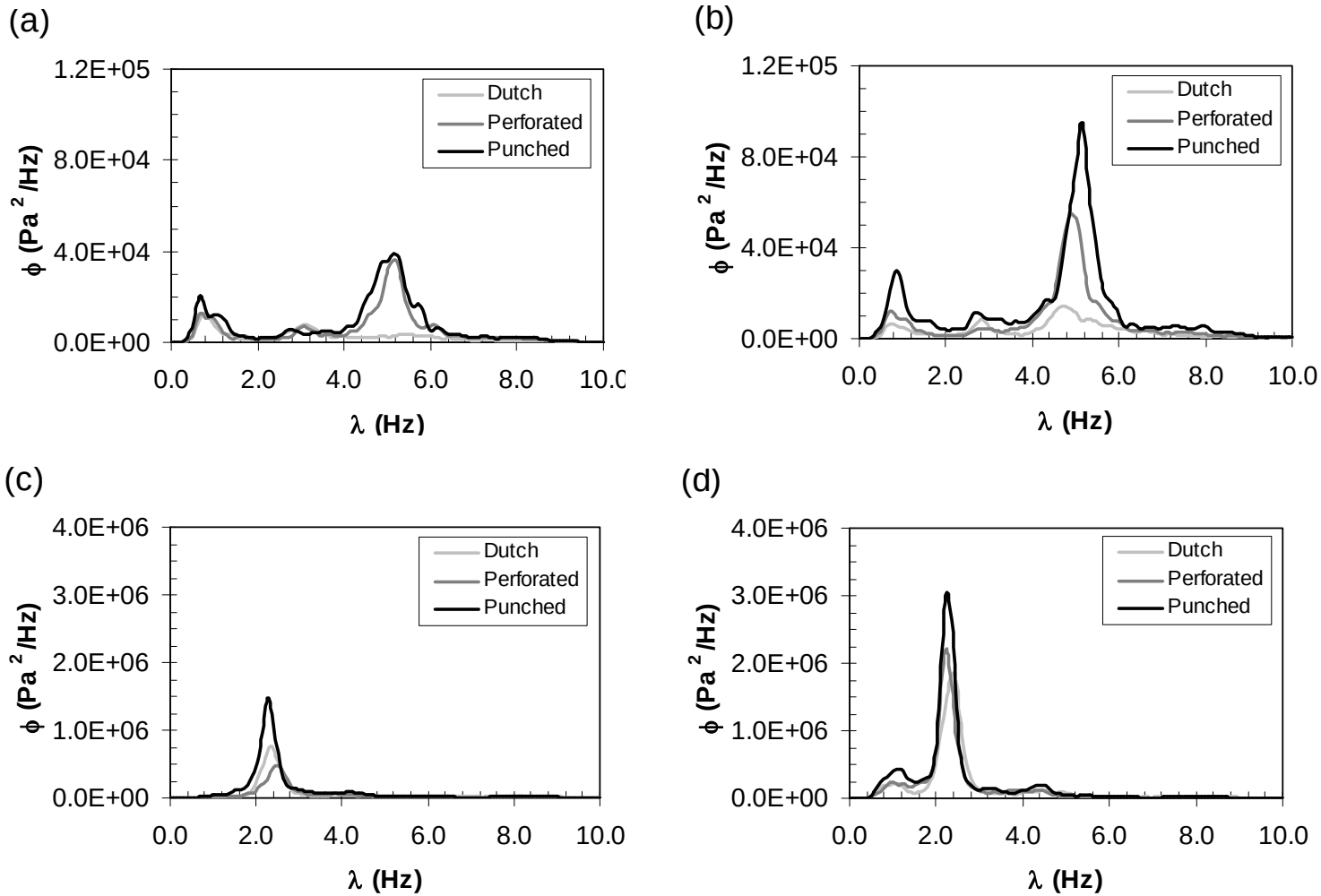

Figure 5.6: Power spectra for 3.0-kg bed loadings dried at 0.64 m/s: (a) 16 minutes into drying, (b) 32 minutes into drying, (c) 56 minutes into drying, (d) 88 minutes into drying.

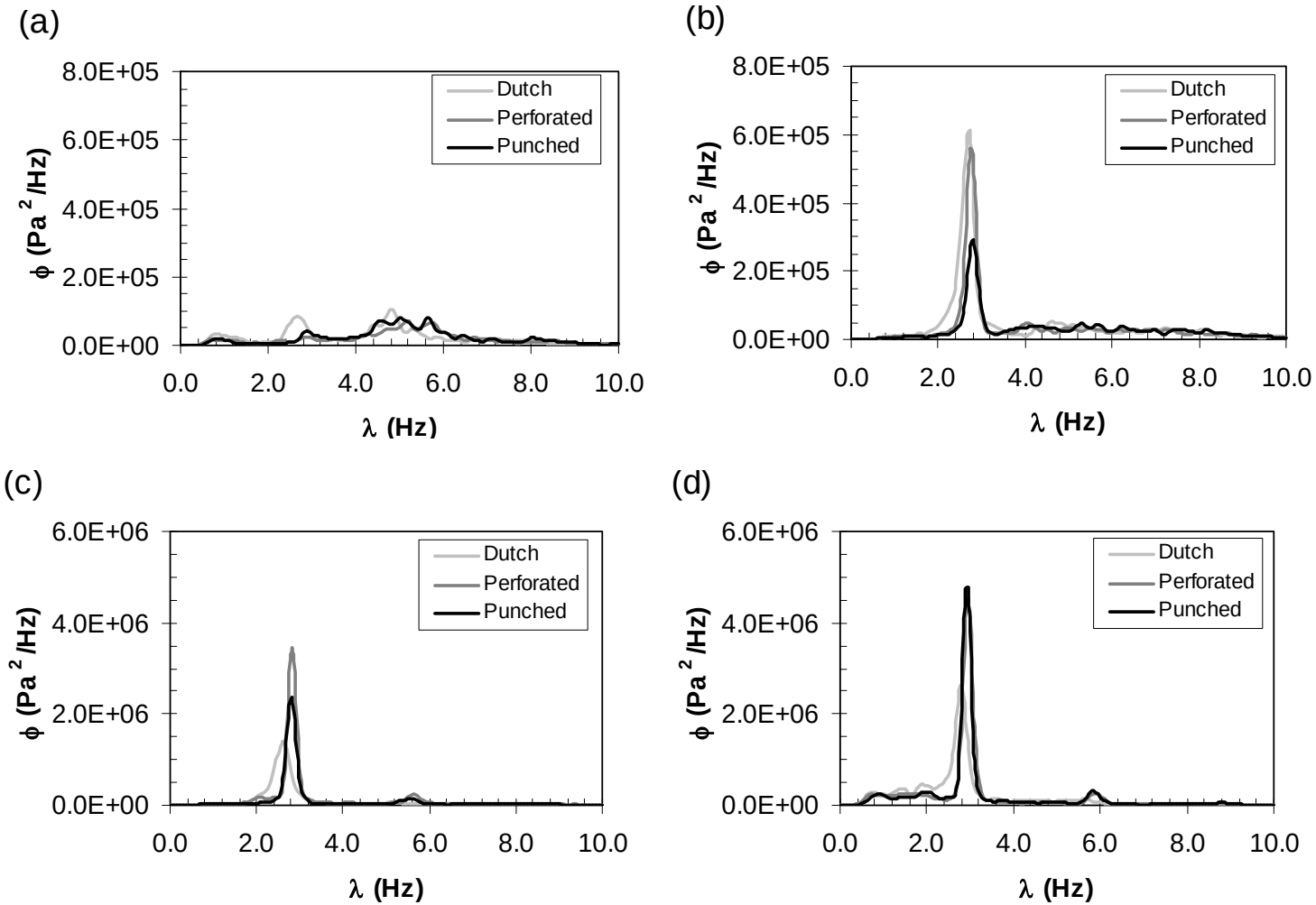

Figure 5.7: Power spectra for 3.0-kg bed loadings dried at 1.3 m/s: (a) 12 minutes into drying, (b) 20 minutes into drying, (c) 28 minutes into drying, (d) 40 minutes into drying.

CHAPTER 6 - Evaluation of Distributor Level Hydrodynamics Using 1-D X-ray Densitometry Imaging in a Fluidized Bed Dryer

The contents of this chapter have not yet been submitted for publication to a journal, but will be done so in a similar version to what appears in this chapter.

Contribution of Ph.D. Candidate

The experiments presented in this paper were a collaborative effort between the University of Saskatchewan and the fluidization research group of J. Ruud van Ommen of Delft University of Technology in Delft, The Netherlands. Internal collaboration within Delft University of Technology was done with Rob Mudde of the Kramers Laboratorium voor Fysische Technologie in order to conduct this x-ray densitometry study. The experiments were planned and performed by Michael Wormsbecker. Rob Mudde, J. Ruud van Ommen and John Nijenhuis provided consultation regarding the

experimental program. Erwin Wagner, the technician responsible for the x-ray densitometer, provided additional support with regards to technical and safety concerns with the x-ray densitometer. The software for data collection was developed in-house by the Kramers Laboratorium and modified by Michael Wormsbecker to meet the needs of the specific experiments conducted. Analysis software was developed by Michael Wormsbecker. The writing of the submitted manuscript was done by Michael Wormsbecker with Todd Pugsley, J. Ruud van Ommen and Rob Mudde providing technical and editorial guidance regarding the content of the paper.

Contribution of this Paper to the Overall Study

This paper provides a different perspective on the hydrodynamics induced by distributor design in fluidized bed dryers. Different from Chapter 5 where global measurements were analyzed, localized hydrodynamic measurements are employed through the use of x-ray densitometry. This way the influence of distributor design during drying can be further investigated with a measurement technique different from pressure fluctuation analysis.

6.1 Abstract

Distributor level hydrodynamics induced by a perforated, punched and porous plate in a 15-cm ID fluidized bed dryer were studied using one-dimensional x-ray densitometry imaging. The time-averaged solids concentration profiles of pharmaceutical

granule were compared with both dry material and with wet granule which was dried under standard drying conditions. Studying the hydrodynamics under steady-state and dynamic conditions illustrated that the porous plate creates even gas distributor across the bed inlet with dry granule, but results in excessive defluidization at the distributor level when the granule is wet. The perforated and punched plates exhibited different solids concentration profiles with dry granule, however, the presence of moisture results in similar hydrodynamics between the plates during drying in this study. Standard deviation analysis of the high frequency solids concentration data were used to corroborate the results of the solids concentration measurements.

6.2 Introduction

The distributor hydrodynamics studies in Chapters 4 and 5 of this thesis, as well as other distributor designs presented in the literature [1-3], are based primarily on time and frequency analyses of pressure fluctuation measurements. The drawback of this approach is that only the global aspects of the hydrodynamics were compared since local phenomena are indistinguishable based on the measurement methods used in these works. In order to better understand the hydrodynamics caused by different distributor designs, localized distributor level measurements, where differences between designs can have the greatest impact, is warranted.

A tool with the ability to accomplish localized hydrodynamic measurements at the distributor level is x-ray densitometry imaging. X-ray densitometry, along with γ-ray densitometry, are more generally referred to as nuclear densitometry techniques. These

techniques use the attenuation of photons generated by a radiation source to measure the density of material, or volume fraction of solids, along a given measurement path. The use of nuclear densitometry (x-ray or γ-ray) is a well-established local measurement tool used in fluidization research [4-9]. Its use is becoming even more popular as the increasing power of data acquisition and computing systems allow larger volumes of data to be handled. The primary advantage of nuclear densitometry over other tomographic measurement devices such as electrical capacitance tomography (ECT) is that it has the power to increase the spatial resolution of the measurements. This is because nuclear techniques rely on hard fields, so resolution in the centre of the bed is not lost. Unfortunately, the current state of nuclear densitometry research does not allow for high temporal resolution. Individual tomograph scans take in the order of seconds to minutes to make [4-8]. Therefore, only time-averaged measurements have been made in fluidized beds since bubbling phenomena occur in times much less than a second. As a result, nuclear densitometry is typically used to measure time-averaged voidage or solids holdup in fluidized beds. For an extensive discussion of nuclear densitometry along with its use in fluidization research, refer to Mudde et al. [9].

The research groups of Apostolos Kantzas and Mike Duduković have made the most significant contributions in this field of research over the past 15 years. The most recent work by the group of Kantzas [6] has used x-ray computed tomography to demonstrate dynamic flow behaviour in gas-solid fluidized beds. The group of Duduković [8] has made similar measurements in liquid-solid fluidized beds using γ-ray

measurements. These studies are focused on characterizing fluidized bed hydrodynamics along their axial and radial dimensions, but under steady-state operating conditions only.

In the current study, x-ray densitometry measurements will be used to investigate distributor level hydrodynamics induced by various distributor designs in a cylindrical fluidized bed dryer (FBD). In particular, the perforated, punched and porous plate distributor designs are examined as they relate to the pharmaceutical industry. Experiments are conducted using dry granule to evaluate the distributor hydrodynamics under steady-state conditions, but also real-time drying experiments are employed to investigate the impact of moisture on the distributor level hydrodynamics of drying.

6.3 Experimental Apparatus

The experimental apparatus used in this study is presented in three parts: (1) a low shear granulator, (2) a cylindrical fluidized bed and (3) an x-ray densitometer. The granulator was used to create the wet placebo pharmaceutical granule which was dried in the FBD. The x-ray densitometer was used as the principal measurement device in this study.

6.3.1 Low Shear Granulator

The placebo granule was comprised of the ingredients listed in Table 2.2. An Eirich Type R02 intensive-action mixer was used for granulation. With this granulator, 1 kg of wet material was produced per batch. The dry ingredients were premixed for three minutes with the impeller and bowl rotational speeds set at low. After pre-mixing, the

water was added to the dry ingredients over a five minute period. Water addition was done using a BETE BJ 001740 low flow flat spray nozzle with a 40˚ fan angle. The nozzle was connected to a pressure pot operating at 2.5 barg and extended down 14.5 cm from the lid of the granulator to introduce the spray to the granulator bowl. After the water addition phase, post mixing was carried out for an additional two minutes to finalize the granulation process. Sieve analysis was used to characterize the dried granule size distribution. The dry granule was found to have a bimodal size distribution with a mass mean diameter of 280 ±12 μm and a particle density of 830 kg/m^3. The size distribution of the granule is shown in Fig. 6.1 where *X* is the mass fraction of the granule that corresponds to the average particle size (*d*) based on the sieve sizes used in the particle size analysis.

6.3.2 Fluidized Bed

The cylindrical fluidized bed has a diameter of 15 cm and wall thickness of 0.5 cm. The cylindrical column is 45-cm tall and constructed of Perspex to allow for visual observations. Three distributor designs were used in the study – perforated, punched, and porous plates. The fundamental difference between these distributors is their orifice design. The perforated plate has 2.7-mm diameter orifices which introduce the fluidization gas via vertical jets whereas the punched plate is constructed in such a manner that a horizontal gas jet is introduced to the bed unidirectionally through semi-circular caps 1.0 mm x 5.75 mm in dimension. The orifice sizes for each plate were chosen to maintain similar open areas between individual orifices. The resulting percent open areas from their designs are 8.9 and 9.0%, respectively. The porous stainless steel

distributor plate is a much different design as it introduces a fine dispersion of air to the fluidized bed through its micron-sized pores.

Flange-connected to the top of the bed is a conical freeboard which is used to disengage any entrained material from the exhaust gas. The freeboard is covered with a cloth to minimize loss of fines from the system. The fluidization air is freeze-dried, compressed air heated with a 9-kW circulation heater from Watlow Electric Manufacturing Company. A PID controller was used to regulate the inlet bed temperature. The inlet humidity was measured prior to the heater with a TESTO humidity sensor. Finally, the superficial gas velocity was controlled using a Bronkhorst 1000-NmL/min mass flow controller. A complete schematic of the cylindrical fluidized bed and accompanying equipment is illustrated in Fig. 6.2.

The temperature and humidity data were collected continuously during drying experiments with a DIFA data acquisition unit. These data were used to complement the hydrodynamic data collected with the x-ray densitometer. Granule moisture samples of 5 – 10 g were also collected during drying. This was done by removing the disengagement section of the bed during operation and manually taking a sample from the bed. Only one sample was taken as homogeneity of moisture in the system was assumed since the sample was collected from a well-mixed fluidized bed. The granule samples were analyzed for loss on drying using a tray dryer. The tray dryer was set at 90°C where the granule dried until moisture removal was negligible.

6.3.3 X-ray Densitometer

The principal component of this unit is the x-ray source. The x-ray source has a type SRO 25 50 – ROT 350 x-ray tube manufactured by Philips Electronics. Mounted to the x-ray tube is a depth collimator. This is used to control the angle and width of the fan beam generated by the x-ray tube. These parameters were measured with a halogen light housed in the collimator. The angle of the fan beam was calculated to be 18.8˚ and its width was approximately 1 cm at the detection bank. These fan beam dimensions were chosen to optimize the active area of the x-ray detectors. More detailed information regarding the x-ray source is provided in Table 6.1.

To detect the photons created by the x-ray source, a bank of detectors is placed opposite the fluidized bed. The detector bank is comprised of 32 detectors, which are an assembly of $CdWO_4$ scintillation crystals optically coupled to S1337 – 1010BR type PIN photodiodes manufactured by Hamamatsu Corporation. The photodiode assembly allows for higher spatial resolution as these detectors have a much smaller dimension as compared to classically used photomultiplier tubes. The detector bank was also shielded with 1 mm of copper sheeting. This was done to ensure the detection capabilities of the photodiodes were not jeopardized by oversaturation due to high photon count rates. This amount of shielding was found experimentally to optimize the detector count rates. More in-depth information regarding the components of the detectors is provided in Table 6.2.

In order to generate densitometry measurements, the fluidized bed described previously was positioned between the x-ray source and photodiode detectors. A plan and

side view of the assembly is shown in Fig. 6.3. The fluidized bed was positioned in such a manner that the outermost detectors (1 and 32) were positioned just outside the walls of the bed, centering it. The beam paths of detectors 2 and 31 pass through a significant portion of the walls of the fluidized bed, so the detectors used for data acquisition in this study are detectors 3 - 30. The numbering scheme used to identify the detectors is their order from left to right when facing the detector bank from the perspective of the source (see Fig. 6.3). The axial position of the fluidized bed was adjusted in order to have the x-ray beam pass through the bed 2.0 cm above the distributor plate. At this height, the bottom flange of the fluidized bed is below the x-ray plane, yet sufficiently close to the distributor plate to measure distributor level hydrodynamics.

The x-ray tube settings were changed manually via its control panel. The tube voltage (150 kV) and current (10 mA) were chosen to optimize the photon energy and photon count rates of the x-ray source, respectively. The x-ray DAQ system itself was comprised of four 2-GHz PCs each housing an 8-channel 12-bit PCI card. The photon count rate measured by the detectors was collected at 25 kHz. The control panel and DAQ system were operated remotely via a master PC using custom software created by the Kramers Laboratory. This software allowed the x-ray source and the DAQ system to be automatically triggered. This way data acquisition was synchronized with the x-ray source to optimize the data collection process.

6.4 Experimental Methods

6.4.1 Detector Calibration

Before fluidization experiments can be run, the detectors must be calibrated. The calibration of the detectors is based on the Lambert-Beer's law for attenuation of photons through a homogenous material:

$$\frac{\Phi(W_g)}{\Phi_0} = e^{-\mu W_g} . \qquad \text{(Eq. 6.1)}$$

Therefore by measuring the photon count rate (Φ) through various known thicknesses of material (W_g), the effective attenuation coefficient of the material (μ) and the incident photon count rate of the beam (Φ_0) can be obtained experimentally. It is important to note that this calibration process measures the packed bed voidage of solids. Therefore, the data can only be presented in terms of the true solids concentration if the packed bed voidage is known.

Calibration of individual photodiode detectors was required for the current study. In theory, this is redundant because each detector should have similar count rates. However, variations in manufactured batches of the photodiodes were found to result in different photon count rates between detectors. With 32 detectors used in the detector bank, individual calibration was not a viable option. Instead, a calibration cell was constructed to allow for simultaneous calibration of the detectors. The calibration cell is rectangular and has a movable Perspex wall that allows the count rates through various

material thicknesses to be measured. The front and movable back walls were 0.5 cm thick. This was done to emulate the wall thickness of the fluidized bed (W_w) and therefore remove the influence of the bed wall from the detector calibration. Unfortunately, this method is only truly representative of the middle detectors (detectors 10 - 23) as the amount of Perspex wall that the x-ray beam passes through increases exponentially with an increase in detector angle from the centreline (see Fig. 6.4). Maximum calibration error will therefore be experienced at the outermost detectors where the x-ray beam was calculated to pass through approximately 2.0 cm of Perspex. To minimize this error, the photon count rate associated with an empty bed is used to subtract out the influence of the wall thickness for each beam path.

Each calibration was conducted with material thicknesses of 3.0, 6.0, 9.0, 12.0 and 15.0 ± 0.1 cm in the calibration cell. In each case, the material was poured into the calibration cell to obtain the attenuation coefficient of the packed bed voidage. To obtain the actual thickness of material the x-ray passes through along an individual beam path, the calibration cell was placed in a known position with respect to the source. With the angle of the fan beam known, geometric calculations allow the actual length of the beam paths to be calculated for each detector. Using these beam path lengths and the acquired photon count rate, the effective attenuation coefficients for individual detectors were determined.

Unique to this study is the influence of granule moisture content on the effective attenuation coefficient. Varying degrees of water in the granule alter the attenuation

coefficient; therefore the impact of moisture needs to be included in the calibration process. A similar dynamic calibration was successfully conducted by Chaplin et al. [10] for use with ECT measurements during drying. The detectors in this study were calibrated with granule which spans the range of moisture contents experienced during drying. In the current study, this is 3 – 32 wt.%. With multiple granule moisture content calibration curves, calibration maps were constructed for each of the detectors. In the studies involving dry granule (phantom image and dry bed tests), the calibration for only the dry granule is required.

6.4.2 Phantom Images

The term 'phantom' typically refers to the reconstruction of an object of known geometry based on multiple view measurements into a tomographic image. This type of reconstruction method is not applicable to the present study since measurements were collected from only one view. However, phantom-like images were still generated in this study as they serve two purposes. First, phantoms demonstrate the accuracy and precision of the x-ray densitometer through its measurement of the concentration of solids along a chordal path length. Secondly, properly chosen phantoms allow 1-D projections to be created that may be expected during fluidization experiments. This gives a basis for analysis and will also help explain the solids concentration profiles measured during fluidization experimentation.

Core-annulus structures were created as the phantoms in this study. Core-annulus refers to a fluidization structure where the core (central) region is of high voidage and

annular (outer) region is dense. The reason for implementing this type of structure is that core-annulus type flow structures have been shown to exist during drying [11]. To create a core-annulus structure, an empty plastic bottle was placed in the centre of the fluidized bed which was then surrounded with dry granule. Two different core-annulus structures were used: 11.8 and 9.2-cm diameter core regions. These core regions were completely void of material and therefore were an exaggeration of what is expected from both an instantaneous, but also time-averaged, perspective.

Static measurements, like phantom images, do not require significant amounts of data. Therefore, for each phantom only 1 s of data were collected. These data were subsequently time-averaged to create an average count rate for each detector. These count rates were then used with the dry granule calibration curves to calculate the average path length of solids measured by each detector. Subtracting the reference state path lengths (empty core and annular region) from the phantom measurement path lengths, an actual path length profile is recreated which represents the phantom image.

6.4.3 Fluidization Experiments

Dry Bed

Dry bed experiments were conducted to determine the influence of distributor design on dry bed hydrodynamics. This provides an initial basis for comparison of distributor designs and is useful in determining the effect of granule moisture content on the hydrodynamics when drying is considered. Also, these experiments allow the reproducibility, as well as the statistical relevance, of the measurements to be tested

under steady-state conditions. Testing the reproducibility is important because the x-ray tube has a finite operating period as a result of the heat generated by the source. This factor must be considered when drying since drying is a time-dependent process; sufficiently long data sets are desired so that basic statistical analysis of the drying data can be performed. Based on the cooling specifications of the x-ray tube, the optimum length of the data sets was determined to be 10 s for this study. At this length of x-ray commissioning time, four minutes of downtime was required to sufficiently cool the x-ray tube. To collect a data set, the x-ray was commissioned ten separate times for 1 s over a period of approximately one minute.

Dried placebo pharmaceutical granule was used to conduct the dry bed experiments. A bed mass of 750 g, corresponding to a static bed height of 8 cm, was used for the study. This bed mass is based on the final bed mass after drying approximately 1 kg of wet material; the wet bed mass from the drying portion of this study. The fluidization air was compressed air at an inlet temperature of 20 ± 1˚C and a relative humidity of 6 ± 1%. Experiments were run with each distributor plate at superficial gas velocities of 0.11, 0.21, 0.32 and 0.42 m/s. The minimum fluidization velocity of the dry granule was found experimentally to be 0.070 m/s, with its full support velocity reached at 0.11 m/s [12]. The full support velocity is defined as the minimum velocity where the entire bed mass is supported by the drag created by the fluidization air [13]. The use of this velocity is relevant for characterizing powders which do not fluidize easily or ones that have wide particle size distribution [12]. In these cases, defluidization and segregation of powders affect standard minimum fluidization velocity measurements. The

maximum velocity used in this portion of the study was chosen based on the steady-state velocity used in the drying experiments. Three data sets were collected at each velocity to check the reproducibility in the measurements.

Drying

As mentioned above, the drying experiments involved drying 1.0 kg of wet placebo pharmaceutical granule. The granule, which is 32.0 ± 0.3 wt.% water after granulation, was dried at 52 ± 1˚C and a relative humidity of 6 ± 1% until the bed temperature approached 50˚C. At this point, the granule is fully dried as virtually no heat is being used to evaporate water from the granule. An elevated gas velocity of 0.63 m/s was used for the first eight minutes of drying. This was required since the full support velocity of the wet granule is approximately 0.40 m/s [12]. Operating above this velocity ensures a well-mixed fluidization state during this period of drying. After eight minutes, the superficial gas velocity was decreased to 0.42 m/s. The reason for this decrease in velocity is to limit the aggressiveness of the fluidity by the end of drying as moisture removal has a significant impact on the hydrodynamic characteristics of the granule [14]. Finally, granule samples were taken at the 0, 8, 18, 30 and 38 minute marks of drying to develop a moisture curve for each experiment. This way the detector calibrations could be corrected for moisture content for each of the densitometry data sets collected during drying.

The densitometry data was collected for 10 s over an interval of approximately one minute. This was repeated every four minutes until the granule was dry. Although the

hydrodynamics are only captured every four minutes, significant changes in distributor level hydrodynamics due to changes in moisture content will be captured. Bed temperature was also collected continuously to characterize the drying process for the purpose of discussing the densitometry data. Three drying trials were run for each of the distributor designs studied to ensure sufficient data were collected for reproducibility purposes. The densitometry data were analyzed with in-house code developed for use with MATLAB®. The code used specifically for analyzing the x-ray data collected during drying experiments is provided in Appendix E.

6.5 Results and Discussion

6.5.1 Calibration

To summarize the influence of moisture on the calibration of the detectors, the average effective attenuation coefficients (μ) for all the detectors at various granule moisture contents (Q_g) are shown in Fig. 6.5. These data demonstrate that as the moisture content increases, the attenuation coefficient decreases. This behaviour is contrary to what is expected as an increase in moisture content should increase the material density and therefore the attenuation coefficient as well. The explanation for this unexpected behaviour is that the packed bed voidage of the granule increases with moisture content (and this increase in voidage affects the effective attenuation coefficient to a greater extent than does the moisture content). In a recently published paper by our group regarding the influence of moisture on granule properties [12], the Hausner ratio (ratio of the tapped and poured densities of a solid) was used to demonstrate the influence of liquid bridging on the stability of pharmaceutical granule in a static environment. This

work showed that an increase in moisture content stabilized the granule which influenced fluidization properties such as the full support velocity and voidage. If this same work is considered in terms of a granule's packed bed state, an increase in Hausner ratio indicates an increase in packed bed voidage. This confirms the impact that moisture content can have on the effective attenuation coefficient.

The error bars associated with the data in Fig. 6.5 represent the 95% confidence limits of the average effective attenuation coefficients for the detectors. The relative standard deviation of the attenuation coefficients is less than 2.2% for all moisture contents, illustrating that there is virtually no difference between detectors at a specific moisture content. Although not presented in the form of data in this study, the relative standard deviation of the incident photon count rate of the beam (Φ_0) was also very low for each detector over the calibrated range of moisture contents (< 1.7%). Based on this finding, the average incident photon count rate of the beam was used for the calibration curves of each detector.

Using the average initial photon count rate for each detector with their effective attenuation coefficients at various moisture contents, a calibration map for each detector was developed. These calibration maps use the measured count rate (Φ) to determine the chordal path length, or thickness, of granule (W_g) measured by the detector at a given moisture content. One of these calibration maps is shown in Fig. 6.6. These maps are used to interpolate the calibration curve for granule at specific moisture contents for the data collected during the drying studies. For a complete list of effective attenuation

coefficients and incident photon count rates for the detectors used in this study, see Tables F.1 and F.2 of Appendix F.

6.5.2 Phantom Images

The measured solids path lengths (W_g) arising from the 9.2 and 11.8-cm core-annulus phantoms, along with a packed bed measurement, are illustrated in Fig. 6.7. The packed bed path length profile (denoted as 'none' in the figure, referring to the absence of a phantom in this measurement) demonstrates the accuracy of the detector calibration. Detectors 16 and 17, the centreline detectors, represent the diameter of the bed. These detectors measure packed bed solids path length values of 14.96 and 14.88 cm, respectively, which are within 0.8% of the actual bed diameter. Although not illustrated through Fig. 6.7, the centreline data from the core-annulus structures can also be used to confirm the known core diameters of the phantoms. Using a separate analysis of the data, core diameters of 9.27 and 9.20 cm and 11.74 and 11.64 cm were measured by the x-ray densitometer for the 9.2 and 11.8-cm core-annulus phantoms, respectively. These values are within 0.8% and 1.4% of the measured sizes, respectively. These data illustrate that both the bed and core-annulus diameter measurements are within the tolerance of the actual diameters measured with a graduated rule (± 0.1 cm). Thus, it can be concluded that the x-ray densitometry used in this study exhibits a high level of spatial accuracy.

The phantoms also provide insight into 1-D solids distribution profiles caused by core-annulus structures. As shown in Fig. 6.7, the length of measured solids decreases once the edge of the core region is detected. A more convenient way of presenting these

data is in terms of a solids concentration profile. In this study, solids concentration is defined as the percentage of an x-ray path that is occupied by solids in a packed bed state (W_g/W_{max}). Therefore a solids concentration of unity implies the solids in the beam path are packed (or defluidized if considered with respect to a fluidization process where gas voids may be present). It is important to note that solids concentration defined in this way is different from the concept of voidage and solids holdup used in many fluidization studies. This method was chosen since packed bed voidage of the granule changes with moisture content.

The solids concentration is calculated by normalizing the measured solids concentration against the maximum length of solids that can be present along a given beam path (i.e. the chordal lengths associated with each of the detectors). These maximum path lengths are illustrated through the packed bed measurement of Fig. 6.7. The solids concentration profiles for the 9.2 and 11.8-cm core-annulus phantoms are shown in Fig. 6.8. These profiles demonstrate that when the core region is not in the beam path of the detector the solids concentration approaches 1.0. As with the measured solids, once the core region intercepts a beam path, the solids concentration decreases in magnitude.

6.5.3 Dry Bed Experiments

Each distributor plate appears to demonstrate different hydrodynamic behaviour when operated with dry granule. The perforated plate demonstrates a W-shaped solids concentration profile across the bed as the velocity increases (see Fig. 6.9(a)). At 0.11

m/s, the average solids concentration profile is relatively high with a maximum value of approximately 1.0 (i.e packed bed) at the walls and minimums of 0.80 – 0.85 towards the middle of the bed. These high solids concentration values are a result of the bed operating at the full support velocity, therefore the excess gas in the system is negligible and bubbles only begin to form higher up in the bed. The lack of a discernable profile is attributed to potential segregation of large granule in the bottom of the fluidized bed at this low velocity. As the gas velocity increases to 0.21 m/s, the average solids concentration associated with individual detectors decreases, but also flattens out in the middle of the bed. Beyond 0.21 m/s, a distinct W-shape solids concentration profile takes shape. At these velocities, the average solids concentration is still high at the wall, but decreases to solids concentration as low as 0.60 – 0.70 towards the middle of the bed.

The time-averaged W-shape profile suggests that near the distributor, the gas (i.e. bubbles) moves axially but not at the centreline of the bed. Work done with electrical capacitance tomography by our group found a similar W-shaped profile in a conical fluidized bed of dry pharmaceutical granule operating with a perforated plate distributor. Wiens and Pugsley [15] attributed this behaviour to annular bubbling caused by segregation at low velocities and the presence of penetrated and splitting bubbles at higher velocities. Their work was carried out well above the distributor, however, so an exact comparison between their work and the present study cannot be made.

To verify the annular passage of gas through the bed with the perforated plate, the relative standard deviation of the high frequency solids concentration data was calculated

for each detector. Fluctuations in the solids concentration profile indicate a variation of solids along the detector path. An increase in relative standard deviation is related to the passage of gas, presumably in the form of bubbles. Fig. 6.10(a) shows the relative standard deviation (*RSD*) profiles for the measured solids associated with the perforated plate experiments. These data support the notion that bubbles rise axially off the centreline of the bed. The standard deviation reaches local maxima at detectors 9 and 22 and a local minimum at the centre of the bed. Furthermore, as the velocity increases the relative standard deviation of the solids fluctuations increases. This suggests that larger bubbles are created at the distributor level as the superficial gas velocity increases.

The punched plate exhibits a different time-averaged solids distribution profile (see Fig. 6.9(b)). The solids concentration profile takes on a U-shaped profile as the superficial gas velocity increases. As with the perforated plate, the punched plate has a high solids concentration at low velocities which decreases as the superficial gas velocity increases. Like the perforated plate, the punched plate also experiences high solids concentration at the bed periphery which decreases towards the centre of the bed. As the superficial gas velocity increases above 0.11 m/s, the U-shaped profile begins to develop. By 0.42 m/s, the solids concentration profile appears to be fully developed with a solids concentration above 0.90 at the wall and a minimum concentration of 0.55 occurring at the centreline detectors.

This profile is different from that of the perforated plate as it suggests that the gas is preferentially moving through the centre of the bed. The relative standard deviation

profile (Fig. 6.10(b)) supports this finding as the standard deviation reaches a maximum between detectors 10 and 20, corresponding to the centre region of the fluidized bed. The standard deviation profiles with the punched plate shown in Fig. 6.10(b) are significantly higher towards the middle of the bed, but smaller towards the peripheral detectors as compared to the perforated plate beyond 0.21 m/s. This suggests that bubbles move upward in the middle of the bed and that the overall hydrodynamics between the two distributor designs are different. The differences in the profiles imply that the lateral direction imposed on the fluidization gas by the punched plate has an effect on the segregation tendencies in the system at higher velocities or that it alters the circulation pattern of solids in the bed resulting in a change in bubble formation at the distributor level.

The porous plate has a solids concentration profile that contrasts both the punched and perforated plates. With this design, the solids concentration profile indicates that gas flows preferentially around the periphery of the bed; the solids concentration profile appears as an inverted U-shape in Fig. 6.9(c). Although not intuitive, the behaviour suggested by the porous plate's solids concentration profile has been reported in the literature. Werther and Molerus [16] demonstrated that bubbles form near the wall with porous plates then migrate towards the middle of the bed as they travel up through the solids. At 0.11 m/s the solids concentration is approximately 1.0 in the centre region of the bed and decreases to 0.70 towards the bed periphery. This suggests that the middle region of the bed is in a defluidized state under these conditions. This defluidization is due to the high degree of segregation which was observed through the Perspex wall of the

bed at the height of the measurement plane. As with the other distributor plates, the solids concentration profile flattens as the gas velocity is increased. At 0.42 m/s, the solids concentration in the middle of the bed is 0.75 and the wall regions are approximately 0.55.

Again, the relative standard deviation analysis supports the gas flow behaviour induced by the porous plate. As shown in Fig. 6.10(c), the standard deviation is highest with the outer detectors and decreases towards the centre of the bed. The segregation mentioned above is also supported by the relative standard deviation in the solids concentration data. At 0.11 m/s, the relative standard deviation approaches zero at the middle detectors.

Apart from establishing the influence of velocity and distributor design on dry bed hydrodynamics, these experiments were used to address the validity of conducting analysis with 10-s data sets for the drying experiments. As shown in Figs. 6.9 and 6.10, there is some variability in the data at 0.11 and 0.21 m/s, which is most likely due to the transition from a segregated to a well-mixed fluidization state. Above 0.21 m/s, there is good reproducibility in the solids concentration profiles. Therefore, using data sets of this length for drying experiments where the fluidization velocity is above 0.42 m/s is valid.

In attempts to quantify the validity of the statistics used in this study, preliminary analysis of the frequency content in the data was done. Obviously, the statistical accuracy of any analysis is dependent on the number of events occurring in a data set. In the

current study, it was found that anywhere between 30 - 50 fluctuations in solids concentration occurred with each detector during a 10-s data set at velocities of 0.32 and 0.42 m/s. Enwald and Almstedt [17] found that 75 bubbles suffice for defining statistical properties in experimental data whereas our group has demonstrated reasonable statistics with 58 - 81 [18] and 30 - 110 bubbles [15] for calculating time-averaged voidage profiles with ECT data. Similarly, Makkawi and Wright [19] found that 10 s of data are quite sufficient for making average solids fraction measurements with ECT data. However, they suggest upwards of 60 s for calculating dynamic measurements such as standard deviation, bubble frequency and rise velocity [19]. Regarding nuclear techniques, Wright et al. [9] recommend a 30-s scan for obtaining accurate time-averaged voidage profiles whereas Kumar et al. [7] found about 1 – 2% variability in the absolute voidage measurements with 5.8 s of data. The solids fluctuations in the current study can clearly be related to the passing of bubbles. So based on the precedents in literature, a 10-s data set should provide representative data at the velocities used in the drying portion of the study. However, the authors accept there are still limitations with the statistical accuracy of the data due to the limited size of the data sets. As a result, the extent of the analysis performed in this study has been limited to only time-averaged solids concentration and standard deviation analysis.

6.5.4 Drying Experiments

Process Data

Basic drying data allow for a basis of interpretation when presenting the densitometry data. When considering pharmaceutical granule, the drying process can be

separated into two periods. The first period is the constant rate drying period. In this period, the air used for drying becomes saturated with moisture; hence the drying rate is constant and maximized. The second period, termed the falling rate period, exists when the rate of moisture removed from the granule is continually dropping. At this point, the product temperature starts to rise since the heat supplied by the fluidization air does not go entirely to vapourization of moisture. The transition point between the constant and falling rate periods of drying is termed the critical moisture content. Accompanying this change in drying is a change in the bed hydrodynamics. The magnitude of interparticle forces decreases once the falling rate period is reached, corresponding to a reduction in the extent of liquid bridging between particles. A more in-depth review of drying fundamentals, along with its impact on the hydrodynamics of fluidized bed dryers has already been discussed in Chapter 3 of this thesis.

The critical moisture content is most easily detected by a change in product temperature. The product temperature increases from its saturation temperature once the falling rate period is reached. Fig. 6.11(a) illustrates the average product temperatures (T) for each distributor plate studied. As seen in this figure, the critical moisture content is reached at approximately 28 minutes for all of the plates. Using this information, the critical moisture content can be interpolated from the average moisture content (Q_g) profiles which are shown in Fig. 6.11(b). The critical moisture content was found to be 8.1 ± 0.3 wt.% for the granule in this study. This critical moisture content is in the same range as those found in Chapter 3 and also previous studies done by our group where

values between 9 – 14 wt.% were reported [14, 20, 21]. Variation in these values is a result of different dryer operating conditions.

X-ray Data

To demonstrate the dynamic change in the densitometry data between the different distributor plates, topographical representation of the data is presented. As was the case with the dry bed studies, transient profiles of the average solids concentration and the relative standard deviation are presented. One representative data set is provided for each figure in this portion of the study.

The solids concentration profiles shown in Fig. 6.12(a) and (b) illustrate that perforated and punched plates exhibit similar distributor level hydrodynamics during drying. In the constant rate drying period, the perforated and punched plates have high solids concentrations which approach 1.0 at the wall regions. Away from the wall, the average solids concentration gradually decreases to a less dense hydrodynamic state. The solids concentration in the middle of the bed is considerably lower than the wall region, suggesting that the gas is bubbling up through the middle of the bed. The high solids concentrations at the wall followed by a decrease in solids density towards the middle of the bed is analogous to the profiles observed in the tests using the core-annulus phantoms. Therefore, solids concentrations approaching 1.0 suggest that the bed is defluidized in this region of the bed as the solids are in their packed bed state. Using the average distance (D) between the beam path and the centreline of the bed defined in Fig. 6.13, the diameter of the fluidized core region is approximately 11.6 cm for both the

perforated and punched plate; with the remainder area outside this region being defluidized. The authors believe that the assumption that this behaviour is symmetric is valid as the outer three detectors on both sides of the bed (detectors 3 - 5 and 28 - 30) detect similarly high solids concentration. Furthermore, defluidization at the wall of the bed was visually observed around the entire bed periphery during the constant rate period of drying.

The defluidized periphery associated with the perforated and punched plates is believed to be a result of the reduced flowability of the granule at high moisture contents. This is because the fluidization experiments with dry granule do not yield distinct deadzones at the wall region of the bed; the average solids concentration profiles typically decreases and *RSD* increases with detector position from the walls at 0.42 m/s. This occurs regardless the fact that the orifices of the perforated and punched plates do not fully reach the walls of the bed; the outermost orifices are 1.1 and 0.6 cm from the walls for the perforated and punched plates, respectively. Improved fluidity with decreasing moisture content is best illustrated in the solids concentration profiles during drying shown in Fig. 6.12. The outermost detectors measure a decrease in average solids concentration as drying proceeds.

Beyond the presence of defluidized regions with the perforated and punched plates, there is a general transition in the solids concentration profile as drying proceeds. While operating at 0.63 m/s (represented by the 4 minute profile), the centre region of the bed is much more dilute and demonstrates a more distinct transition to higher solids

concentration at the walls. Obviously, this is expected due to the increase in volumetric flow of gas in the system. At 8 minutes, when the gas velocity is decreased to 0.42 m/s, the middle of the bed becomes less dilute. As drying proceeds in the constant rate period, the detectors 3-10 and 24-30 demonstrate a gradual decrease in the solids concentration. This means that the fraction of the bed cross-section occupied by the fluidized core region of the bed is increasing as drying proceeds. The growth of the fluidized core region during drying has also been reported by our group through ECT tomographs [11]. By 28 minutes, which coincides with the critical moisture content of the granule, the solids concentration becomes relatively low in the middle of the bed with the outer regions of the bed also being more dilute. This suggests that the bed is well-fluidized across the entire cross-section at this point. This increased fluidity was visually observed at the bed wall as the defluidized bed mass was engulfed into the fluidized region of the bed between the 24 and 28 minute marks. Furthermore, when the data at 28 minutes are compared to the dry bed hydrodynamics at 0.42 m/s, similarities in the average solids concentration of both the perforated and punched plates are seen. This suggests beyond the critical moisture content, the hydrodynamics of the system do not change significantly. This parallels the findings of Chapter 3 of this thesis which employed spectral analysis of high-frequency pressure fluctuations during fluidized bed drying in a conical fluidized bed.

Similar to the dry bed hydrodynamic analysis, the porous plate (Fig. 6.12(c)) induces significantly different distributor level hydrodynamics during drying. In the constant rate period of drying, the porous plate generates a relatively high solids

concentration across the entire bed cross-section which does not vary significantly between detectors. This constant cross-sectional solids concentration is caused by the extensive segregation and defluidization generated by the porous plate in the early stages of drying. As mentioned previously in the description of the porous plate, the fluidization air enters the bed as a fine dispersion rather than being introduced as gas jets. This results in the gas carrying little momentum and an inability to fluidize the wet granule. This air does however migrate through permanent voids and small channels created in the defluidized granule, thus resulting in the solids concentration less than 1.0 (see Fig. 6.12(c)). This behaviour exhibited with a porous plate in a bed of sticky material has been alluded to in a review presented by Geldart and Baeyans [22]. Although not able to be presented quantitatively, visual observations of the fluidity further up in the bed did show marked improvements as it took on similar hydrodynamic characteristics to that of the other distributor designs. This is a result of coalescence of the gas after passing through the defluidized entrance region.

A sharp transition in the solids concentration profile of the porous plate occurs at the critical moisture content. Like the perforated and punched plates, this change is due to the break-up of the defluidized granule. The fact that the transition is much sharper is an indication of the high degree of defluidization at the distributor level with the porous plate. Afterwards, the solids concentration profile becomes dilute over the bed cross-section and takes on the same inverted U-shaped profile previously described for the porous plate under dry bed conditions.

Finally, to corroborate the hydrodynamics behaviour revealed by the solids concentration profiles, the transient relative standard deviation profiles during drying are presented. Mostly notably in these profiles, the relative standard deviation is less than 3% at the wall of the bed for the perforated and punched plates whereas the entire bed cross-section is very low for the porous plate during the constant rate period (see Fig. 6.14). This indicates that the solids fluctuations along a beam path length are not varying significantly in these regions; supporting the theory that the granule is defluidized in Fig. 6.12.

The distinct change in each of the relative standard deviation profiles at the critical moisture content demonstrates the impact of moisture on the hydrodynamics of the system. At this point, the gas-solids contacting becomes much more aggressive based on the increase in the relative standard deviation. The moisture content in the system at this point is 8 wt.%. According to previous work by our group [14], this change in fluidization behaviour is expected as the critical moisture content has been surpassed and therefore interparticle forces are significantly reduced. The decrease in interparticle forces allows the bubbles to coalesce more easily which in turn will result in larger fluctuations in solids in the bed.

With any measurement technique, there are always limitations. An important limitation to consider in the current work is that in order to employ a calibration for the detectors, moisture homogeneity must be assumed throughout the bed. This is likely not the case in the defluidized regions of the bed as this granule will dry somewhat

differently than the granule in the fluidized core region. The extent of the moisture variation is not known for this study, so the error in the average solids concentration profile cannot be quantified. Fortunately, this is not a serious issue in the current work as the presence of defluidization is corroborated with the relative standard deviation in the solids concentration.

6.6 Conclusions

The reality of distributor induced hydrodynamics in the entry region of a fluidized bed dryer has been proven using 1-D x-ray densitometry imaging. Although precise differences in the hydrodynamics induced by different distributor designs cannot be determined in all cases presented in this study, general differences in the hydrodynamics were found to exist at an x-ray plane height 2 cm above the distributor plate.

Using dry granule, it was found that the perforated and punched plates, which have orifice designs that introduce air into a fluidized bed as jets, tend to generate hydrodynamics where the gas travels up the middle of the bed. The porous plate induced different hydrodynamics where the gas is more evenly distributed, but prefers to travel towards the periphery of the bed. During drying, the hydrodynamics induced by the porous plate proved to exhibit very poor hydrodynamics as compared to the other distributor designs; a result which is counter-intuitive from conventional distributor design theory. The fine dispersion of air introduced by the porous plate did not carry sufficient momentum to properly fluidize the wet granule in the bottom zone of the fluidized bed resulting in a defluidized cross-section during the constant rate period of

drying. The perforated and punched plates did generate a fluidized core region at this bed height, which grew in size during drying, but also exhibited a defluidized periphery that was approximately 1.7 cm thick. No substantial differences between the perforated and punched plate hydrodynamics were determined during drying although dry bed studies suggest differences occur between the plates.

The impact of these findings is important to pharmaceutical research from a product quality perspective. Poor mixing in fluidized bed dryers results in uneven drying, hence variation in moisture contents in a batch of dried solids. The inability to control this moisture content can lead to the rejection of entire batches of products. Therefore implementing a distributor design that best initiates solids circulation at the distributor level during drying is of great importance to fluidized bed dryer design. To overcome the defluidized periphery, which is the most influential phenomenon related to maldistribution of moisture in the granule, a conical fluidized bed geometry can be used.

6.7 Nomenclature

d	particle diameter, μm
D	distance between chordal measurement path and the bed centreline, cm
Q	moisture content, wt.%
W	thickness of material along a measurement path, cm
RSD	relative standard deviation, -
t	time, min
T	product temperature, ˚C
X	mass probability function, wt.%
Φ	photon count rate, counts/s
μ	attenuation coefficient of granule, cm^{-1}

Subscripts

crit	critical
g	granule
max	maximum
w	wall
0	incident

6.8 References

[1] Ouyang, F., Levenspiel, O. Spiral distributor for fluidized beds. Industrial and Engineering Chemistry Process Design and Development 1985, 25, 504-507.

[2] Chyang, C.-S., Lin, Y.-C. A study in the swirling fluidization pattern. Journal of Chemical Engineering of Japan 2002, 35(6), 503-512.

[3] Yang, H.Y., Lee, D.H., Han, G.Y. Pressure fluctuation characteristics of polyethylene particles in a gas-solid fluidized bed with different distributors. Korean Journal of Chemical Engineering 2002, 19(6), 1112-1116.

[4] Kantzas, A., Kalogerakis, N. Monitoring the fluidization characteristics of polyolefin resins using x-ray computer assisted tomography scanning. Chemical Engineering Science 1996, 51, 1979-1990.

[5] Wright, I., Hamilton, K., Kruychkov, S., Chen, J., Li, F., Kantzas, A. On the measurement of hydrodynamic properties of an air-polyethylene fluidized bed system. Chemical Engineering Science 2001, 56, 4085-4097.

[6] Wu, B., Yu, G., Bellehumeur, C., Kantzas, A. Dynamic flow behaviour measurements in a gas-solid fluidized beds using different non-intrusive techniques and polyethylene powder. Flow Measurement and Instrumentation 2007, 18, 197-203.

[7] Kumar, S. B., Moslemian, D., Duduković, M.P. A γ-ray tomographic scanner for imaging voidage distribution in two-phase flow systems. Flow Measurement and Instrumentation 1995, 6, 61-73.

[8] Limtrakul, S., Chen, J., Ramachandran, P.A., Duduković, M.P. Solids motion and holdup profiles in liquid fluidized beds. Chemical Engineering Science 2005, 60, 1889-1900.

[9] Mudde, R.F., Bruneau, P.R.P., van der Hagen, T.H.J.J. Time-resolved γ-densitometry imaging within fluidized beds. Industrial and Engineering Chemistry Research 2005, 44, 6181-6187.

[10] Chaplin, G., Pugsley, T., van der Lee, L., Kantzas, A., Winters, C. The dynamic calibration of an electrical capacitance tomography sensor applied to the fluidized bed drying of pharmaceutical granule. Measurement Science and Technology 2005, 16, 1281-1290.

[11] Pugsley, T., Chaplin, G., Khanna, P. Application of advanced techniques to conical lab-scale fluidized bed dryers containing pharmaceutical granule. Transactions of the Institute of Chemical Engineers, Food and Bioproducts Processing 2007, 85(C3), 273 – 283.

[12] Wormsbecker, M., Pugsley, T. The influence of moisture on the fluidization behaviour of porous pharmaceutical granule. Accepted to Chemical Engineering Science 2008. (Chapter 2)

[13] Dry, R.J., Judd, M.R., Shingles, T. Two-phase theory and fine powders. Powder Technology 1983, 34, 213-223.

[14] Wormsbecker, M., Pugsley, T. Interpretation of the hydrodynamic behaviour in a conical fluidized bed dryer. Submitted to Chemical Engineering Science, February 2008, Ref No. CES-D-08-00186. (Chapter 3)

[15] Wiens, J., Pugsley, T. Tomographic imaging of a conical fluidized bed of dry pharmaceutical granule. Powder Technology 2006, 169, 49-59.

[16] Werther, J., Molerus, O. The local structure of gas fluidized beds – II. The spatial distribution of bubbles. International Journal of Multiphase Flow 1973, 1, 123-128.

[17] Enwald, H., Almstedt, A.E. Fluid dynamics of a pressurized fluidized bed: comparison between numerical solutions from two-fluid models and experimental results. Chemical Engineering Science 1999, 54, 329-342.

[18] McKeen, T., Pugsley, T. Simulation and experimental validation of a freely bubbling bed of FCC catalyst. Powder Technology 2003, 129, 139-152.

[19] Makkawi Y.T., Wright, P.C. Electrical capacitance tomography for conventional fluidized bed measurements – remarks on the measuring technique. Powder Technology 2004, 148, 142-157.

[20] Chaplin, G, Pugsley, T., Winters, C. Application of chaos analysis to pressure fluctuation data from a fluidized bed dryer containing pharmaceutical granule. Powder Technology 2004, 142, 110-120.

[21] Chaplin, G., Pugsley, T., Winters, C. The s-statistic as an early warning of entrainment in a fluidized bed dryer containing pharmaceutical granule. Powder Technology 2005, 149, 148-156.

[22] Geldart, D., Baeyens, J. The design of distributors for gas-fluidized beds. Powder Technology 1985, 42, 67-78.

[23] Mudde, R., Alles, J., van der Hagen, T.H.J.J. Feasibility study of a time-resolving x-ray tomographic system. Measurement Science and Technology 2008, 19, 085501, 14 pg.

Table 6.1: X-ray source specifications

X-ray tube	
Manufacturer	Philips
Type	SRO 25 50 – ROT 350
Peak Voltage	150 kV
Anode material	Rhenium alloyed tungsten molybdenum
Anode angle	15˚
Anode diameter	90 mm
Inherent filtering	2.5 mm Al/90kV

Tube collimator	
Type	9804 602 615 01 XD

X-ray generator	
Type	Super 100 CP
Ripple	12-pulse equivalent

Table 6.2: Detector specifications

Scintillation crystal	
Type	V10 C10 $CdWO_4$
Dimension	10 mm x 10 mm x 10 mm
Housing	Aluminium
Decay time	14 μs
Emission maximum	475 nm
Scintillation yield	12 – 15 photons/keV

Photodiode	
Manufacturer	Hamamatsu
Type	S 1337 – 1010BR
Sensor dimension	16.5 mm x 16.5 mm
Active dimension	10 mm x 10 mm

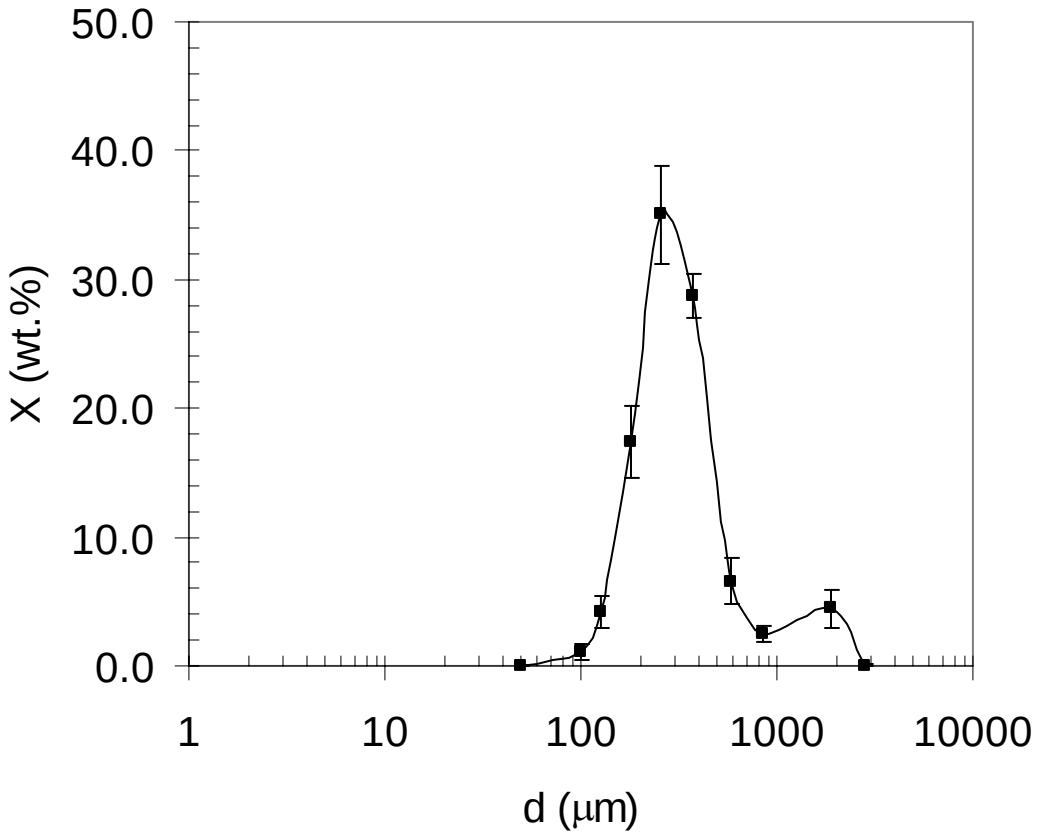

Figure 6.1: Particle size distribution of dried placebo pharmaceutical granule. Error bars represent ± 2σ of the mean values.

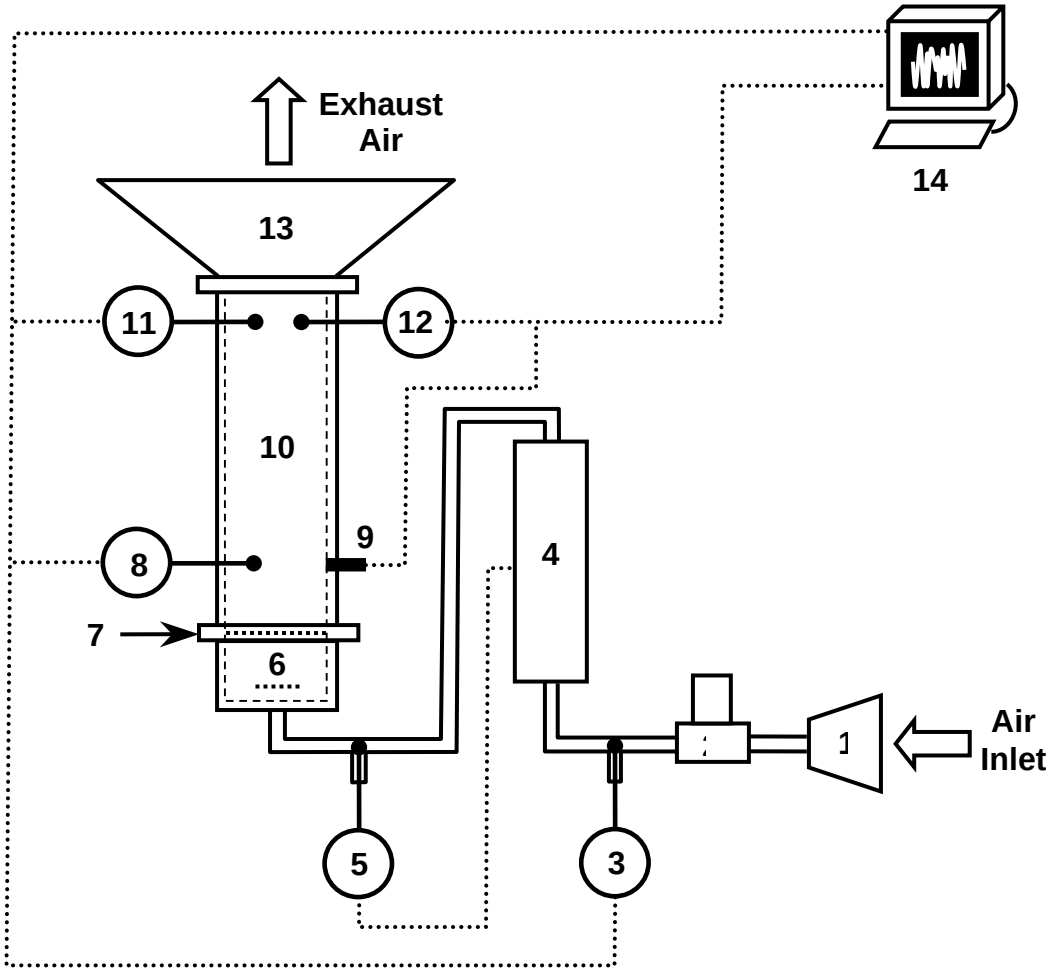

Figure 6.2: Schematic of the cylindrical fluidized bed dryer (not to scale): (1) compressor, (2) mass flow controller, (3) inlet humidity sensor, (4) heater, (5) inlet temperature thermocouple, (6) windbox with perforated deflection plate, (7) perforated plate distributor, (8) dense bed thermocouple, (9) pressure transducer, (10) product bowl/freeboard, (11) exhaust thermocouple, (12) exhaust humidity sensor, (13) disengagement section with cloth filter, (14) data acquisition computer.

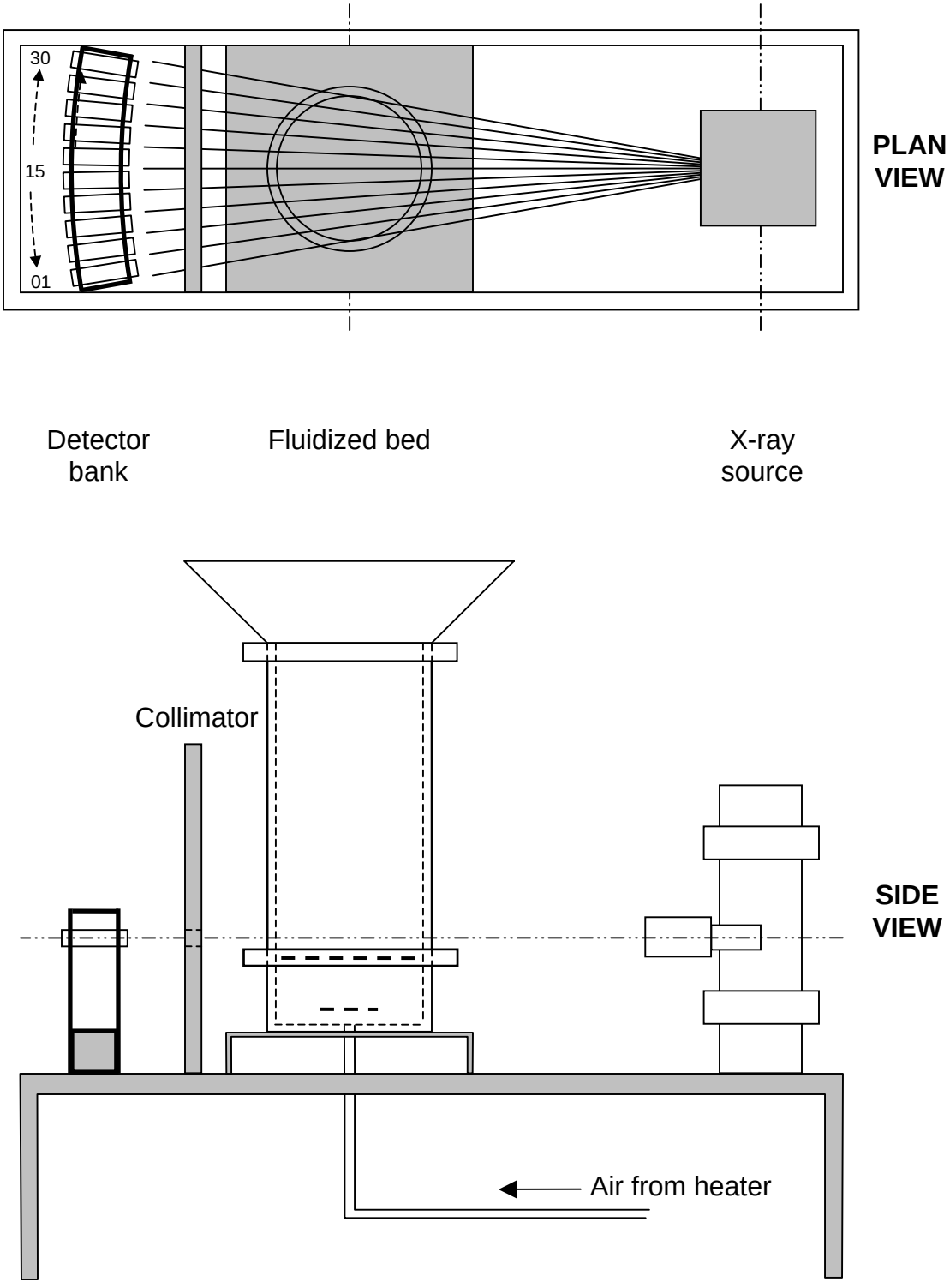

Figure 6.3: Schematic of the fluidized bed/x-ray densitometer assembly (modified after Mudde et al. [23]). Not to scale.

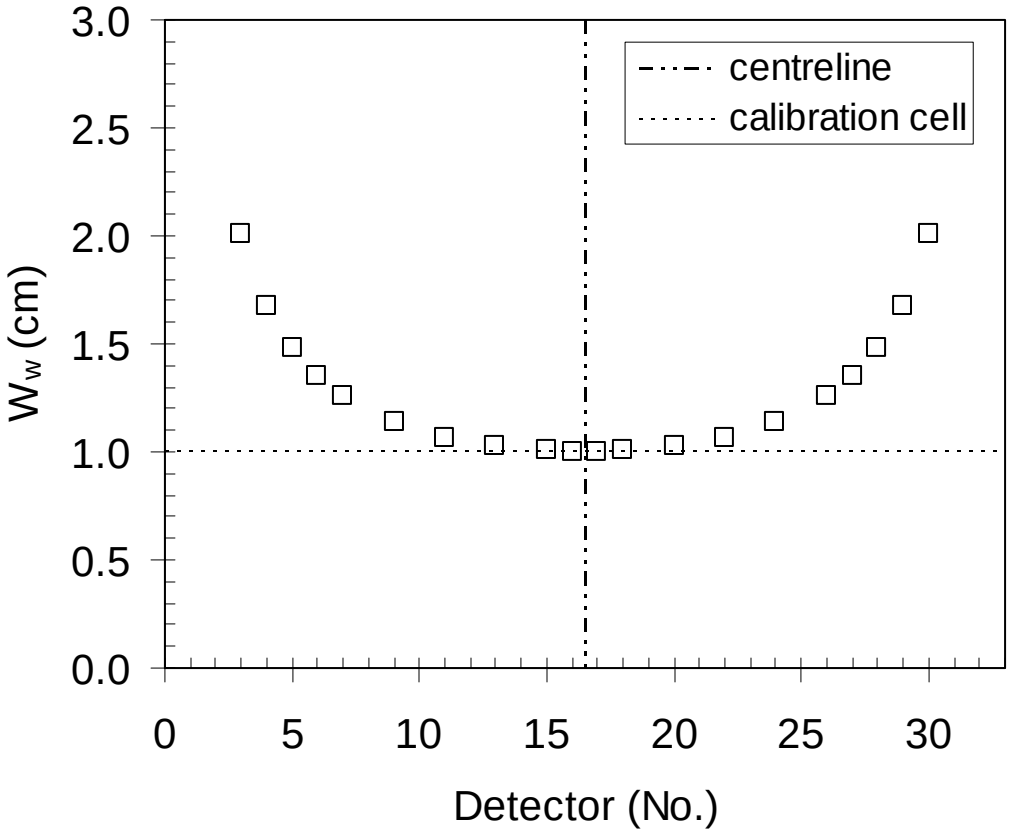

Figure 6.4: Calculated wall thickness along a given detector path. The single dashed line represents the calibration cell wall thickness.

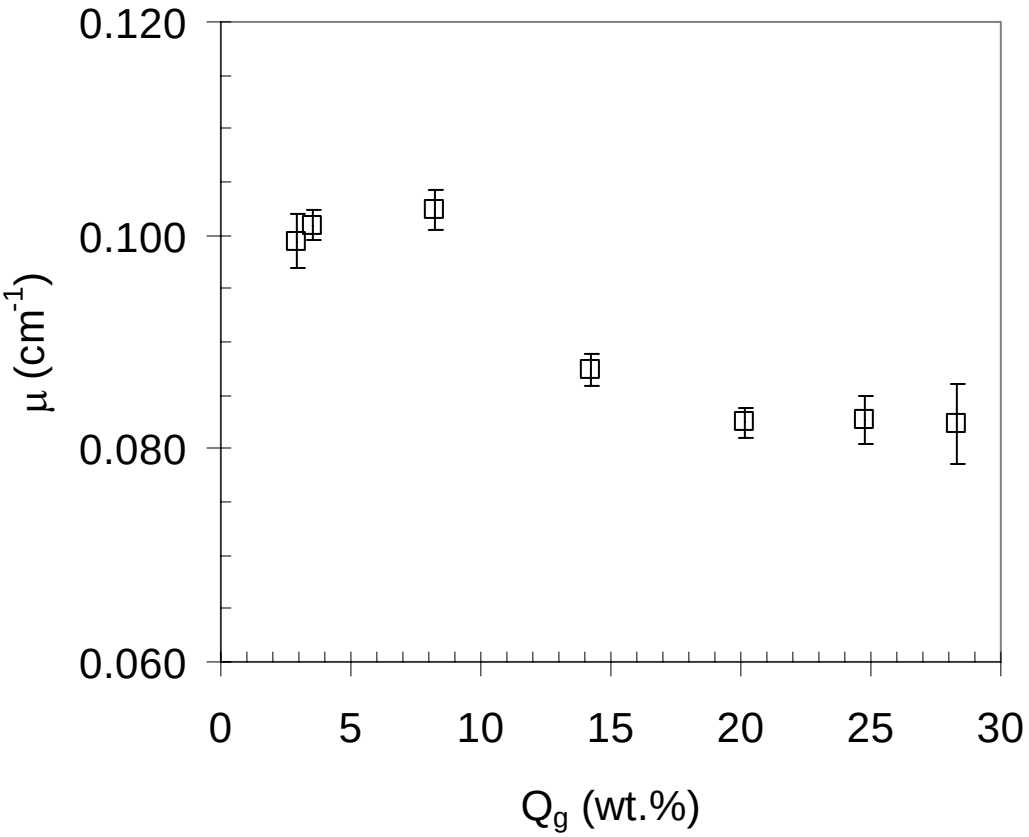

Figure 6.5: Average effective attenuation coefficient at various moisture contents.

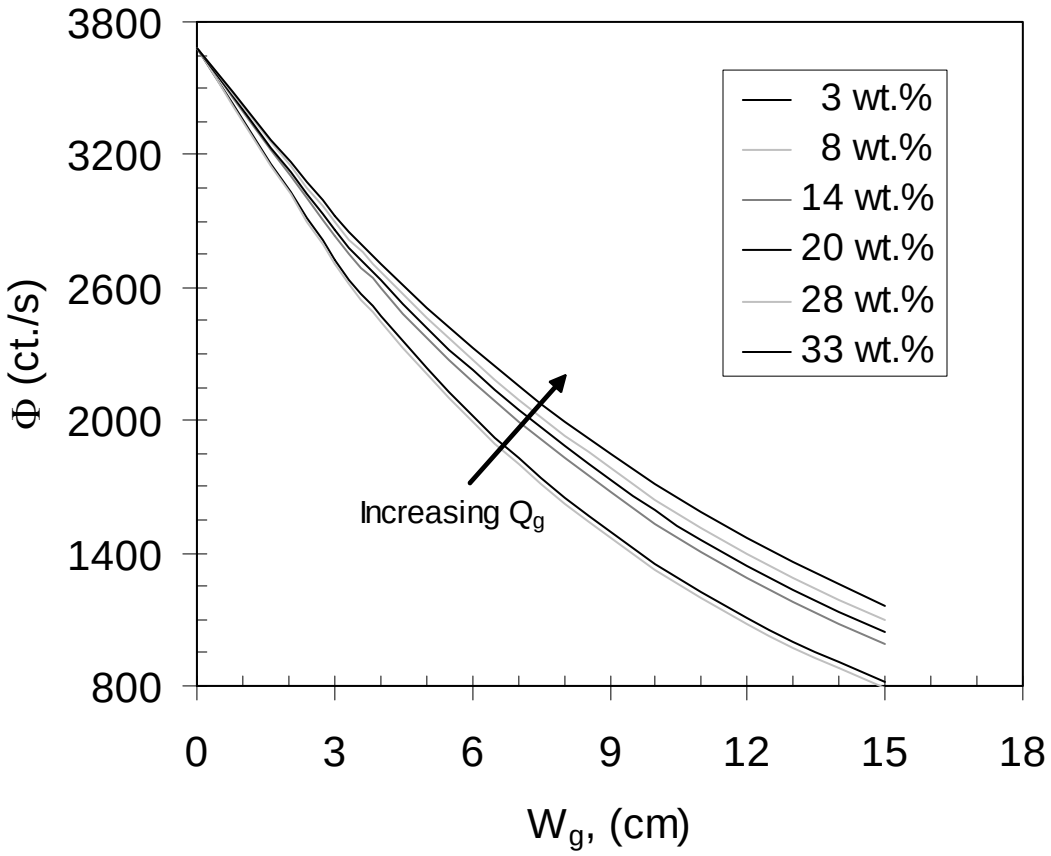

Figure 6.6: Sample calibration map for a single detector.

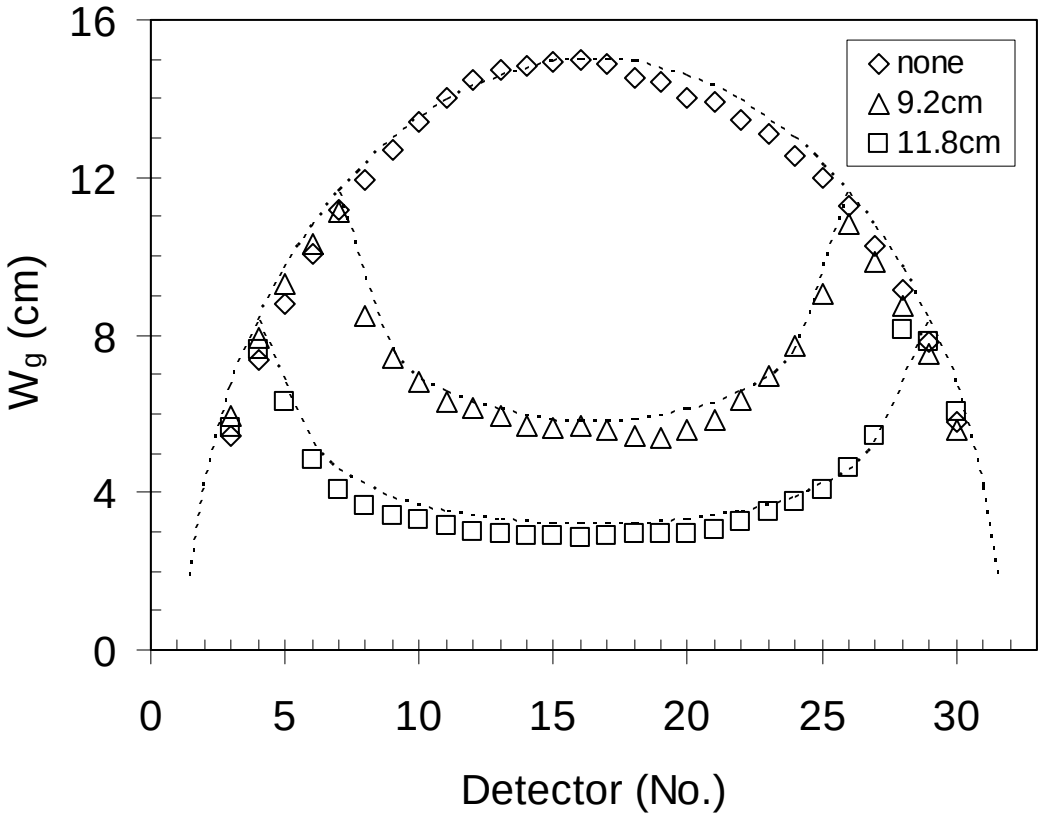

Figure 6.7: Measured solids along a chordal path length for packed bed and core-annulus phantoms. The dashed line represents the theoretically calculated chordal length of solids for each of the detector paths.

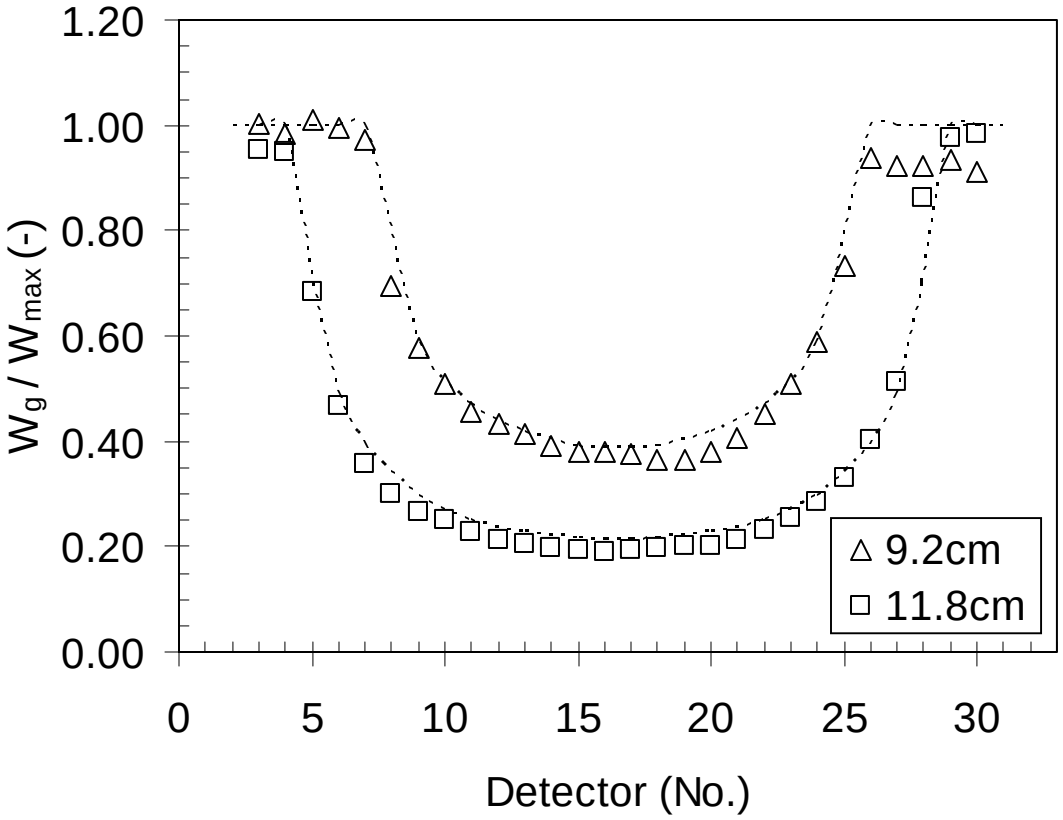

Figure 6.8: Solids concentration for the core-annulus phantoms. The dashed line represents the theoretically calculated solids concentration for each of the beam paths.

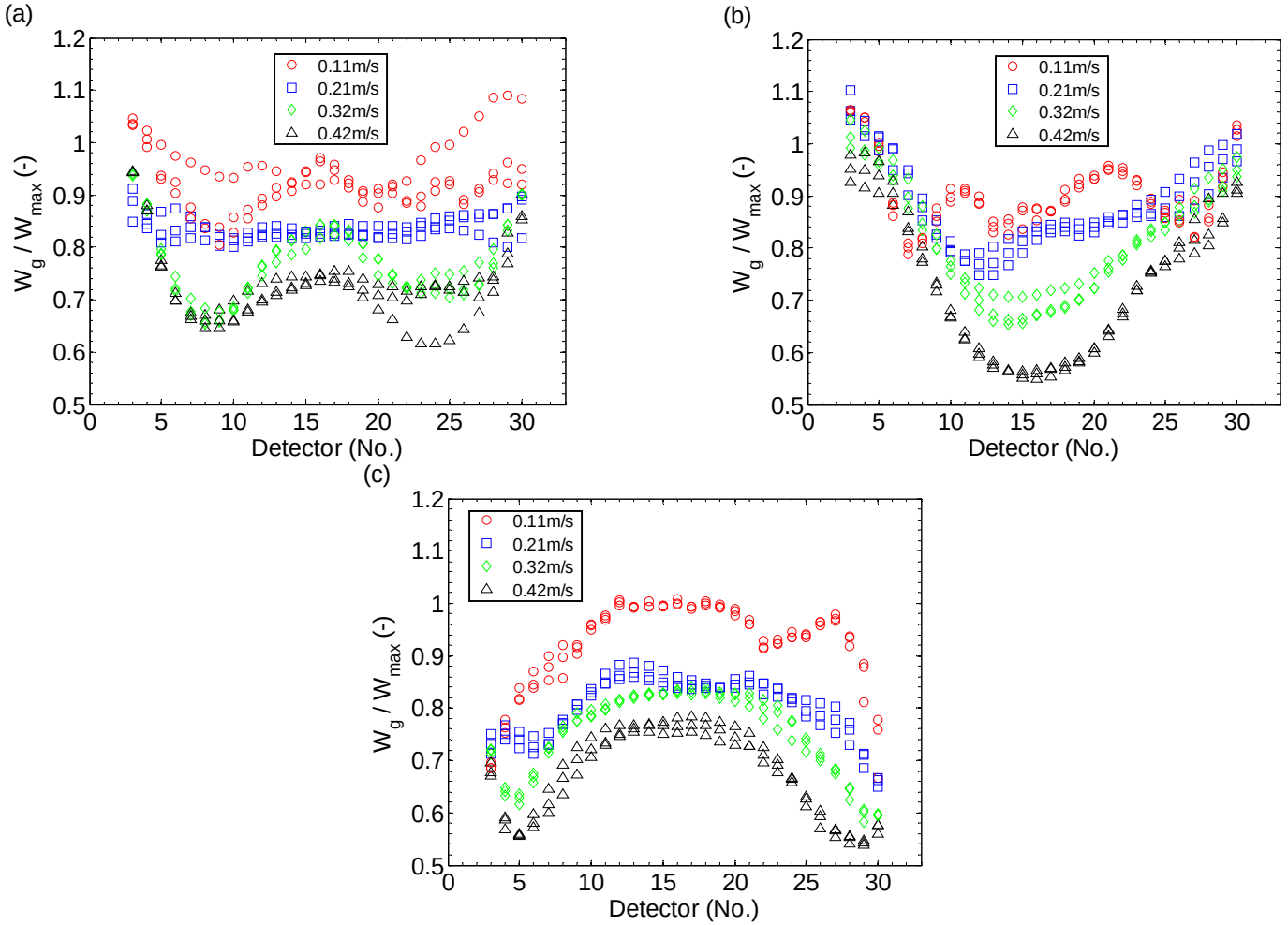

Figure 6.9: Average solids concentration profile for dry bed experiments with the (a) perforated plate, (b) punched plate, (c) porous plate.

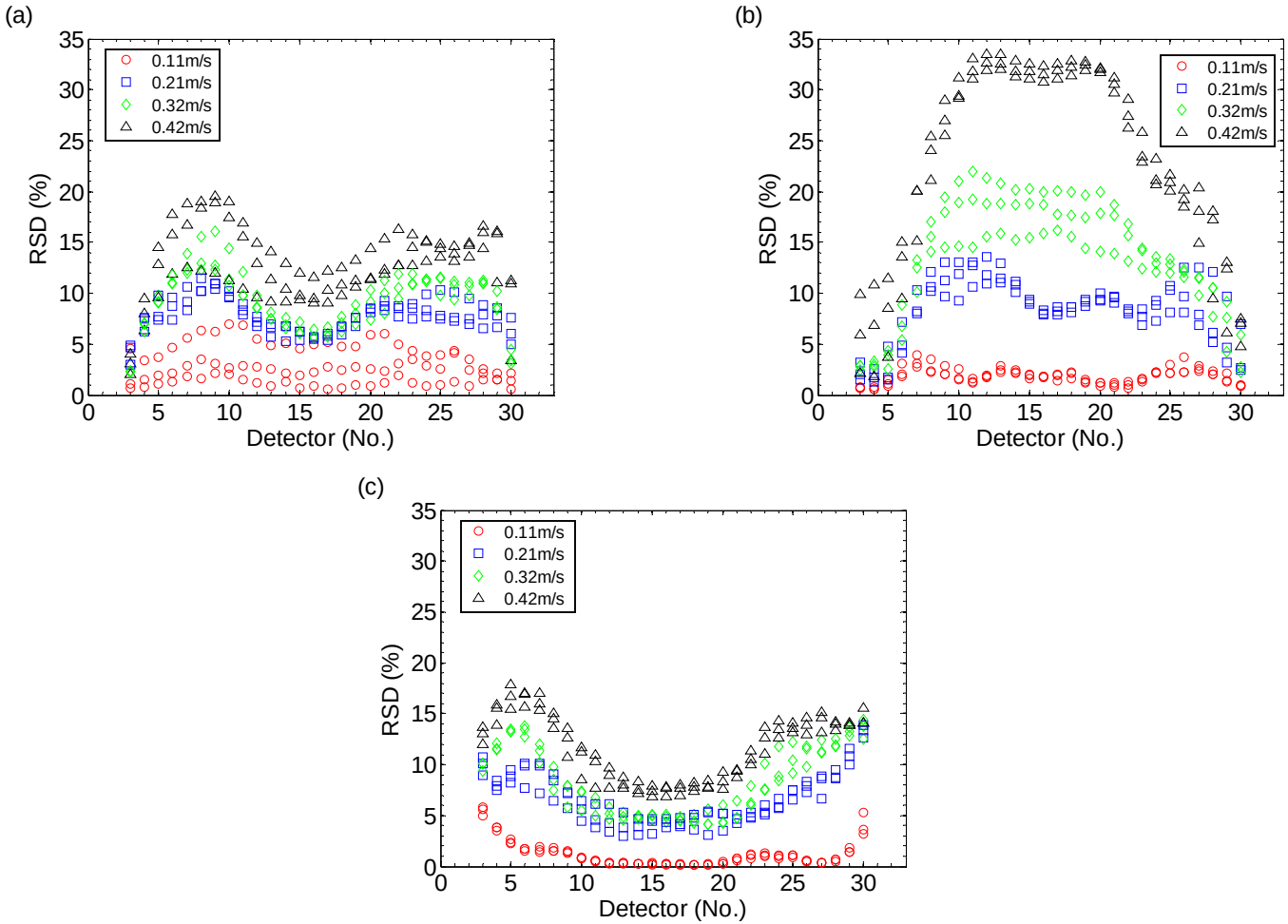

Figure 6.10: Relative standard deviation profile of the measured solids along a beam path for dry bed experiments with the (a) perforated plate, (b) punched plate, (c) porous plate.

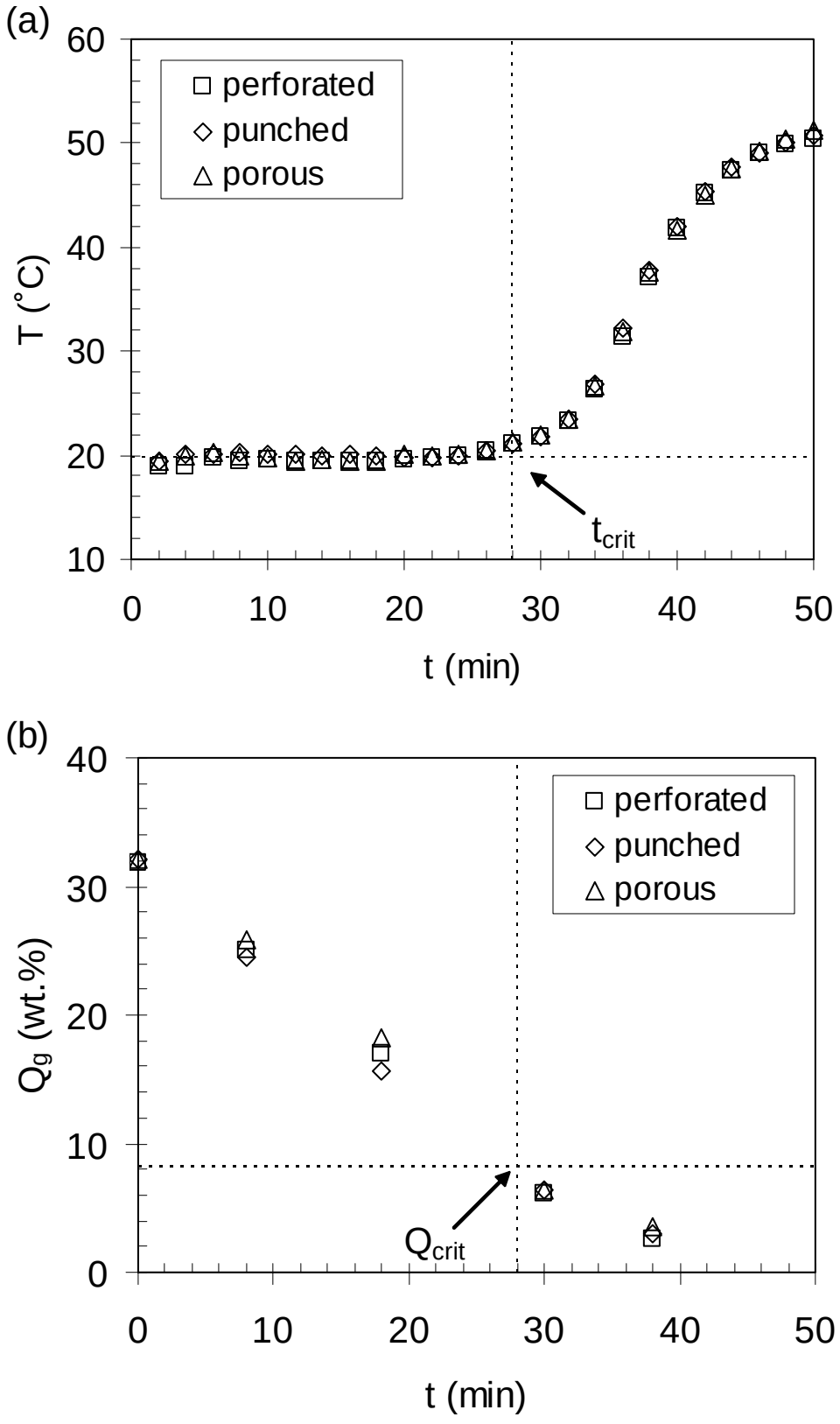

Figure 6.11: Average process data profiles from the drying experiments: (a) product temperature, (b) moisture content.

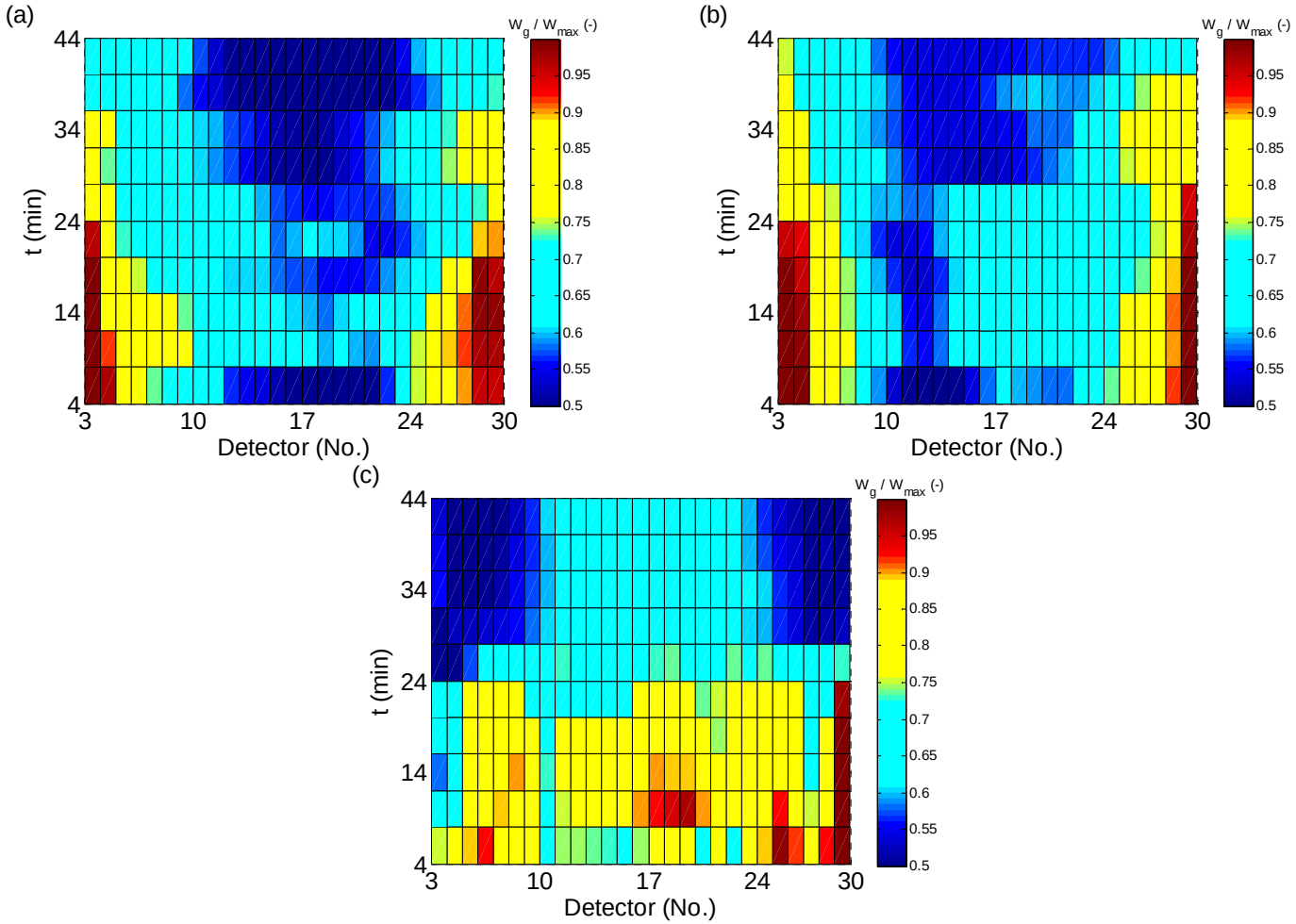

Figure 6.12: Topographic profile of the average solids concentration during drying with the (a) perforated plate, (b) punched plate, (c) porous plate.

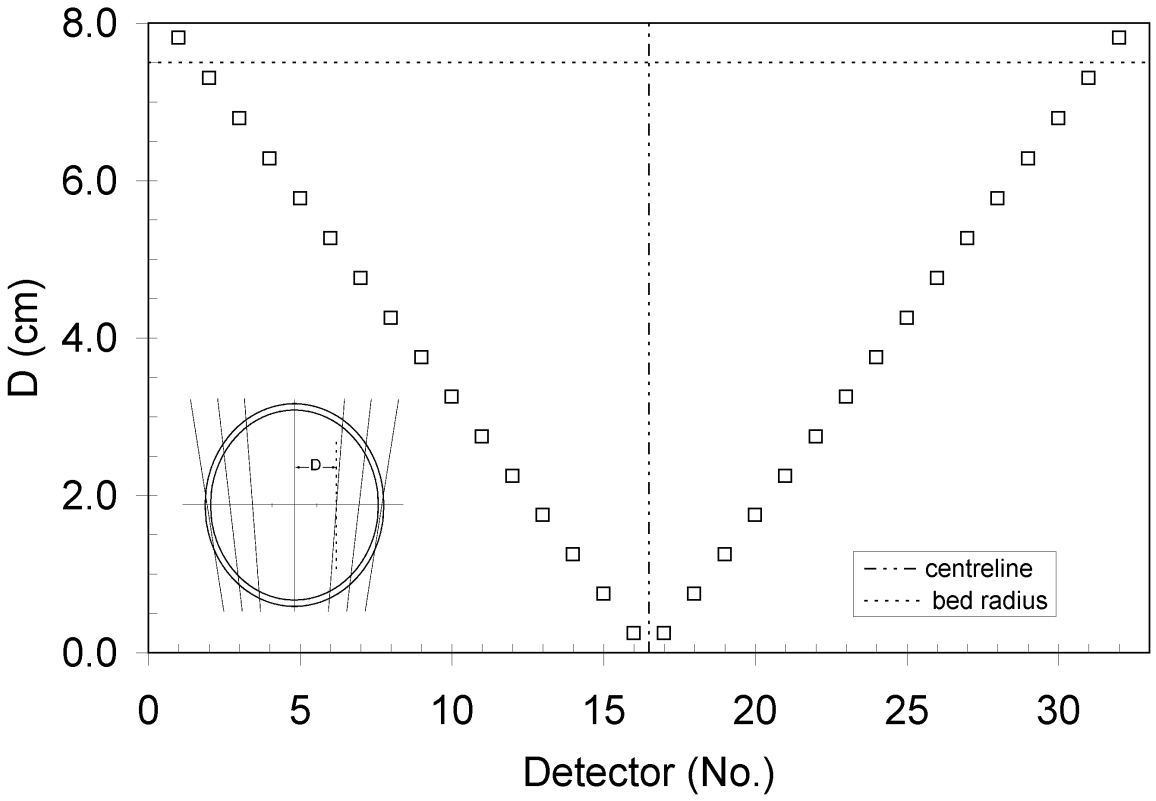

Figure 6.13: Average distance between the beam path and the centreline of the bed.

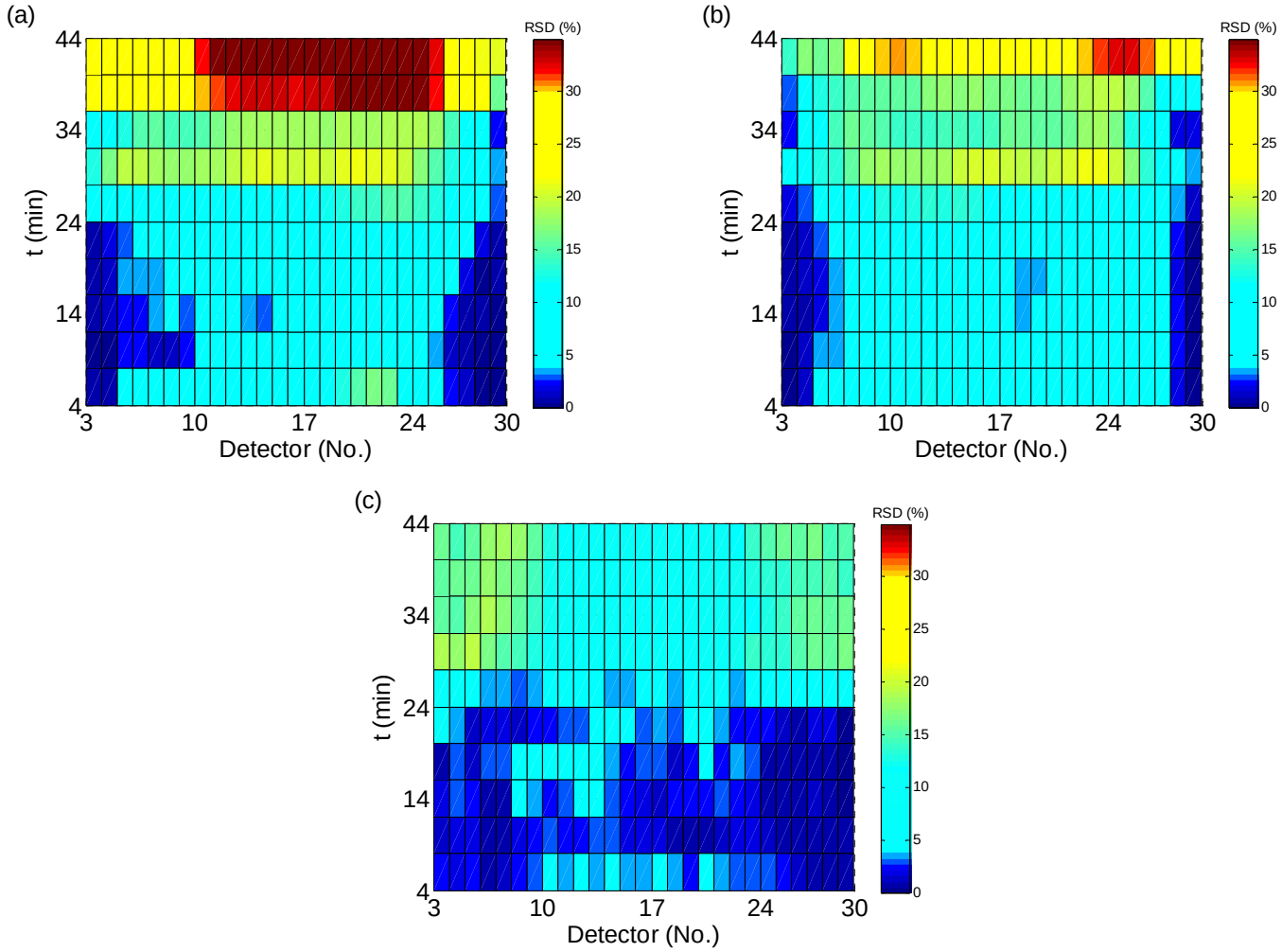

Figure 6.14: Topographic profile of the relative standard deviation profile of the measured solids along a beam path during drying with the (a) perforated plate, (b) punched plate, (c) porous plate.

CHAPTER 7 - The Influence of Vessel Geometry on Fluidized Bed Dryer Hydrodynamics

The contents of this chapter have been submitted for publication in the journal ***Powder Technology*** in a similar version to what appears in this chapter.

Citation

Wormsbecker, M., van Ommen, J.R., Nijenhuis, J., Tanfara, H., Pugsley, T. Influence of vessel geometry on fluidized bed dryer hydrodynamics. Submitted to Powder Technology in July 2008 (Ref No. POWTEC-D-08-00288).

Contribution of Ph.D. Candidate

The experiments presented in this paper were conducted by Michael Wormsbecker. The conical bed experiments were done at the facilities of Merck Frosst Canada Ltd. in Kirkland, QC, whereas the cylindrical bed experiments were done at Delft University of Technology in Delft, The Netherlands. The experiments were planned and performed by Michael Wormsbecker. Helen Tanfara and Todd Pugsley provided

consultation regarding the experimental program conducted at Merck Frosst. Ruud van Ommen and John Nijenhuis of Delft University of Technology did the same for those experiments done at Delft University of Technology. The software for all data collection and analysis was developed by Michael Wormsbecker. All of the writing of the submitted manuscript was done by Michael Wormsbecker with Todd Pugsley and Ruud van Ommen providing editorial guidance regarding the style and content of the paper.

Contribution of this Paper to the Overall Study

This paper addresses the influence of a major reactor design specification in fluidized bed dryers - vessel geometry. Most fluidized bed dryers employ a conical, or tapered, geometry. However, limited research is presented in the literature which quantifies the rationale behind this design feature. This paper employs drying of pharmaceutical granule in both vessel geometries with the purpose of quantifying the difference in hydrodynamics resulting from vessel geometry.

7.1 Abstract

Wet placebo pharmaceutical granule was dried in both conical and cylindrical laboratory scale fluidized bed dryers to determine the influence of vessel geometry on the hydrodynamic behaviour experienced during fluidized bed drying. Using pressure fluctuation analysis, it was shown that the bubbling phenomena hydrodynamics transitioned from 5.0 to 2.6 Hz in the conical bed whereas an increase in the bubbling

frequency phenomena from 3.9 to 4.7 Hz was experienced in the cylindrical bed. The lower bubbling frequency phenomena seen with the cylindrical bed in the beginning of drying is attributed to the formation of a defluidized bed periphery in the bottom region of the bed. This defluidization region formed due to the cohesive nature of the granule which constricted the bed inlet resulting in larger bubbles being formed in the bed. Once the granule fluidity became non-cohesive in nature due to drying, coalescence was experienced in the conical bed whereas the defluidized region in the cylindrical bed broke and higher bubbling frequency phenomena resulted.

7.2 Introduction

In the production of many solid-dose pharmaceutical products, drying of granule is a required manufacturing step. When wet, this granule tends to be cohesive in nature. It has a tendency to form large agglomerates and can even exhibit channelling under certain fluidization conditions [1]. With these Geldart C type properties, the wet granule can be difficult to fluidize under normal fluidization conditions. To improve the fluidity of cohesive powders, researchers have proposed several techniques including mechanical vibration [2-5,7], bed stirring [4,6,7] and gas pulsation [8,9]. However, the pharmaceutical industry does not employ any of these assisting techniques to aid their granule fluidity during drying. Rather, the industry attempts to rectify these fluidization phenomena using a conical, or tapered, bed geometry in their dryer design.

The notion of using a conical geometry for drying is believed to stem from the concept of the spouted bed. In the early 1950's, Gishler and Mathur [10] created the

cylindrical spouted bed as a means of drying wheat. To enhance solids motion and eliminate dead spaces in the bottom of these beds, a diverging cone base was used with the air fed to the system through the truncated apex of the cone [11]. In the following years, spout bed research progressed and purely conical spouted beds were developed [12]. Later, batch conical fluidized beds were proposed by Romankov [13] for spray drying applications.

The hydrodynamic behaviour associated with conical fluidized beds is a cross between conventional fluidization and spouted bed behaviour. Conical fluidized beds experience gross circulation of particles much like a spouted bed due to the geometry, but the intimate gas-solids contacting associated with conventional fluidization is still maintained. In order to generate these fluidization characteristics, certain operating conditions are required. Most importantly, distributor plates are used to distribute air across the fluidized bed inlet in conical fluidized beds, whereas an orifice is used at the base in spouted beds to initiate solids mixing. Also, conical fluidized beds are typically operated with conventional fluidized bed material such as Geldart A and B powders [14-19], whereas true spouted bed operation is generated with Geldart D powders [20-22]. Furthermore, conical fluidized beds are typically operated at relatively shallow static bed heights, H, as compared to their inlet diameter, D_i, such that $H/D_i \leq 1$. These conditions limit the potential for either slug or spout behaviour.

The earliest description of conical fluidized bed hydrodynamics was by Toyohara and Kawamura [14]. Their study introduced the notion of partially fluidized regimes

which exist between the fixed bed and 'perfect mixed-fluidization' regimes in gas-solid systems of binary mixtures. These regimes consist of a partially or completely fluidized core region and a downward moving non-core, or annular region. This distinct circulation pattern is a defining characteristic of conical fluidized beds which has been quantified by many researchers. Schaafsma et al. [15] used positron emission particle tracking (PEPT) to quantify this circulation pattern in a shallow bed of Geldart B powders. They found that the particles rose quickly through the fluidized core region of the bed and back downward through the slower moving annular region which fit the description of Toyohara and Kawamura [14]. This same type of circulation pattern has been reported by our group with pharmaceutical granule. Khanna et al. [16] also used a PEPT system to describe conical bed circulation patterns with a bed of dry pharmaceutical granule. More importantly however, our group has also demonstrated the circulation patterns generated during the drying of pharmaceutical granule. Transient electrical capacitance tomography (ECT) images from a conical fluidized bed dryer reported by Pugsley et al. [17] illustrate that the circulation pattern evolves from a dilute core, dense annulus regime to one where the centralized core region breaks down and a greater extent of the bed is involved in fluidization.

Apart from these circulation patterns, detailed information regarding the bubbling hydrodynamics in conical fluidized beds has also been proposed. Using electrical capacitance tomography (ECT), Wiens and Pugsley [18] studied the hydrodynamics of a conical fluidized bed of pharmaceutical granule over an inlet velocity range of 0.5 – 3.0 m/s. They found that the bubbling behaviour with this powder transitioned from spherical

bubbling to splitting bubbles at 2.5 m/s; indicating the onset of turbulent fluidization. The bubbling frequency associated with these regimes also decreased from approximately 10 Hz to a minimum of 4 Hz over the velocity range of 0.5 – 2.5 m/s. This decrease in frequency indicates bubble coalescence was also prevalent in their system at these velocities. Finally, the voidage distribution profiles for their mono-dispersed particle size distribution showed that the cross-sectional area of the fluidized core region of the bed increased with gas velocity as well. This same phenomenon was observed by Gernon et al. [19] who studied the fluidized core region in detail using 2-D tapered beds.

The majority of conical bed research documented in the literature has been studied with respect to non-cohesive powders. The most relevant work related to the benefits of the conical geometry operated with cohesive material was done by the group of Chaouki [23]. They improved the fluidity of NiO/Al_2O_3 cryogels, which are Geldart C powders, using a conical bed. Based on the description of the bed hydrodynamics provided in their study, these cryogels did not fluidize well in cylindrical beds. They used visual observations to compare the cylindrical bed hydrodynamics to that of a conical bed and concluded that the hydrodynamics improved significantly when the conical bed was employed.

While conical fluidized bed dryers have been used in the pharmaceutical industry for years, research related to the effect of the conical geometry versus that of a cylindrical bed on fluidized bed drying hydrodynamics has not been quantified in the literature. Furthermore, the impact of the geometry on the hydrodynamics, especially in a process

that has changing hydrodynamic conditions such as drying [1,17, 24], is unknown. The focus of this work is to investigate the impact of vessel geometry on the hydrodynamic behaviour during the drying of placebo pharmaceutical granule. More specifically, the hydrodynamics resulting from cylindrical and conical laboratory scale fluidized beds will be compared using pressure fluctuation analysis.

7.3 Material and Methods

7.3.1 Cylindrical Bed Apparatus

The placebo granule was comprised of the ingredients listed in Table 2.2 and was created with the low shear granulator described in Section 6.3.1 of this thesis. Sieve analysis was used to characterize the dried granule size distribution. The dry granule was found to have a bimodal size distribution with a mass mean diameter of 235 μm and a particle density of 830 kg/m^3. The frequency (φ) and cumulative (Φ) size distribution corresponding to the average particle size (d) for a specific size class of the granule is shown in Fig. 7.1.

The cylindrical fluidized bed used was that described in Section 6.3.2 of this thesis. The fluidized bed was equipped with a type 7261 piezoelectric pressure transducer manufactured by Kistler to measure the pressure fluctuations in the system. Swagelok^{TM}-connected to the sensor chamber was a 10-cm long probe with a 4-mm inside diameter. The probe was flush-mounted to the inner wall of the bed 5 cm above the distributor plate and purged with building air at 0.5 m/s to prevent plugging. This purge velocity was found to have no significant influence on the pressure signal recorded. Similar findings

have been demonstrated by Nijenhuis et al. [25]. The probe position in the bed corresponds to 19% of the initial static bed height and 33% of the final static bed height. These positions are in the range of the limits suggested by van Ommen [26] for monitoring pressure fluctuations. The data were collected with a DIFA data acquisition unit. In addition, granule samples of 5 – 10 g were collected during drying. This was done by removing the disengagement section of the bed during operation and manually taking a sample from the bed. Only one sample was taken as homogeneity of moisture in the system was assumed since the sample was collected from a well-mixed fluidized bed. The granule samples were analyzed for loss on drying using a tray dryer. The tray dryer was operated at 90˚C until the granule was dried and moisture removal was deemed negligible. Triplicate experiments were run to demonstrate reproducibility between drying experiments.

7.3.2 Conical Bed Apparatus

The conical bed studies used the granule formulation presented in Table 2.2. The granule was created using the high shear granulator described in Section 3.3.1 of this thesis.

The particle size distribution of the granule used with the conical bed apparatus has a bimodal distribution with a mass mean particle size diameter of 258 μm. Both this method of granule preparation, and that described in the previous section for the cylindrical bed have similar frequency and cumulative size distributions (see Fig. 7.1). The only difference seen between the granules produced is the percentage of large

granules formed. These large granules are a result of the granulators and their respective procedures. Fortunately, the difference in large granules makes up only a small portion of the overall granule mass and therefore should not influence the objectives of this study.

The conical fluidized bed used in this study, along with its associated measurement devices, has already been described in Section 3.3.2 of this thesis. Experiments were repeated twice to check the reproducibility between drying experiments.

7.3.3 Operating Conditions

An important aspect of this study was to decide on a basis for hydrodynamic comparison of the two fluidized beds of differing geometries. A summary of the important process variables chosen for consideration in this study is provided in Table 7.1. It is recognized that the basis of comparison used in this study is not necessarily the only means to compare vessel geometry, but rather an interpretation proposed by the authors'.

An elevated gas velocity (U_e) was required to maintain fluidity in the initial stages of drying with both geometries due to the excess moisture in the system. In the cylindrical bed, the elevated velocity was maintained for eight minutes whereas ten minutes was used in the conical bed. After this, the gas velocity was decreased to a lower steady-state velocity (U_{SS}) for the remainder of the experiment. This reduction in velocity was necessary because operation at the elevated gas velocity was too high for operation

in the latter stages of drying (owing to high entrainment rates). Furthermore, typical industrial practice for batch drying is to decrease the gas velocity periodically during the process. In the current work, a one-time step decrease was used instead to maintain a constant velocity throughout the majority of drying. This was done for the purpose of studying the hydrodynamics under steady-state conditions.

It is important to note the differences in the superficial gas velocities between the two apparatus. These velocities are based on the inlet diameters of the beds. This means the superficial gas velocity changes with axial position in the conical apparatus, whereas it is constant in the cylindrical one. These velocities were chosen based on visual observations of the fluidization behaviour while maintaining similar volumetric flows per unit mass of wet granule between geometries. By maintaining this proportionality during the drying process, the influence of drying rates (and subsequently the rate of change in moisture contents) attributed to the heat supplied by the gas flow rate will have a limited impact on the hydrodynamics. This is important because if drying rates are different, then any differences in the hydrodynamics associated with the vessel geometry may not be distinguishable from those caused by the differences in moisture content due to varying drying rates. The elevated volumetric flow rate (Q_e/m) for the cylindrical bed is 21% higher as compared to the conical bed, whereas its steady-state values (Q_{SS}/m) is only 9% higher. The larger differences in Q_e/m at elevated conditions are less significant as they last for only eight and ten minutes for the cylindrical and conical bed experiments (25% difference when compared to the conical bed), respectively. Regardless, hydrodynamic comparisons between geometries are not discussed in detail during this time period.

In order to achieve similar drying rates, a lower inlet air temperature (T_{IN}) was required in the cylindrical bed apparatus. This was done in order to better match drying potentials between the apparatus. Here, the drying potential is defined as the amount of moisture that the fluidization gas can evaporate per unit mass of dry air. In terms of psychrometry, this is the difference between the inlet and outlet mixing ratios (ΔMR) of air from the dryer. The reason for a lower inlet air temperature is that the air supplied to the cylindrical bed was freeze-dried, not drawn from the laboratory as was the case in the conical bed apparatus. With a substantially lower inlet humidity (RH_{IN}), the drying potential of the fluidization gas is much greater if the inlet temperature is not changed. By lowering the inlet air temperature, the drying potentials between apparatuses were more closely matched; therefore the granule should dry at similar rates since the Q_e/m proportionality was also maintained. This is proven by means of drying curves which are shown later in this chapter.

For the purpose of clarity, a schematic which illustrates how to obtain the drying potential from a psychrometric chart is shown in Fig. 7.2. Using the inlet air temperature and humidity to the fluidized bed, the mixing ratio (MR) of the inlet air is obtained. Next, by moving along the enthalpy of saturation line (denoted as h in Fig. 7.2) to the wet bulb temperature (T_{wb}) the maximum mixing ratio of the gas can be obtained. The difference between these mixing ratios (ΔMR) is the drying potential of the gas. In the initial stages of drying, the drying potential is achieved as the outlet air is saturated. However, as drying proceeds, the drying potential is no longer reached as the system becomes mass transfer limited. The idea behind using similar drying potentials is that by

having similar maximum values, it can be assumed the actual moisture content of the granule over the course of the entire drying process will also be similar. This is based on the assumption that the granule produced has similar internal mass transfer coefficients between apparatus.

Finally, 3.0 kg of wet bed mass (m) was dried in each conical bed drying experiment; whereas only 2.0 kg was used in the cylindrical bed. This bed mass is 50% greater than the cylindrical bed studies. The reason for this is to maintain the Q/m proportionality already discussed, but also to achieve similar initial ($H_{s,i}$) and final ($H_{s,f}$) static bed heights between the geometries. This criterion was deemed necessary for comparative analysis of the hydrodynamics of drying since significantly different bed heights may also affect the hydrodynamics between geometries. Namely, slugging may occur in the cylindrical bed if the same bed masses are used as the initial static bed height will increase to 39 cm (a 50% increase in bed height). Comparisons made in this study are targeted with respect to the bubbling hydrodynamic states that ensue from operation. Therefore, initiating a slugging regime is undesirable. It is important to note that the aspect ratios of static bed height to inlet diameter used in the present study are larger than the aspect ratios typical of conical beds. This was required to provide adequate pressure fluctuation sensor coverage in the conical bed apparatus when the material was dry.

7.3.4 Data Treatment

All data analysis was performed using in-house code developed for use with MATLAB® (see Appendix G). The pressure fluctuation data were collected at 400 Hz

and then bandpass filtered with a high pass filter of 1 Hz and low pass filter of 170 Hz. This was done to remove the influence of drift and other low frequency phenomena that do not represent the bubbling phenomena in the bed. It is important to note that the filter does not reduce the number of data points per unit time, but rather shapes the frequency content of the time series data based on the bandpass frequencies used in the filter. The standard deviation analysis of the data was calculated with this filtered data whereas the average cycle frequency (ACF) analysis was calculated using a 20 Hz re-sampled data set. The justification for using a re-sampled data set is that with filtered data, the higher frequency components contribute additional fluctuations in the data that are not representative of low frequency bed behaviour itself. By resampling the data at a frequency that is still sufficiently high, hydrodynamic information captured by ACF analysis is more accurately identified. Time segments of 4 minutes were used in the data analysis. This was chosen to optimize time resolution, yet provide enough data for the various analysis methods used in this study.

The power spectra of the filtered pressure time-series data was estimated using the *psd* function in MATLAB®. This function transforms the time series data into the frequency domain using Welch's averaged periodogram method for the spectral estimate. The estimation of the power spectra involves a tradeoff between frequency resolution and noise sensitivity. The number of fast Fourier transform points (NFFT) determines the frequency resolution of a spectrum based on the sample frequency whereas the segment length of the window influences the noise associated with the spectral estimation. The parameters used in the calculation of the spectra are displayed in Table 7.2. The resulting

resolution in the frequency data is 0.20 Hz. The degree of noise deemed acceptable was determined through a sensitivity analysis using various window sizes. A window segment length of 1024 points resulted in the best representation of the spectra with this frequency resolution. A smaller segment length resulted in a significant degree of smoothing of the spectra whereas larger windows produced significant noise which over-complicated the numerical representation of the frequency data. No data overlap was used in estimating the spectra. For further information on the calculation of power spectra, refer to MATLAB® [27].

7.4 Results

7.4.1 Visual Observations

Visual observations are simple, yet effective, means of assessing the qualitative state of fluidized beds. Typically, these observations identify gross behaviour, thus do not provide much detail in the overall comparison of different hydrodynamic states. Regardless, the observations made in this study suggest that the cylindrical geometry results in the occurrence of undesirable fluidization phenomena which were not observed with the conical geometry.

Although particle circulation during the early stages of drying was achieved in the cylindrical bed, a significant degree of defluidization and channelling existed around the bed periphery. Stagnant material at the wall extended upwards as much as 10 cm above the distributor plate. Above this stagnant material, downward circulation of the granule was observed at the wall. Localized channelling was also observed through the

defluidized region of the cylindrical bed. These channels existed due to the formation of large agglomerates at the base of the bed which could not be fluidized. The agglomerates, which are formed because of the cohesive nature of the wet material, reached sizes greater than 1cm in diameter. Manual pulsing of the gas velocity during start-up did not prove beneficial as these stagnant regions and large agglomerates re-formed upon return to normal operating velocities. Apart from these undesirable phenomena, the observed bubbling in the first eight minutes of drying (during which time the gas velocity was 0.64 m/s – see Table 7.1) suggests that large voids moved through the bed. No bubbling was observed at the bed wall and only single eruptions appeared at the bed surface. The only distinguishable observation was the periodic formation of approximately 1 to 2-cm high voids which occupied a majority of the bed cross-section in the upper portion of the dense bed phase. A schematic resembling these voids is presented in Fig. 7.3. These voids would quickly collapse once a portion of the void reached the bed surface. This may suggest the onset of slugging behaviour under the operating conditions used in this study.

After reduction of the gas velocity to 0.43 m/s (U_{SS} in Table 7.1), the bubbling hydrodynamics appeared to be similar to the state described above. The only difference was that the fluidization was more uniform with slower moving bubbles erupting at the bed surface. This change in fluidity is a direct result of the decrease in the superficial gas velocity. Unfortunately, the defluidization, channelling and segregation of large agglomerates still existed. As drying proceeded, the fluidized state became more aggressive. The downward circulation of material at the vessel wall changed from a

stepwise pattern to a virtually continuous one. With this change in fluidization behaviour, the defluidized periphery that was predominant throughout the drying process also began to break up. At 50 ± 2 minutes, the defluidized region broke and subsequently became engulfed by the bed in each of the experiments. After this point, fluidization became uniform across the bed and was much more aggressive. Multiple eruptions now occurred at the bed surface and voids also became visible at the bed wall. Although the channelling and defluidized regions were no longer present, segregation of granule greater than approximately 1-mm diameter still existed. The agglomerates of approximately 1 cm and greater in diameter alluded to earlier in the drying process were not present in the dry granule after discharging it from the bed at the end of an experiment. This is likely because once partially dried, the agglomerates became friable and, like the defluidized region, broke up upon being engulfed in the fluidized region of the bed.

The extent of channelling and defluidization seen in the cylindrical bed was not observed when the conical bed was used. Initial operation of the conical fluidized bed at the elevated inlet velocity of 0.85 m/s created a hydrodynamic state where the bed was operating well into the bubbling regime and exhibited excellent particle circulation. No signs of defluidization or channelling at the bed wall were observed through the sight-glass. Upon reduction of the fluidization velocity to 0.64 m/s, the particle circulation slowed and the bubbling was reduced to a state that was visually similar to that just in excess of minimum fluidization. The bubbling hydrodynamics appeared similar to the cylindrical bed after the reduction in gas velocity: more uniform with slower moving bubbles erupting at the surface. As the granule dried, the bubbling again became more

aggressive. Also, the particle circulation pattern at the wall transitioned from a downward moving, step-wise pattern to a continuous one. By the end of drying, a very aggressive bubbling fluidization state existed in which large voids erupted at the bed surface. Voids were also now observed in the dense bed through the sight-glass.

7.4.2 Drying Rates

In order to quantitatively assess any similarities or differences in the hydrodynamics associated with cylindrical and conical beds, similar drying rates are desired. This will allow for direct comparison of the pressure fluctuation data as the changes in the granule fluidization properties described in Chapter 2 of this thesis will occur at similar times. Based on the operating conditions for each apparatus described above, the granule was expected to dry at similar rates and therefore similar times.

To ensure the drying rates between experiments were similar, the granule moisture content (w_g) was measured and drying curves were constructed. As illustrated in Fig. 7.4, the drying curves are very similar between the sets of experiments. Based on these similarities, the drying times associated with each experiment are also expected to parallel one another. This is confirmed as the drying times, defined as the time in which it takes the bed temperature to reach 40˚C, were 90, 92 and 93 ± 2 minutes for the cylindrical bed and 89 and 94 ± 2 minutes for the conical bed.

7.4.3 Pressure Fluctuation Analysis

In order to quantify the differences in hydrodynamic behaviour between the cylindrical and conical geometries, more detail than that provided by visual observations is required. This can be achieved with the aid of pressure fluctuation measurements as they are a universally accepted means of identifying hydrodynamic behaviour in fluidized beds. A number of analysis techniques using the pressure fluctuation data were employed in the present study. These techniques include both time domain (standard deviation and average cycle frequency) and frequency domain (dominant frequency and power spectra) analyses.

7.4.4 Frequency Domain Analysis

Power Spectral Density (PSD)

Estimation of the power spectra over the course of drying provides the most descriptive information regarding the pressure fluctuation time series. PSD analysis yields information on the frequency components, along with their respective intensities, of the hydrodynamic state. The PSD frequency range studied in this work (1 – 10 Hz) represents the frequencies associated with bubbling in fluidized beds. Higher frequencies provide insight into other phenomena such as particle interactions and turbulence; which are not the focus of the present study.

Figs. 7.5 and 7.6 illustrate the average transient power spectra over the course of drying for the conical and cylindrical geometries, respectively. These spectra were

obtained by first calculating the power spectra for each of the four-minute time segments that make up a drying experiment. The spectra from individual experiments were then averaged together using the absolute time as the basis for comparison (e.g. the power spectra that represent the 0 – 4 minutes of drying were averaged together). Although this means that the average transient power spectra for the conical bed consists of averaging only two spectra, frequency domain analysis of the individual data sets illustrated insignificant differences. Also, data from the time domain analysis, which will be presented later in this article, demonstrate reproducibility between the two data sets.

Dissimilarities in the power spectra shown in Figs. 7.5 and 7.6 are apparent with respect to both power (ϕ) and frequency (f). In the initial stages of drying, the conical bed spectrum exhibits relatively low power, with the dominant frequency (frequency of greatest power) of 5.0 Hz. When the velocity is decreased after ten minutes, the power decreases further, but the frequency remains the same. As drying continues, the power of the peak frequency slowly increases up to the 48 minute mark of drying. At this point there is a shift in the bubbling frequency to 2.3 Hz. Wormsbecker and Pugsley [24] have linked this shift in frequency to the critical moisture content (Chapter 3 of this thesis); where the drying process results in the surface moisture no longer being continually maintained on the surface of the particles. This results in a change in bed hydrodynamics.

Accompanying this transition in drying hydrodynamics is a dramatic increase in the power and a broadening of the power spectra. In the beginning stages of drying, the spectra spans only 4 – 6 Hz, whereas after surpassing the critical moisture content it

spans 1 - 5 Hz. Beyond the critical moisture content, the power components of the spectra increase sharply while the bubbling related frequencies remain constant. By the 80 minute mark of drying, the power of the spectra plateau and remain virtually constant until the end of drying.

The cylindrical bed demonstrates much different behaviour (see Fig. 7.6). In the initial stages of drying, the cylindrical geometry produces power spectra with a dominant frequency component of 2.8 Hz. As with the conical geometry, the power of the dominant frequency increases as drying proceeds. However, as drying in the cylindrical bed reaches the critical moisture content, the dominant frequency shifts from approximately 2.8 to 4.7 Hz – an increase in the bubbling phenomena frequency. This is in contrast to the conical bed which exhibited a decrease in its bubbling phenomena frequency. The shift in the dominant frequency is also more gradual in the case of the cylindrical bed. Although not easily distinguishable through the topographic view of the transient power spectra shown in Fig. 7.6(b), the shift in frequency starts around the 52 minute mark of drying and ends by 64 minutes.

Along with the difference in the dominant frequencies, the power components of cylindrical bed power spectra do not exhibit a significant increase during the transition in the bubbling phenomena frequency. The frequency spectrum does however broaden, suggesting an increase in bubbling phenomena frequencies in the bed as well. Lastly, it is interesting to note that the power of the dominant frequency increases significantly at the 76 minute mark of drying. This increase occurs late in the drying process where the outlet

humidity is in the range of 20% RH. It is possible that the low humidity fluidization air creates electrostatic charging of the bed since the granule is dielectric. Many researchers have shown that relative humidities below 70% can create an electrostatically charged environment which significantly influences the hydrodynamic behaviour of fluidized beds [28, 29].

Dominant Frequency (*DF*)

To better illustrate the differences in the frequency component of the power spectra, the *DF*s of the two geometries were compared in a single graph. This analysis method represents the most predominant bubbling frequency in the fluidized beds therefore providing a more rudimentary analysis of the transient power spectra regarding the hydrodynamics. As shown in Fig. 7.7, there is a distinct change in *DF* at 48 and 52 minutes for the conical and cylindrical beds, respectively. As mentioned in the description of the PSD analysis, the directional changes in frequency are in contrast to one another.

7.4.5 Time Domain Analysis

Although describing the hydrodynamics of a fluidized bed using the power spectra of pressure fluctuation data is sufficient, the analysis is quite cumbersome and can be difficult to interpret. Therefore, independent analysis techniques that can corroborate the power spectra analysis are warranted. In this work, time series analysis techniques of average cycle frequency and standard deviation are presented.

Average Cycle Frequency (*ACF*)

Calculation of *ACF* can be used as a means to identify the frequencies associated with the bubble phenomena in a fluidized bed. Simply speaking, *ACF* is the number of cycles in the pressure fluctuation data per second. *ACF* is therefore calculated by identifying the number of crossings of the mean pressure data per unit time. As discussed previously, *ACF* should be calculated using re-sampled data. For the purposes of this study, the re-sample frequency was chosen to be 20 Hz since the major bubbling frequencies experienced in this study are below 10 Hz. This way, any higher frequency fluctuations such as those generated by localized turbulence phenomena or particle – particle interactions are not incorporated into *ACF*.

ACF profiles for each of the geometries are shown in Fig. 7.8. Similar to the dominant frequency, the *ACF* profiles between the conical and cylindrical bed contrast one another. In the case of the conical bed, the *ACF* identifies a more gradual transition in frequency around the critical moisture content as compared to its dominant frequency analysis. This is because *ACF* incorporates the less predominant low frequency in its calculation during the transition from high to low frequency. Therefore when the low frequency starts to grow in power, *ACF* starts to decrease. Only when the system has completely transitioned from high to low frequency does *ACF* equal the dominant frequency again.

Discrepancies between the *ACF* and *DF* analyses are also evident with the cylindrical bed. In this system, *ACF* is considerably higher for the first 80 minutes. This

is most easily demonstrated in the first 40 minutes of drying where *ACF* is 3.9 Hz whereas *DF* is 2.8 Hz. The difference between the *ACF* and *DF* values is because the frequency distribution over this time period is right-skewed – the right tail of the frequency distribution is longer. This skewness results in a higher calculated value for *ACF* compared to *DF*. The right-skewed distribution is real and therefore *ACF* is a better representation of the bubbling phenomena frequencies in the cylindrical bed. Similarity between the *ACF* and *DF* after 80 minutes is a result of a more Gaussian-type frequency distribution. The differing degrees of skewness during drying can be deduced from the transient power spectra for the cylindrical bed (see. Fig. 7.6).

Standard Deviation, (σ)

Calculation of the standard deviation of pressure fluctuations is another common form of time series analysis associated with pressure fluctuation data. Standard deviation can be used to provide a qualitative indicator of bubble size. Simply put, larger bubbles produce larger fluctuations in pressure [30]. Therefore, as bubbles grow the standard deviation should increase. This phenomenon is related to the bed mass that bubbles can displace as they pass through a fluidized bed. As mentioned in section 1.5 of this thesis, because the measurements in this study are global in nature, accurate representation of bubble sizes in the bed cannot be determined. In order to do this, the standard deviation of the incoherent spectra must be used instead [31].

Similar to *ACF*, the standard deviation profiles associated with conical and cylindrical bed drying illustrate differences in behaviour after the critical moisture

content is surpassed (see Fig. 7.9). The standard deviation profiles associated with the conical bed experience a marked increase just prior to the critical moisture content, whereas only marginal increases in the standard deviation profiles are experienced after the critical moisture content with the cylindrical geometry. Furthermore, the standard deviation profile associated with the cylindrical geometry reaches a maximum at 64 minutes which subsequently decreases from that point onward until drying is complete.

7.5 Discussion

The visual and experimental results presented above demonstrate that the hydrodynamics during drying are distinctively different between the conical and cylindrical bed geometries. Apart from the poor hydrodynamics in the cylindrical bed based on visual observations (i.e. defluidization, segregation and localized channelling), the bubbling phenomena frequency and standard deviation analyses suggest a hydrodynamic difference resulting from the bed geometry.

7.5.1 Bubbling Frequency

The defluidized bed periphery at the cylindrical bed inlet is believed to be the major contributor to the low bubbling phenomena frequency prior to the critical moisture content. The defluidized material constricts the bed inlet leading to, in effect, a conical entrance to the bed (see Fig. 7.10). The fluidization gas therefore has a smaller cross-sectional entrance and as a result forms larger bubbles at the inlet. Furthermore, the cross-sectional area of the cylindrical bed does not change with axial position. Therefore coalescence, and potentially slugging behaviour, is more likely as radial gas distribution

to a non-core region like that associated with the expanding cross-sectional area in the conical bed does not occur. Based on the bubble phenomena frequency alone, it is evident slugging does not occur in the early stages of drying in the cylindrical bed. Typically, slug frequencies are less than 2 Hz [32]; the average cycle frequency in the early stages of drying in the cylindrical bed is 3.9 Hz. However, this frequency is lower than the frequency after the critical moisture content which suggests the defluidized portion of the bed affects the hydrodynamics. A recent study published on pulse fluidized bed drying of the same pharmaceutical granule as that used in the present study supports this [9]. Pulsation of the fluidization gas improved the mixing in the bottom region of the cylindrical bed and also changed the hydrodynamics. Dominant frequency analysis of the pressure fluctuation data showed that the bubbling phenomena frequency in the constant rate period increased to approximately 5 Hz and then transitioned to 3 Hz after the critical moisture content was surpassed. This suggests the poor gas-solids contacting in the base of the cylindrical bed creates the change in the hydrodynamics.

The presence of the defluidized periphery is related to the cohesive nature of the wet granule. Research from our group has shown that pharmaceutical granule demonstrates poor flowability, especially at moisture contents above 20 wt.% moisture [1]. As a result, dead zones around the periphery of the bed naturally develop to create a more favourable geometry for the circulation of solids. As the granule dries to moisture contents below 20 wt.%, the excess gas in the system increases significantly due to the decrease in bed voidage [1]. This creates a much more aggressive fluidization state in the system which contributes to the break up of the defluidized periphery. Subsequently, the

previously blocked portion of the distributor plate is available for gas distribution and improved gas-solids contacting through the formation of smaller bubbles (see Fig. 7.10).

From the description of the cylindrical bed hydrodynamics above, the benefits of the conical bed are apparent. By employing a conical bed, the defluidization at the bed inlet can be avoided as the tapered wall provides the geometry required for the circulation of material. Furthermore, the conical bed geometry allows for a significantly higher inlet velocity as compared to the cylindrical bed when the volumetric flow per unit mass of granule dried is kept constant between the geometries. This higher velocity generates a distinct circulation of material that is analogous to a spouted bed. The difference is that in a conical fluidized bed the core region experiences bubbling-type hydrodynamics, but still maintains a downward circulating annular region similar to a spouted bed [14, 19].

An interpretation of the conical bed hydrodynamics prior to the critical moisture content is shown in Fig. 7.10. Initially, the cohesive nature of the granule creates a spout-like circulation pattern where the gas tends to travel up the middle of the bed and particles circulate down the walls. Again, a change in bubbling phenomena frequency occurs due to an increase in excess gas in the system. At this point, it is believed the extent of the dense annular region decreases significantly due to the increase in excess gas. This hypothesis is supported by the work of Gernon et al. [19]. They show that the fraction of the vessel cross-section occupied by the annular region decreases with increasing excess gas. With a larger fluidized core region and the decrease in bed height that accompanies drying, the excess gas results in a coalescence-dominated fluidization

regime. This type of regime has been reported to have relatively high power and low frequency spectra, which is demonstrated through the shift in the transient power spectra [33].

7.5.2 Standard Deviation

The standard deviation profiles prior to the critical moisture content are very similar for both geometries. After the reduction in gas velocities from U_e to U_{SS}, the standard deviation profiles are relatively low in value and then start to increase as the critical moisture content is approached. Like the *ACF* and *DF* analyses, the increase in standard deviation is also attributed to the decrease in bed voidage that is experienced at approximately 20 wt.% moisture. The increase in excess gas results in larger bubbles being formed in the bed. These bubbles have the ability to displace larger amounts of bed mass and therefore result in an increase in the standard deviation of the pressure fluctuations. The standard deviation profiles for both geometries continue to increase until approximately 64 minutes. At this point, the ACF and the transient power spectra indicate that the transition in the bubbling frequency is virtually complete.

It is interesting to note that the increase in standard deviation between 40 and 64 minutes, where the transition in the bubbling phenomena frequency occurs, is less distinct with the cylindrical bed. This minimal increase in standard deviation is due to competing effects of the increasing frequency and the increase in excess gas velocity on relative bubble size. Typically, an increase in excess gas velocity results in a bubble growth. The fact that *ACF* and *DF* analyses illustrate that there are more bubbles passing through the

bed, the change in relative bubble size must be small as the excess gas goes into the formation of additional bubbles rather than contributing solely to bubble growth. This small increase in bubble size will create an equally small increase in standard deviation. Conversely, the conical bed experiences a drastic increase in standard deviation. The increase in excess gas coupled with a decrease in bubble frequency will result in a significant increase in bubble size and therefore a large increase in standard deviation.

After 64 minutes, the cylindrical and conical bed standard deviation profiles diverge from one another. The standard deviation gradually increases until the granule is dry in the conical bed while it decreases in the cylindrical bed. It is believed that the decrease in standard deviation in the cylindrical bed is a result of elutriation of fines. Previous work by our group has shown that the S-statistic can identify hydrodynamic changes due to elutriation [34]. Although not presented by Chaplin et al. in their article, analysis of the pressure fluctuation data shows that the standard deviation begins to decrease just prior to the onset of elutriation. This is shown in Fig. 7.11. In the present work, the cylindrical bed experienced elutriation approximately 64 minutes into drying. This occurred because the entrained material adhered to the surface of the disengagement section. As a result, the fines were permanently removed from the bed. In the case of the conical bed, the tapered disengagement section along with mechanically shaken filter bags limited the effect of entrainment significantly.

The influence of filter bag shaking was tested by comparing pressure fluctuations collected from the conical bed with and without the use of the mechanical shaker on the

filter bag. The test used approximately 2.1 kg of dry granule; the resulting bed mass from drying 3.0 kg of wet granule. The standard deviation of the pressure fluctuations decreases from 367 ± 3 Pa to 348 ± 2 Pa when filter bag shaking was not used. Even though this decrease in standard deviation is small, it is the same magnitude of the decrease experienced during the drying tests with the cylindrical bed. This suggests that elutriation of fines may cause the decrease in the standard deviation after the transition in bubbling frequency is reached.

The reason for the increase in standard deviation with the conical bed is also not apparent. One would assume that only a very small change would occur since the granule moisture is low (less than 10 wt.%) and does not contribute to any drastic changes in granule properties below this value [1]. However, the standard deviation experiences an increase of nearly 30%. This measurable increase is attributed to the decrease in the relative humidity of the fluidization gas as the end of drying is approached. This hypothesis is derived from the work of Yao et al. [29]. Their work provides data that show the standard deviation in pressure fluctuations increase from approximately 32 to 51 Pa as the relative humidity drops from 70 – 10%. Although the extent of electrostatic charging in the present study is unknown, the fact that granule is dielectric material and reached relative humidities around 15% by the end of drying suggests that its influence could be significant.

7.6 Conclusions

The present study has illustrated differences in the hydrodynamics during drying between conical and cylindrical fluidized bed dryers. The major difference is seen in the bubbling dynamics where the conical bed transitions from high to low frequency in pressure fluctuations whereas the cylindrical bed experiences an increase in its bubbling phenomena frequency during drying. These differences are a result of the different particle circulations patterns both prior to and after the granule fluidization behaviour transitions from cohesive to non-cohesive behaviour. Furthermore, the study has shown that the tapered walls of the conical fluidized bed initiate superior particle circulation at the bed inlet while maintaining bubbling hydrodynamics in the core region of the bed. This is especially important in the initial stages of drying when the wet granule is cohesive and tends to take on a spout-like circulation pattern regardless of the vessel geometry.

The study also illustrates the problems associated with fluidization applications that employ cylindrical beds. Although the cylindrical geometry results in similar drying times and suitable bubbling hydrodynamics, it develops undesirable fluidization phenomena such as segregation, channelling and defluidization when the granule is wet. With respect to drying, this may result in variations in moisture content or temperature degradation of the material in the defluidized region due to poor mixing. This will have an adverse affect on the quality of the product and may lead to the rejection of entire batches of material.

7.7 Nomenclature

ACF	average cycle frequency, Hz
d	particle size, μm
DF	dominant frequency, Hz
f	frequency, Hz
h	enthalpy of saturation, J/kg dry air
H	static bed height, m
m	wet bed mass, kg
MR	mixing ratio, kg H_2O/kg dry air
Q	volumetric flow rate, m^3/s
t	time, min
T	temperature, ˚C
U	superficial gas velocity, m/s
w	weight percent, %
Δ	difference
ϕ	power spectral density, Pa^2/Hz
Φ	cumulative function, %
φ	probability function, %
σ	standard deviation, Pa

subscripts

db	dry bulb
e	elevated
f	final
g	granule
i	initial
IN	inlet condition
SS	steady-state
wb	wet bulb

7.8 References

[1] M. Wormsbecker, T. Pugsley, The influence of moisture on the fluidization behaviour of porous pharmaceutical granule. Chem. Eng. Sci. 63 (2008) 4063 - 4069. (Chapter 2)

[2] E.K. Levy, B. Celeste, Combined effect of mechanical and acoustical vibrations on fluidization of cohesive powders. Powder Technol. 163 (2006) 41 – 50.

[3] C. Xu, J. Zhu, Parametric study of fine particle fluidization under mechanical vibration. Powder Technol. 161 (2006) 135 -144.

[4] N.J.M. Kuipers, E.J. Stamhuis, A.C.M. Beenackers, Fluidization of potato starch in a stirred vibrating fluidized bed. Chem. Eng. Sci. 51 (1996) 2727-2732.

[5] K. Noda, Y. Mawatari, S. Uchida, Flow patterns of fine particles in a vibrated fluidized bed under atmospheric or reduced pressure. Powder Technol. 99 (1998) 11-14.

[6] M.C.B. Ambrosio, O.P. Taranto, The drying of solids in a modified fluidized bed. Braz. J. Chem. Eng. 19 (2002) 355-358.

[7] B. Caussat, Experimental study on fluidization of micronic powders. Powder Technol. 157 (2005) 114-120.

[8] G.G. Getz, H. Torab, Mixing characteristics of a pulse fluidized bed of fine powder. AIChE Symp. Ser. v 85 (1989) 468-474.

[9] A. Akhavan, J.R. van Ommen, J. Nijenhuis, X.S. Wang, M.-O. Coppens, M. Rhodes, Improved drying in a pulsation-assisted fluidized bed. Submitted to Ind. Eng. Chem. Res. (2008)

[10] P.E. Gishler, K.B. Mathur, Method of contacting solid particles with fluids. U.S. Patent No. 2,786,280 to Nat. Res. Council of Can., 1957 (filed 1954). Brit. Patent No. 801,315.

[11] K.B. Mathur, N. Epstein, Spouted Beds, Academic Press Inc., New York, 1974, pg. 2.

[12] P.G. Romankov, N.B. Rashkovskaya, Drying in a suspended state, 2nd Ed., Chem. Publ. House, Leningrad Branch, 1968.

[13] P.G. Romankov, Drying, in: J.F. Davidson, D. Harrison (Eds.), Fluidization, 1st Ed., Academic Press Inc., New York, 1971, 569 – 598.

[14] H. Toyohara, Y. Kawamura, Fluidization of a tapered fluidized-bed of a binary particle mixture. Int. Chem. Eng. 32(1) (1992) 164 – 171.

[15] S.H. Schaafsma, T. Marx, A.C. Hoffmann, Investigation of the particle flowpattern and segregation in tapered fluidized bed granulators. Chem. Eng. Sci. 61 (2006) 4467 – 4475.

[16] P. Khanna, T. Pugsley, H. Tanfara, H. Dumont, Radioactive particle tracking in a lab-scale conical fluidized bed dryer containing pharmaceutical granule. Can. J. Chem. Eng.

[17] T. Pugsley, G. Chaplin, P. Khanna, Application of advanced techniques to conical lab-scale fluidized bed dryers containing pharmaceutical granule. Trans. Inst. Chem. Eng, Food and Bioproducts Processing 85(C3) (2007) 273 – 283.

[18] J. Wiens, T. Pugsley, Tomographic imaging of a conical fluidized bed of dry pharmaceutical granule. Powder Technol. 169 (2006) 49 - 59.

[19] T.M. Gernon, M.A. Gilbertson, R.S.J. Sparks, M.Field, Tapered fluidized beds and the role of fluidization in mineral emplacement. in: X. Bi, F. Berutti, T. Pugsley (Eds.), Fluidization XII, ECI, Harrison Hot Springs, Canada, 2007, 545 - 552.

[20] A. Markowski, W. Kaminski, Hydrodynamic characteristics of jet-spouted beds. Can. J. Chem. Eng. 61 (1983) 377 – 381.

[21] M. Olazar, M.J. San José, A.T. Aguayo, J.M. Arandes, J. Bilbao, Stable operation conditions for gas-solid contact regimes in conical spouted beds. Ind. Eng. Chem. Res. 31 (1992) 1784 – 1792.

[22] S. Jing, Q. Hu, J. Wang, Y. Jin, Fluidization of coarse particles in gas-solid conical beds. Chem. Eng. Process 39 (2000) 379 – 387.

[23] R. Dieva Venkatesh, J. Chaouki, D. Kivana, Fluidization of cryogels in a conical column. Powder Technol. 89 (1996) 179 – 186.

[24] M. Wormsbecker, H. Tanfara and T. Pugsley, Interpretation of the hydrodynamic behaviour in a conical fluidized bed dryer. Submitted to Chem. Eng. Sci. (2008). (Chapter 3)

[25] J. Nijenhuis, R. Korbee, J. Lensselink, J.H.A. Kiel, J.R. van Ommen, A method for agglomeration detection and control in full-scale biomass fired fluidized beds, Chem. Eng. Sci. 62 (2007) 644-654.

[26] J.R. van Ommen, J. van der Schaaf, J.C. Schouten, B.G.M van Wachem, M.-O. Coppens, C.M. van den Bleek, Optimal placement of probes for dynamic pressure measurements in large-scale fluidized beds. Powder Technol. 139 (2004) 264-276.

[27] The Mathworks Inc., Signal Processing Toolbox, 2008. http://www.mathworks. com/access/helpdesk/help/toolbox/signal/ (accessed January 16, 2008).

[28] A. Wolny, W. Kazmierczak, The influence of static electrification on dynamics and rheology of fluidized bed. Chem. Eng. Sci. 48 (1993) 3529-2534.

[29] L. Yao, H.T. Bi, A-H Park, Characterization of electrostatic charges in freely bubbling fluidized beds with dielectric particles. J. Electrostatics 56 (2002) 183-197.

[30] J.R. Grace, G. Sun, Influence of particle size distribution on the performance of fluidized bed reactors. Can. J. Chem. Eng. 69 (1991) 1126-1134.

[31] J. van der Schaaf, J.C. Schouten, F. Johnsson, C.M. van den Bleek, Non-intrusive determination of bubble and slug length scales in fluidized beds by decomposition of the power spectral density of pressure time series. Int J Multiphase Flow 28 (2002) 865–880.

[32] J. Baeyens, D. Geldart, An investigation into slugging fluidized beds. Chem. Eng. Sci. 29 (1974) 255-265.

[33] F. Johnsson, R.C. Zijerveld, J.C. Schouten, C.M. van den Bleek, B. Leckner, Characterization of fluidization regimes by time-series analysis of pressure fluctuations, Int. J. Multiphase Flow 26 (2000) 663-715.

[34] G. Chaplin, T. Pugsley, C. Winters, The S-statistic as an early warning of entrainment in a fluidized bed dryer containing pharmaceutical granule. Powder Technol. 149 (2005) 148-156.

Table 7.1: Comparison of operating conditions apparatus

Parameter	Cylindrical Bed	Conical Bed
m (kg)	2.0	3.0
w_g (wt.%)	31.9 ± 0.1	31.6 ± 0.1
$H_{s,i}$ (m)	0.26 ± 0.01	0.25 ± 0.01
$H_{s,f}$ (m)	0.15 ± 0.01	0.15 ± 0.01
U_e (m/s)	0.64	0.85
U_{SS} (m/s)	0.43	0.64
Q_e/m (m^3s^{-1}/kg)	0.0057	0.0047
Q_{SS}/m (m^3s^{-1}/kg)	0.0038	0.0035
T_{IN} (˚C)	50 ± 1	65 ± 1
RH_{IN} (%)	7 ± 1	25 ± 2
ΔMR (kg H_20/kg air)	0.013	0.016

Table 7.2: Power spectral density parameters

Parameter	Value	Description
Sample frequency (Hz)	400	Data collection frequency.
Number of Fast Fourier Transforms (NFFT)	2048	Determines the frequency resolution of the spectral estimate.
Window Type (size)	Hamming (1024)	The number of samples (data points) used to calculate the frequency functions.

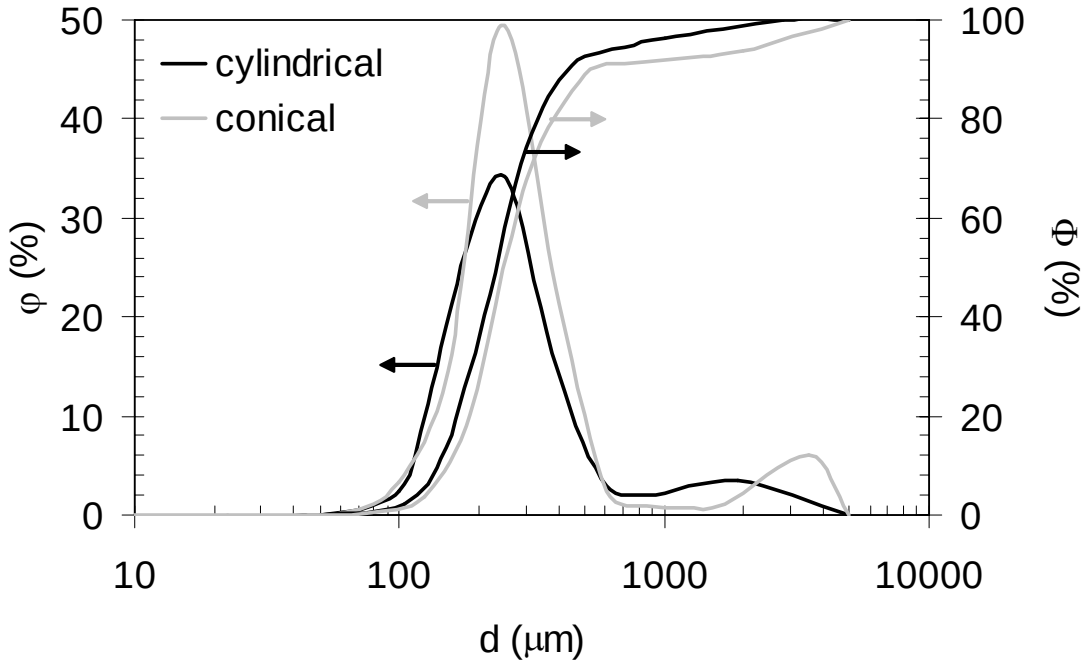

Figure 7.1: Particle size distributions of the granule made with the conical and cylindrical bed granulation procedures.

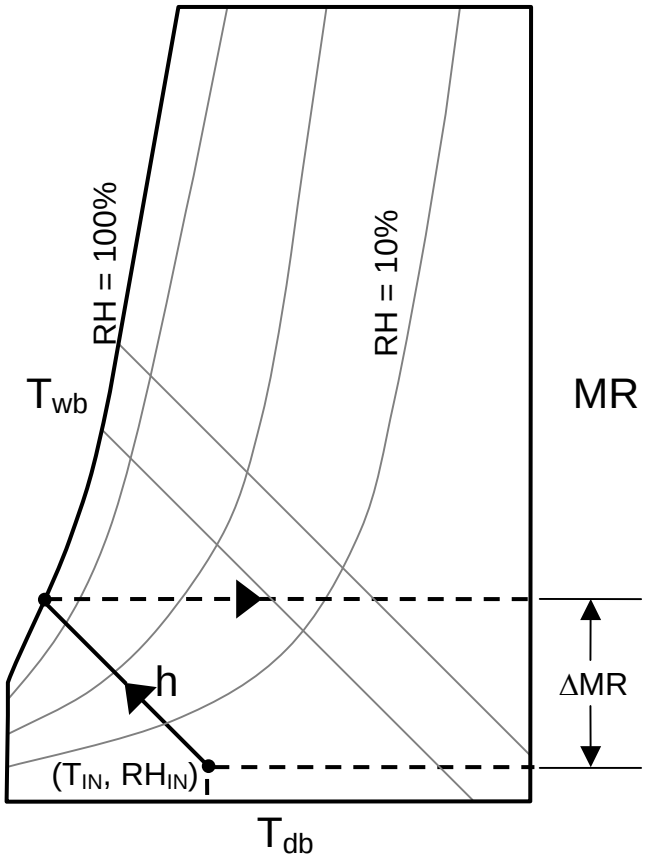

Figure 7.2: Schematic describing the drying potential of an air stream using psychrometry.

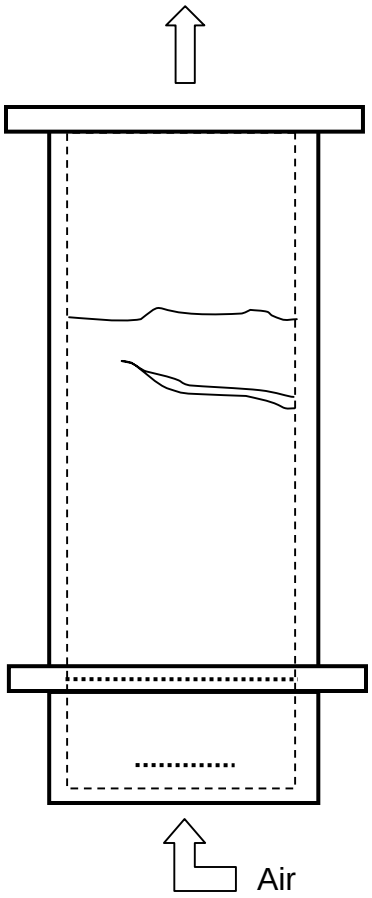

Figure 7.3: Schematic of periodic voids formed in the cylindrical bed during the early stages of drying. Based on visual observations.

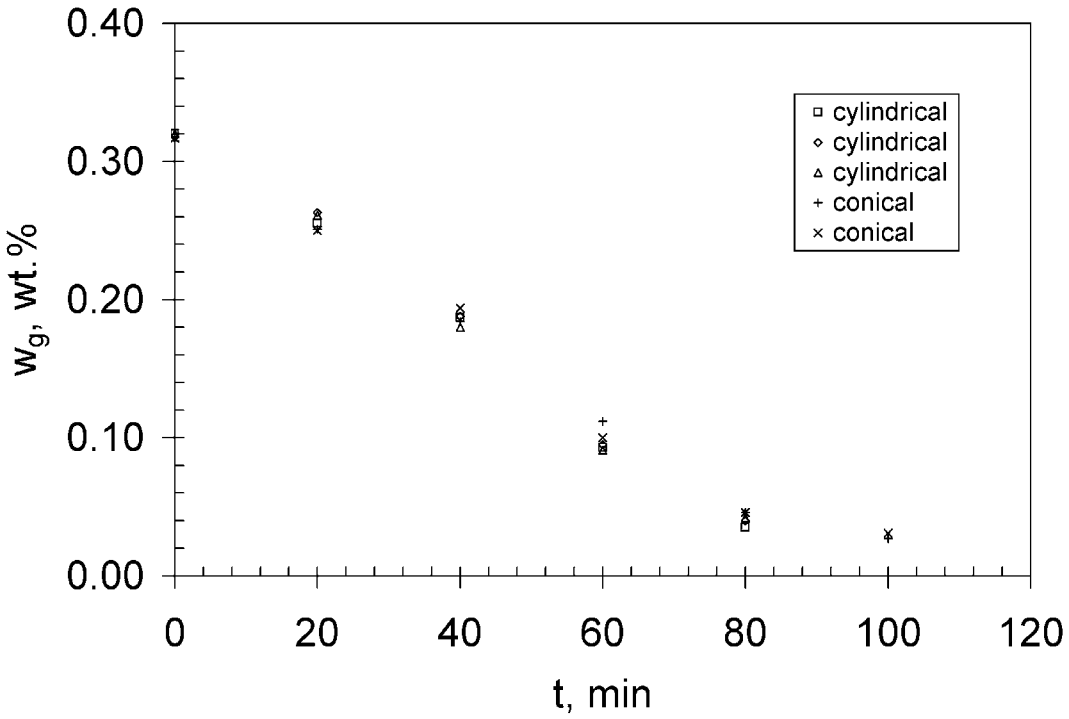

Figure 7.4: Drying curves for individual experiments.

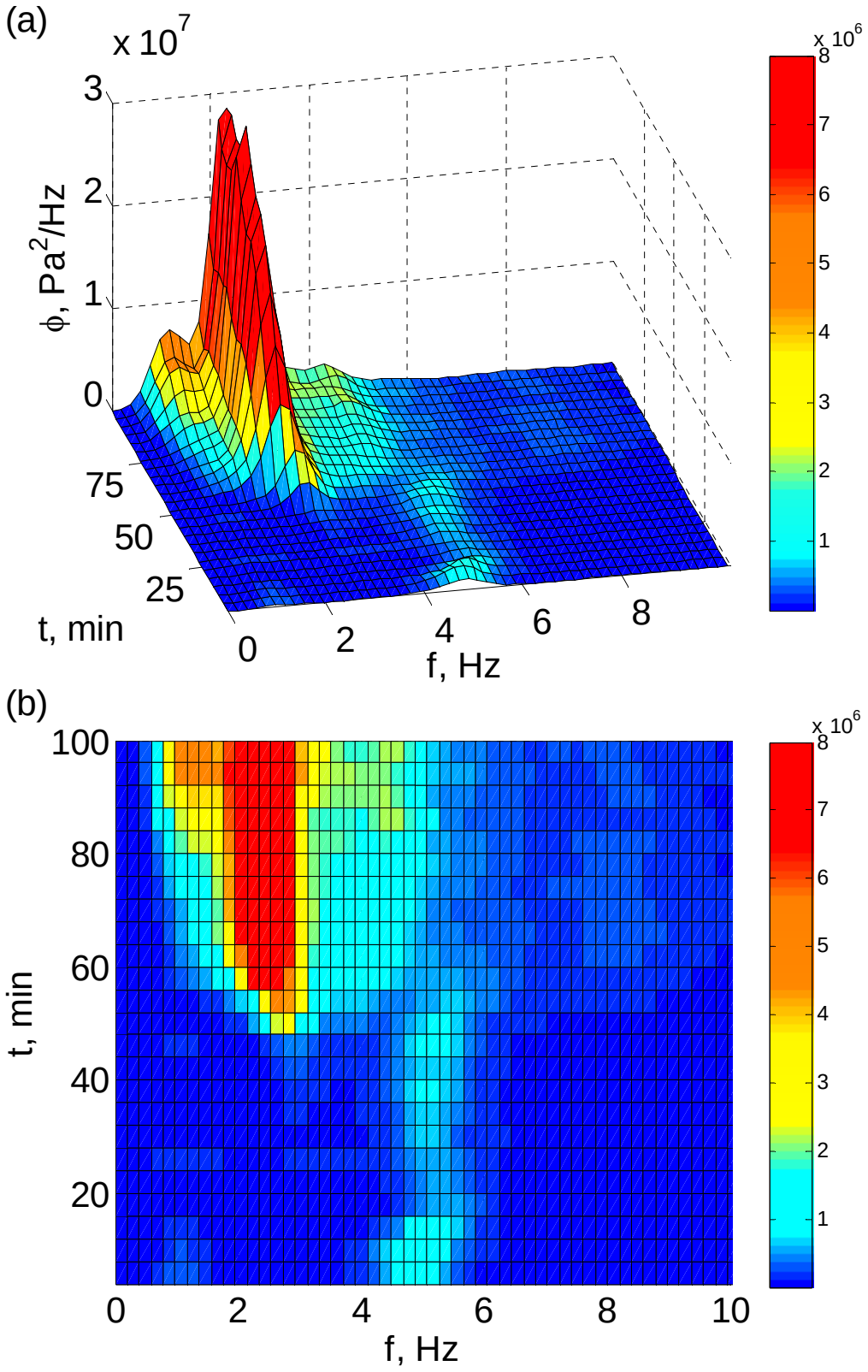

Figure 7.5: Transient power spectra during drying in the conical bed: (a) oblique view, (b) topographic view.

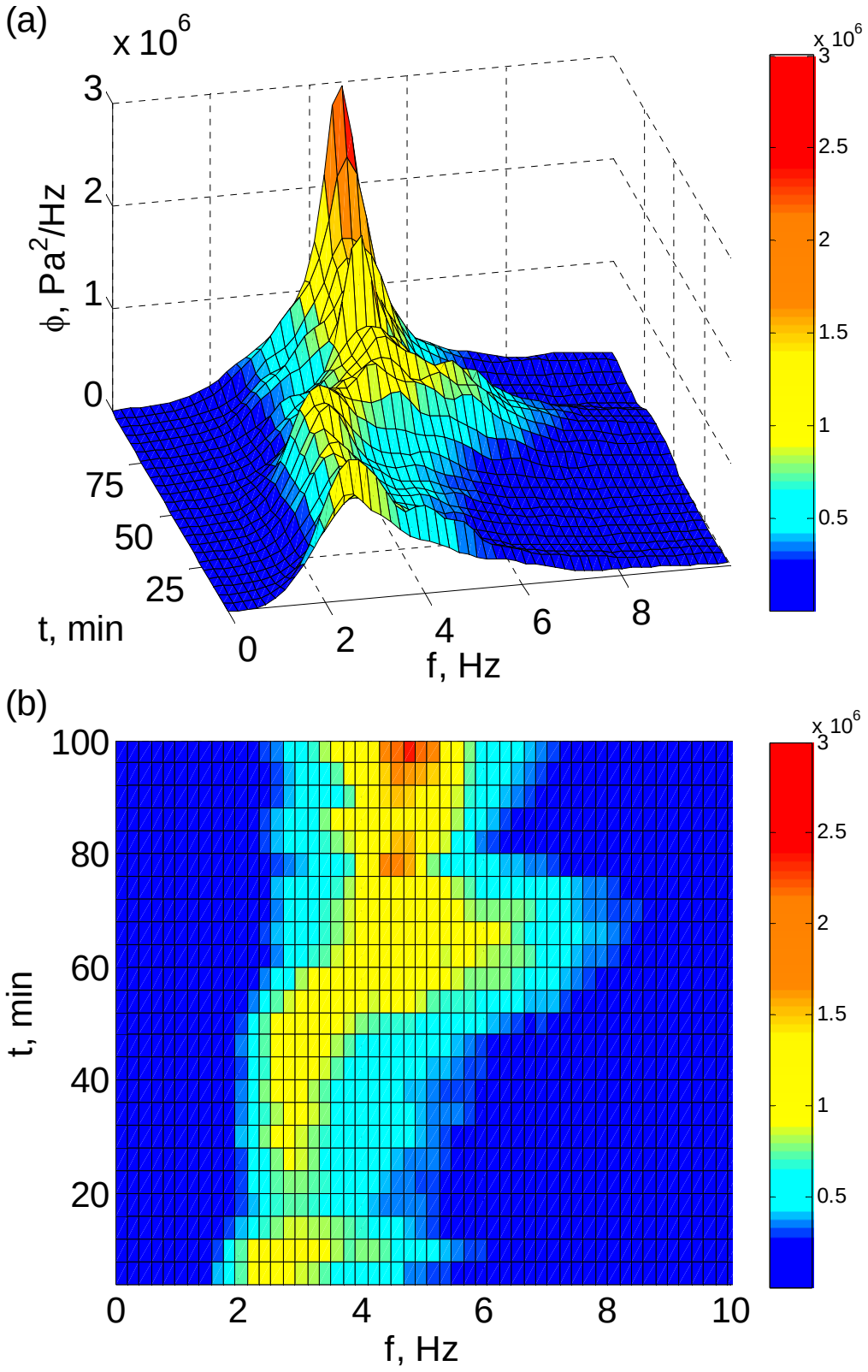

Figure 7.6: Transient power spectra during drying in the cylindrical bed: (a) oblique view, (b) topographic view.

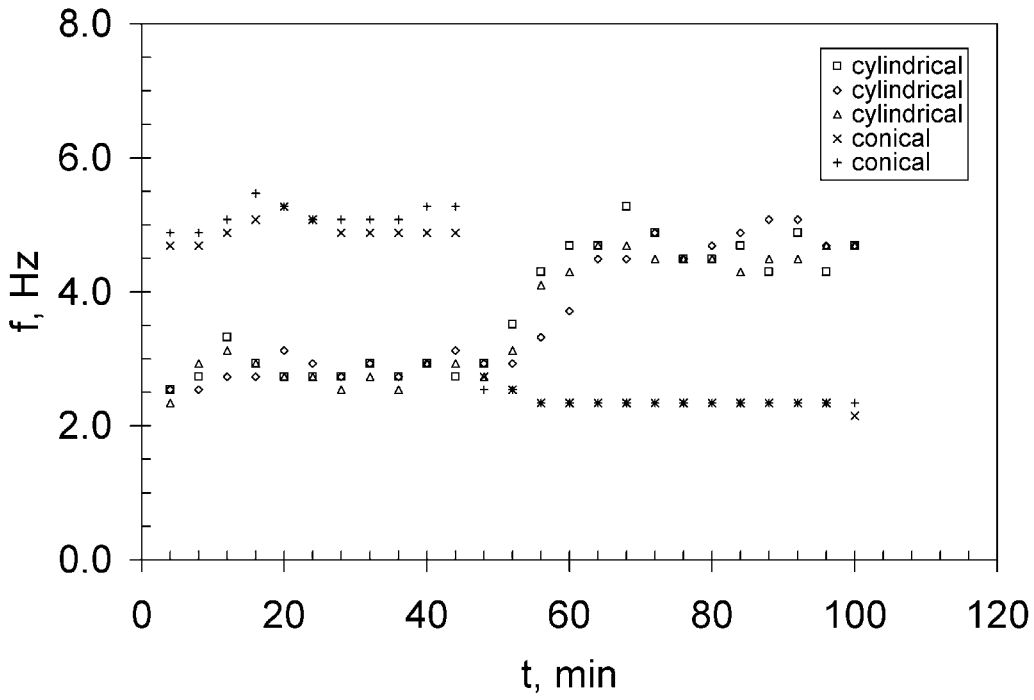

Figure 7.7: Dominant frequency profile during drying.

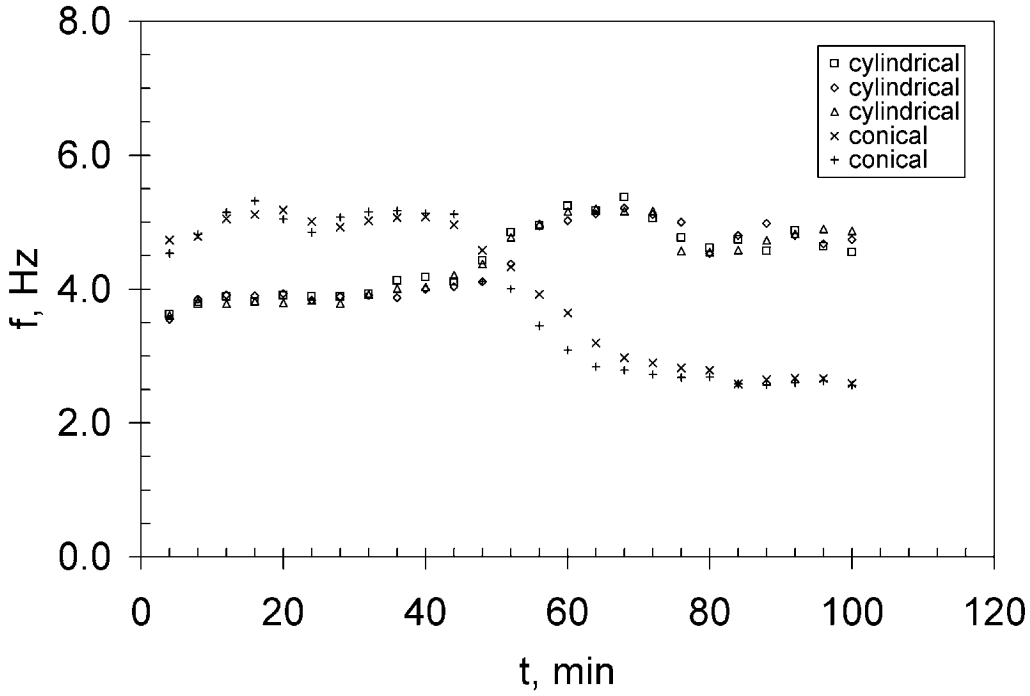

Figure 7.8: Average cycle frequency (ACF) profile during drying.

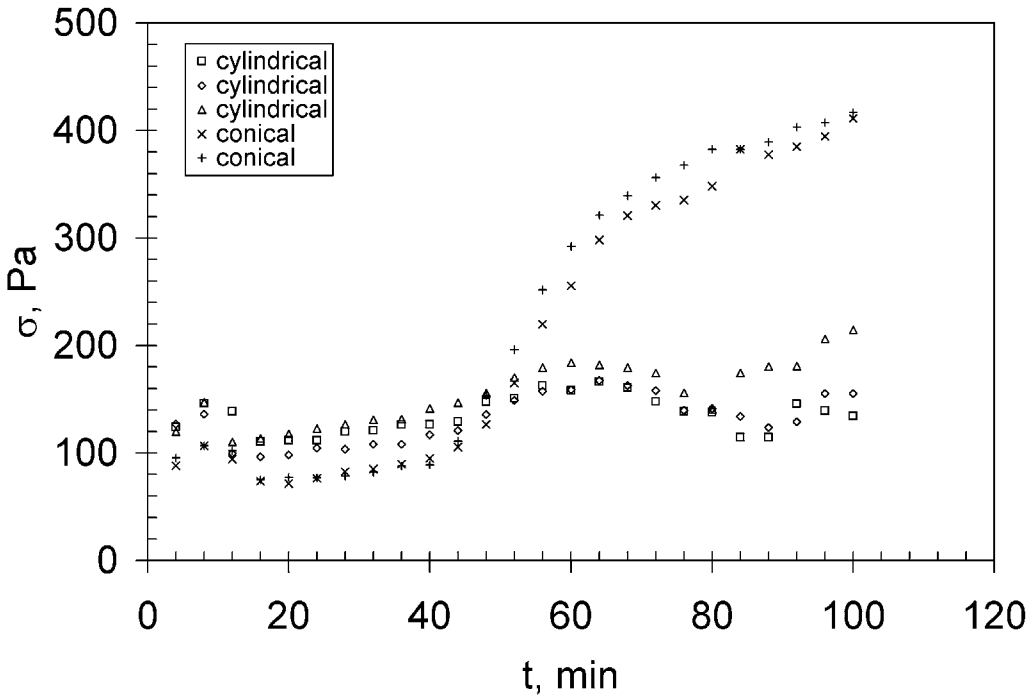

Figure 7.9: Standard deviation profile of pressure fluctuation measurements during drying.

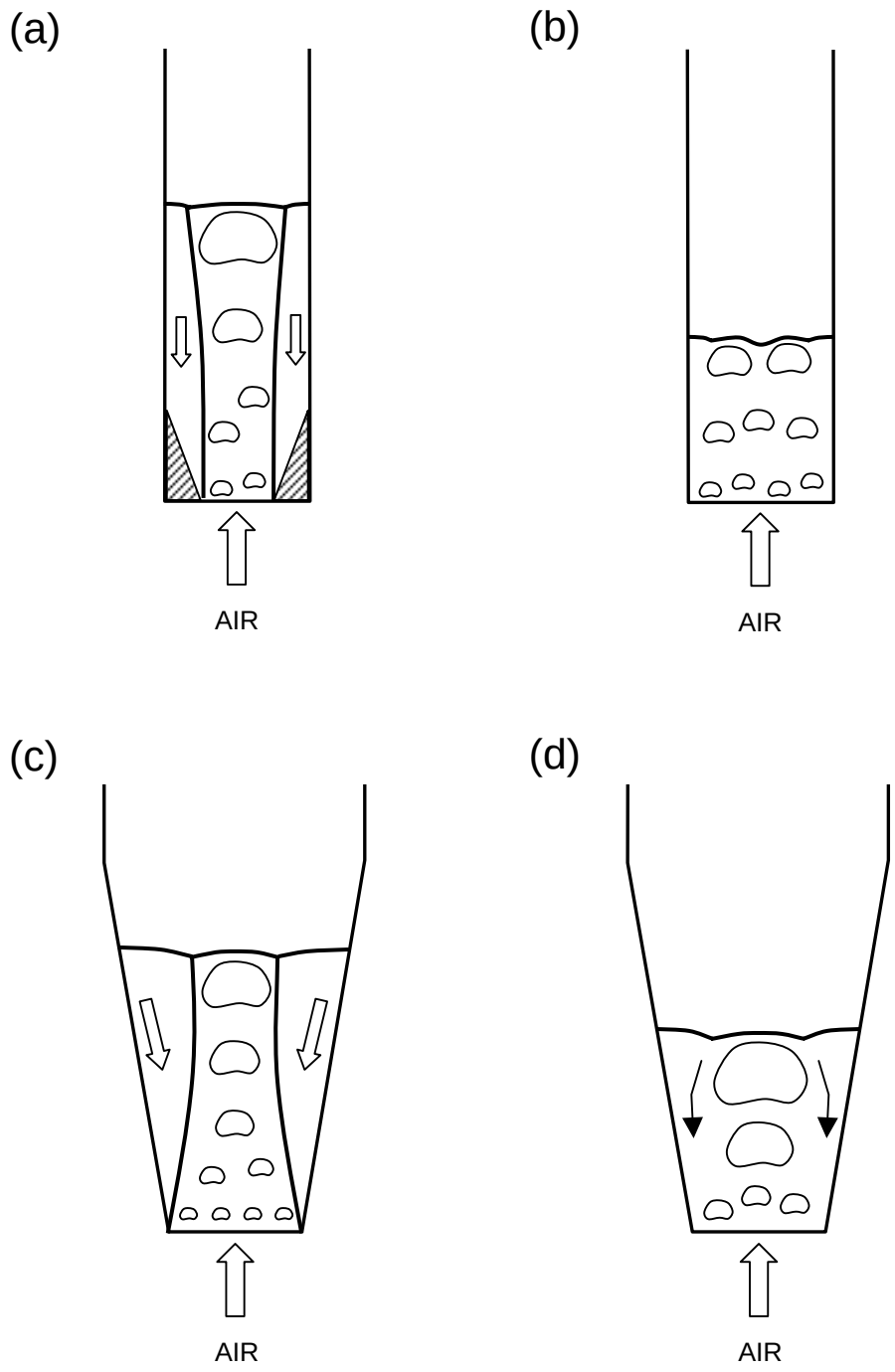

Figure 7.10: Proposed circulation pattern in the (a) cylindrical bed prior to critical moisture content, (b) cylindrical bed after critical moisture content, (c) conical bed prior to critical moisture content, (d) conical bed after critical moisture content. Hatched regions signify defluidized material.

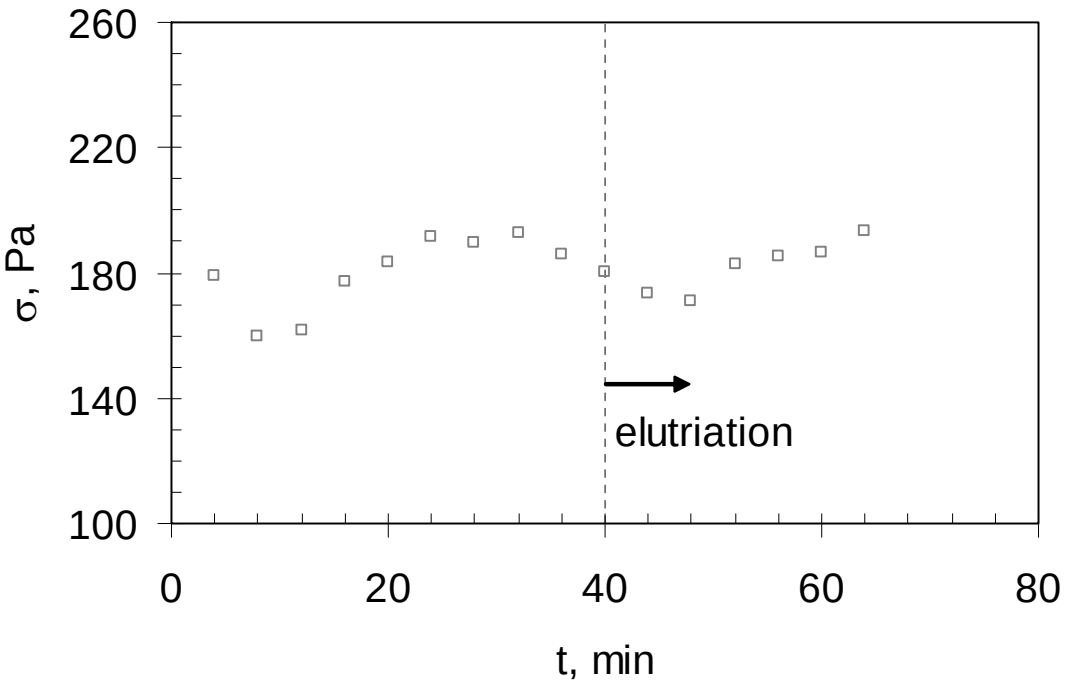

Figure 7.11: Standard deviation profile data when elutriation occurs. Dashed line is when elutriation is first measured. Data collected, but not published, by Chaplin et al. [34].

CHAPTER 8 - Conclusions and Recommendations

8.1 Conclusions

This compilation of research studies has two primary areas of focus: (1) interpretation of the hydrodynamics associated with drying and (2) the impact of fluidized bed design parameters, namely distributor design and vessel geometry, on the hydrodynamics of drying. Both subjects provide valuable insight into fluidized bed applications as drying introduces the particle moisture content as a process variable.

Chapters 2 and 3 demonstrate that the presence of moisture within porous materials such as pharmaceutical granule has a pronounced effect on its hydrodynamic behaviour. At high moisture contents, an increased velocity is required to reach a fully fluidized state. The full support velocity of wet granule (30 wt.% moisture) was found to be 0.60 m/s, which is 5.5 times greater than that of dry granule (5 wt.% moisture). This increase in the full support velocity was found to be a result of the moisture on the surface of the granule which stabilizes the ensemble of particles. Using the fluidized bed pressure drop, the full support voidage was found to decrease from approximately 0.7 to

0.5 as the moisture content decreased. As a result, transient hydrodynamic behaviour is experienced during drying under constant velocity conditions in a conical fluidized bed dryer. The changes in the hydrodynamics suggest that once the critical moisture content is reached, the granule transitions into a coalescing state of very aggressive bubbling fluidization. This behaviour is a result of the disappearance of surface moisture on the particles and the coinciding decrease in interparticle liquid-bridging forces. This behaviour is supported by simple two-phase theory. As the excess gas increases (due to a decrease in the full support fluidization velocity), larger bubbles are formed at the distributor. These larger bubbles continue to grow during drying through coalescence.

With knowledge of the hydrodynamics associated with drying, Chapters 4 - 6 addresses the impact of distributor plate design on hydrodynamics in a conical fluidized bed dryer. Dry bed studies demonstrate that the punched plate reduces coalescence resulting in an improved hydrodynamic state as compared to the perforated and Dutch weave plates at inlet superficial gas velocities below 2.0 m/s. The Dutch weave exhibited excessive segregation below 2.0 m/s due to the small apertures associated with its design. The dryer performance study was used to test the performance of these distributor designs with respect to drying. The punched plate showed superior hydrodynamic behaviour which resulted in faster drying under 0.64-m/s drying conditions. At drying velocities of 1.3 m/s, the drying performance was similar between plates because the gas velocity was sufficiently high thus limiting the influence of the lateral component of the punched plate. Similar findings were found with higher gas velocities in the dry bed study as well.

Localized distributor level hydrodynamics were also presented in Chapter 6. This study compared various distributor designs in a cylindrical fluidized bed dryer using x-ray densitometry imaging to capture the hydrodynamic behaviour. Dry bed experiments found the solids concentration profile of the punched and perforated plates suggest bubbles pass through the middle portion of the bed whereas the porous plate has bubbles pass preferentially around the periphery of the bed. The punched and perforated plate designs also demonstrated similar hydrodynamics during drying where the core region of the fluidized bed grew as drying proceeded. Experiments with both of these designs also generated a defluidized region around the bed periphery in the constant rate period of drying. This phenomenon was found to be a result of poor granule fluidity when it is wet rather than poor gas distributor associated the distributor designs. On the other hand, the porous plate created poor distributor level hydrodynamics during drying in the constant rate period. Excessive defluidization and channelling was measured across the bed cross-section during this period of drying. Similar to dry bed studies with the Dutch weave, it is believed this is due to the limited momentum carried by fine dispersion of gas generated by the porous plate design.

Finally, Chapter 7 revealed the contrasting hydrodynamic behaviour created by the cylindrical and conical vessel geometries during drying. The conical bed created superior particle circulation and mixing as compared to the cylindrical geometry which exhibits defluidization around the base of the bed when the granule is wet. Furthermore, the conical geometry has hydrodynamic behaviour where coalescence dominates as drying proceeds whereas the cylindrical bed creates bubbling phenomena frequencies that

transition from low to high frequency. The latter occurs due to a constricted bed inlet arising from defluidization of wet granule, which eventually breaks as drying proceeds. This study demonstrates the advantage of using the conical vessel geometry as circulation of material down the wall regions of the fluidized bed promotes superior solids mixing. This enhanced solids mixing will help limit moisture variation in the granule which in turn improves the granule product quality.

8.2 Recommendations

These studies have provided valuable insight towards drying hydrodynamics as well as fluidized bed dryer design. However, specific recommendations should be considered for the advancement of this research, but also research related to other applications that have external interparticle forces acting on their systems.

This thesis has provided an initial understanding of fluidized bed drying hydrodynamics and demonstrated the effectiveness of power spectrum analysis to predict its global behaviour. This global behaviour allows us to sufficiently study the hydrodynamic behaviour of the system. However, one of the major shortcomings related to this thesis is that a single pressure fluctuation measurement cannot accurately determine local bubble characteristics such as bubble diameter or frequency because these variables change with axial position in the bed. Instead, a single pressure fluctuation measurement measures all the bubbling related phenomena such as bubble formation, coalescence, passage and eruption. In order to get accurate bubble characteristics throughout a fluidized bed, multiple measurements are required along the

axial height of the bed as well as in the windbox. With these measurements, the pressure fluctuation data can be decomposed into its global and local behaviour, where the local behaviour has been proven to provide more detailed information regarding the bubble characteristics. This type of analysis would provide more detailed information regarding the influence of moisture on the hydrodynamics in terms of bubble size and frequency.

Process variables associated with drying should be more carefully considered. In particular, inlet fluidization air should be conditioned with respect to its humidity. Experiments at Merck Frosst Canada Ltd. and the University of Saskatchewan used air drawn from their respective laboratories. The problem with this is that the air is not conditioned and therefore humidity changes occur on a day-to-day, but more importantly, a seasonal basis. The benefit of humidity control is that it will improve reproducibility of results, especially towards the end of drying where the inlet humidity can influence the system. This is extremely important for future work on endpoint control using the S-statistic since this method is a measure of hydrodynamic behaviour. Conditioned air was used at Delft University of Technology, but this air was freeze-dried and then not re-humidified. This extremely dry air has an effect on the interparticle forces through electrostatics, especially with finer particles, which affects the hydrodynamics of the fluidized bed towards the end of drying. The relative humidity should be controlled to minimize the electrostatic effects yet not cause capillary induced interparticle forces. Although this is an expensive upgrade for large scale operation, it can be done easily on laboratory scale equipment to test the theory of humidity effects. By proving its

importance at lab scale, the benefits of large scale air conditioning can then be considered.

Regarding specific details of this thesis work, the fluidization voidage calculated using the bed pressure drop in Chapter 2 should be confirmed experimentally. Measurement techniques exist (i.e. fibre optic probes) which have the ability to measure this particle characteristic accurately. This would allow the influence of moisture on the particle voidage to be more accurately described. Also, these voidages could have been used in the x-ray densitometry study of Chapter 6 in order to obtain a more accurate solids concentration profiles. Furthermore, only a total of 6 minutes of data was used for analysis in the dry bed experiments of Chapter 4. Although the data show good reproducibility in the results, additional data could have easily been collected to further strengthen the statistical significance of this work, especially where differences in the analysis techniques are questionable. Similar to this, only two trials were conducted to make the dryer performance comparisons in Chapter 5. This did not allow for proper use of statistics with the analysis techniques used. Although the trends in the data described in Chapter 5 are real phenomena resulting from distributor design, from a statistical perspective the results are limited with regards to their significance. Similar statistical questions can be raised with the 10-s data sets collected in the x-ray densitometry study of Chapter 6. The difference here is that the x-ray source limited the amount of data collected so little could have been done to prevent this.

The progression from this work is to focus on using the knowledge gained regarding drying hydrodynamics for determining the endpoint of drying. Current endpoint techniques used in the pharmaceutical industry are inadequate. Typically, empirical correlations between granule moisture content and product temperature are used to predict moisture content during drying. However, these techniques are not capable of incorporating variation in process conditions such as fluidization velocity or relative humidity. Therefore, the pharmaceutical industry is actively pursuing new measurement techniques to improve the current state of endpoint detection. By creating a tool that can both monitor drying and predict its endpoint, without being intrusive, is ideal for the pharmaceutical industry because it will be easily adaptable to their strict protocol. This work would include revisiting the use of the S-statistic in the attempts to improve its ability to predict the hydrodynamics associated with moisture contents towards the end of drying.

Finally, the conclusions from this thesis work could also be related to other fluidization processes. Many processes, including particle coating, fluidized bed granulation, top spray drying, polymerization reactors and fluidized bed cokers involve some form of liquid addition or stickiness factor. Based on this thesis work, this will change the interparticle force load in their systems and ultimately affect fluidization behaviour. Incorporating the work conducted in this thesis into the research related to these processes will help improve their understanding as well as strengthen the position of using pressure fluctuation measurements as a robust analysis and monitoring tool in fluidized bed applications.

Appendix A - Chapter 2 supplementary data: bed pressure drop *vs.* velocity data and tapped density data as a function of moisture content

Table A.1: Data from 5 wt% moisture experiments

Trial	U_o (m/s)	ΔP (mbar)	$\sigma_{\Delta P}$ (mbar)	Bed Height (cm)
1	0.40	7.51	1.63	22.0
	0.25	7.47	1.134	22.0
	0.21	7.46	0.935	22.0
	0.17	7.48	0.764	22.0
	0.15	7.49	0.687	22.0
	0.11	7.34	0.281	22.0
	0.079	6.62	0.125	22.0
	0.053	5.90	0.042	21.5
	0.046	5.05	0.042	21.0
	0.042	4.51	0.018	21.0
2	0.36	7.90	1.29	22.0
	0.31	7.84	1.09	22.0
	0.25	7.82	0.91	22.0
	0.20	7.85	0.68	22.0
	0.15	7.90	0.58	22.0
	0.15	7.88	0.53	22.0
	0.11	7.85	0.25	21.5
	0.079	6.97	0.14	21.0
	0.053	6.13	0.04	21.0
	0.046	5.64	0.02	20.0
	0.042	5.26	0.01	20.0
	0.038	4.72	0.01	20.0
3	0.40	7.79	1.65	22.0
	0.31	7.71	1.34	22.0
	0.25	7.69	1.05	22.0
	0.20	7.73	0.78	22.0
	0.16	7.73	0.66	22.0
	0.15	7.53	0.58	22.0
	0.11	7.54	0.27	22.0
	0.079	6.72	0.14	21.0
	0.053	5.92	0.04	20.5
	0.046	5.36	0.03	20.0
	0.042	4.84	0.03	20.0
	0.038	4.19	0.04	19.5

U_o – superficial gas velocity (m/s), ΔP – differential pressure drop (mbar),
$\sigma_{\Delta P}$ – standard deviation of differential pressure drop (mbar).

Table A.2: Data from 10 wt% moisture experiments

Trial	U_o (m/s)	ΔP (mbar)	$\sigma_{\Delta P}$ (mbar)	Bed Height (cm)
1	0.40	8.37	1.78	29
	0.31	8.32	1.280	28
	0.26	8.28	1.003	28
	0.21	8.32	0.784	28
	0.18	8.35	0.692	28
	0.15	8.11	0.485	28
	0.11	7.65	0.226	26
	0.079	7.03	0.066	25
	0.053	6.20	0.028	24
	0.046	5.31	0.014	24
	0.042	4.68	0.012	24
2	0.40	8.64	1.45	28
	0.31	8.56	1.08	26
	0.25	8.54	0.78	26
	0.20	8.57	0.60	26
	0.16	8.48	0.44	26
	0.15	8.40	0.41	26
	0.11	7.99	0.18	26
	0.079	7.38	0.05	25
	0.053	6.54	0.01	24
	0.046	5.68	0.01	23
	0.038	4.76	0.01	23
3	0.40	8.69	1.57	30
	0.31	8.64	1.12	29
	0.25	8.61	0.83	29
	0.20	8.45	0.65	29
	0.16	8.33	0.44	28
	0.15	8.19	0.37	27
	0.15	8.27	0.39	27
	0.11	7.90	0.20	26
	0.079	7.24	0.08	25.5
	0.053	6.19	0.02	25
	0.046	5.33	0.02	24.5
	0.038	4.44	0.01	24

U_o – superficial gas velocity (m/s), ΔP – differential pressure drop (mbar),
$\sigma_{\Delta P}$ – standard deviation of differential pressure drop (mbar).

Table A.3: Data from 15 wt% moisture experiments

Trial	U_o (m/s)	ΔP (mbar)	$\sigma_{\Delta P}$ (mbar)	Bed Height (cm)
1	0.40	9.20	1.40	38.0
	0.31	9.11	0.935	38.0
	0.25	9.02	0.678	35.0
	0.21	8.60	0.523	33.0
	0.18	8.07	0.362	32.0
	0.15	7.37	0.251	31.0
	0.11	6.88	0.218	29.0
	0.079	6.00	0.067	29.0
	0.066	5.21	0.019	28.0
	0.053	4.49	0.011	28.0
	0.046	3.62	0.010	26.0
2	0.61	9.35	1.86	37.0
	0.50	9.26	1.55	37.0
	0.40	9.16	1.24	35.0
	0.31	9.13	0.86	35.0
	0.20	8.92	0.43	33.0
	0.15	8.62	0.24	31.0
	0.15	8.52	0.21	30.0
	0.11	7.86	0.11	30.0
	0.079	7.10	0.05	28.0
	0.053	5.63	0.01	27.0
	0.046	4.72	0.01	26.0
	0.038	3.81	0.01	26.0
3	0.50	9.36	1.69	37.0
	0.40	9.30	1.31	37.0
	0.36	9.25	1.12	37.0
	0.31	9.21	0.87	37.0
	0.25	8.87	0.63	35.0
	0.20	8.49	0.38	33.0
	0.16	8.16	0.24	32.0
	0.15	8.02	0.18	31.0
	0.11	7.33	0.12	30.0
	0.079	6.69	0.01	29.0
	0.053	5.15	0.01	28.0
	0.046	4.27	0.02	28.0
	0.038	3.41	0.01	28.0

U_o – superficial gas velocity (m/s), ΔP – differential pressure drop (mbar),
$\sigma_{\Delta P}$ – standard deviation of differential pressure drop (mbar).

Table A.4: Data from 20 wt% moisture experiments

Trial	U_o (m/s)	ΔP (mbar)	$\sigma_{\Delta P}$ (mbar)	Bed Height (cm)
1	0.70	10.04	2.24	47.0
	0.61	9.91	1.955	42.0
	0.50	9.79	1.620	42.0
	0.40	9.60	1.175	42.0
	0.36	9.44	0.980	41.0
	0.30	9.13	0.715	37.0
	0.25	8.64	0.582	36.0
	0.19	7.61	0.516	33.0
	0.15	7.41	0.385	31.0
	0.11	6.71	0.249	29.0
	0.079	5.95	0.063	28.0
	0.053	4.46	0.013	28.0
	0.046	3.61	0.02	28.0
2	0.61	10.01	1.69	42.0
	0.50	10.03	1.34	42.0
	0.40	10.01	1.05	42.0
	0.36	10.09	0.84	42.0
	0.31	10.05	0.67	36.0
	0.25	9.70	0.50	37.0
	0.20	8.96	0.29	34.0
	0.15	7.95	0.24	31.0
	0.15	8.02	0.20	30.0
	0.11	7.27	0.26	29.0
	0.079	7.55	0.21	29.0
	0.053	5.74	0.02	28.0
	0.046	4.86	0.02	28.0
	0.038	4.04	0.01	28.0
3	0.61	10.07	1.87	42.0
	0.50	9.89	1.47	42.0
	0.40	9.88	1.07	41.0
	0.36	9.67	0.86	40.0
	0.31	9.19	0.74	36.0
	0.25	8.27	0.51	35.0
	0.20	7.13	0.39	31.0
	0.16	6.30	0.55	31.0
	0.15	6.96	0.41	31.0
	0.11	6.15	0.34	30.0
	0.079	5.57	0.12	28.0
	0.053	4.10	0.02	28.0
	0.046	3.28	0.03	28.0
	0.038	2.58	0.03	28.0

U_o – superficial gas velocity (m/s), ΔP – differential pressure drop (mbar),
$\sigma_{\Delta P}$ – standard deviation of differential pressure drop (mbar).

Table A. 5: Data from 25 wt% moisture experiments

Trial	U_o (m/s)	ΔP (mbar)	$\sigma_{\Delta P}$ (mbar)	Bed Height (cm)
1	0.70	10.62	2.05	47.0
	0.61	10.38	1.777	47.0
	0.50	10.29	1.538	42.0
	0.40	9.97	1.139	41.0
	0.36	9.47	1.033	39.0
	0.31	8.67	0.930	36.0
	0.25	7.06	0.864	31.0
	0.19	6.09	1.156	30.0
	0.15	4.44	0.917	30.0
	0.11	4.47	0.867	28.0
	0.079	4.91	0.271	28.0
	0.053	3.97	0.015	28.0
	0.046	3.24	0.01	28.0
2	0.70	10.51	1.89	47.0
	0.61	10.38	1.63	47.0
	0.50	9.80	1.20	42.0
	0.40	8.93	0.87	39.0
	0.36	7.82	0.82	35.0
	0.31	7.43	0.75	35.0
	0.24	7.18	0.62	33.0
	0.20	5.46	0.91	31.0
	0.15	5.79	0.55	31.0
	0.11	3.89	0.67	30.0
	0.079	5.77	0.02	30.0
	0.053	4.28	0.03	30.0
	0.046	3.43	0.04	30.0
	0.038	2.60	0.03	30.0
3	0.70	10.86	1.93	47.0
	0.61	10.66	1.66	47.0
	0.50	10.55	1.27	44.0
	0.40	9.78	0.99	41.0
	0.36	9.00	0.85	37.0
	0.31	6.74	1.30	33.0
	0.25	3.87	0.62	30.0
	0.20	4.56	2.38	28.0
	0.15	4.79	0.74	28.0
	0.11	5.28	0.70	27.0
	0.079	4.86	0.40	27.0
	0.053	4.48	0.07	27.0
	0.046	2.96	0.03	27.0

U_o – superficial gas velocity (m/s), ΔP – differential pressure drop (mbar),
$\sigma_{\Delta P}$ – standard deviation of differential pressure drop (mbar).

Table A. 6: Data from 30 wt% moisture experiments

Trial	U_o (m/s)	ΔP (mbar)	$\sigma_{\Delta P}$ (mbar)	Bed Height (cm)
1	0.76	11.16	1.74	52.0
	0.69	11.09	1.70	52.0
	0.60	10.96	1.44	47.0
	0.50	10.60	1.27	42.0
	0.40	9.66	1.09	39.0
	0.36	6.63	1.05	32.0
	0.32	5.15	1.03	31.0
	0.27	5.00	0.67	32.0
	0.19	5.15	0.64	31.0
	0.15	5.33	0.34	30.0
	0.11	5.18	0.14	30.0
	0.079	4.01	0.01	30.0
	0.053	2.83	0.03	30.0
	0.046	2.07	0.03	30.0
2	0.74	11.28	1.71	50.0
	0.70	11.04	1.55	50.0
	0.61	10.63	1.37	42.0
	0.50	4.58	0.65	30.0
	0.38	4.46	0.53	30.0
	0.34	4.56	0.51	30.0
	0.31	4.66	0.47	30.0
	0.25	4.68	0.55	30.0
	0.19	4.24	0.50	30.0
	0.15	3.45	0.45	30.0
	0.11	2.97	0.12	30.0
	0.079	2.12	0.08	30.0
	0.053	1.28	0.01	30.0
	0.046	0.95	0.01	30.0
3	0.74	11.78	1.54	47.0
	0.70	11.67	1.46	47.0
	0.61	11.14	1.29	41.0
	0.50	10.15	1.06	37.0
	0.40	9.43	0.81	36.0
	0.36	8.97	0.76	29.0
	0.31	7.88	0.68	29.0
	0.25	5.00	0.61	29.0
	0.20	7.09	0.50	29.0
	0.15	6.07	0.27	29.0
	0.11	4.21	0.03	29.0
	0.079	2.83	0.06	29.0
	0.053	1.70	0.05	29.0
	0.046	1.19	0.01	29.0

U_o – superficial gas velocity (m/s), ΔP – differential pressure drop (mbar),
$\sigma_{\Delta P}$ – standard deviation of differential pressure drop (mbar).

Table A.7: Tap density data at different moisture contents

Moisture Content (%)	Mass of granule in 100 mL (g)	Tapped Volume (mL)	particle denisty (kg/m^3)	Tapped density (kg/m^3)	Hausner Ratio (-)
2.5	48.6	85.0	486	572	1.18
3.5	47.5	83.0	475	572	1.20
5.4	46.4	84.0	464	552	1.19
5.9	45.7	83.0	457	551	1.20
5.9	46.0	84.0	460	548	1.19
7.0	44.5	82.0	445	543	1.22
10.1	38.8	77.0	388	504	1.30
10.6	40.7	80.0	407	509	1.25
12.5	38.8	78.0	388	497	1.28
15.6	36.5	72.0	365	507	1.39
16.2	38.2	75.0	382	509	1.33
16.6	36.3	71.0	363	511	1.41
18.6	37.4	71.0	374	527	1.41
20.3	37.0	69.0	370	536	1.45
25.5	36.0	64.0	360	563	1.56
26.0	37.2	66.0	372	564	1.52
30.1	39.3	64.0	393	614	1.56

Appendix B - Chapter 3 supplementary data: pressure fluctuation analysis data from trial 2

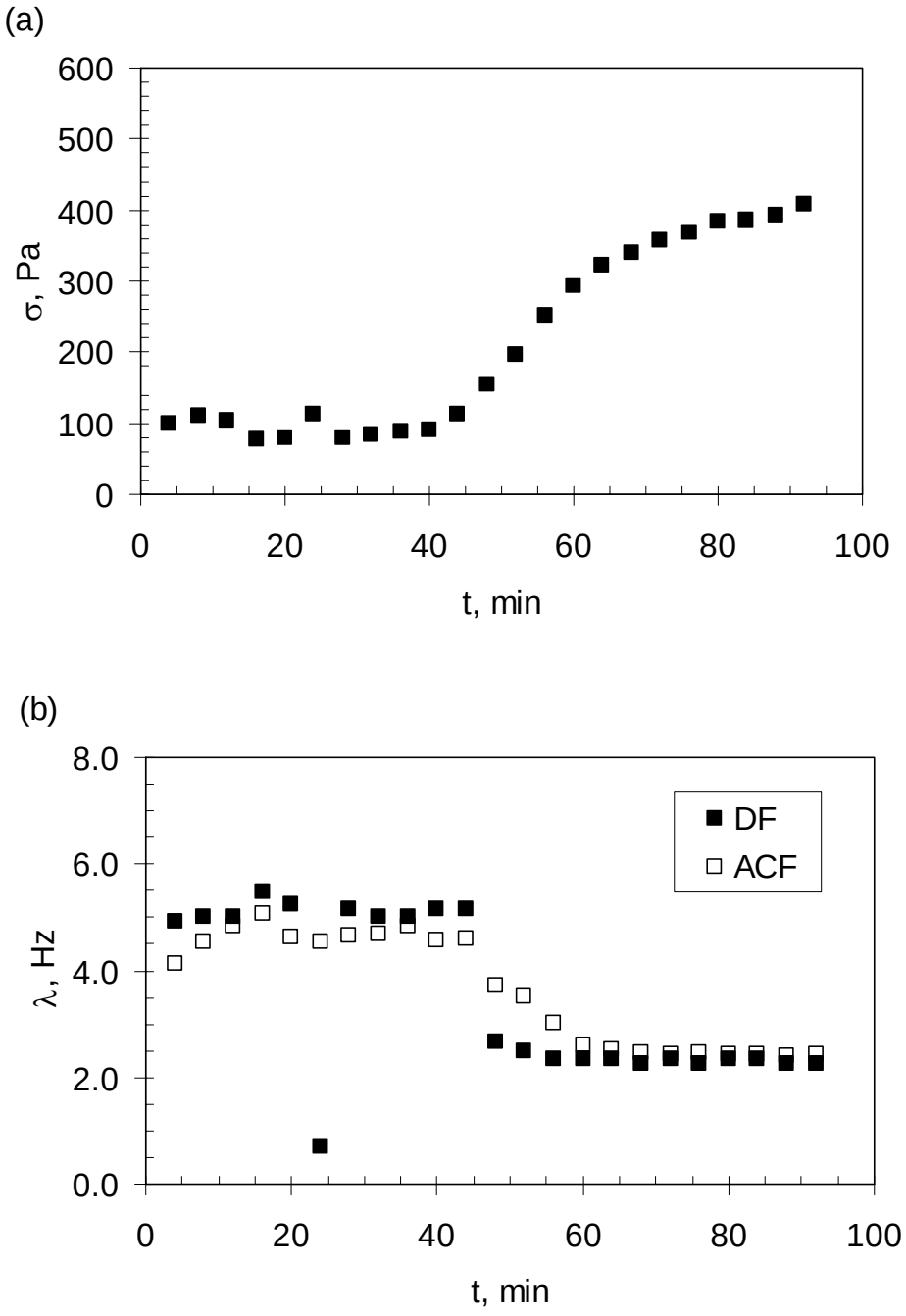

Figure B.1: Pressure fluctuation frequency analysis for drying at a superficial air velocity of 0.64 m/s (trial 2): (a) standard deviation, (b) dominant frequency.

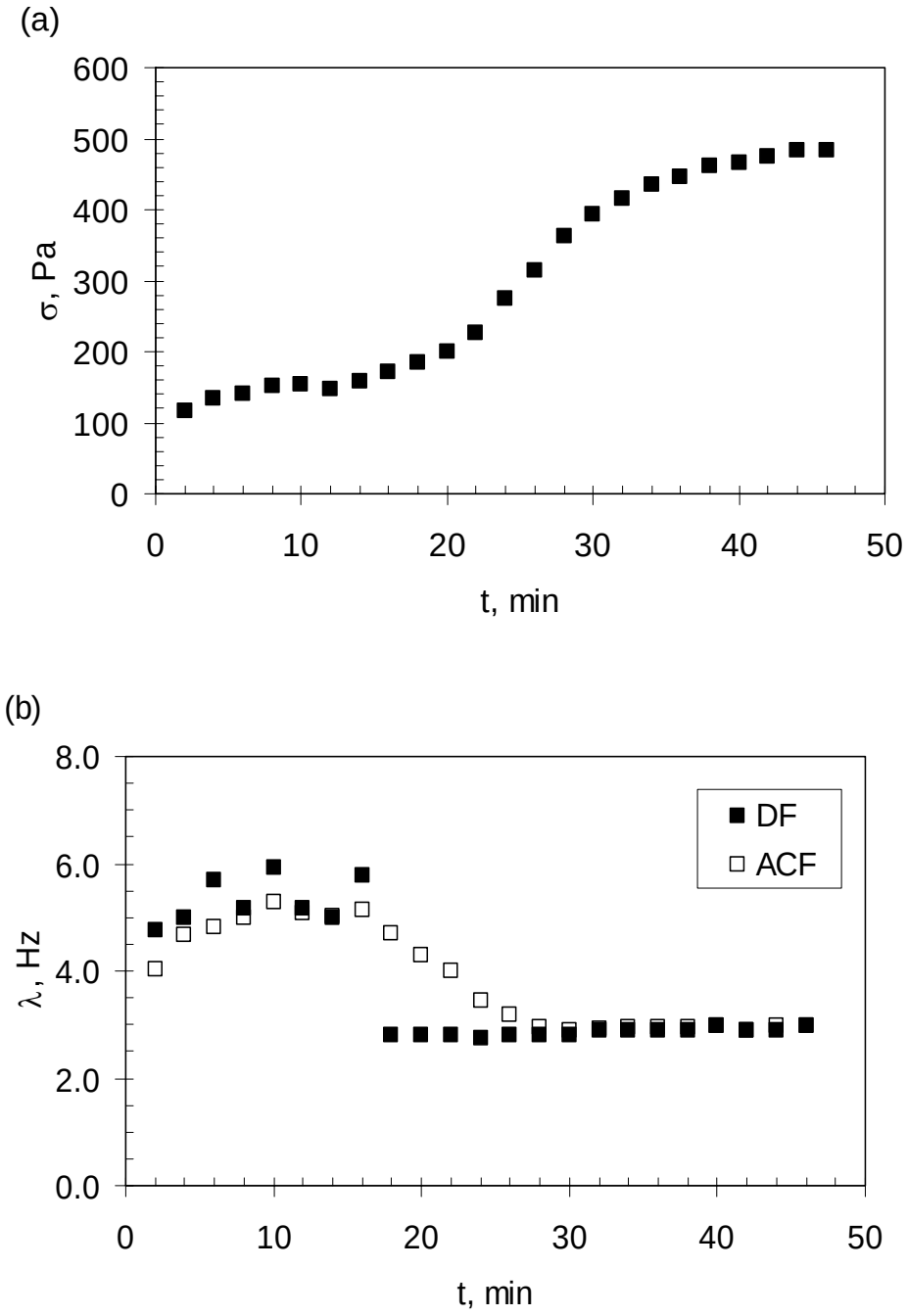

Figure B.2: Pressure fluctuation frequency analysis for drying at a superficial air velocity of 1.3 m/s (trial 2): (a) standard deviation, (b) dominant frequency.

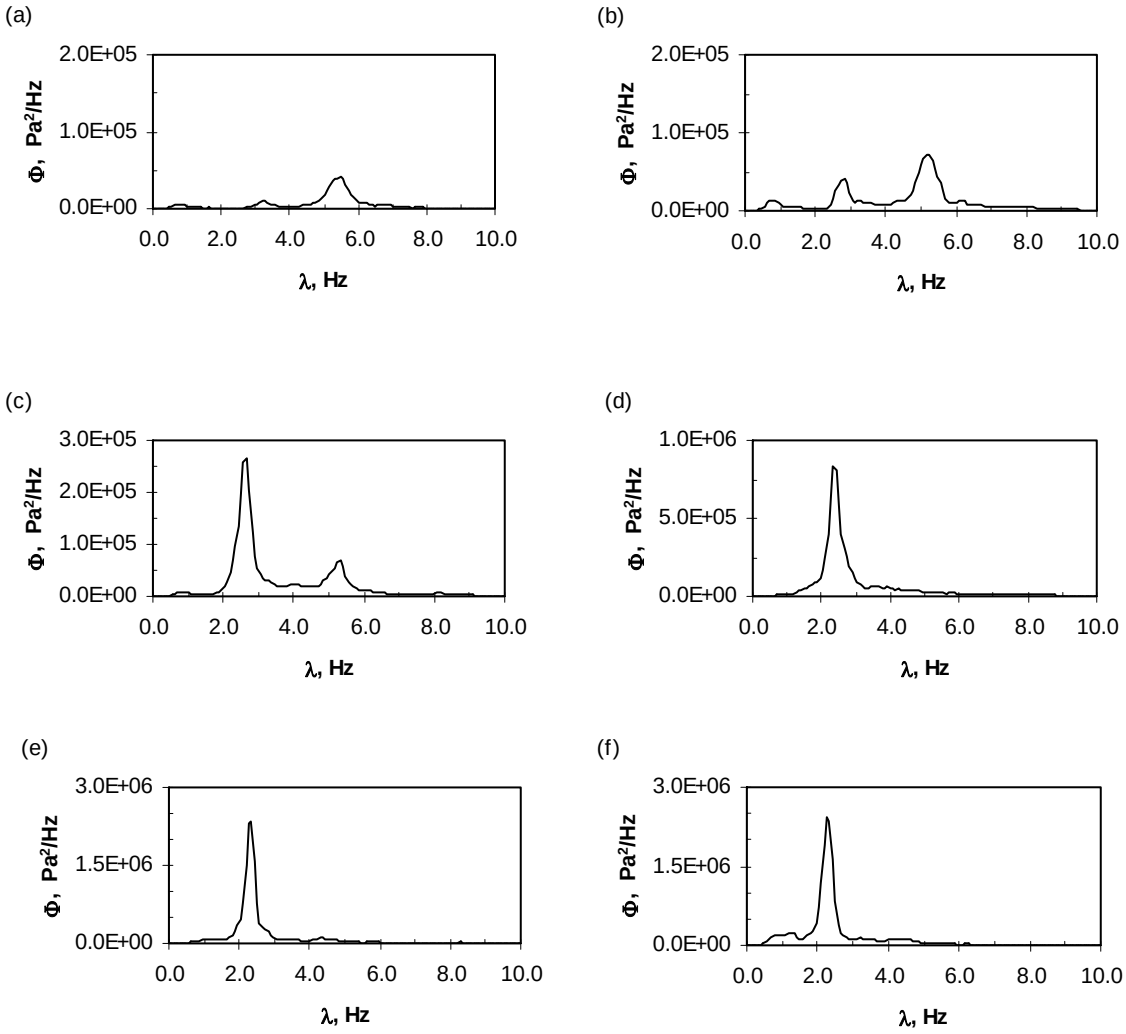

Figure B.3: Pressure fluctuation power spectra over the course of drying for the 0.64 m/s superficial air velocity condition (trial 2): (a) 16 minutes, (b) 44 minutes, (c) 48 minutes, (d) 56 minutes, (e) 72 minutes, (f) 88 minutes.

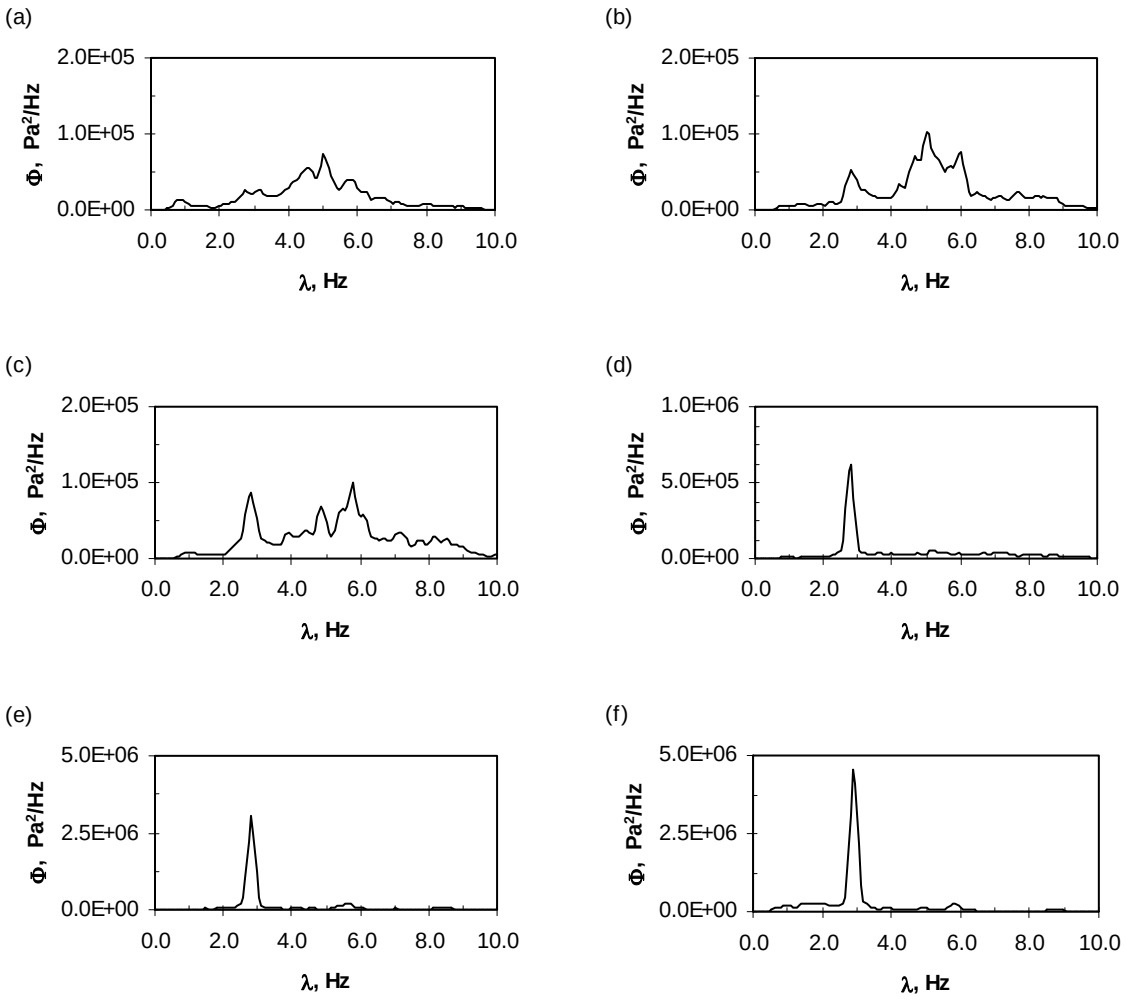

Figure B.4: Pressure fluctuation power spectra over the course of drying for the 1.3 m/s superficial air velocity condition (trial 2): (a) 4 minutes, (b) 14 minutes, (c) 16 minutes, (d) 22 minutes, (e) 28 minutes, (f) 42 minutes.

Appendix C - Chapter 4 supplementary data: standard deviation and average cycle frequency *vs.* velocity data with different distributor designs

Table C.1:Pressure fluctuation data analysis for distributor design hydrodynamics in a dry bed

Superficial gas velocity (m/s)	Standard deviation (Pa)			Average cycle frequency (Hz)		
	Perforated	Punched	Dutch	Perforated	Punched	Dutch
0.5	133	140	122	7.3	7.1	6.7
0.5	138	140	124	6.9	6.9	6.7
0.5	142	141	127	6.8	6.9	6.5
1.0	121	178	131	5.7	6.3	5.8
1.0	114	181	126	5.6	6.3	5.7
1.0	138	186	134	5.6	6.3	5.8
1.5	281	292	161	4.7	5.1	5.6
1.5	266	298	156	4.8	5.1	5.6
1.5	276	293	151	4.9	5.2	5.7
2.0	395	384	240	3.9	4.2	5.0
2.0	394	384	302	3.9	4.1	4.5
2.0	388	379	308	4.0	4.0	4.4
2.5	423	521	404	3.8	4.2	3.7
2.5	401	487	406	3.9	4.2	3.6
2.5	399	487	426	3.9	4.3	3.5
3.0	536	639	477	3.6	4.1	3.6
3.0	513	643	454	3.6	4.1	3.6
3.0	507	642	448	3.7	4.0	3.6
3.5	507	530	464	4.0	4.4	3.9
3.5	503	538	447	4.2	4.2	3.9
3.5	489	514	443	4.2	4.1	3.9

Appendix D - Chapter 5 supplementary data: standard deviation and power spectra data for 2.5-kg bed loadings

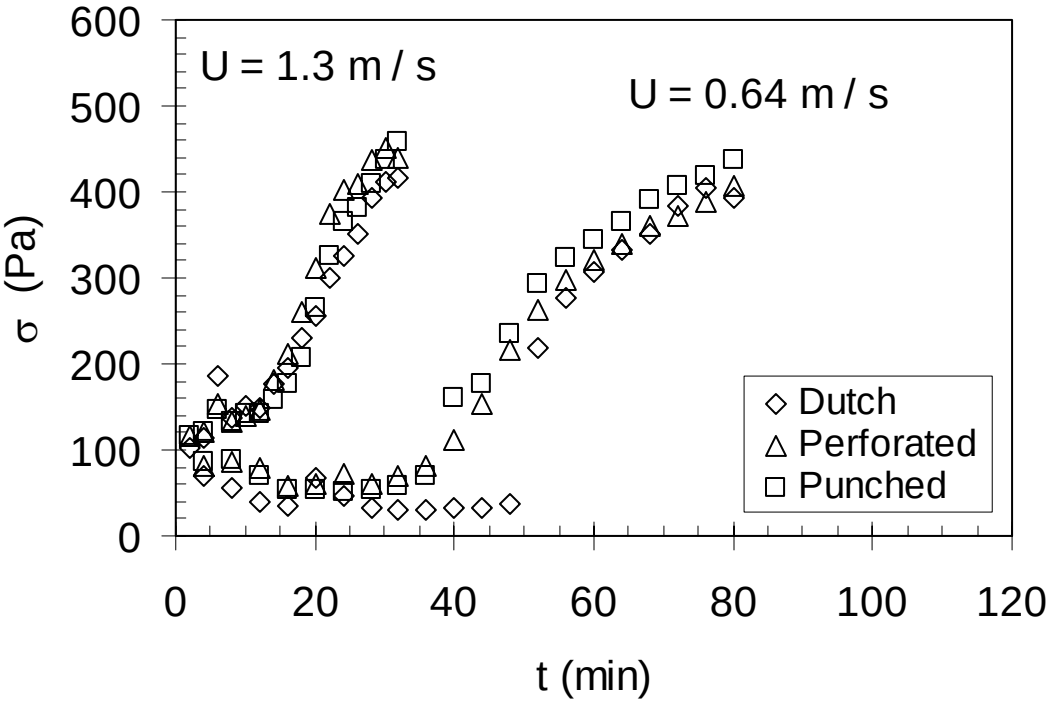

Figure D.1: Standard deviation of pressure fluctuations for drying 2.5-kg bed loadings.

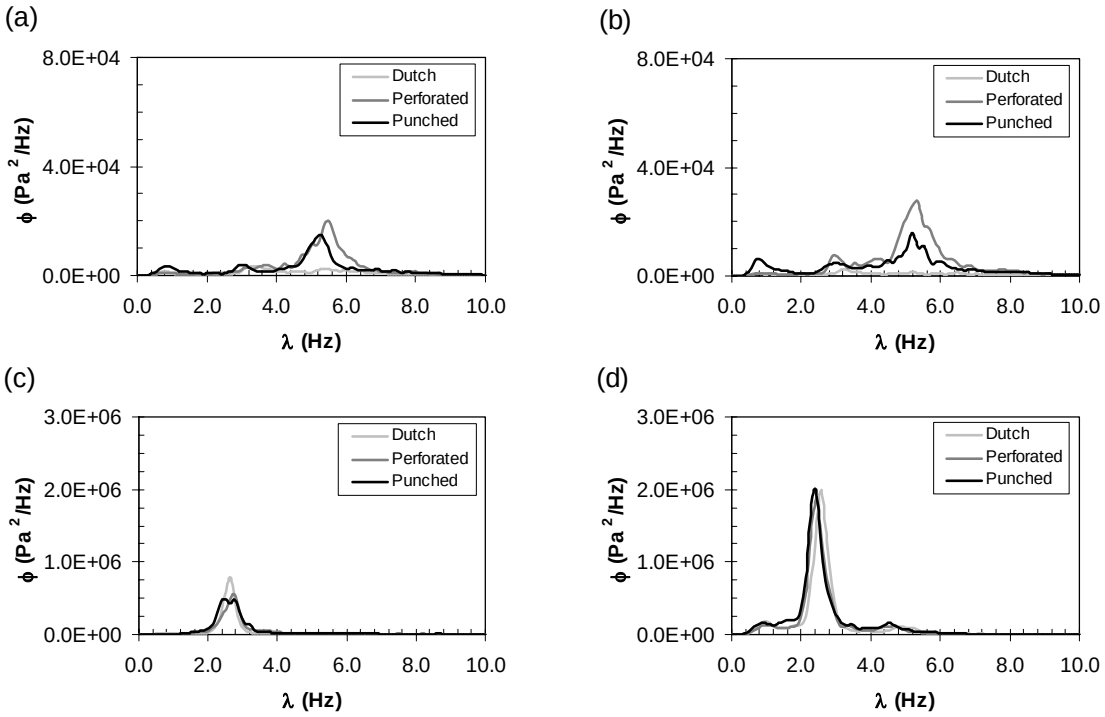

Figure D.2: Power spectra for 2.5-kg bed loadings dried at 0.64 m/s: (a) 16 minutes into drying, (b) 32 minutes into drying, (c) 48 minutes into drying, (d) 64 minutes into drying.

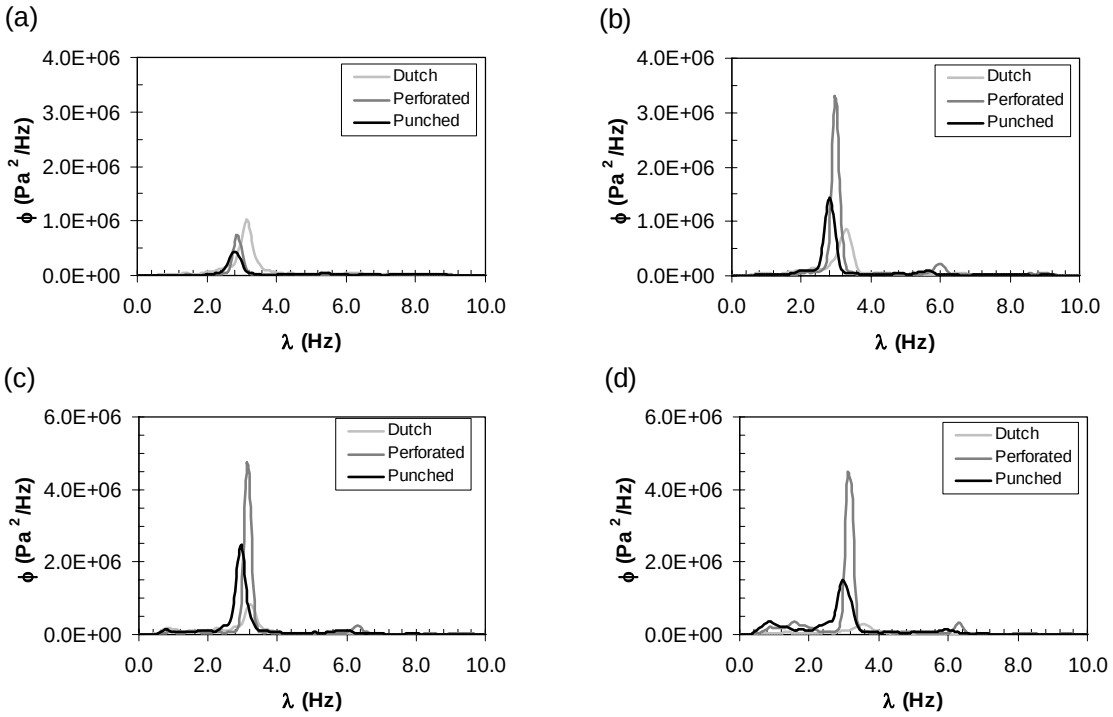

Figure D.3: Power spectra for 2.5-kg bed loadings dried at 1.3 m/s: (a) 12 minutes into drying, (b) 18 minutes into drying, (c) 24 minutes into drying, (d) 30 minutes into drying.

Appendix E - Sample MATLAB® codes for x-ray densitometry data analysis

This MATLAB® code takes the photon count rates collected during drying for each detector and converts the data into a length of solids along its beam path. These measured solids path lengths are then converted in solids concentration and relative standard deviation profiles. This code was written specifically for the analysis pertaining to Chapter 6. Separate code, which is not provided, was used for the detector calibration, phantom image and dry bed experimental data analysis.

Start of code:

```
clear all
close all


%-----------READ THE CALIBRATION DATA FILES FOR ALL DETECTORS----------

%the calibration constants were determined at various moisture contents
%via a detector calibration process (not executed in this code).

%count rate = Bcal * exp(-x/Ccal) for each detector

%this code solves for x (the distance of the pathlength occupied by
%solids) for each detector

%calibration moisture contents used in the calibration process. The
zero moisture content is not 'real'; it represents the dry granule.
calmc = [30.9,26.9,23.0,18.3,12.5,5.9,1.1,0];

%loads the separate detector calibration constants
for z = 1:length(calmc);
    C=load(['0402cal',num2str(z-1),'.csv']);
    C=C';
    %organizes the calibration constants into separate arrays
    Bcalvalues(z,:) = C(1,:);
    Ccalvalues(z,:) = C(2,:);

end

%mean Bcal value for each sensor. Used because it is virtually constant
%(less than 2% RSD) over moisture content range for each detector.
Bcal = mean(Bcalvalues,1);


%----------------------------USER INPUTS----------------------------

%moisture contents of samples taken during drying
moisture =[27,23,15,7,1.5];
```

```
%times that moisture samples were taken. 50 is added so that the later
%xray files are compared to the dry calibration curve.
mstime = [0,7.5,18,30,38,50];

%moisture sample values at the sample times (0.001 so that they are
%compared to the dry calibration curve
msv = [31.1,24.1,15.9,5.3,0.9,0.001];
%times at which x-ray data was collected
xrtime = [4,8,12,16,20,24,28,32,36,40,44];

counter = 1;

%interpolated moisture contents for the times the xray data was
%collected
for a = 1:length(xrtime);
    leavewhile = 0;
    while leavewhile == 0;

   if xrtime(a) > mstime(counter) && xrtime(a) < ...
   mstime(counter+1);
      moisture(a) = msv(counter) -(msv(counter) - ...
      msv(counter+1))/(mstime(counter)-mstime(counter+1))...
      *(mstime(counter)-xrtime(a));
      leavewhile = 1;
   else
      counter = counter +1;
      end
   end

   %reset counter
   counter = 1;
end

%filename tags
file = 1:length(xrtime);

%initialize counter for calibration interpolation
count=1;

%loop for separate data sets (at different times and moisture contents)
for q= 1:length(file);

    %variable to exit while loop
    leavewhile2 = 0;

    %interpolates Ccal(attenuation coeff)for each data set
    while leavewhile2 == 0;
        if moisture(q) < calmc(count) && moisture(q) > calmc(count+1);
            Ccal = Ccalvalues(count,:) +(Ccalvalues(count,:) - ...
            Ccalvalues(count+1,:))/(calmc(count)-calmc(count+1))...
            *(moisture(q)-calmc(count));
            leavewhile2 = 1;
        else
            count = count +1;
        end
    end
```

```
%nested loop to calculate the length of solids in the pathlength
%for every detector going through the bed (3 through 30) at a
specific time during drying. Analysis of data is also done in this
%loop.
for k  = 1:32;
    sensor(k) = k;

    %re-initializes the array
    image_plot = [];


      %loop for calculating data according to the entire 10s of
      %data collected. Data was collected in 1s increments!
      for j = 1:10;

        %sets path to data file
        data_file=['0403data/0403perf',num2str(file(q)),'/v',...
        num2str(j),'.ray',num2str(k),'.bin'];

        %opens data file
        fid1 = fopen(data_file);

        %reads data into dat1
        dat1 = fread(fid1, inf,'int16');
        fclose(fid1);

        %opens reference file, which is a measurement of an empty
        %bed, to remove the influence of the walls on the signal
        reference_file=['0403data/0403emptyperf/v1.ray',...
        num2str(k),'.bin'];
        fid2 = fopen(reference_file);
        dat2 = fread(fid2, inf,'int16');
        fclose(fid2);

        %full bed measurement used as bed coordinates. Better
        %because if the bed has moved slightly due to changing
        %distributor plates then the maximum pathlengths associated
        %with a detector are re-adjusted for the specific condition
        coordinates_file=['0403data/0403fulldryperf/v1.ray',...
        num2str(sensor(k)),'.bin'];
        fid3 = fopen(coordinates_file);
        dat3 = fread(fid3, inf,'int16');
        fclose(fid3);

        count1 = 0;

        %determines analysis frequency 25000/1250 = 20 Hz
        block = 1250;

        %total points measured by the detectors=26215. However
        %totalpoints must be a multiple of block so that the for
        %loop below can run properly.
        totalpoints = 25000;

        %analysis frequency
        newfreq = totalpoints/block;
```

```
        %averages the high frequency datasets into a lower
        %frequency data (newfreq)
        for i = 1:block:totalpoints;
            count1 = count1 +1;
            Data(count1)= mean(dat1(i:i+block-1));
            Reference(count1)= mean(dat2(i:i+block-1));
            Coordinates(count1) = mean(dat3(i:i+block-1));
        end


        %Convert detector signal values to pathlengths through
        %granule using the calibration.
        p_data = 1/Ccal(sensor(k))*log((Data)/Bcal(sensor(k)));

        p_reference = 1/Ccal(sensor(k))*log((Reference)/...
        Bcal(sensor(k)));

        %Ccalvalues(8,:) is the dry granule calibration.
        %Coordinates based on dry granule measurements.
        p_coordinates =1/Ccalvalues(8,sensor(k))*log...
        ((Coordinates)/Bcal(sensor(k)));

        %subtraction of the wall influence out of the actual
        %measurement
        image = p_data(2:newfreq-1) - p_reference(2:newfreq-1);

        %build array by concatenating 1s data sets together
        image_plot = [image_plot,image];

        %calculation of bed coordinates
        coordinates_bed = p_coordinates(2:newfreq-1)- ...
        p_reference(2:newfreq-1);

        %mean value of the bed coordinates
        bed_coordinates(k) = mean(coordinates_bed);

    end

    %0.05 seconds – one time increment based on 20Hz frequency
    aa= block/totalpoints;

    %the time unit array for plotting
    time = aa:aa:length(image_plot)*aa;

    %mean value of length of solids along a given pathlength
    meanvalue(q,k) = mean(image_plot);

    %calculation of ACF
    num_crossings = 0;

    %counts the number of crossings of the mean resampled data
    for c = 1:length(image_plot)-1;
        if image_plot(c) < meanvalue(q,k) && image_plot(c+1) > ...
        meanvalue(q,k);
        num_crossings = num_crossings + 1;
        end
    end
```

```
        ACF(q,k) = 1/((newfreq-2)*aa*j/num_crossings);

        %calculation of RSD (relative standard deviation)
        rstdev(q,k) = std(image_plot)/meanvalue(q,k)*100;

        %calculation of solids distribution profile
        SDP(q,k) = meanvalue(q,k)/bed_coordinates(k);

    end
    count = 1;
end


%-----------------------------DATA PLOTS-----------------------------
%font size
font = 16;

%font style in plots
style = 'Arial';


%------------------------LENGTH OF SOLIDS IN PATH----------------------
%surface plot of the length of solids along a pathlength
figure;
surf(sensor(3:30),xrtime,meanvalue(:, 3:30));

%axis settings
xlabel ('Detector, #','FontName',style,'FontSize',font);
ylabel ('t (min)','FontName',style,'FontSize',font);
zlabel ('Solids, cm','FontName',style,'FontSize',font);

%axis min and max settings (x,y,z)
axis([3,30,4,44,0,15]);

%axis format settings
set(gca,'FontName',style,'FontSize',font,'XTick',[3;10;17;24;30],...
'YTick',[4;14;24;34;44]);

%topographic view of plot
view(0,90);

%inclusion of a colorbar
colorbar;


%----------------------SOLIDS CONCENTRATION PLOT----------------------
%surface plot of the solids concentration profile
figure;
surf(sensor(3:30),xrtime,SDP(:,3:30));

%axis settings
xlabel ('Detector (No.)','FontName',style,'FontSize',font);
ylabel ('t (min)','FontName',style,'FontSize',font);
zlabel ('W_g / W_{max} (-)','FontName',style,'FontSize',font);

%axis min and max settings (x,y,z)
```

```
axis([3,30,4,44,0,1.5]);

%axis format settings
set(gca,'FontName',style,'FontSize',font,'XTick',[3;10;17;24;30],...
'YTick',[4;14;24;34;44]);

%topographic view of plot
view(0,90);

%inclusion of a colorbar
colorbar;
%positioning of text boxes
text(-2.1,46.6,'(b)','FontName','Arial','FontSize',16);
text(30.3,45,'W_g / W_{max} (-)','FontName','Arial','FontSize',10);


%-------------------------RELATIVE STDEV PLOT-------------------------
%surface plot of the solids concentration profile
figure;
surf(sensor(3:30),xrtime,rstdev(:, 3:30));

%axis settings
xlabel ('Detector, #','FontName',style,'FontSize',font);
ylabel ('t, min','FontName',style,'FontSize',font);
zlabel ('RSTDEV (%)','FontName',style,'FontSize',font);

%axis min and max settings (x,y,z)
axis([3,30,4,44,0,40]);

%axis format settings
set(gca,'FontName',style,'FontSize',font,'XTick',[3;10;17;24;30],...
'YTick',[4;14;24;34;44]);

%topographic view of plot
view(0,90);

%inclusion of a colorbar
colorbar;

%positioning of text boxes
text(-2.1,46.6,'(b)','FontName','Arial','FontSize',16);
text(31.2,45,'RSD (%)','FontName','Arial','FontSize',10)
```

Appendix F - Chapter 6 supplementary data: effective attenuation coefficients and incident photon count rates *vs*. moisture content for the detectors

Table F.1: Effective attenuation coefficient of the granule at various moisture contents measured at each detector

Detector	Granule Moisture Content (wt.%)							
(No.)	2.9	3.5	8.2	14.2	20.2	24.8	28.3	32.7
1	0.099	0.101	0.102	0.088	0.082	0.081	0.080	0.079
2	0.100	0.101	0.102	0.088	0.082	0.082	0.082	0.078
3	0.099	0.100	0.101	0.088	0.083	0.083	0.081	0.078
4	0.099	0.100	0.101	0.087	0.083	0.082	0.081	0.075
5	0.101	0.102	0.104	0.089	0.084	0.083	0.083	0.079
6	0.100	0.101	0.102	0.088	0.084	0.082	0.081	0.077
7	0.100	0.101	0.103	0.087	0.084	0.083	0.083	0.075
8	0.098	0.100	0.101	0.087	0.082	0.081	0.082	0.076
9	0.099	0.101	0.102	0.087	0.083	0.082	0.082	0.074
10	0.099	0.102	0.104	0.088	0.083	0.081	0.082	0.075
11	0.098	0.101	0.103	0.087	0.083	0.082	0.081	0.074
12	0.097	0.101	0.102	0.088	0.082	0.082	0.081	0.076
13	0.098	0.101	0.103	0.088	0.082	0.082	0.082	0.075
14	0.098	0.101	0.103	0.087	0.083	0.084	0.081	0.076
15	0.098	0.101	0.102	0.087	0.082	0.083	0.081	0.077
16	0.098	0.101	0.101	0.087	0.081	0.084	0.081	0.076
17	0.098	0.100	0.102	0.087	0.082	0.082	0.079	0.076
18	0.097	0.100	0.101	0.086	0.082	0.082	0.080	0.077
19	0.099	0.101	0.103	0.087	0.083	0.082	0.080	0.080
20	0.101	0.102	0.103	0.087	0.083	0.085	0.083	0.080
21	0.099	0.101	0.103	0.087	0.082	0.084	0.082	0.081
22	0.101	0.102	0.104	0.088	0.082	0.083	0.083	0.081
23	0.101	0.102	0.103	0.087	0.082	0.083	0.083	0.081
24	0.100	0.101	0.102	0.087	0.082	0.084	0.083	0.079
25	0.101	0.102	0.104	0.089	0.082	0.084	0.085	0.077
26	0.100	0.101	0.102	0.088	0.082	0.084	0.085	0.078
27	0.101	0.102	0.103	0.088	0.083	0.083	0.084	0.077
28	0.101	0.101	0.102	0.087	0.082	0.084	0.085	0.076
29	0.098	0.100	0.100	0.086	0.081	0.082	0.084	0.075
30	0.100	0.101	0.101	0.086	0.082	0.081	0.084	0.077
31	0.101	0.102	0.103	0.088	0.083	0.083	0.087	0.078
32	0.101	0.102	0.103	0.088	0.084	0.085	0.086	0.076
AVG	**0.099**	**0.101**	**0.102**	**0.087**	**0.082**	**0.083**	**0.082**	**0.077**
RSD	**1.3**	**0.7**	**0.9**	**0.8**	**0.9**	**1.4**	**2.2**	**2.7**

Table F.2: Incident photon count rate at various moisture contents measured at each detector

Detector	Granule Moisture Content (wt.%)									
(No.)	2.9	3.5	8.2	14.2	20.2	24.8	28.3	32.7	AVG	RSD
1	3674	3659	3713	3675	3685	3638	3627	3600	**3659**	**1.0**
2	3541	3518	3566	3541	3528	3533	3523	3457	**3526**	**0.9**
3	3472	3449	3490	3468	3489	3485	3446	3376	**3459**	**1.1**
4	3560	3526	3566	3554	3585	3546	3548	3412	**3537**	**1.5**
5	3690	3659	3742	3671	3698	3670	3691	3593	**3677**	**1.1**
6	3713	3668	3744	3682	3746	3696	3644	3583	**3685**	**1.5**
7	3662	3631	3704	3637	3691	3660	3667	3547	**3650**	**1.3**
8	3430	3429	3481	3439	3475	3432	3442	3399	**3441**	**0.8**
9	3901	3923	3957	3914	3983	3931	3922	3829	**3920**	**1.1**
10	3586	3623	3672	3618	3664	3575	3572	3550	**3608**	**1.2**
11	3538	3573	3605	3547	3607	3571	3531	3454	**3553**	**1.4**
12	2612	2645	2658	2647	2661	2648	2631	2597	**2637**	**0.9**
13	2036	2054	2071	2051	2071	2050	2057	2017	**2051**	**0.9**
14	2241	2257	2284	2247	2283	2290	2254	2225	**2260**	**1.0**
15	1901	1922	1929	1913	1934	1938	1924	1912	**1921**	**0.6**
16	3073	3110	3089	3091	3103	3146	3091	3057	**3095**	**0.9**
17	3147	3164	3182	3154	3190	3188	3141	3158	**3166**	**0.6**
18	3466	3502	3512	3494	3539	3531	3495	3512	**3506**	**0.6**
19	3526	3536	3567	3529	3537	3541	3523	3593	**3544**	**0.7**
20	3376	3392	3408	3351	3379	3434	3393	3420	**3394**	**0.8**
21	3603	3602	3644	3580	3619	3666	3600	3692	**3626**	**1.1**
22	3620	3615	3654	3590	3616	3640	3632	3676	**3630**	**0.7**
23	3477	3488	3516	3444	3471	3483	3507	3527	**3489**	**0.8**
24	3639	3658	3686	3639	3646	3695	3707	3692	**3670**	**0.8**
25	3461	3484	3501	3445	3454	3468	3528	3421	**3470**	**1.0**
26	3635	3650	3673	3637	3645	3660	3741	3654	**3662**	**0.9**
27	3851	3861	3886	3814	3869	3816	3921	3799	**3852**	**1.1**
28	3537	3541	3554	3502	3544	3551	3633	3470	**3541**	**1.3**
29	3303	3309	3313	3277	3320	3297	3417	3264	**3313**	**1.4**
30	3492	3487	3487	3441	3506	3445	3591	3427	**3485**	**1.5**
31	1882	1874	1889	1864	1894	1881	1950	1858	**1886**	**1.5**
32	3403	3390	3412	3383	3433	3425	3497	3290	**3404**	**1.7**

Appendix G - Sample MATLAB® code for pressure fluctuation analysis

This MATLAB® code calculates the standard deviation, average cycle frequency, dominant frequency and power spectra of pressure fluctuation data collected during drying. Drying process variables are time-averaged within this code as well. This code was created specifically for analysis of data pertaining to Chapter 7. A similar version, which is not provided, was used for Chapters 3 and 5. The difference between the codes is the handling of the data files as they pertain to the different data acquisition systems.

Start of code:

```
close all
clear all

%----------Data Input and Processing Prior to Data Analysis------------
% choose the data file to be divide
[filename,directory] = uigetfile('V:\Matlab\*.dat','Select Time Series…
for Division');
fname = strcat(directory,filename);

%User inputs for the data acquisition system (DAQ)
prompt = {'Number of channels','Frequency (Hz)','Block Size','Number…
of Blocks'};
title_GUI1 = 'Enter the Required Inputs ';
lines = 1;
def = {'6', '400', '2048', '352'};

%defines user DAQ inputs as variables
user_input_matrix = inputdlg(prompt,title_GUI1,lines,def);
nchann = str2num(user_input_matrix{1});
freq = str2num(user_input_matrix{2});
blocksize = str2num(user_input_matrix{3});
blocks = str2num(user_input_matrix{4});

%initializes the start and end points of the data file. Used to define
%data set from user inputs
i_start = 1;
i_end=blocks*blocksize;

%calls read_dat.m function to transfer data into array form
%Outputs the array called 'input'
input = read_dat(fname,nchann,i_start,i_end);

%calibration for the sensors from bit to volt
volt=10/(2^15);
```

```
%--------------------TEMPERATURE AND RH ANALYSIS----------------------
%thermocouple calibrations (done experimentally)
M3 = 259.4*volt*input(:,3)+1.0866;  %product air thermocouple (DEGC)
M4 = 260.5*volt*input(:,4)-.6102;  %exhaust air thermocouple (DEGC)

% inlet humidity from DP to RH (testo sensor)
temp = 18;
Es = 6.11*10^((7.5*temp)/(237.7+temp));
M5 = -60+5.625*((1000/250)*volt*input(:,5)-4);
M5 = 6.11*10.^((7.5*M5)./(237.7+M5));
M5 = M5/Es*100;

% exhaust humidity  in %RH (JLC Int.)
M6 = 20*volt*input(:,6);

%creates an array of temperature and RH data
tempRH = [M3 M4 M5 M6];

%call TempRH.m: outputs the average and standard deviation of the
%temperature and %humidity data based on user defined time intervals
[tempRHfinal, stdev] = TempRH(freq, i_start, i_end, tempRH);


%---------------ANALYSIS OF PRESSURE FLUCTUATION DATA-----------------
%User inputs for pressure fluctuation analysis
prompt = {'Evaluation Time Duration (min)','High-Pass filter…
Frequency','Low-Pass Resample Frequency'};
gui_title = 'Input Time Series Analysis Parameters';
lines = 1;
def = {'2','0.1','50'};
user_input_matrix = inputdlg(prompt,gui_title,lines,def);

%sets user inputs as variables
eval_time_min = str2num(user_input_matrix{1});

%converts evaluation time into seconds from minutes
eval_time = eval_time_min*60; %sec
l_stop = str2num(user_input_matrix{2}); %high pass filter in chebychev1
rs_freq = str2num(user_input_matrix{3}); %resample frequency

%chebychev1 filter
[b,a] = cheby1(4,0.01,2*l_stop/freq,'high');
[h,w] = freqz(b,a,400);

%calculates the size of the data set based on user input
evalset =eval_time*freq;

%creates an array from the pressure fluctuation measurements
M1 = 0.01*volt*100000*input(:,1); %windbox kistler (Pa)
M2 = 0.01*volt*100000*input(:,2); %bed kistler in (Pa)
pressure = [M1 M2];

%loop that calculates PSDs and other pressure data analysis
for i = 1:i_end/evalset;


    %time array which is used for plotting data
```

```
time(i,1)=eval_time_min*i;

%places desired pressure data into a new analysis array
px_analysis(1:evalset,1)=pressure((i-1)*evalset+1:i*evalset,1);
px_analysis(1:evalset,2)=pressure((i-1)*evalset+1:i*evalset,2);

%filters the desired pressure data with the chebychev1 filter
px_analysis_filter = filter(b,a,px_analysis);

%average of pressure fluctuation time series
avg_pressure (i,1)= mean(px_analysis_filter(:,1));
avg_pressure (i,2)= mean(px_analysis_filter(:,2));

%-----------standard deviation of pressure fluctuation-------------
stdev_pressure (i,1)= std(px_analysis_filter(:,1));
stdev_pressure (i,2)= std(px_analysis_filter(:,2));


% ----------------average cycle frequency (ACF)--------------------
%resample data to remove higher frequencies
px_analysis_filter_rs = resample(px_analysis_filter,rs_freq,freq);
avg_pressure_rs(1) = mean(px_analysis_filter_rs(:,1));
avg_pressure_rs(2) = mean(px_analysis_filter_rs(:,2));

%counting of axis crossings with resampled data
num_crossings_1 = 0;
num_crossings_2 = 0;

%counts the number of crossings of the mean resampled pressure
  for c = 1:length(px_analysis_filter_rs)-1;
        if px_analysis_filter_rs(c,1) < avg_pressure_rs(1) &...
       px_analysis_filter_rs(c+1,1) > avg_pressure_rs(1);
    num_crossings_1 = num_crossings_1 + 1;
    end
        if px_analysis_filter_rs(c,2) < avg_pressure_rs(2) &...
       px_analysis_filter_rs(c+1,2) > avg_pressure_rs(2);
    num_crossings_2 = num_crossings_2 + 1;
    end
end


% calculation of ACF
ACF(i,1) =  num_crossings_1/eval_time;
ACF(i,2) = num_crossings_2/eval_time;

%-----------------calculation of power spectrum------------------
% number of fast Fourier transforms to get a frequency resolution ~
%0.2 Hz with 400 Hz signal.
NFFT = 2048;

%size of window
win = hamming(NFFT/2);



%Use 'psd' because it is more sensitive with respect to power than
```

```
    %'pwelch'
    [Pxx(:,1),F1] = psd(px_analysis_filter_rs(:,1),NFFT,rs_freq,win,0);
    [Pxx(:,2),F2] = psd(px_analysis_filter_rs(:,2),NFFT,rs_freq,win,0);


    %--------------determination of the dominant frequency-------------
    %finds maximum power and its corresponding index at which it occurs
    [maxpower1,index1] = max(Pxx(:,1));
    [maxpower2,index2] = max(Pxx(:,2));
    %put maximum power into an array
    powerdata (i,1)= maxpower1;
    powerdata (i,2) = maxpower2;

    %use index to find the frequency of the maximum power
    df(i,1)= F1(index1);
    df(i,2) = F2(index2);

    %writes the PSD data to an Excel spreadsheet
    cell =['B', num2str(i+3)];
    xlswrite('data template',Pxx(:,1)', 'WB PxFluct', cell);
    xlswrite('data template',Pxx(:,2)', 'DB PxFluct', cell);

end


%--------------WRITES OTHER DATA INTO EXCEL: SPREADSHEET---------------

%writes power spectra headings into the spreadsheet
xlswrite('data template',F1', 'WB PxFluct', 'B3');
xlswrite('data template',F2', 'DB PxFluct', 'B3');
xlswrite('data template',time, 'WB PxFluct', 'A4');
xlswrite('data template',time, 'DB PxFluct', 'A4');


%Writes temperature and RH data into the spreadsheet
xlswrite('data template',tempRHfinal, 'TRH', 'B3');

%Writes pressure fluctuation analysis data into the spreadsheet
xlswrite('data template',time, 'Px analysis', 'B3');
xlswrite('data template',powerdata, 'Px analysis', 'C3');
xlswrite('data template',df, 'Px analysis', 'E3');
xlswrite('data template',stdev_pressure, 'Px analysis', 'G3');
xlswrite('data template',ACT, 'Px analysis', 'I3');
```

Other functions called by this code:

read_dat.m

```
function z=read_dat(fname,nchann,i_start,i_end)

fid=fopen(fname,'r');
startpoint=fread(fid,1,'short')+(i_start)*nchann*2;
status=fseek(fid,startpoint,-1);

npoints=i_end-i_start+1;
```

```
z=fread(fid,[nchann,npoints],'int16');
z=z';
fclose(fid);
```

TempRH.m:

```
function [tempRHfinal, stdev] = TempRH(freq, i_start, i_end, tempRH);

%User inputs for temperature and RH averaging
prompt = {'Length of time step (min)'};
title_GUI1 = 'Enter the Desired Time Step (min)';
lines = 1;
def = {'1'};

%defines time step input as a variable
user_input_matrix = inputdlg(prompt,title_GUI1,lines,def);
timestep = str2num(user_input_matrix{1});

%number of data points to average
points = timestep*60*freq;

%counters
sum = 0;
count = 0;
%creation of a new array for average and standard deviation values
tempRHavg = [];
stdev = [];

%loop that calculates the average and standard deviation data
count=0;
for k= i_start:points:i_end-points+1;
    count = count +1;
    mean1 = mean(tempRH(k:k-1+points,1));
    mean2 = mean(tempRH(k:k-1+points,2));
    mean3 = mean(tempRH(k:k-1+points,3));
    mean4 = mean(tempRH(k:k-1+points,4));

    stdev1 = std(tempRH(k:k-1+points,1));
    stdev2 = std(tempRH(k:k-1+points,2));
    stdev3 = std(tempRH(k:k-1+points,3));
    stdev4 = std(tempRH(k:k-1+points,4));

    tempRHavg(count,1:4)= [mean1 mean2 mean3 mean4];
    tempRHstdev (count, 1:4)= [stdev1 stdev2 stdev3 stdev4];
end

%initialization of arrays for writing outputs
tempRHfinal  = [];
time = timestep:timestep:i_end/freq/60;
timefinal = time';
tempRHfinal=[timefinal(:,1), tempRHavg(:,1:4)];
stdevfinal =[timefinal(:,1), tempRHstdev(:,1:4)];
```